ISSN 0915-6348

NATIONAL INSTITUTE FOR FUSION SCIENCE

Physics and Applications of High Energy Density Plasmas -Extreme state driven by pulsed electromagnetic energy

Dec.20-21, 2001
National Institute for Fusion Science

Edited by K. Horioka

(Received - June 15, 2002)

NIFS-PROC-51 June 2002

This report was prepared as a preprint of work performed as a collaboration reserch of the National Institute for Fusion Science (NIFS) of Japan. This document is intended for infomation only and for future publication in a journal after some rearrangements of its contents.

Inquiries about copyright and reproduction should be addressed to the Research Information Center, National Institute for Fusion Science, Oroshi-cho, Toki-shi, Gifu-ken 509-5292 Japan.

RESEARCH REPORT
NIFS-PROC Series

TOKI, JAPAN

Physics and Applications of High Energy Density Plasmas
—Extreme state driven by pulsed electromagnetic energy

Edited by Kazuhiko Horioka

December 20-21, 2001
National Institute for Fusion Science
Toki, Japan

Abstract

The papers presented at the symposium on "Physics and application of high energy density plasmas, held December 20-21, 2001 at NIFS" are collected in this proceedings. The topics covered in the meeting include dense z-pinches, plasma focus, intense charged particle beams, intense radiation sources, discharge pumped X-ray lasers, their diagnostics, and applications of them. The papers reflect the present status and trends in the research field of high energy density plasmas.

Keywords: z-pinches, plasma focus, X-ray sources, X-ray lasers, intense charged particle beams, material processing, pulse power technology, medical applications

PREFACE

The symposium "Physics and Applications of High Energy Density Plasma" was organized as a collaboration research program of National Institute for Fusion Sciences (NIFS), and held December 20-21, 2001 at NIFS, Toki. During the 2-days symposium, 29 papers were presented and totally 48 scientists including peoples abroad attended in the discussion. These proceedings retain all the presentations, and I think, they are well reflecting the present status of the research field in high energy density plasma in Japan.

This research program started in 1990 and the efforts have been continued for more than 10 years. During the intervening period, research on high energy density plasmas has evolved into a well-developed subject in the field of plasma physics, plasma engineering and pulse power technology.

As the field of high energy density plasma has a multi-disciplinary nature, the extensive discussion of related subjects is difficult in conventional scientific meetings. The purpose of the workshop has been to provide a forum to discuss important technical developments, some applications, increased understandings, new trends, and also the future prospects in the field of high energy density plasmas. Especially, keeping this field attractive for younger scientists has been of primary concern for all of the organizing members of this program. We wish to extend our thanks to all of the authors, participants, and the member of advisory council of NIFS.

Kazuhiko Horioka
Department of Energy Sciences
Tokyo Institute of Technology

CONTENTS

Characteristics of soft-Xrays generated from plasma focus device with gas-puff operation · 1
N.Iwami, K.Shimoda and M.Sato (Gunma University)

Spatial structure and X-ray emission of a gas-puff Z-pinch plasma · · · · · · · · · 11
S.Narisawa and K.Takasugi (Nihon University)

Characteristics of X-ray radiation from a gas-puff Z-pinch plasma · · · · · · · · · 17
N.Akiyama and K.Takasugi (Nihon University)

Investigation of stability and X-ray spectrum in gas-puff Z-pinch plasmas driven by inductive energy storage pulsed power generator with a plasma opening switch · · 24
K.Murayama, I.Fukudome, Y.Teramoto, S.Katsuki and H.Akiyama
(Kumamoto University)

Optical observation of plasma produced from metal powder · · · · · · · · · · · · 32
T.Yokoyama, T.Kuraoka, K.Ogasawara, S.Ibuka, K.Yasuoka and S.Ishi
(Tokyo Institute of Technology)

Consideration of scaling laws in plasma focus devices · · · · · · · · · · · · · · · 39
M.Kashani and T.Miyamoto (Nihon University)

Dynamics of capillary discharge plasmas and lasing conditions · · · · · · · · · · 45
N.Sakamoto, G.Niimi, M.Nakajima, E.Hotta and K.Horioka
(Tokyo Institute of Technology)

A study on relative populations and gain coefficients of neon-like krypton for fast moving plasma in cylindrical discharges · 55
M.Masnavi, T.Kikuchi, M.Nakajima and K.Horioka (Tokyo Institute of Technology)

Observation of plasma motion in a coaxial plasma opening switch with a chordal laser interferometer · 73
Y.Teramoto, S.Kohno, H.Urakami, S.Katsuki and H.Akiyama
(Kumamoto University)

Propagation of pulsed streamer discharges in atmospheric air · · · · · · · · · · · 82
T.Namihira, H.Hori, S.Katsuki and H.Akiyama (Kumamoto University)

Simulation of non-linear coaxial line using ferrite beads · · · · · · · · · · · · · · 91
S.Furuya, H.Matsumoto, K.Tachi, S.Takano and J.Irisawa
(Nagaoka University of Technology

Experimental support for a ferrite-core model for supertrons · · · · · · · · · · · 97
H.Matsuzawa and K.Mikami (Yamanashi Univeristy)

Generation of pulsed ion beam by repetitive pulsed power generator "ETIGO-IV" · · 102
Y.Hayashi, W.Jiang and K.Yatsui (Nagaoka University of Technology)

Beam emittance and output waveforms of high-flux laser ion sources · · · · · · · · 108
M.Nakajima, M.Asahina, M.Yoshida, J.Hasegawa, M.Ogawa and K.Horioka
(Tokyo Institute of Technology)

Transport window of high current heavy ion beams in a final buncher · · · · · · · · 113
T.Kikuchi, M.Nakajima and K.Horioka (Tokyo Institute of Technology)

Characteristics of energetic ions produced in plasma focus · · · · · · · · · · · · · 120
M.Shiotani, K.Takao, T.Honda, I.Kitamura, T.Takahashi and K.Masugata
(Toyama Univeristy)

Development of bipolar pulse accelerator · 127
K.Kawahara, Y.Doi, I.Maetubo, C.Mitsui, I.Kitamura, T.Takahashi, K.Masugata, Y.Tanaka, H.Tanoue and K.Arai (Toyama University)

Measurement of the electron energy distribution using electrostatic analyzer in the plasma disturbed by an intense relativistic electron beam · · · · · · · · · · · · · 132
H.Morishita, M.Nitta, H.Koguchi, R.Ando and K.Kamada (Kanazawa University)

Trains of electron pulses generation using multi-stage cavities · · · · · · · · · · · 141
M.Kamada, M.Mori, K.Sugawara, Y.Yamada, K.Kurihara, H.Shirasaka, T.Nishiguchi, R.Ando and K.Kamada (Kanazawa University)

Generation of nanosecond S band microwave pulses based on superradiance ・・・・151
N.S.Ginzburg, I.V.Zotova, R.M.Rozental, A.S.Sergeev, M.Kamada, K.Sugawara, K.Kurihara, H.Shirasaka, R.Ando and K.Kamada (Kanazawa University)

Study on ion induced secondary emission electron gun ・・・・・・・・・・・・・・・160
P.R.Chalise, M..Watanabe, A.Okino and E.Hotta (Tokyo Institute of Technology)

Modification of BSCCO surface by excimer laser annealing ・・・・・・・・・・・・167
A.Ibi, T.Akitsu and H.Matsuzawa (Ymanashi University)

NOx removal in distant gas chamber by pulsed, intense relativistic electron beam ・172
G.Imada, T.Sakurai, N.Ohshima and K.Yatsui (Nagaoka University of Technology)

Characteristics of deposition process of thin films by ion-beam evaporation ・・・・178
S.Kitayama, F.Endo, T.Suzuki, H.Suematsu, W.Jiang and K.Yatsui
(Nagaoka University of Technology)

Substrate bias effect on crystallinity of polycrystalline silicon thin films prepared by pulsed ion-beam evaporation method ・・・・・・・・・・・・・・・・・・・・・・・188
F.Ali, M.Gunji, S.C.Yang, T.Suzuki, H.Suematsu, W.Jiang and K.Yatsui
(Nagaoka University of Technology)

Pulsed power laser radiation effects on *mycoplasma agalactiae* ・・・・・・・・・・196
C.Z.Dinu, C.Grigoriu, M.Dinescu, F.Pascale, A.Popovici, L.Gheorghescu, A.Cimileanu, E.Avram and K.Yatsui (Nagaoka University of Technology)

Characteristics of a high-current pulse glow discharge ・・・・・・・・・・・・・・203
K.Takaki, D.Taguchi, S.Mukaigawa and T.Fujiwara (Iwate University)

Optimization to synthesize nanosize powder of AlN by pulsed wire discharge ・・・・213
C.Cho, Y.Kinemuchi, T.Suzuki, H.Suematsu, W.Jiang and K.Yatsui
(Nagaoka University of Technology)

Preparation of nanosize carbon powders by pulsed wire discharge ・・・・・・・・・221
C.Minami, T.Hirata, R.Hatakeyama, Y.Kinemuchi, T.Suzuki, H.Suematsu, W.Jiang and K.Yatsui (Nagaoka University of Technology)

List of participants

Akiyama.H	Kumamoto University
Akiyama.N	Nihon University
Chalise.C.C	Tokyo Institute of Technology
Chiba.T	Nihon University
Cho.C	Nagaoka Uiniversity of Technology
Fazlat.A	Nagaoka Uiniversity of Technology
Furuya.S	Nagaoka Uiniversity of Technology
Ginzburg.H	Kanazawa University
Grigoriu.G	Nagaoka Uiniversity of Technology
Hayashi.Y	Nagaoka Uiniversity of Technology
Honda.T	Toyama University
Horioka.K	Tokyo Institute of Technology
Ibi.A	Yamanashi University
Imada.G	Nagaoka Uiniversity of Technology
Ishii.S	Tokyo Institute of Technology
Iwami.N	Gunma University
Jiang.W	Nagaoka Uiniversity of Technology
Kamada.K	Kanazawa University
Kamada.M	Kanazawa University
Kashani.M	Nihon University
Kawahara.Y	Toyama University
Kikuchi.T	Tokyo Institute of Technology
Kitayama.S	Nagaoka Uiniversity of Technology
Kondo.H	Gunma University
Kuraoka.T	Tokyo Institute of Technology
Masnavi.M	Tokyo Institute of Technology
Masugata.K	Toyama University
Matsuzawa.H	Yamanashi University
Minami.C	Nagaoka Uiniversity of Technology
Miyamoto.T	Nihon University
Morishita.H	Kanazawa University
Murayama.K	Yatsusiro National College of Technology

Nakajima.M	Tokyo Institute of Technology
Namihira.T	Kumamoto University
Narisawa.S	Nihon University
Okino.A	Tokyo Institute of Technology
Ritoku.A	Kanazawa University
Sakamoto.N	Tokyo Institute of Technology
Sato.M	Gunma University
Shiotani.M	Toyama University
Someya.T	Utsunomiya University
Takagi.K	Iwate University
Takasugi.K	Nihon University
Tazima.T	National Institute for Fusion Science
Teramoto.Y	Kumamoto University
Teshima.R	Toyama University
Yatsui.K	Nagaoka Uiniversity of Technology
Yokoyama.T	Tokyo Institute of Technology

CHARACTERISTICS OF SOFT X-RAYS GENERATED FROM PLASMA FOCUS DEVICE WITH GAS-PUFF OPERATION

N. Iwami, K. Shimoda and M. Sato

Department of Electronic Engineering, Gunma University,
1-5-1 Tenjin-cho, Kiryu, 376-8515, Japan

ABSTRACT

We performed the experiments with the small plasma focus device. In order to make the plasma with higher temperature, we tried the experiments with gas-puff operation. The effect by gas-puff operation was verified by the pinhole photograph and by the PIN diode signals in the case of oxygen gas. Although the intensities of the soft X-rays became high, the line spectra in the grazing incident spectrometer were not obtained. The silicon nitride membrane was used as the filter in the PIN diode and the pinhole camera. The difference from the beryllium foil was verified by the experimental results with these measurement tools

I. Introduction

The plasma focus device is well known as an inexpensive and compact source of intense soft X-rays. It has been used for number of applications: soft X-ray microscopy[1], soft X-ray lithography[2], X-ray backlighting for high-density plasmas[3]. The soft X-rays ranged from 2.33 to 4.37 nm (so-called water window) are required for the soft X-ray microscopy, because the soft X-rays ranged in these wavelengths are not absorbed by oxygen and are absorbed by carbon; those can be used to observe living cells. We tried generation of the soft X-rays ranged in these wavelengths by using a gas-puff Z-pinch device[4], but the intensities of the generated X-rays were very low. So we started the experiments with a small plasma focus device as the soft X-ray source[5].

The small plasma focus device was successfully operated, but the intensities of the soft X-rays were still low. Therefore line spectra were not obtained with a crystal spectrometer in the case of argon gas[5]. In order to make the plasma with higher temperature, we tried the experiments with gas-puff operation[6,7]. In the case of gas-puff operation, a small amount of gas is injected from the top of the inner electrode through a fast opening valve. The plasma focus device is operated with only hydrogen gas, and the pinched current sheet compress the injected gas. In this operation heavier ions are not contained in the current sheet. So the velocity of the current sheet become high, and the plasma is compressed to the smaller radius. As a result it is predicted that the plasma with higher temperature is generated.

In our experiments, hydrogen gas was used as a working gas, and a small amount of oxygen or nitrogen gas was mixed or puffed to the working gas. Line spectra generated from these gases are ranged in the water window region[8]. For soft X-rays ranged in the water window region, a beryllium foil is not able to use as the filter due to its transmittance for the soft X-rays. So a silicon nitride membrane was used as the filter. Since this membrane makes to pass through the soft X-rays ranged in the water window region, the membrane is usable in the case of the oxygen and nitrogen gas. These membranes were used in the PIN diode and the pinhole camera. The results of preliminary experiments are

presented in this paper.

II. Experimental Setup

Figures 1 show the schematic drawings of the experimental setup. Configuration of a plasma focus device and an external circuit are shown in Fig. 1 (a). The plasma focus device consists of an inner electrode, an outer electrode and an insulator. The outer electrode is constructed from 24-copper rods of which diameters are 8 mm; the geometry of the plasma focus device is like a square cage. The inner diameter of the outer electrode is 100 mm.

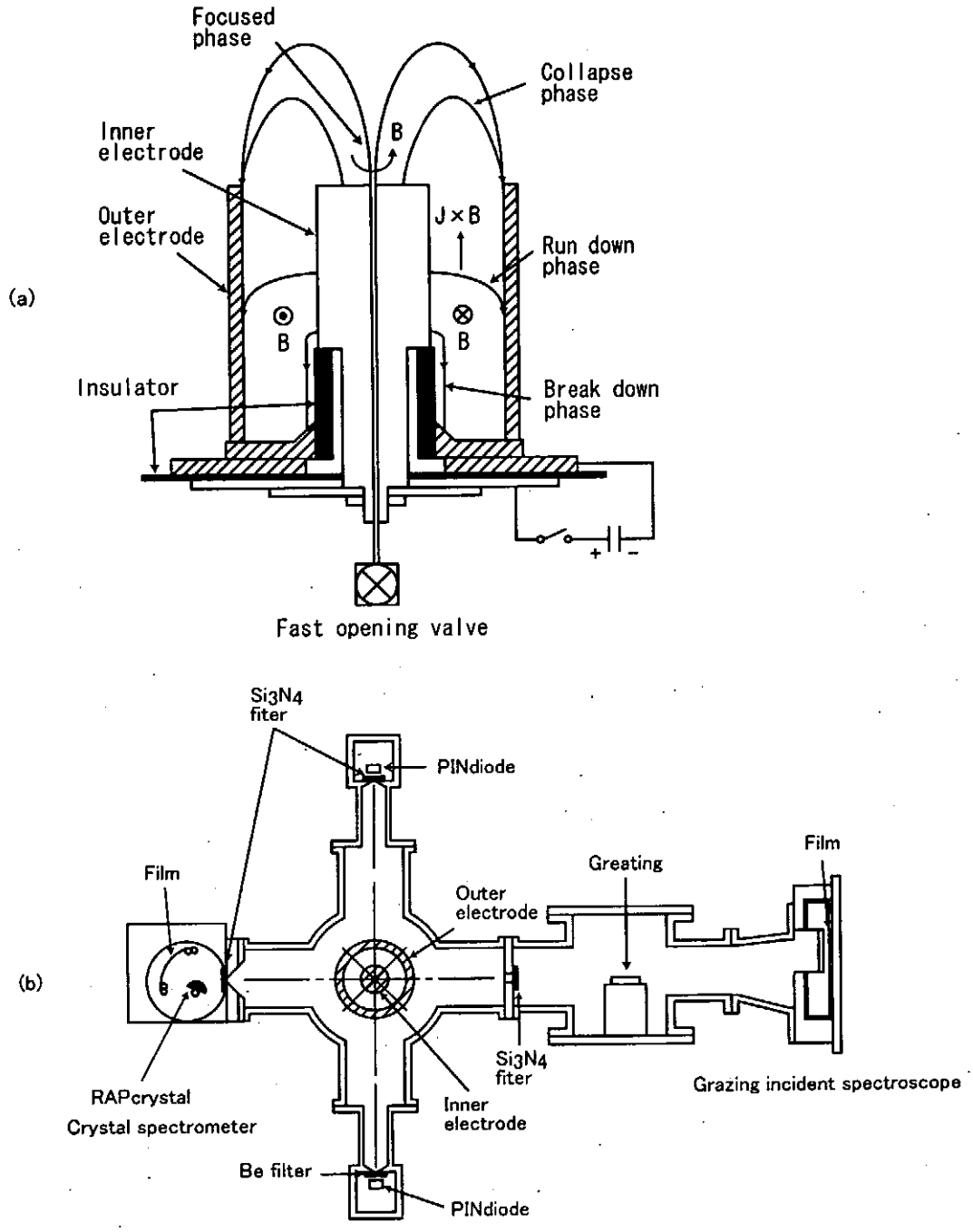

Fig. 1 Schematic drawings of experimental setup; configuration of plasma focus device (a), location of measurement tools (b).

In order to make discharge with gas-puff operation by a fast opening valve[6], a small hole is drilled along the centerline of the inner electrode. The diameter of the hole is 8 mm at the top of the anode. The outer diameter of the inner electrode is 50 mm. The lengths of the electrodes are 155 mm. The insulator is made of a Pyrex glass, and the outer diameter and the length of it are 55 and 51 mm, respectively. The maximum voltage and the maximum stored energy of a condenser bank are 30 kV and 25 kJ, respectively. In all the experiments reported here, the condenser bank was used with the charged voltage of 15 kV. Hydrogen gas was used as a working gas, and a small amount of nitrogen or oxygen gas was mixed to the working gas. In the case of gas-puff operation, only hydrogen gas was used as a working gas, and a small amount of nitrogen or oxygen gas was puffed through the fast opening valve at the top of the anode. In this case the fast opening valve was firstly fired, and after several milliseconds the condenser bank was fired.

In the experiments, two PIN diodes, a crystal spectrometer and a grazing incident spectrometer were located as shown in Fig. 1 (b). The PIN diodes were used to detect the soft X-rays generated from the pinched plasma. In front of one PIN diode, the beryllium foil of which thickness was 25 micrometers was set as a filter. In front of another PIN diode, a silicon nitride membrane was set as a filter. The thickness of the silicon nitride membrane was 0.1 micrometers. The membrane was also coated with aluminum of which thickness

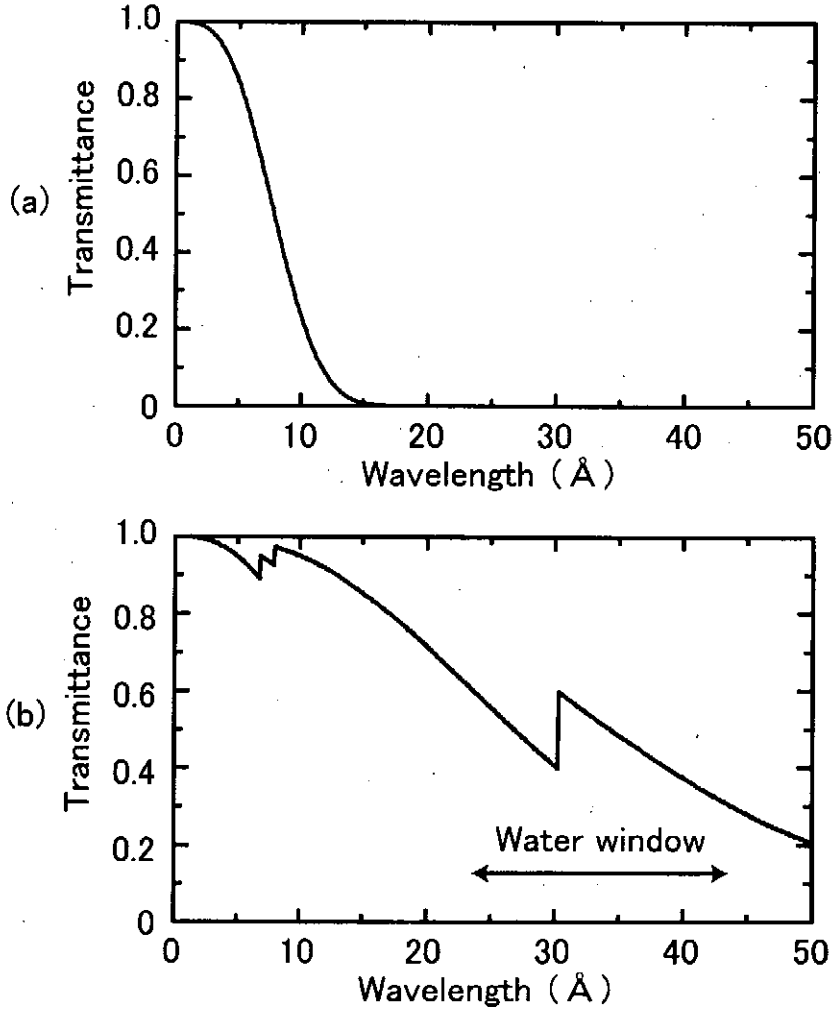

Fig. 2 Transmittances of the filters in the function of the wavelengths of the soft X-rays; the beryllium foils (a), the silicon nitride membrane (b).

was 0.05 micrometers to prevent incidence of visible lights. The membrane was made on the part of the silicon substrate, and the geometry of it was a square. The length of a bit of the square was approximately 1 mm. Figures 2 show the transmittances of the filters for the soft X-rays. As shown in Fig. 2 (a), the soft X-rays ranged in the water window region are not able to pass through the beryllium foil of which thickness is 25 micrometers. Figure 2 (b) shows the transmittances in the case of the silicon nitride membrane. By using the membrane, the transmittances of the soft X-rays ranged in the water window region are obtained by several tens of percents. Since the membrane does not have a cut-off for shorter wavelength of the X-rays, the signals obtained with these two PIN diodes were compared.

The crystal spectrometer consists of a slit, a convex rubidium acid phthalate (RbAP) crystal and a film (KODAK TRI-X) [7]. A pinhole image by the soft X-rays was made on the film of the spectrometer. This pinhole image is only used, and is not used as the spectrometer. The grazing incident spectrometer was adapted to the vacuum vessel. The spectrometer has a grating coated with gold, and it is able to analyze the X-rays of which wavelengths range from 2 to 5 nm. The grating had 2400 grooves per millimeter, and the grooves were ruled by a varied space. As a result the grating has a focusing property, and has a flat field at 236 mm from the center of it[4]. The film as the detector is set as shown in Fig. 1 (b). Many shots were superimposed with this grazing incident spectrometer, but the clear line spectra were not obtained. In several shots of the experiments, the grazing incident spectrometer was replaced by a streak camera (IMACON-700). By using the streak photographs obtained with the streak camera, the pinched velocities of the plasmas are compared between the shot with admixture of gases and the shot with gas-puff operation.

III. Experimental Result

The waveforms of a discharge current, di/dt and the signals of the PIN diodes are shown in Figs. 3. The waveforms shown in Figs. 3 were obtained by the experiments with 11.3 % admixture of oxygen gas (a) and 9.3 % admixture of nitrogen gas (b) to hydrogen gas. The total pressures of the working gases in the case of the figure (a) and (b) were 1.5 torrs. The experiments were performed with changing the mixture rate of the gases, and the maximum voltages of the PIN diode output are displayed in the function of the mixture rate (Fig. 4). In Fig. 4, the voltages of the PIN diode output do not largely depend on the mixture rates, but those have peak values at 7 or 14 %. Therefore the experiments reported here were performed at these mixture rates. The experiments were also performed at the total gas pressure ranged from 1.5 to 2.5 torrs. In the figures, the discharge currents reach to about 550 kA by 2 microseconds from initiation of discharge, and the dips are seen at the tops of the total currents. The difference by changing the admixture gas was not distinguished in the signals of the total currents. The waveforms of di/dt are displayed because the pinching of the current sheet is clearly seen from the waveforms. Sharp spikes appear in the signals of the PIN diodes, and appearances of these spikes are coincident with the timings of the dips in the discharge currents. After that one or two more spikes appear in the signals of the PIN diodes with the beryllium foil. The soft X-rays forming these spikes are generated from the electrode plasmas. This fact had been confirmed with a time resolved X-ray pinhole camera[5]. In the signals of the PIN diodes with the silicon nitride membrane, the voltages decay slowly after reaching to the peak voltages. It is considered that these decay parts in the signals composed of the soft X-rays generated by the continuum radiation. The differences between the signals with the beryllium foil and with the silicon nitride membrane mean generation of the soft X-rays having several tens of angstroms in wavelength. The

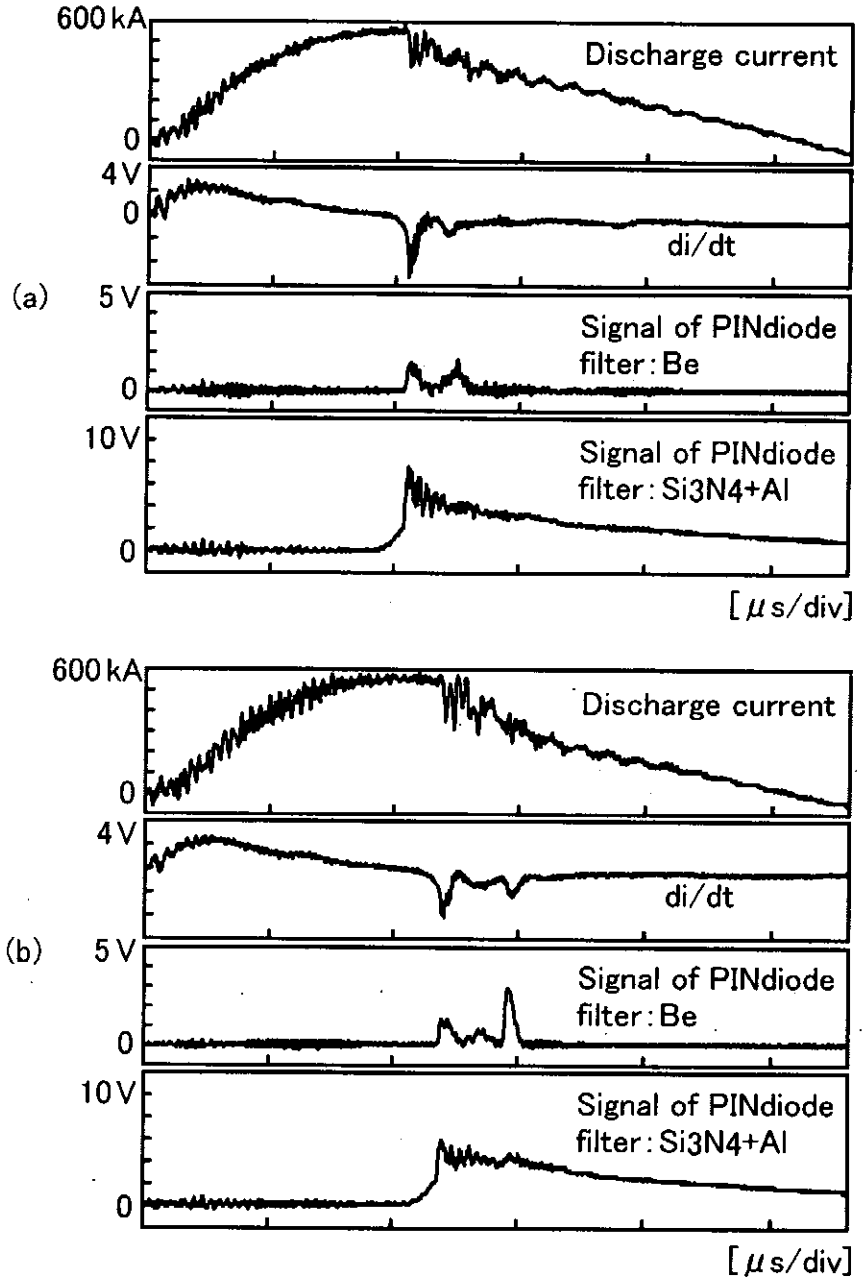

Fig. 3 Waveforms of discharge current, di/dt and signals of PIN diodes with admixture of oxygen gas (a) and nitrogen gas (b).

experiment with the grazing incident spectrometer is required to make clear decision generation of the soft X-rays ranged in the water window region.

The waveforms of the discharge currents, di/dt and the signals of the PIN diodes are also shown in Figs. 5. The waveforms shown in Figs. 5 were obtained by the experiments with gas-puff operation of oxygen gas (a) and nitrogen gas (b). Initially only hydrogen gas is used as the working gas, and the initial pressures of hydrogen gas were 3 torrs. In the experiment, the fast opening valve is firstly operated, and after about 2 ms from opening of the valve discharge of the condenser bank is started. The experiments were performed with changing the delay time, and the maximum voltages of the PIN diode output are displayed in the function of the delay time (Fig. 6). In Fig. 6, the voltages of the PIN diode output do not

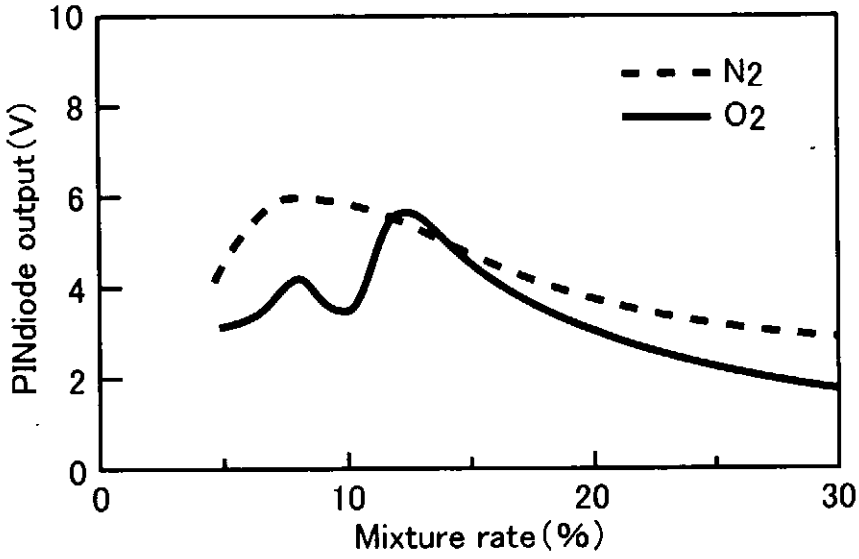

Fig. 4 PINdiode output voltage in the function of mixture rate of gases.

largely depend on the delay times, but those have relatively large values from 2.4 to 2.5 ms. Therefore the experiments reported here were performed by these delay times. The almost all the waveforms shown in Figs. 5 are not largely different from those shown in Figs. 3, but the peak voltage of the PIN diode output with the silicon nitride membrane shown in Fig. 5 (a) becomes higher than that in Fig. 3 (a); the peak voltage increases approximately 50 %. This result is caused by the effect of gas-puff operation. The increase of the peak voltage is not seen in the case of nitrogen gas.

Pinhole photographs obtained with admixture of oxygen gas are shown in Figs. 7. In these figures, I.E. shows the position of the top of the inner electrode. The photographs shown in Figs. 7 (a) and (b) were taken with the silicon nitride membrane and the beryllium foil, respectively. The difference in these figures is caused by the difference in the transmittances of the filters for the soft X-rays shown in Figs. 2. For example, it is considered that branched lighting areas around the plasma column are due to the soft X-rays generated by the continuum radiation. These soft X-rays have several tens of angstroms in wavelength, and are only detected with the silicon nitride membrane. Since the intensities of the soft X-rays are displayed as the blackness of the images, it is distinguished that the intensity of the plasma column in Fig. 7 (a) is stronger than that in Fig. 7 (b). This fact shows that the soft X-rays having several tens of angstroms in wavelength are generated from the plasma column.

Figures 8 show pinhole photographs obtained with the silicon nitride membrane. These images were obtained with admixture of gases or with gas-puff operation. The conditions are shown in Figs. 8. From comparison of the images, the intensities in the case of gas-puff operation slightly become higher than that in the case of admixture of gases. From the result by the signals of PIN diode output, the intensity of the soft X-rays does not increase in the case of nitrogen gas. This difference is originated by the difference in field of view of each measurement tool; the soft X-rays generated from large areas are received with the PIN diode, but the soft X-rays generated from each position are compared in the pinhole photographs. In the case of gas-puff operation, localized emitting areas are seen. This may be caused by the distribution of the injected gases.

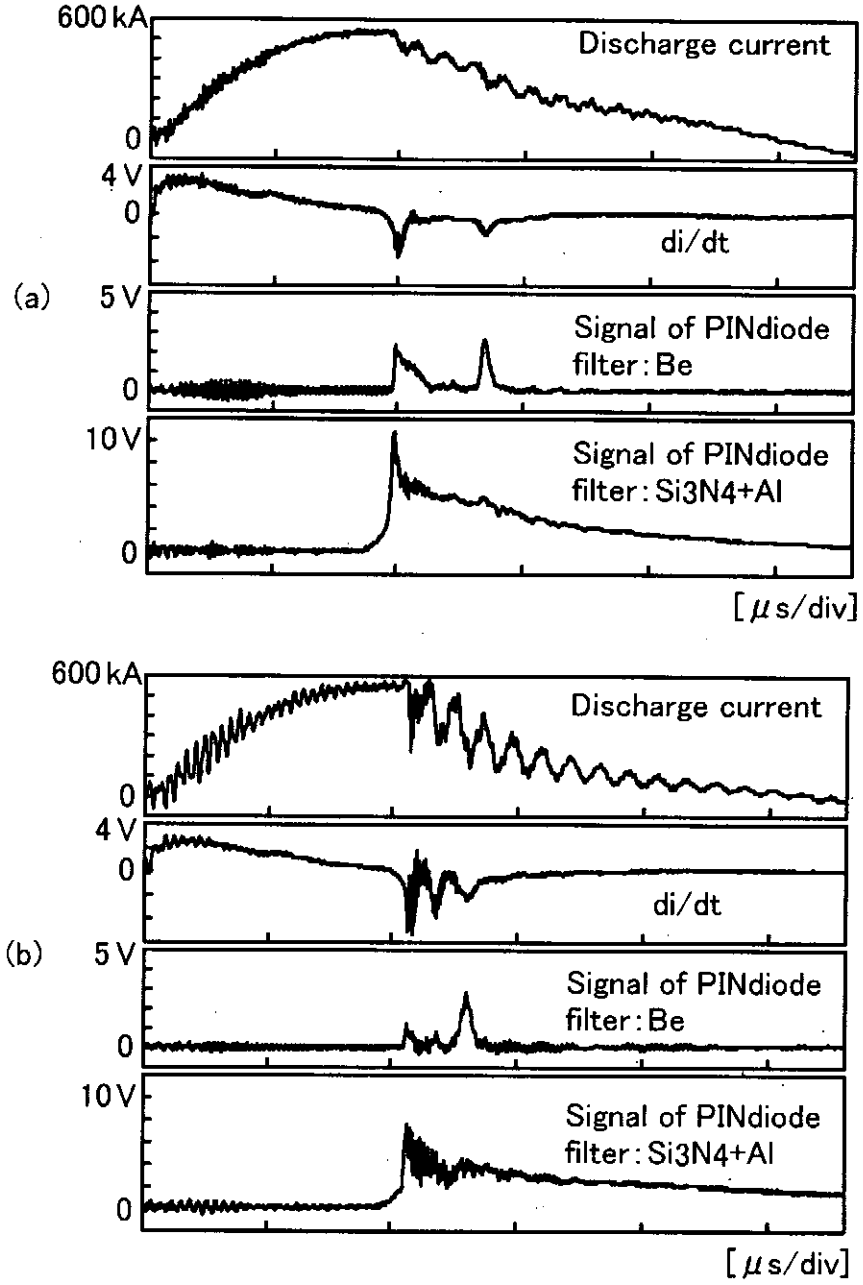

Fig. 5 Waveforms of discharge current, di/dt and signals of PIN diodes with gas-puff operation of oxygen gas (a) and nitrogen gas (b).

Figures 9 show the streak photographs of the pinched plasmas. The streak photographs were taken with the streak camera through the slit located at 5 mm from the top of the inner electrode. Figure 9 (a) was taken with admixture of oxygen gas to hydrogen gas. The total pressure and the mixture rate of the working gas were 1.6 torrs and 11.3%, respectively. In Fig. 9 (a), the plasma is focused on the centerline of the diode, and after that the plasma disappears. The lifetime of the focused plasma is approximately 30 ns. The pinched velocity of the plasma is estimated by 1.3×10^5 m/sec from Fig. 9 (a). Figure 9 (b) was taken with gas-puff operation of oxygen gas to hydrogen gas. The initial pressure of hydrogen gas and the delay time were 3.0 torrs and 2.3 ms, respectively. In Fig. 9 (b), the plasma is also focused on the centerline of the diode, and after that the plasma disappears.

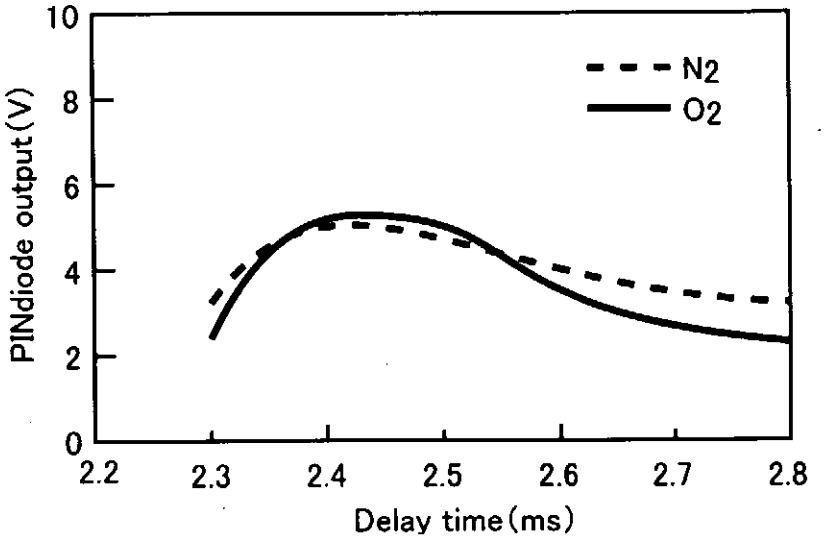

Fig. 6 PINdiode output voltage in the function of delay time from opening of the fast opening valve.

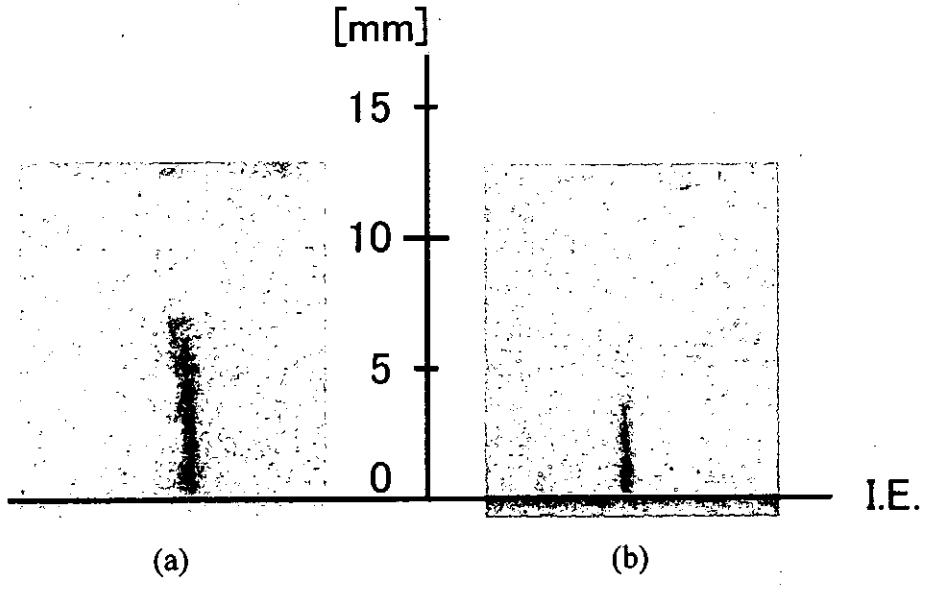

Fig. 7 Pinhole photographs obtained with the silicon nitride membrane (a), the beryllium (b).

From Fig. 9 (b), the lifetime and the pinched velocity of the focused plasma is obtained by 14 ns and 1.8×10^5 m/sec, respectively. From comparison of these two photographs, it is made clear that the thickness of the current sheet in Fig. 9 (a) is thicker than that in Fig. 9 (b), and the pinched velocity of the plasma in Fig. 9 (b) is faster than that in Fig.9 (b). These results are caused by difference in composition of ions in the current sheet; oxygen ions are contained in the current sheet in Fig 9 (a) and only hydrogen ions are contained in the current sheet in Fig 9 (b).

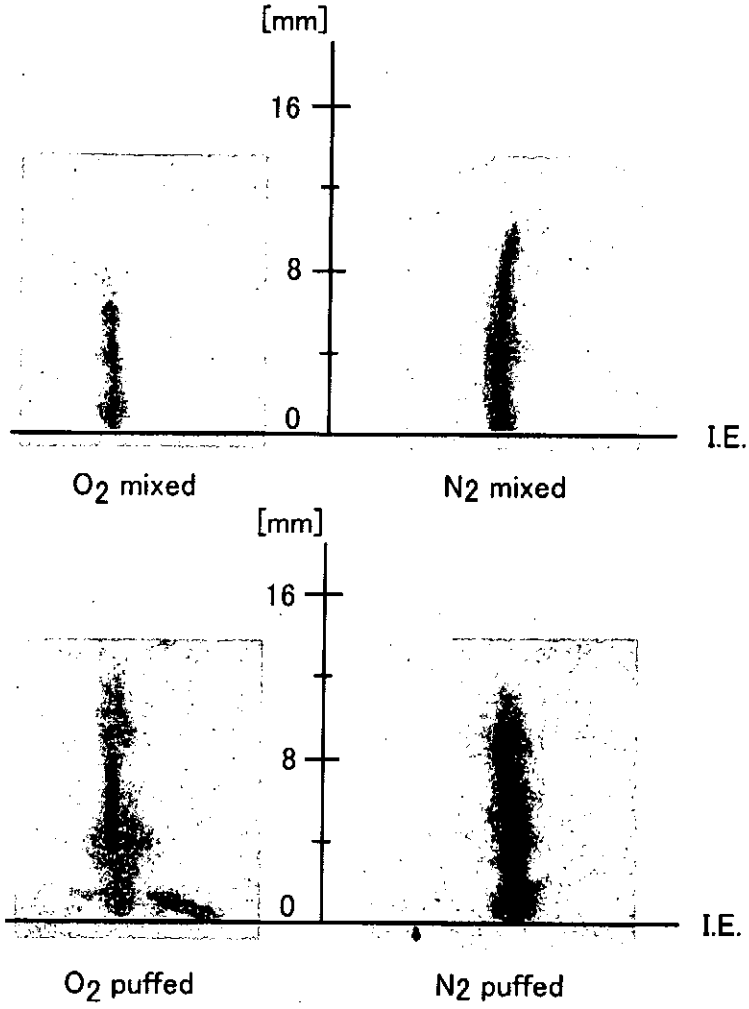

Fig. 8 Pinhole photographs obtained with the silicon nitride membrane.

IV. Summary

We performed the experiments with the small plasma focus device. In order to make the plasma with higher temperature, we tried the experiments with gas-puff operation. The effect by gas-puff operation was verified by the pinhole photograph and by the PIN diode signals in the case of oxygen gas. Although the intensities of the soft X-rays became high, the line spectra in the grazing incident spectrometer were not obtained. The silicon nitride membrane was used as the filter in the PIN diode and the pinhole camera. The difference from the beryllium foil was verified by the experimental results with these measurement tools. Further experiments are planed with 120 kJ condenser bank.

References

1) M. Howells, J. Kirz and D. Sayre, Sci. Am., **264** (1991) 42.
2) Y. Kato, I. Ochiai, Y. Watanabe and S. Murayama, J. Vac. Sci. Technol., **B6** (1988) 195.
3) F. Beg, I. Ross, A. Lorenz, J. Worley, A. Dangor and M. Haines, J. Appl. Phys., **88** (2000) 3225.
4) H. Maeda, K. Shimoda and M. Sato, NIFS-PROC-45 (2000) 58.

5) H. Itano, N. Iwami, K. Shimoda and M. Sato, NIFS-PROC-50 (2001) 131.
6) P. Rowekamp, G: Decker, W. Kies, B. Lucas, F. Schmitz, G. Ziethen, D. Simanovskii and S. Bobashev, Proc. 11th Int. Conf. High Power Particle Beams, Prague, (1996) 174.
7) T. Yanagidaira, K. Shimoda, Y. Ono and K. Hirano, Rev. Sci. Instrum., **71** (2000) 88.
8) A. Krejci, J. Raus, V. Piffl, V. Golubev, Y. Platonov, E. Krousky and O. Renner, IEEE Trans. Plasma Sci., **21** (1993) 584.

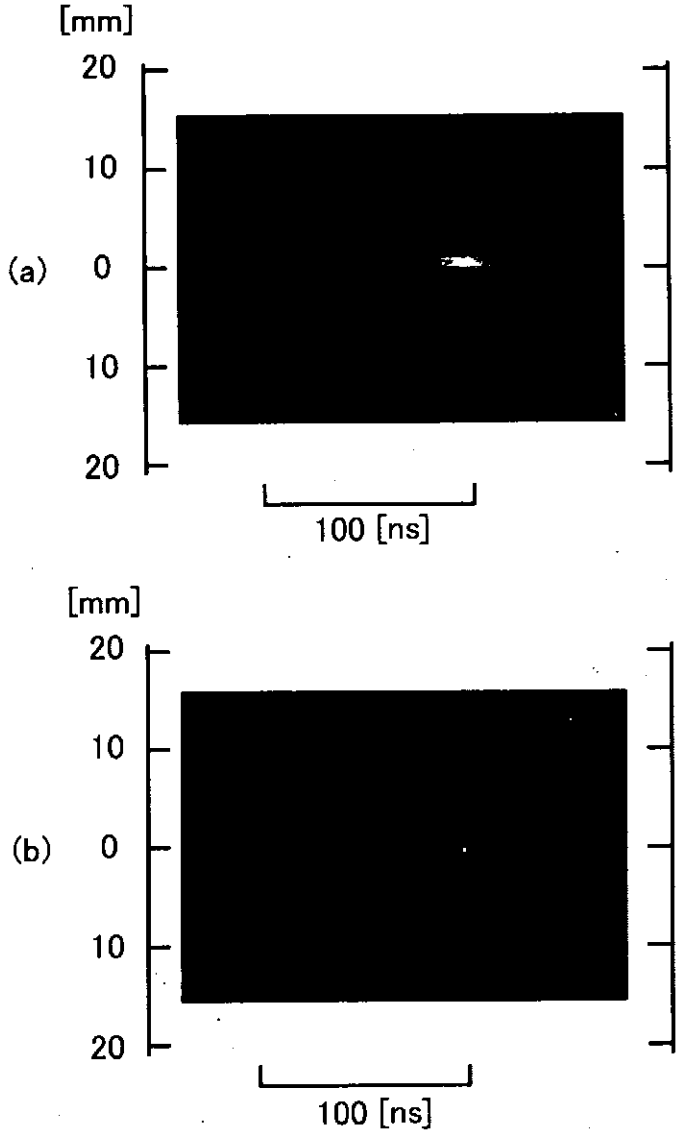

Fig. 9 Streak photographs of pinched plasmas with admixture of oxygen gas (a), gas puff operation (b).

SPATIAL STRUCTURE AND X-RAY EMISSION OF A GAS-PUFF Z-PINCH PLASMA

S. Narisawa[+] and K. Takasugi

Atomic Energy Research Institute, Nihon University
[+]College of Science and Technology, Nihon University
1-8-14 Kanda-surugadai, Chiyoda-ku, Tokyo 101-8308, JAPAN

ABSTRACT

Spatial and spectral characteristics of Ar gas-puff z-pinch plasma were investigated using a convex crystal spectrograph. Radial distribution of He-like Ar line corresponded to hot spots. H-like Ar line was observed in Cu electrode experiment. K_α lines of metal atoms had a wide distribution, which corresponded to cloud structure of x-ray image. Fe K_α spectrum was again observed in Al electrode experiment.

I. Introduction

As gas-puff z-pinch plasma is reproducible and easy in handling, it is noticed as a repetitive radiation source of x-ray. Hot spots generated in the pinch column are strong source of radiation. Spatial structure of hot spots was analyzed, and it was found to be well related to the spatial mode of MHD instability.[1-4] Cloud structure of x-ray image has been observed in gas-puff z-pinch experiment,[5] but the characteristics and mechanism of generation have not been clarified.

Spectra of x-ray radiation emitted from gas-puff z-pinch plasma have been measured, and K-shell radiations of Ar ions have been observed.[6] In order to observe wide spectral range of x-ray radiation, a convex crystal spectrograph was employed. As the spectrograph has no focusing spatial image of selected spectrum can be obtained.

In this research spectral and spatial characteristics of x-ray radiation emitted from Ar gas-puff z-pinch plasma was studied using a convex crystal spectrograph. Axial distribution of x-ray was also obtained by attaching a vertical slit. Spatial structures of K-shell radiations of Ar ions were investigated, and spectra for cloud structure were obtained.

II. Experimental Setup

Figure 1 shows outline of the SHOTGUN z-pinch device. The capacitor bank consists of 24 μF high-speed capacitors, which is charged up to 25 kV (7.5 kJ). Gas is injected through a hollow nozzle mounted on the anode using a high-speed electromagnetic gas valve. Ar gas is used in the experiment. The interval between the electrodes is 30 mm. The cathode has many holes in order not to prevent the gas flow. The electrode material is Cu or Al.

Rogowski coils are installed in both electrodes to measure discharge currents. The anode coil measures the input electric current into the discharge chamber, and the cathode coil measures the electric current through the z-pinch column. A discharge probe is installed in the point of the gas nozzle, which detects the emission of the gas from the gas valve. Trigger signal of main discharge refers to this signal, and this system ensures the reproducibility of discharge.

A convex crystal spectrograph, which is small and mobile, is employed for the observation of wide spectral range of x-ray emission. As the spectrograph has no focusing, it can take spatial information simultaneously (Figure 2). A mica crystal ($2d$ = 19.884 Å) is used in this device. This crystal has the characteristic that reflectance is high for higher order reflection with odd number. The radius of curvature of the crystal is 19.5mm, and the radius of x-ray film is 75 mm. The x-ray films used here was Kodak DEF-392.

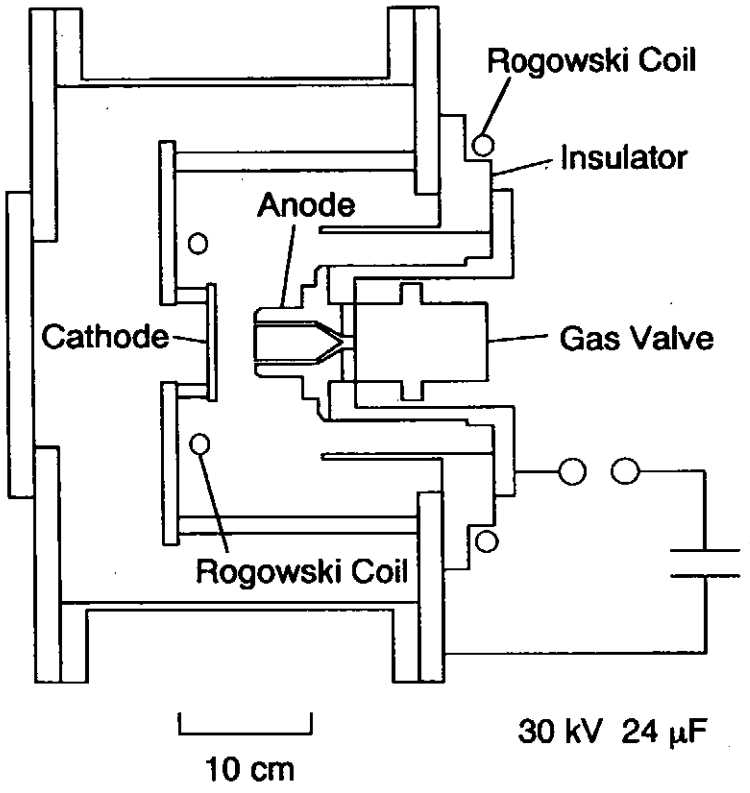

Fig. 1 Outline of the SHOTGUN z-pinch device.

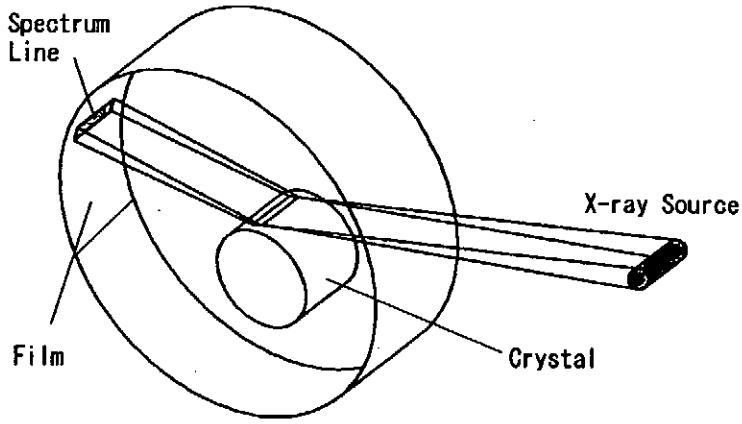

Fig. 2. Convex crystal spectrograph.

III. Experimental Results

Figure 3 (a) shows the spectrogram and its intensity distribution obtained in the experiment. The spectrogram was exposed over 134 shots. The electrode used here is made of Cu. Three sets of Ar XVII (He-like) and Ar XVIII (H-like) lines appeared in the spectrogram, which corresponds to n = 1, 2 and 3 of reflections. Enlarged image of the spectrogram around 3rd-order reflection and its trace are shown in Fig. 3 (b). The He-like image is widely expanded and the H-like image is composed of thin lines. Among the darkened film of Fig. 3 (a) a widely spread image of Cu K_α line (1.542 Å) is observed.

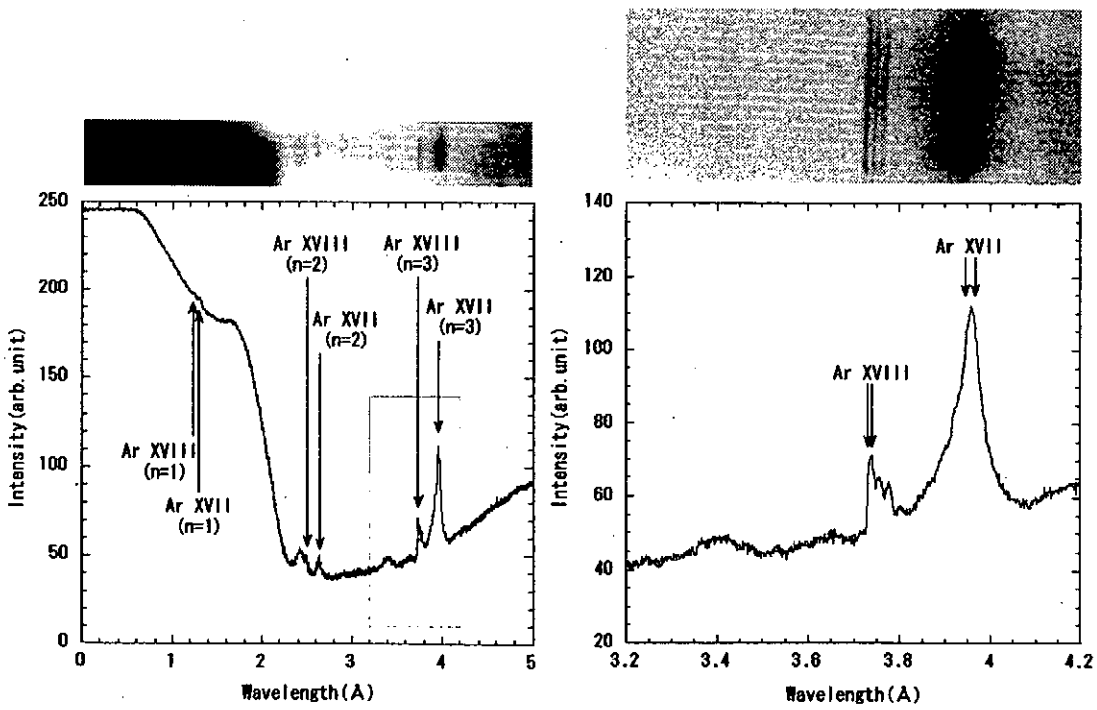

(a) (b)

Fig. 3. X-ray spectrogram and its intensity distribution.

Next, a vertical slit is installed in front the spectrograph in order to observe axial distribution of x-ray emission of the plasma (Fig. 4). Figure 5 shows the spectrograms and those intensity distributions (a) with Cu electrodes and (b) with Al electrodes. The spectrograms are exposed over 200 shots. Cu K_α line is again observed in the Cu electrode discharge, and Fe K_α line (1.938 Å) is observed in the Al electrode discharge. The spreads of these lines were about 30 mm, which corresponds to the distribution of cloud structure.

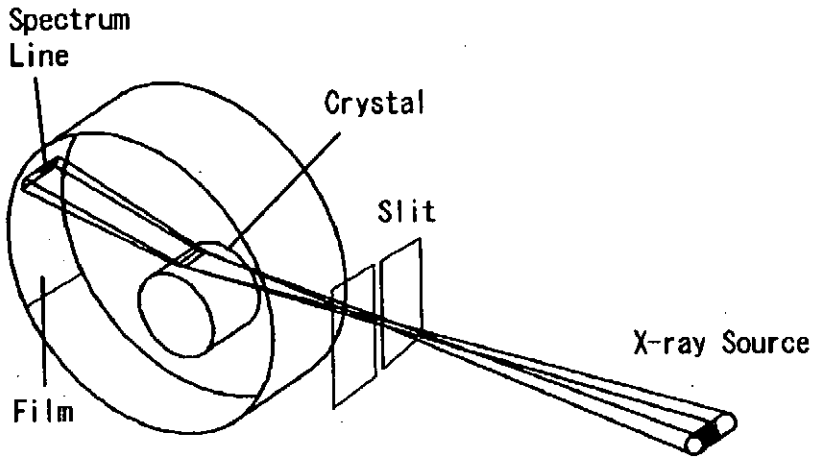

Fig. 4. Convex spectrograph with vertical slit.

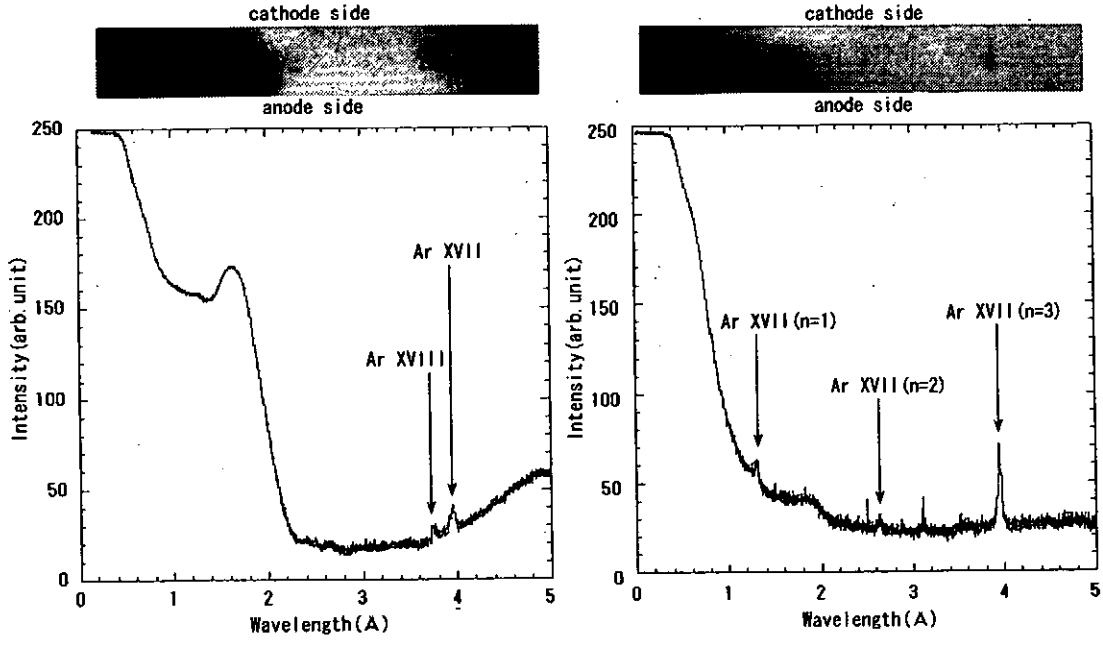

(a) Cu electrode (b) Al electrode

Fig. 5. X-ray spectrograms taken with vertical slit.

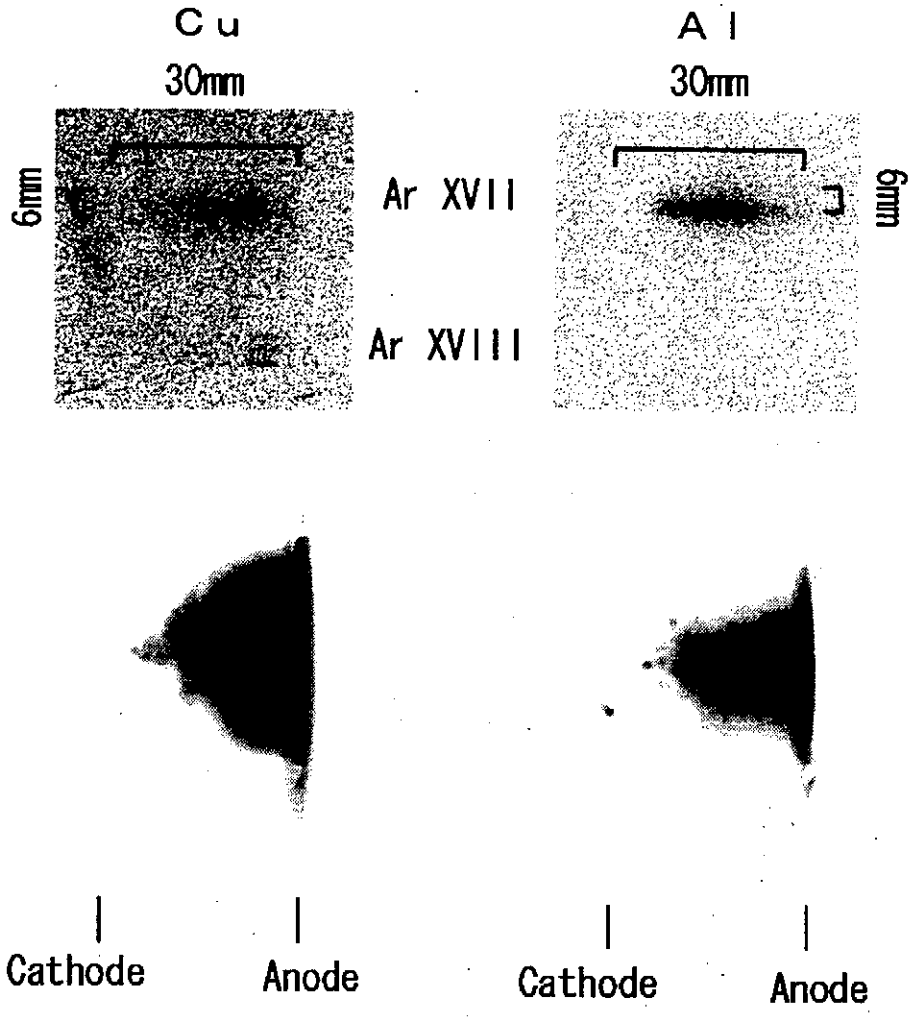

Fig. 6 X-ray spectral lines compared with x-ray pinhole photographs.

Figure 6 compares the images of Ar XVII (He-like) and Ar XVIII (H-like) with x-ray pinhole photographs. Each photograph is exposed over 47 shots. In the Cu electrode experiment, both Ar XVII (He-like) and Ar XVIII (H-like) images were observed. The H-like image was made up of three spots locating close to the anode surface. In the Al electrode experiment, only Ar XVII (He-like) image was observed. The diameter of Ar XVII (He-like) image was about 6 mm, which expressed radial distribution of hot spots.

IV. Summary and Discussion

Spectral characteristics of x-ray radiation from Ar gas-puff z-pinch plasma have been investigated using a convex spectrograph. First, second and third orders of reflections of K-shell radiations of Ar ions were observed. Radial spread of He-like Ar line was about 6 mm, which corresponds to the distribution of hot spots. The H-like Ar image observed in Cu electrode experiment was made up of three spots locating close to anode.

K_α line of Cu atom was observed in the Cu electrode experiment, and K_α line of Fe atom was observed in the Al electrode experiment. Both width were about 30 mm, which corresponds to the cloud structure of x-ray image. As no other lines were found in the spectra, it is concluded that the cloud structure was formed by K_α lines of metal atoms.

H-like Ar line was observed only in the Cu electrode experiment. This indicates that the electron temperature was higher than that of Al electrode experiment. If high-Z material is mixed into the plasma, it will release energy by radiation, and the pinch proceeds further. This is the so-called radiative collapse, and finally the pinch reaches high temperature.[1)]

Fe was not contained in the electrode. This might have come from the chamber wall. The z-pinch plasma would break up after maximum pinch, and it would hit the wall. The evaporated materials would have lain on the electrodes.[6)]

References

1) K. Takasugi, T. Miyamoto, K. Moriyama and H. Suzuki: AIP Conf. Proc. **299**, 251 (1993).
2) K. Moriyama, K. Takasugi, H. Suzuki and T. Miyamoto: NIFS-PROC-14, 43 (1993).
3) K. Moriyama, K. Takasugi, T. Miyamoto and K. Sato: NIFS-PROC-18, 90 (1994).
4) R. Muto, K. Takasugi and T. Miyamoto: NIFS-PROC-50, 139 (2001).
5) K. Takasugi, A. Takeuchi, H. Takada and T. Miyamoto: Jpn. J. Appl. Phys. **31**, 1874 (1992).
6) E. O. Baronova, K. Takasugi, V. V. Vikhrev and T. Miyamoto: Proc. 13th Int. Conf. High Power Particle Beams 784 (2001).

CHARACTERISTICS OF X-RAY RADIATION FROM A GAS-PUFF Z-PINCH PLASMA

N. Akiyama[+] and K. Takasugi

Atomic Energy Research Institute, Nihon University
[+]College of Science and Technology, Nihon University
1-8-14 Kanda-surugadai, Chiyoda-ku, Tokyo 101-8308, JAPAN

ABSTRACT

Characteristics of x-ray radiation from Ar gas-puff z-pinch plasma have been investigated by changing delay time of discharge from gas puffing. Intense cloud structure of x-ray image was observed at small delay time region, but the total x-ray signal was not so intense. The x-ray signal increased with increasing the delay time, and hot spots of x-ray image also became intense. Electron temperature was evaluated from x-ray spectroscopic data, and no significant difference in temperature was observed.

I. Introduction

Gas-puff z-pinch is easy in handling, and is used as a repetitive x-ray radiation source. The efficiency of energy transfer to the plasma is high,[1] and it is expected as a high power radiation source. Several operating regions exist for the gas-puff z-pinch plasma depending on the delay time of discharge from gas puffing.[2] Cloud structure of x-ray image has been observed near vacuum discharge region.

X-ray spectroscopy near He-like resonance line of Ar ion has been investigated, and K_α line of Fe atom has been observed.[3] Satellite lines have also been observed in the long wavelength side of the resonance line. Intensity ratio of Li-like satellite line to He-like resonance line is a simple function of electron temperature.[4-6] Here the electron temperature is evaluated according to the model, and investigated for different delay times.

II. Experimental Setup

The SHOTGUN gas-puff z-pinch device used in the experiment is shown in Fig. 1. The capacitance of the main bank is 24 μ F, which is charged up to 25kV (7.5kJ). The distance between the electrodes is 30mm. Annular gas is injected through a hollow gas nozzle mounted

on the anode. The diameter of gas nozzle is 28mm. Ar gas is used in the experiment. The gas pressure or the density simply increases with time from gas puffing. We define the time of discharge from gas puffing as "delay time". Discharge currents are detected by Rogowski coils located at the entrance of the chamber (anode) and on the cathode. The cathode current represents discharge current between the electrodes.

The devices used for the measurement of x-ray radiation are scintillation probes, an x-ray spectrograph and a pinhole camera. The scintillation probe used here is filtered by 10 μm Be foil and it can take temporal x-ray signal with energy exceeding 1keV. The pinhole camera can take four plasma images simultaneously with different filters, 5 μm Be ($E > 1$ keV), 15 μm Al ($E > 3$ keV), 100 μm Al ($E > 8$ keV), and 500 μm Al ($E > 12$ keV). A Johansson type spectrograph with a curved quartz crystal ($2d = 6.62$ Å) is used for x-ray spectroscopy around He-like resonance line of Ar ions. The radius of Rowland circle is 250 mm. The x-ray film used both for spectroscopy and pinhole photography is Kodak DEF film.

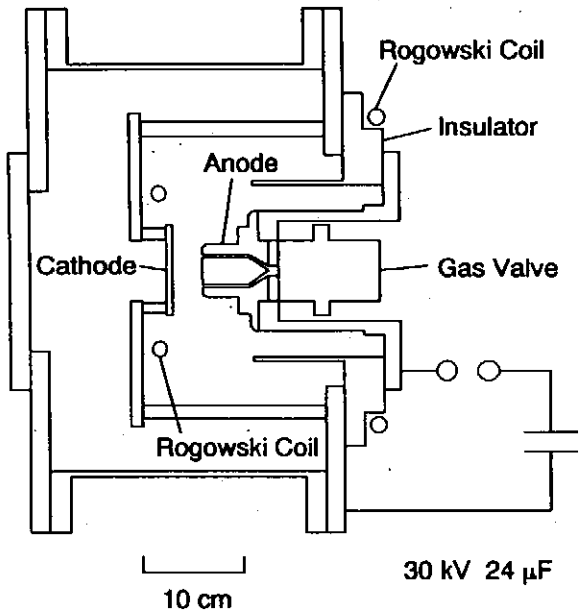

Fig. 1 The SHOTGUN gas-puff z-pinch device.

III. X-ray Spectra

The x-ray radiation of He-like and Li-like ions is analyzed based on Refs. 4 - 6. The excited state of He-like resonance line is excited by collisional excitation and dielectronic recombination. The intensity of He-like resonance line is

$$I = N_{He} N_e (C + D) \ , \tag{1}$$

where N_{He} and N_e are densities of He-like ion and electron respectively. The rate coefficients C and D are collisional excitation and dielectronic recombination.

The excited state of Li-like satellite line is populated by dielectronic recombination of He-like ion. This level is depopulated by autoionization and radiation. The intensity of Li-like satellite line is

$$I_s = N_{He} N_e C_d \frac{A_r}{(A_a + A_r)} \quad , \tag{2}$$

where C_d is dielectronic recombination rate, A_a is autoionization rate, and A_r is radiation rate. The intensity ratio of Li-like satellite line and He-like resonance line is

$$\frac{I_s}{I} = \frac{1.048 \times 10^{-17}}{1+\alpha} \frac{E_0}{T} \frac{1}{fP} \exp\left\{\frac{E_0 - E_s}{T}\right\} \times g_s \frac{A_a A_r}{A_a + \Sigma A_r} \quad , \tag{3}$$

where E_0 and E_s are energies of He-like resonance line and Li-like satellite line respectively, and T is electron temperature. The factor g_s is statistical weight of the excited level, f is oscillator strength, P is Gaunt factor, and $\alpha = D/C$. The summation is taken over related levels.

In the experiment several satellite lines are observed in the same wavelength region. Here we used three lines, j, k, and l defined in Ref. 4. The total intensity ratio of relating lines as a function of temperature is shown Fig. 2. The ratio decreases monotonically with temperature.

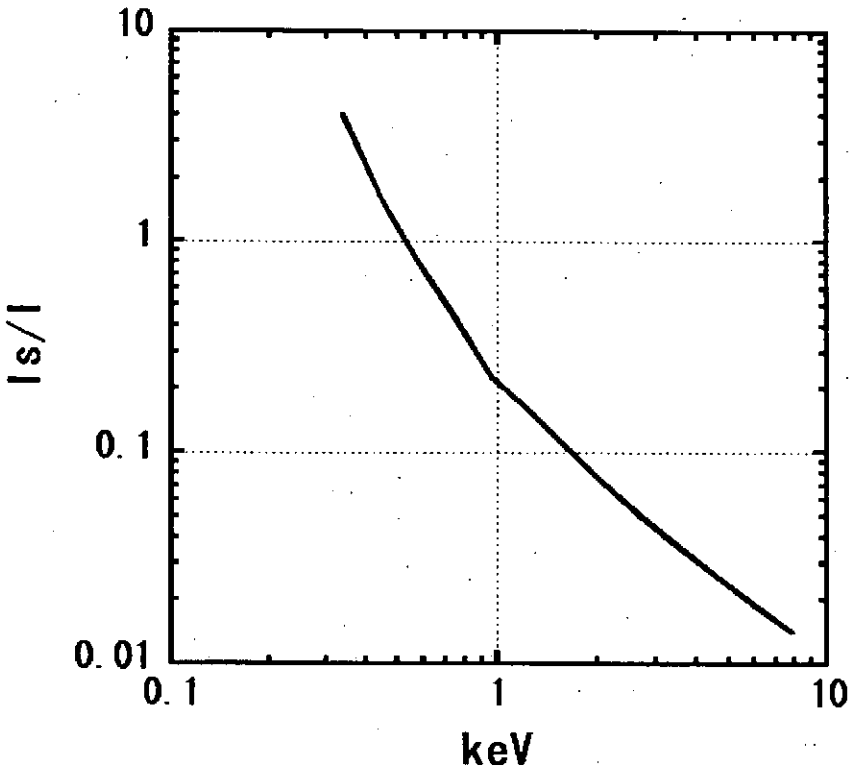

Fig. 2 Line intensity ratio vs. electron temperature.

IV. Experimental Results

Typical current waveforms and x-ray signal detected by a scintillation probe are shown in Fig. 3. As the z-pinch column shrinks, its inductance increases, and the dip is formed in the current waveform. The moment of x-ray pulse corresponds to this current dip. Let's define "pinch time" as the time interval between the start of discharge and the x-ray pulse. As the delay time increases, the pinch time also increases (Fig. 4). This is due to the increment of pinch mass. Net input energy into the pinch column is obtained from the current waveform[3] and is shown in Fig. 5. The energy increases with the delay time.

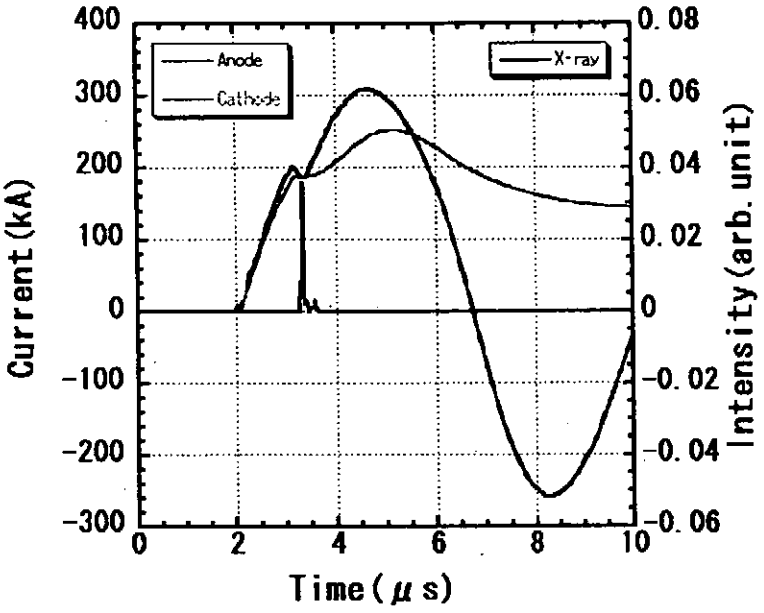

Fig. 3 Typical current waveforms and x-ray signal.

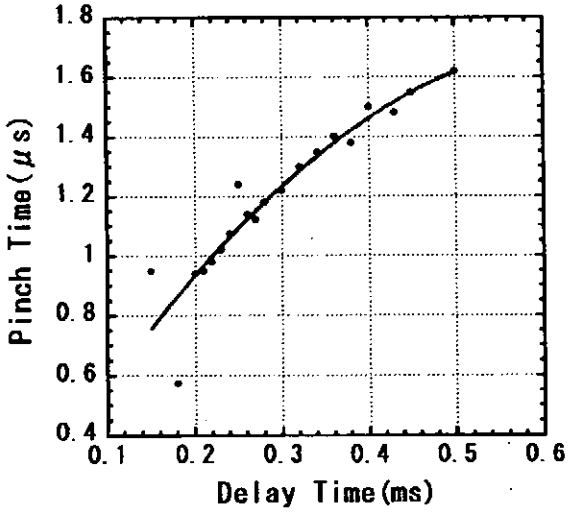

Fig. 4 Pinch time vs. delay time.

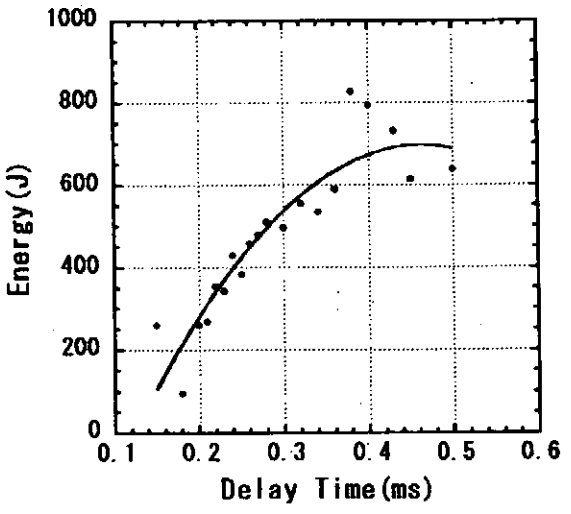

Fig.5 Net input energy vs. delay time.

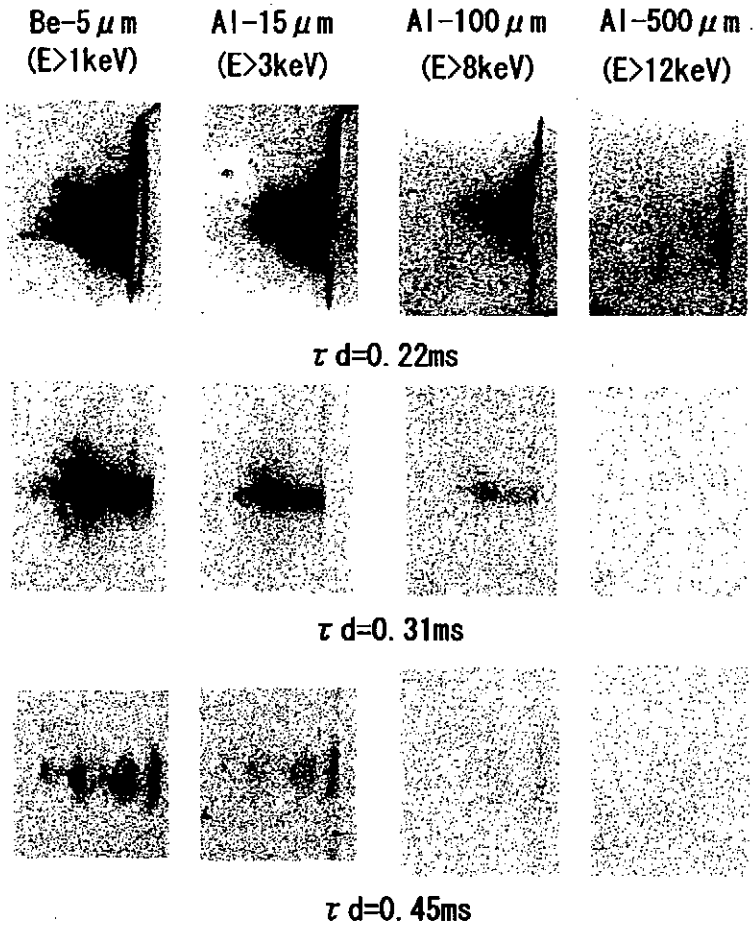

Fig. 6 X-ray pinhole photographs at different delay times.

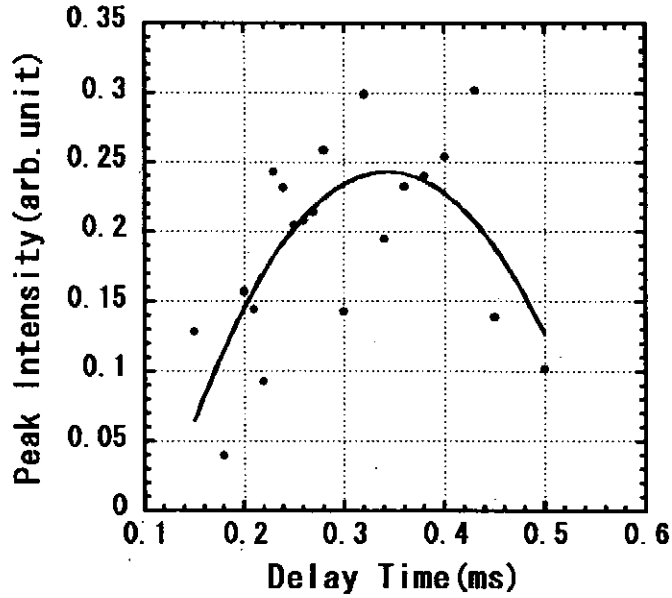

Fig. 7 X-ray intensity vs. delay time.

X-ray images taken by the pinhole camera is shown in Fig. 6 for three different delay time τ_d. Cloud structure of the x-ray is obvious and hard component of x-ray (Al-500 μm) is observed on the surface of anode at short delay time (τ_d = 0.22 ms). With increasing the delay time the hard component of x-ray decreases, and hot spots becomes intense. Figure 7 shows peak intensity of x-ray detected by a scintillation probe. The signal increases with the delay time up to 0.4 ms. Further increasing the delay time, the x-ray intensity drops.

X-ray spectra and its intensity are shown in Fig. 8. The strongest line is Ar XVII He-like resonance line (3.9488 Å). The next lines to long wavelength side are Ar XVII He-like intercombination line (3.9691 Å), Ar XVI Li-like satellite line (3.989 Å), and Ar XV Be-like satellite line (4.010 Å). The lines observed to the left are not from Ar but from Fe. The lines around Fe K_α line (1.938 Å) are observed by secondary reflection of the crystal.[3)]

The electron temperature is evaluated using the intensity ratio of Eq. (3). In Fig. 9 the temperature is plotted against the delay time. The temperature is distributed around 1 keV, and there is no systematic tendency with the delay time.

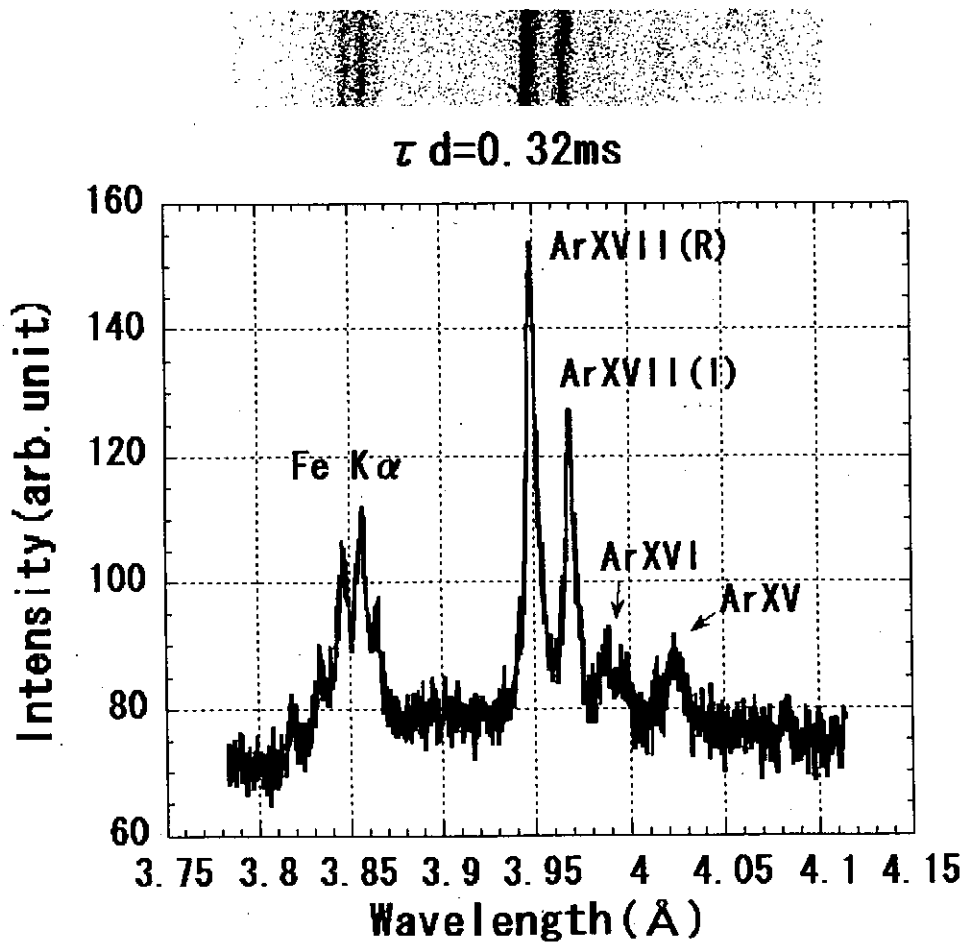

Fig. 8 X-ray spectra and its intensity.

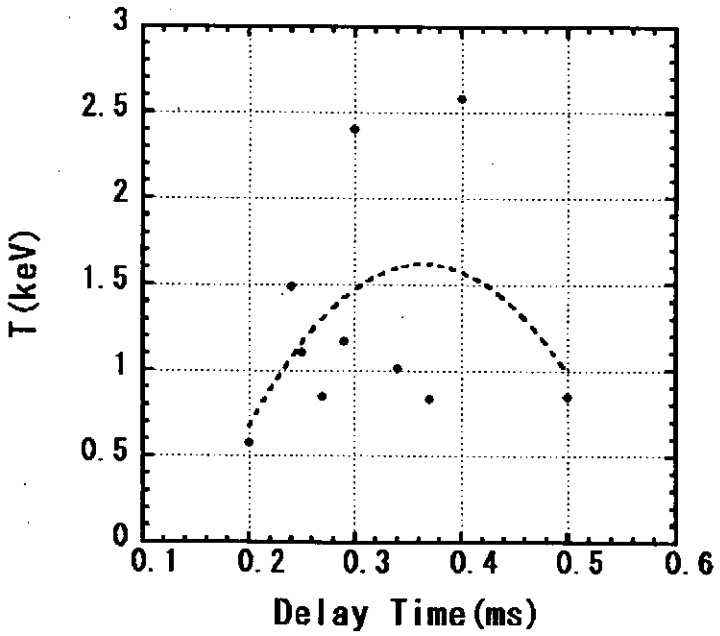

Fig. 9 Electron temperature vs. delay time.

V. Summary

The characteristics of x-ray radiation from the SHOTGUN gas-puff z-pinch plasma have been investigated by changing the delay time. Discharge cannot occur properly at the delay time less than 0.2 ms. With the increase in the delay time both the pinch time and the pinch current increase, then the net input energy increases. At small delay time hard component of x-ray is observed, but hot spots are not produced, and the x-ray signal is weak. The cloud structure of x-ray image is intense in this operating region. The hot spots are effectively produced at larger delay time. The x-ray signal became intense as the delay time increased. Spectroscopic data shows that electron temperature has no significant differene by changing the delay time.

References

1) K. Takasugi, H. Suzuki, K. Moriyama, and T. Miyamoto: Jpn. J. Appl. Phys. **35**, 4051 (1996).

2) K. Takasugi, A. Takeuchi, H. Takada and T. Miyamoto: Jpn. J. Appl. Phys. **31**, 1874 (1992).

3) E.O. Baronova, K. Takasugi, V.V. Vikhrev and T. Miyamoto: Proc. 13th Int. Conf. High Power Particle Beams 784 (2001).

4) A.H. Gabriel and T.M. Paget: J. Phys. **B 5**, 673 (1972).

5) A.H. Gabriel: Mon. Not. R. astr. Soc. **160**, 99 (1972).

6) C.P. Bhalla: Mon. Not. R. astr. Soc. **172**, 359 (1975).

INVESTIGATION OF STABILITY AND X-RAY SPECTRUM IN GAS-PUFF Z-PINCH PLASMAS DIRIVEN BY INDUCTIVE ENERGY STORAGE PULSED POWER GENERATOR WITH A PLASMA OPENING SWITCH

K. Murayama*, I. Fukudome*, Y. Teramoto, S. Katsuki and H. Akiyama

Department of Electrical and Computer Engineering, Kumamoto University, 2-39-1 Kurokami, Kumamoto, 860-8555, Japan
**Also Department of Mechanical and Electrical Engineering, Yatsushiro National College of Technology, 2627 Hirayamashinmachi, Yatsushiro, 866-8501, Japan*

ABSTRACT

Gas-puff z-pinch plasmas are driven by an inductive voltage adder – inductive energy storage pulsed power generator "ASO-X". ASO-X has the performance of the maximum output voltage and current are 180 kV and 400 kA respectively and can provide a fast rise time current with operating POS. The stability of the plasma column, spectrum radiated from z-pinch plasmas and the spatial distribution of hot spots are investigated in the case with and without operating POS. By driving ASO-X with operating POS the kink instability is restrained and the stability of plasma column is improved about three times in regard to the average dispersion. Furthermore the duration of soft x-ray radiation is increased and the spatial distribution of hot spots is 50 % improved with regard to kurtosis of the intensity profile of pinhole photographs compared to those without operating POS.

I. Introduction

Soft x-rays, especially in the range of water window, are well worthy for industrial applications such like x-ray lithography[1], microscopy[2], physical or experimental measurement and so on. Several methods for radiating soft x-rays are studied in many institutes and gas-puff z-pinch scheme is one of favorable methods for soft x-ray radiation. This scheme has the advantage of cost performance for the equipment in comparison with synchrotron orbital radiation (SOR) and relatively high intensity in comparison with laser excitation method. But it is difficult to produce stable and reproducible soft x-ray radiation and hot spots due to lack of the uniformity of injected gas distributions, current value and rise time flowing through the plasmas in the experimental conditions.[3][4] They cause Rayleigh-Taylor, kink (m=1 mode) and sausage (m=0 mode) instabilities in the z-pinch plasmas. In order to improve the uniformity of the injected gas between the electrodes, using a mesh cathode is one of the solutions. By the influence of a reflection of the injected gas on the cathode surface, the gas flow is fallen into disorder and then the uniformity of the gas distribution between the electrodes becomes deficient. In our previous work an inductive energy storage pulsed power generator ASO-II was used as a power source and then the stability of plasma column and the spatial stability of hot spots was improved by using the mesh cathode and wire fuses as an opening switch.[5][6] The current with improved rise time flows thorough the plasmas then the constriction velocity of plasmas is faster and the localized instability on plasma column is restrained.

In this study, a pulsed power generator ASO-X[7] was used as a driver for the z-pinch plasmas. ASO-X utilizing an inductive voltage adder technology delivers a current with a short rise time to the z-pinch plasmas as a load. The rise time is shorten by operating the plasma opening switch (POS). The behavior of z-pinch plasmas associated with the rise time of the current was investigated. The current with different rise time is generated by with and without operating the POS and then the stability of plasma column, x-ray spectrum and spatial distribution of hot spots are observed. Those experimental results and discussion are described in this paper.

II. Experimental setup

Figure 1 shows the schematic illustration of the gas-puff z-pinch plasmas driver ASO-X. ASO-X is using an inductive voltage adder technology and consists of three stages and total 6 capacitors, magnetic cores, field distortion spark gap switches and POS. The length, width and height of ASO-X generator are about 3.0 m, 1.8 m and 1.6 m, respectively. The capacitance of each capacitor is 3.2 μF and the total inductance of the generator is approximately 330 nH. The maximum charging voltage at each capacitor is 60 kV and the total stored energy is 35 kJ. The maximum output voltage is 180 kV and the peak current is 400 kA with 1.4 μs of the quarter period. In this experiment the charging voltage is 30 kV. The magnetic cores have the high relative permeability (50000) and these make the current flow through the selective path in the circuit. The field distortion spark gap switches are connected with each capacitor and triggered these capacitors when they are fired by a single trigatron spark gap switch. The POS is constituted by 6 plasma guns to produce the plasma source for opening switch operation. The conduction time of the switch is varied by adjusting the delay time between the triggering the plasma guns and the firing ASO-X.

In the gas-puff z-pinch section, the anode electrode of the gas-puff z-pinch plasmas is made of brass and the diameter is 30 mm. The gas spout hole, the diameter of 5mm, is in the center of the anode. The cathode electrode is copper tube with a diameter of 60 mm and the top is covered with stainless steel mesh wires for decreasing the reflection of the injected gas on the cathode surface. The separation between the electrodes is about 10 mm. The Ar gas for plasmas source is filled in the magnetic fast valve at the pressure of 0.15 MPa and then inject into the z-pinch region from the anode spout hole by actuating the valve. The pressure in the chamber of z-pinch device section is about 5 x 10^{-2} Pa.

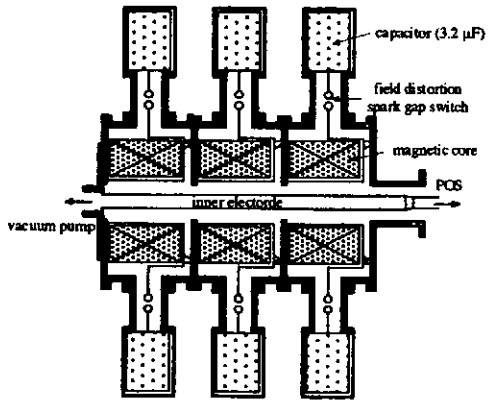

Figure 1. Schematic illustration of the ASO-X generator.

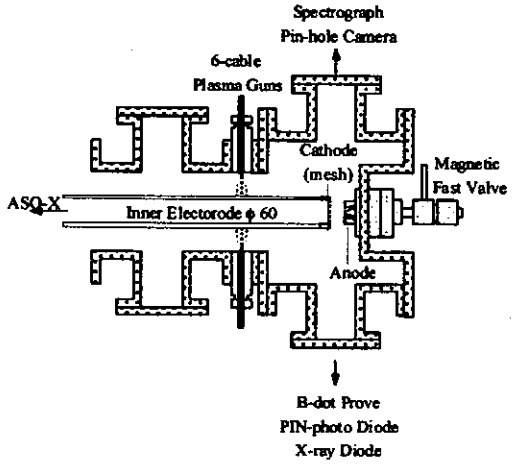

Figure 2. Configuration of the z-pinch device with POS section.

In this experiment the behavior of plasma column, the spectrum from z-pinch plasmas and the spatial distribution of hot spots in the case of ASO-X without operating POS (no-POS mode) and with operating POS (POS mode) are investigated. The behavior of the plasma column is observed with image converter camera (Hadland photonics IMACON 750) with framing mode. The x-ray spectra radiated from z-pinch plasmas are recorded on the x-ray film (Kodak DEF-392) by a spectrograph (Yogansson type 07-200 made by firm Ecopulse in USA together with Kurchakov Institute in Russia, $2d$ =6.68 A). The spatial distribution of hot spots is observed with a pinhole camera that the diameter of pinhole is 300 μm and covered with a 3 μm-thick Al filter. Soft x-rays are detected by a PIN-photo diode covered with a 3 μm-thick Al filter. The source and load currents are measured by a Rogowski coil and a B-dot probe, respectively. The configuration of the z-pinch device with POS section is shown in Fig. 2.

III. Experimental results and discussion

Figure 3 shows the typical waveforms of current for ASO-X and PIN-photo diode for soft x-rays. (a) is in the case of ASO-X without operating POS (no-POS mode) and (b) is in the case of ASO-X with operating POS (POS mode). In (b), the light gray line means the generator current and the dark black line means the load current flowing through the z-pinch plasmas. When the POS is not operated a quarter period of the current is about 1.4 μs and the peak current value is about 180 kA. Soft x-rays are detected at 1.3 μs after the current begins to flow through the plasmas. On the other hand the current rise time becomes faster for operating POS although the peak current value is almost same compared with no-POS mode. This means that the POS section does not consume the energy practically and the opening operation in POS is performed satisfactorily. X-rays are detected at 0.8 μs after the load current begins to flow.

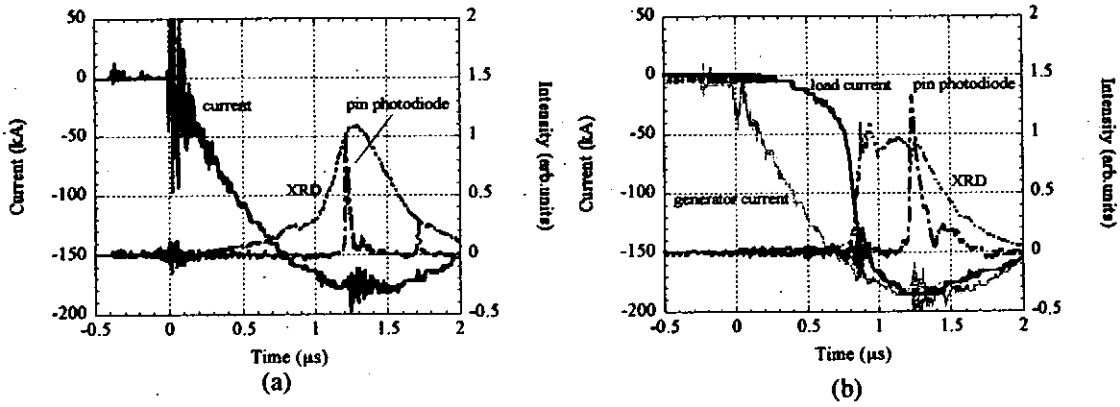

Figure 3. Typical current and x-ray waveforms for ASO-X. (a) is in no-POS mode. (b) is in POS mode.

Figure 4 shows the typical framing photographs of the discharge luminosity with the waveforms of soft x-ray and monitor signal of image converter camera. (a) is no-POS mode and (b) is POS mode, respectively. The numbers indicated on the soft x-ray waveform correspond to the numbers on the framing photograph. The exposure time and inter-frame time for these photographs are 10 ns and 50 ns. In both modes, plasmas are generated along the shape of injected gas that spreads out from the anode to the cathode. But the plasma column bents obviously and strong kink (m=1) instability occurs on the photograph number 2

in no-POS mode. Furthermore the column is torn off partly and the soft x-ray is emitted around this time. Then the plasma column is torn off completely and diffuses between the electrodes. On the other hand the plasma column at the photograph number 2 in POS mode is stable along the z-axis although the parts of the sausage instability (m=0) are seen. Then the plasma column is torn off partly as same as that in no-POS mode but the kink instability is not seen. The soft x-ray signal is detected just after photograph number 3 and the plasma column diffuses in the photograph number 4 and afterward.

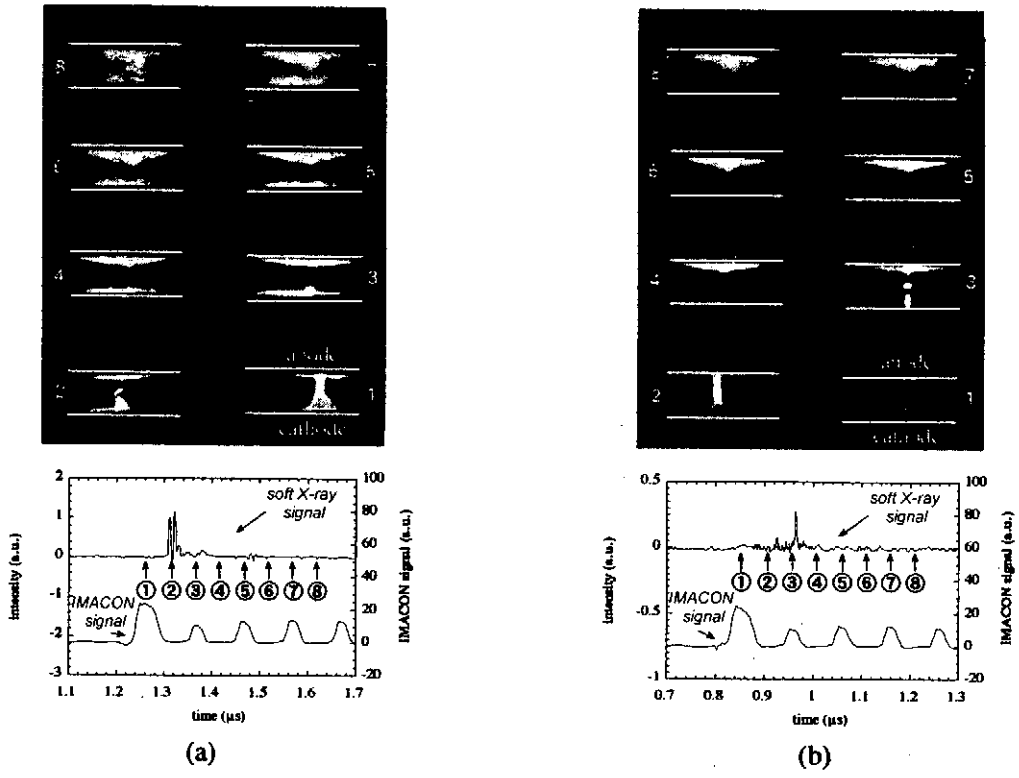

Figure 4. Framing photographs of the discharge luminosity and the waveforms of soft X-ray and image converter camera monitor signals. (a) is no-POS mode (b) is POS mode

Based on the results of figure 4 the incidence inclinations of kink or sausage instability at the difference of current rise time are investigated to calculate the centerline of plasma column on 10 framing photographs in each mode. As the concrete method, the most unstable plasma column is chosen for each framing photograph and is converted to a binary image on the computer. And then the centerline of plasma column is calculated in the range of plus-minus 3.5 mm from the middle of between anode and cathode. Figure 5 shows this process for instance and the result of centerlines obtained by this method is shown in figure 6. These

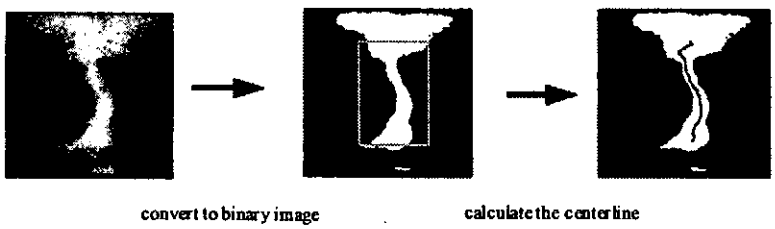

Figure 5. process of calculating the centerline of plasma column.

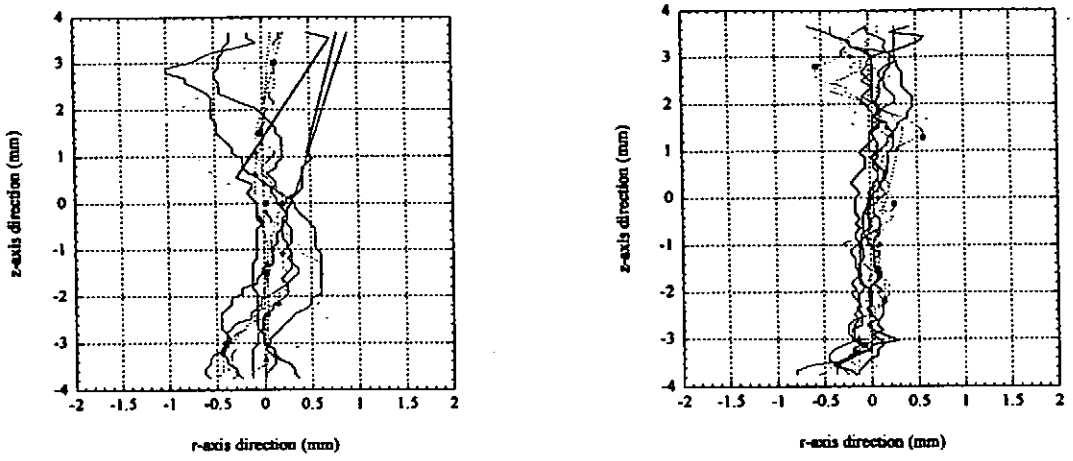

Figure 6. Centerlines of plasma column. (a) is no-POS mode. (b) is POS mode.

centerlines of plasma column for 10 shots are superposed on each graph. Comparing (a) with (b) generally, the frequency and the amplitude of centerlines in no-POS mode are lower and larger than that in POS mode. The low frequency and the large amplitude of centerline mean the strong kink instability occurs in the plasma column. The average dispersion calculated from these centerlines is 0.10374 for no-POS mode and 0.035587 for POS mode. These results indicate the incidence tendency of kink instability is dominant for no-POS mode and sausage instability is dominant for POS mode. And furthermore the stability in regard to the average dispersion is improved about three times by operating POS.

Figure 7 (a) and (b) show the time-integrated photographs of soft x-rays spectra and the intensity profiles along the wavelength. (a) is in no-POS mode and (b) is in POS mode,

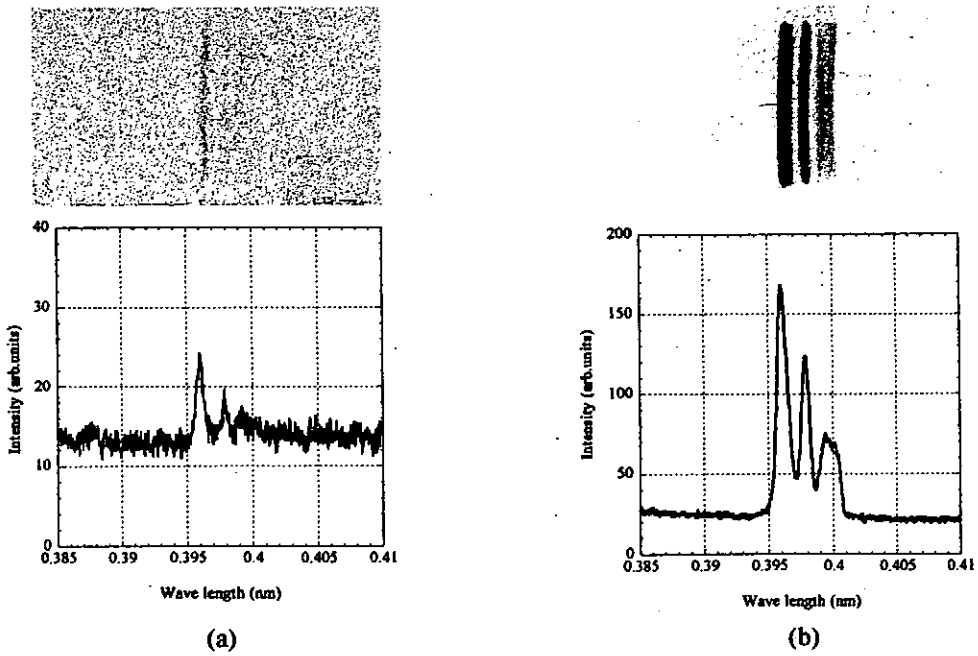

Figure 7. Time-integrated photographs of soft x-ray spectrum and the intensity profiles of spectrum scanned along the wavelength. (a) is in no-POS mode. (b) is in POS mode. Each photograph is superposed for 10 shots of z-pinch discharges.

respectively. Each photograph is superposed for 10 shots of z-pinch discharge. In both photographs three spectra are appeared and these lines are estimated to come from Ar XVII (1s2-1s2p) 1P, 3P and Ar XVI ion.[8][9] But the exposure intensity of spectra in POS mode is obviously higher compared with that in no-POS mode.

The dependence of soft x-ray intensity on t_p is shown in fig. 8. The t_p is defined as the time between the current begins to flow through the plasmas and the soft x-ray is detected by the PIN-photo diode. The empty and solid circles correspond to no-POS mode and POS mode, respectively. The t_p for POS mode is less than that for no-POS mode in fig. 8. This means the average velocity of pinched plasmas for POS mode is faster than that for no-POS mode although the overall intensity of soft x-ray is not so different for both cases. Figure 9 shows the average integrated value of soft x-ray waveform measured with PIN-photo diode. In this result the integrated value of soft x-ray in POS mode is twice as high as that in no-POS mode. This means the pulse width of soft x-ray waveform is extended, namely, the radiation time of soft x-ray from hot spot increases because of repressing the instability of z-pinch plasmas for POS mode. Therefore, the light exposure of spectra for POS mode increases as compared with that for no-POS mode in fig. 7.

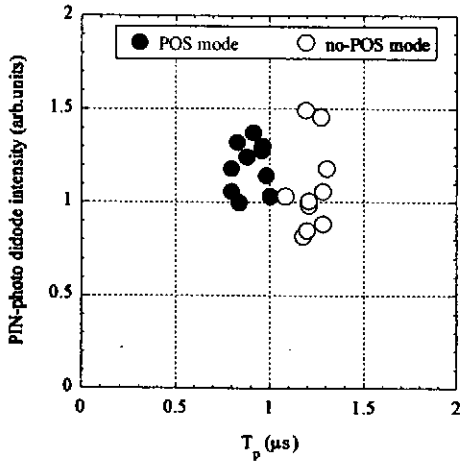

Figure 8. Dependence of PIN-photo diode maximum intensity on T_p.

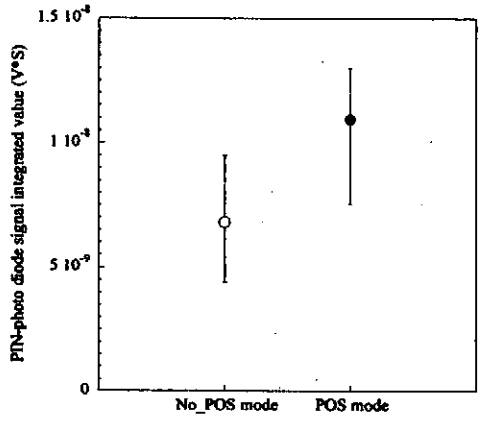

Figure 9. Integrated value of PIN-photo diode signal

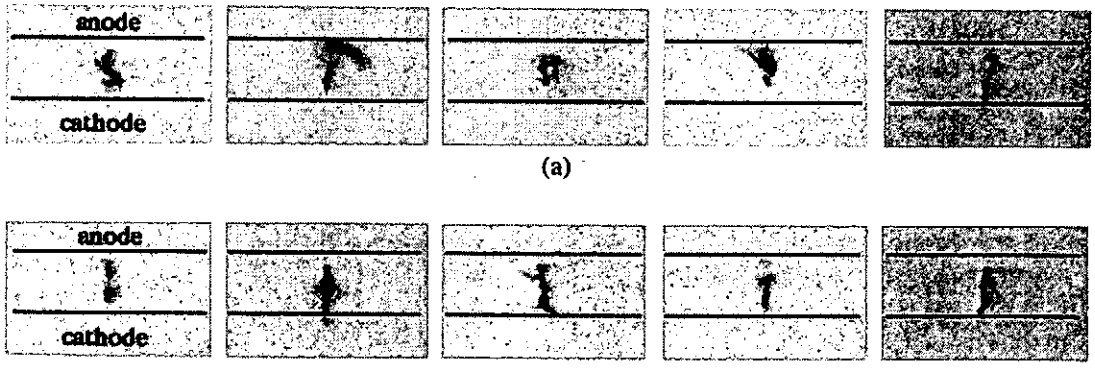

Figure 10. Pinhole photographs of hot spots. (a) is in no-POS mode. (b) is in POS mode.

Typical pinhole photographs of hot spots in each mode are shown in Fig. 10(a) and (b). Some hot spots in (a) stray off the z-axis and are mainly generated in the middle of between the electrodes. In contrast, the hot spots in (b) are almost distributed on the z-axis uniformly and the spatial stability of hot spots in radial direction seems to be improved. In order to evaluate the stability of the hot spots, the intensity profiles integrated along the z-axis which are obtained from Fig. 10 are shown in Fig. 11(a) and (b). Furthermore, the kurtosis for those profiles in each mode is calculated. The kurtosis is an index for expressing the sharpness of the distribution profile and calculated by equation (1),

$$kurtosis = \frac{1}{n}\sum_{i=1}^{n}\left(\frac{x_i - \bar{x}}{s}\right) \qquad (1)$$

where $\bar{x}$ is average value, s is standard deviation.

The kurtosis values for no-POS mode and POS mode are 12.898 and 19.476 respectively. The larger kurtosis indicates the less scattering of hot spots in the radial direction and the good spatial stability of hot spots. Spatial stability for POS mode is improved 51% compared with that for no-POS mode in terms of the average value of kurtosis. This reduction of hot spots in the radial direction is important thing when z-pinch plasmas are used for industrial applications.

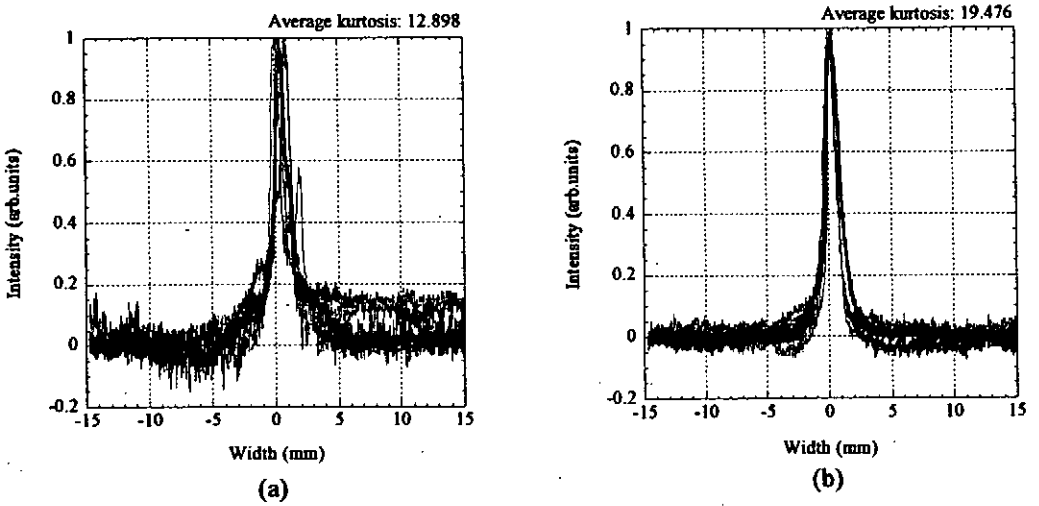

Figure 11. Integral intensity profiles obtained from fig. 6 and other 5 shots. (a) is in no-POS mode. (b) is in POS mode.

IV. Conclusion

Gas-puff z-pinch plasmas are driven by an inductive voltage adder - inductive energy storage pulsed power generator ASO-X. The plasma behavior is observed and the incidence tendency of kink or sausage instability at the difference of current rise time is investigated to calculate the centerline of plasma column on the photographs in the case of ASO-X without operating POS and with operating POS. Moreover the spectrum radiated from z-pinch plasmas and the spatial stability of hot spots are investigated and those results are compared in each case.

As an analysis of the centerline of plasma column calculated from the framing photographs

of plasma behavior the kink instability in plasma column is restrained and the stability in regard to the average dispersion is improved about three times by operating POS.

The exposure intensity of spectrum is increased by operating POS. There is no significant difference in the intensity of PIN-photo diode signal in each case but the average time-integrated value of PIN-photo diode signal is increased in POS mode. Moreover the spatial stability of hot spots is about 50 % improved with regard to kurtosis of the intensity profile of pinhole photographs.

The t_p with operating POS is shorter than that without operating POS, namely, the average drift velocity of plasma column is faster. So the instability on the plasma column is restrained and the uniform constriction over the plasma column is attained. Consequently the duration of soft x-ray radiation is increased and the spatial stability of hot spots is improved by the current with short rise time.

V. References

1) E. W. Becker, W. Ehrfeld, P. Hagmann, A. Maner and D. Munchmeyer, "Fabrication of microstructures with high aspect ratios and great structural heights by synchrotron radiation lithography, galvanoforming, and plasticmoulding (LIGA process)", Microelectronic Engineering, **4**, 35-56(1986)
2) J. Kirz and H. Rarback, "Soft x-ray microscopes", Rev. Sci. Instrum., **56(1)**, 1-13(1985)
3) H. P. Stormberg, S. Murayama and Y. Watanabe, "Angular distribution of x-ray radiation from optically thick z-pinch plasmas", J. Appl. Phys., **62(10)**, 4090-4095(1987)
4) K. Takasugi, H. Akiyama, N. Shimomura, M. Sato and T. Tajima, "X-ray generation from a gas-puff z-pinch driven by a pulsed power generator with a self-crowbar switch", Rev. Sci. Instrum. **64(8)**, 2403-2404(1993)
5) K. Murayama, T, Shinkai, S. Katsuki, and H. Akiyama, "Gas-puff z-pinch plasmas driven by inductive energy storage pulsed power generator", Jpn. J. Appl. Phys., **37(5A)**, 2676-2680(1998)
6) K. Imasaka, K. Kawazoe, K. Kawauchi, S. Hara, J. Suehiro and M. Hara, "Reduction of the source size of gas-puff z-pinch plamsas using an inductive pulsed power system", Rev. Sci. Inst., **71(12)**, 4438-4444(2000)
7) S.Kohno, Y.Teramoto, I.V.Lsitsyn, S.Katsuki and H.Akiyama, "High-Current Pulsed Power Generator ASO-X Using Inductive Voltage Adder and Inductive Energy Storage System", Jpn. J. Appl. Phys., **39(5A)**, 2829-2833(2000)
8) G. Mahlman, P.G.Burkhalter, S. J. Stephanakis, F. C. Young and D. J. Nagel, "Quantitative x-ray spectroscopy of neon z-pinch plasmas", J. Appl. Phys. **60(10)**, 3427-3432(1986)
9) G. Nave, C. D. Challis, A. E. Dangor and G. Lunney, "Soft x-ray spectra from a gas-puff z pinch", J. Appl. Phys., **65(9)**, 3385-3390(1989)

Optical Observation of Plasma Produced from Metal Powder

T.Yokoyama, T.Kuraoka*, K.Ogasawara, S.Ibuka, K.Yasuoka, and S.Ishii

Department of Electrical and Electronic Engineering
Tokyo Institute of Technology
2-12-1 O-okayama, Meguro-ku, Tokyo, Japan

ABSTRACT

Plasma was generated from copper powder by pulsed high current discharges. Early stage of discharge with the powder was observed using image-converter cameras. Light emission was found around the surface of powder particles. A filamentary current channel was formed between a cathode and the anode plasma that is seen in vacuum sparks. Laser shadowgraph method was employed to observe evaporation process of the particles. Increase of the particle radius by the vaporization of the surface was confirmed in the hemisphere part of the particle to which electrons bombarded from the cathode.

I. Introduction

The plasma generation from powder is a new method with various advantages in comparison with using gases, which are widely applied in plasma sources. The control of spatial distribution of transiently injected powder is easier because of its larger mass, which makes a diffusion velocity slower than that of pure gases. Since powder is solid state, there are more kinds of plasma material to be used as plasma medium in comparison with gases.

There are variety of applications of the powder plasma such as Z-pinches, intense soft X-ray source, high-voltage insulation techniques, and formation of fine particles or thin-film in material science. Recently, Wire-array Z-pinches and gas-puff Z-pinches that can create high-density plasma are widely studied for intense soft X-ray sources. Although gas-puff Z-pinches are performed with a high repetition rate, it is difficult to control the initial density profile. Wire-array Z-pinches cannot be operated repeatedly so fast, because it takes time to place the wire-array again between the electrodes. The powder-generated plasma can overcome these problems.

We created the plasma by pulsed discharges on the powder that was injected in vacuum. The powder injection is controlled by electrostatic forces, which work effectively to handle small particles in vacuum. In this paper, the early stage of the powder discharge was examined optically. The particle is supposed to become the plasma by passing through complicated processes. Vaporization at the powder surface must be dominant in early stage of the discharge. Since the capacitor energy was so high that high current discharge made

observation of vaporization process of the powder impossible in the previous experiments, in which light emitted from the expanding anode plasma was so intense. The capacitor energy was reduced to suppress the evaporation of the anode surface. The observation scheme of visible light by an image-converter camera was not suitable for detecting the evaporation process that will be examined by measuring the temporal change of outer diameter of the particles. Therefore, we adopted the laser shadowgraphy to observe vaporization process of the powder explicitly.

II. Experimental Apparatus

1. Powder supply system

We employed spherical copper powder of the diameter of about 100 μ.m. Fig.1 shows a micrograph of the copper powder particles with a diameter of 150 μm. It is apparent that particles are spherical and their diameters are almost similar. Exact spatial and temporal control of the powder between the discharge electrodes is required in order to generate the powder plasma. The powder injection must establish the fixed spatial distribution and must be synchronized with the discharge. We have examined various control methods so far, from which we chose an electrostatic method because of high controllability and easy handling in vacuum.

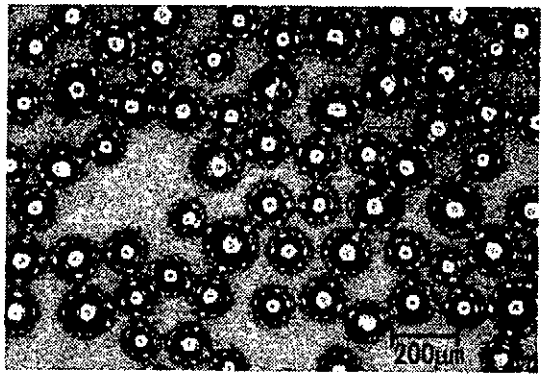

Fig.1 Photomicrograph of powder

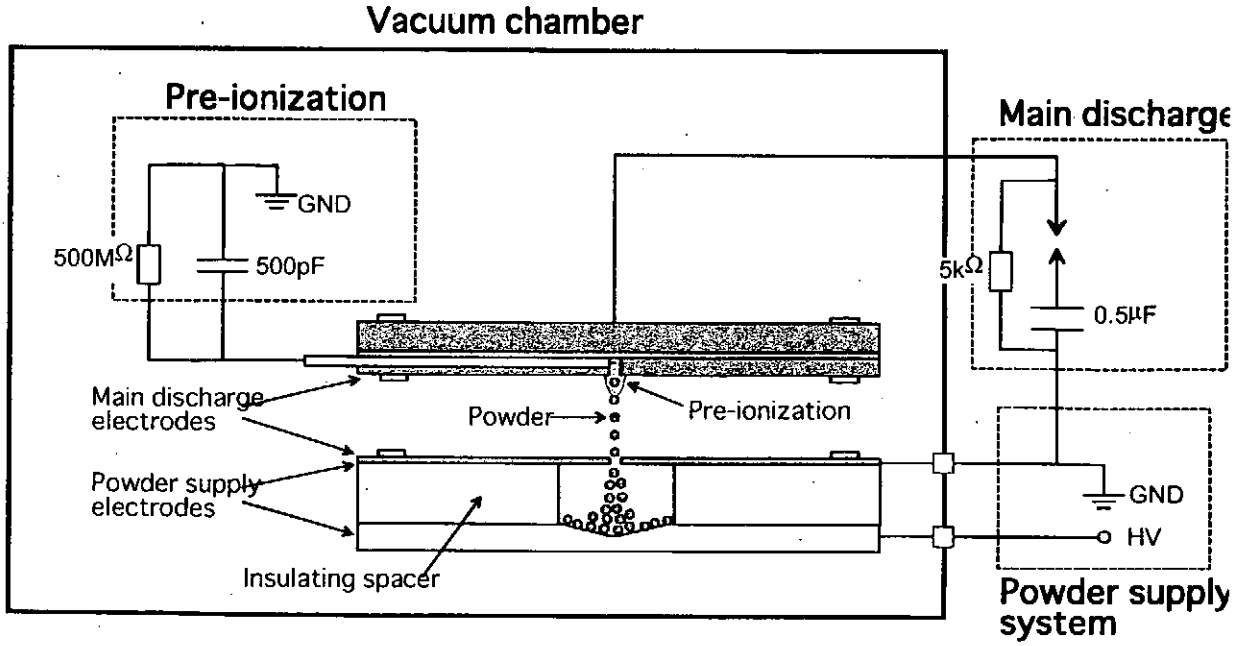

Fig.2 Experimental setup of the pulsed discharge with an electrostatic powder supply system

A schematic of the experimental setup is shown in Fig.2. A powder injection system was placed under the main discharge electrode. Two plane circular electrodes were placed separated by an acrylic insulating spacer with the thickness of 10 mm and the inner diameter of 16 mm. The upper electrode was also the anode for main discharges and has a hole of 2 mm in diameter at the center for the powder injection. The lower electrode was designed to have an inclination so that the powder may always return to the central after the operation. To inject the power, a rectangular pulsed voltage with a voltage of 8 kV and a pulse width of 100 ms was applied between the electrodes. When the pulsed high voltage was applied, the particles were charged and accelerated from the lower electrode to the upper one if the electrostatic force surpasses the gravitational force. Afterwards, the powder was ejected from the hole of the upper electrode to the discharge space.

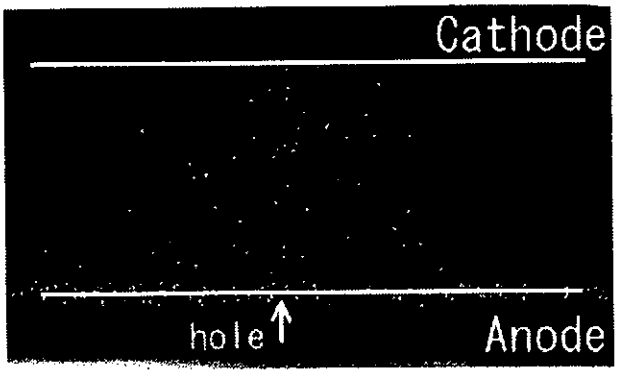

Fig.3 Aspect of powder injection

Fig.3 shows a snapshot of the injected powder between the main discharge electrodes. A stroboscopic lamp illuminated the powder. This picture was taken at 120 ms after applying the rectangular pulsed voltage, when the number of particles becomes maximum value. It was observed that about eighty particles were uniformly distributed between the discharge electrodes.

2. Main discharge system

The pulsed discharges were powered by a capacitor of 0.5 μF charged to –20 kV as shown in Fig.2. The electrode separation was 10mm for the main discharge. The discharge electrodes and the powder injection system were placed in a vacuum chamber at a pressure of 10^{-5} Torr. The tungsten, which has a high boiling point (3680K), was used as electrode material in order to reduce the electrode erosion. The lower main electrode, which was also the electrode of the powder injection system, was a grounded anode.

Since the injected particle distribution was spatially sparse, it was found to be difficult for the powder itself to initiate the discharge in vacuum. To create a powder discharge with good reproducibility, a preionization was employed to supply a sufficient amount of initial electrons. For preionization discharge, we placed a third electrode of a tungsten wire near the center of the high-voltage electrode for cathode. When the main capacitor discharge is fired, a surface discharge occurs between the electrodes, charging a 500pF capacitor.

III. Results and Discussion

1. Evolution of the discharge

The early stage of the powder discharge was observed using two high-speed cameras. Framing pictures were taken by the Imacon 468 (Hadland Photonics) with an exposure time of 50 ns. Streak pictures were taken by the Imacon 792 with a slit width of 50 μm. The slit was installed in the rectangular direction to the electrode plane. Discharge currents were measured using a Rogowskii coil. The temporal change of visible light intensity was measured by a photo-multiplier via an optical fiber.

A set of framing pictures on the discharge without powder is shown in Fig.4. Although these pictures were not taken in a same discharge, they were selected as showing the typical profile at each time. In this case, the discharge had the property as a vacuum discharge. When the capacitor was fired, the initial electrons created by the preionization discharge were accelerated and collided with the anode. The evaporated material from the anode formed anode plasma that expanded toward the cathode. Fig.5 shows a streak picture of the discharge. The discharge current and the light intensity waveforms are shown in Fig.6. As an origin in the time, the light intensity waveform rise-up time was chosen. In Fig.5, the light emission was observed at the center of the anode at 0.5 ns. The peak of light intensity appeared during the phase of current rise. The most part of light emission came from the anode plasma.

Fig.7, Fig.8 and Fig.9 are a set of framing pictures, a streak picture, and the current and light intensity waveforms for the powder discharge, respectively. In comparison with the vacuum discharge, slightly different results are recognized in the powder discharge. In Fig.7(a), light emission only from the particles were recorded. The light was emitted from the surface of the particles caused by electron bombardment. Light emission profile changes from circular to diffusive manner such as in Fig.7(b). It seemed that the particles were made into plasma at this time. In Fig.7(c) and Fig.7(d), the anode plasma developed toward the cathode as was seen in the vacuum discharge mode. However, a pinched plasma channel was formed between the cathode and the anode plasma. Temporal change of the discharge shows complicated behavior as shown in Fig.8. Two peaks were observed in the light intensity waveform in Fig.9. The first peak appeared also in the vacuum discharge. The second peak corresponds to the formation of the plasma channel, which can be seen in Fig.7(c) and Fig.7(d).

In this experiment, plasma creation from the powder was hampered by the development of the anode plasma. Therefore the sufficient energy was not injected to the powder. It may possible to suppress the anode plasma by reducing the effective surface area of the anode.

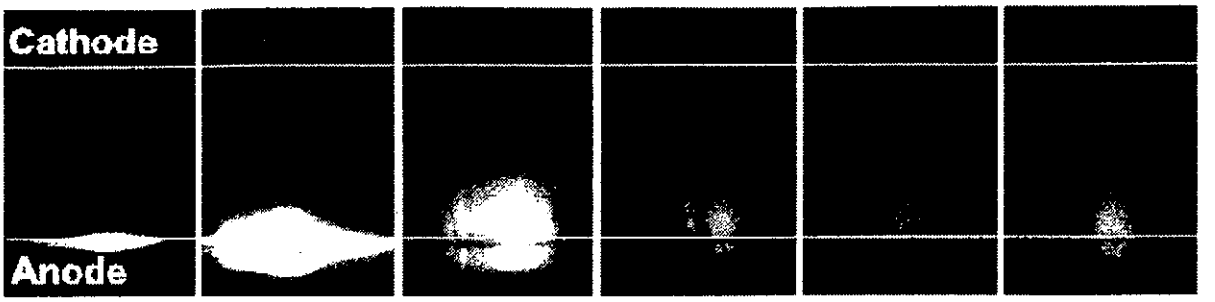

(a) (b) (c) (d) (e) (f)

Fig.4 Sequent frame pictures of the discharge without powder

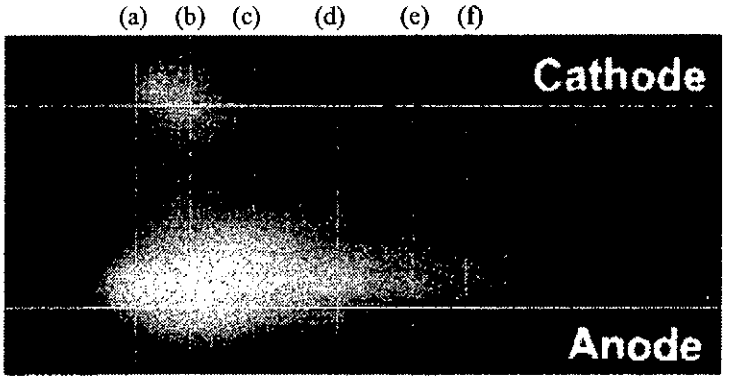

Fig.5 Streak picture of the discharge without powder

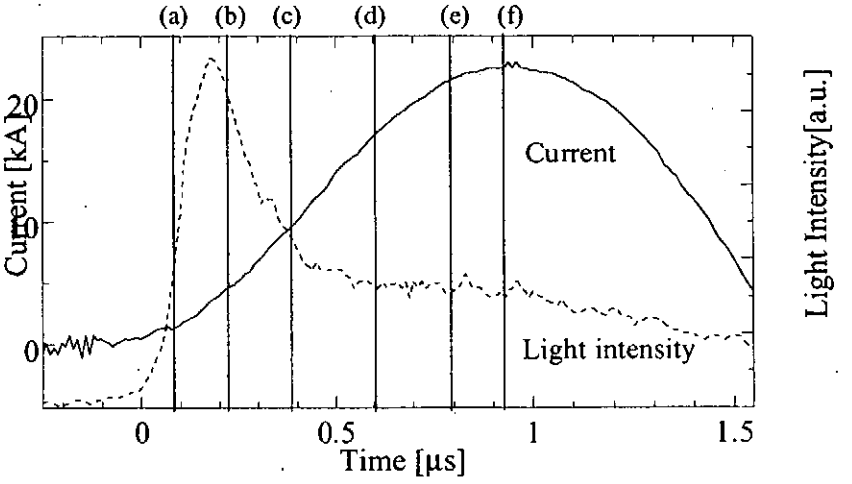

Fig.6 Current and light intensity of the discharge without powder

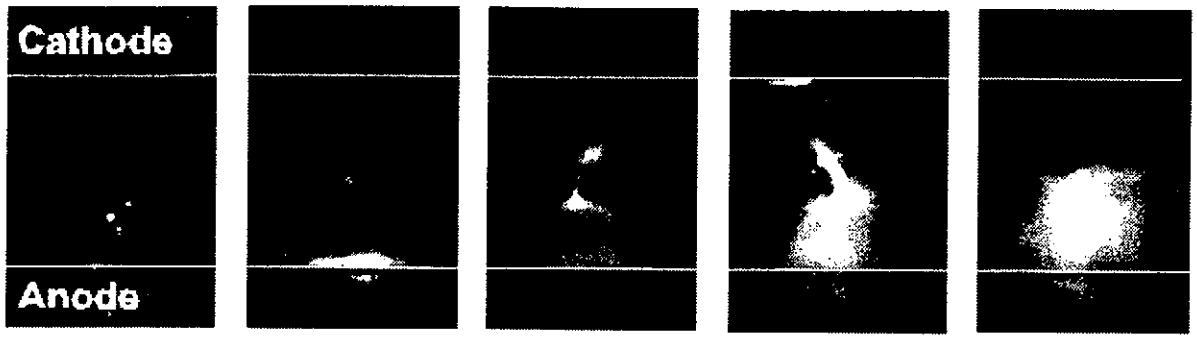

(a) (b) (c) (d) (e)

Fig7. Sequent frame pictures of the discharge with powder

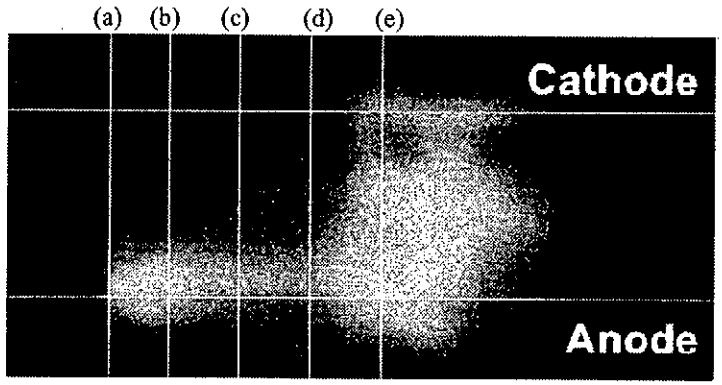

Fig.8 Streak picture of discharge with powder

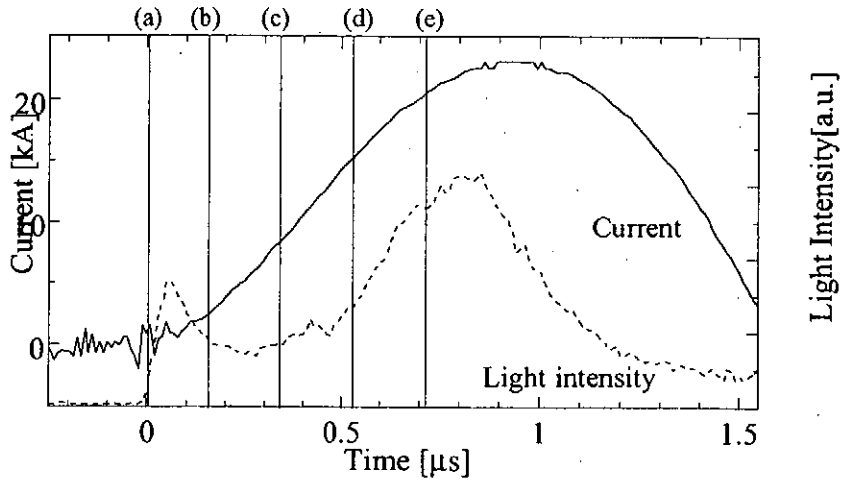

Fig.9 Current and light intensity of the discharge with powder

2. Vaporization process of the powder

Framing pictures could not give us the useful data on the vaporization process of the powder itself such as decrease of powder diameter. We employed the laser shadowgraphy to observe the outer diameter of particles in the powder discharge. The second harmonic, 532nm, of a pulsed Nd:YAG laser with a pulse-width of 8 ns pulse was used. The shadowgraph was recorded on the Polaroid films.

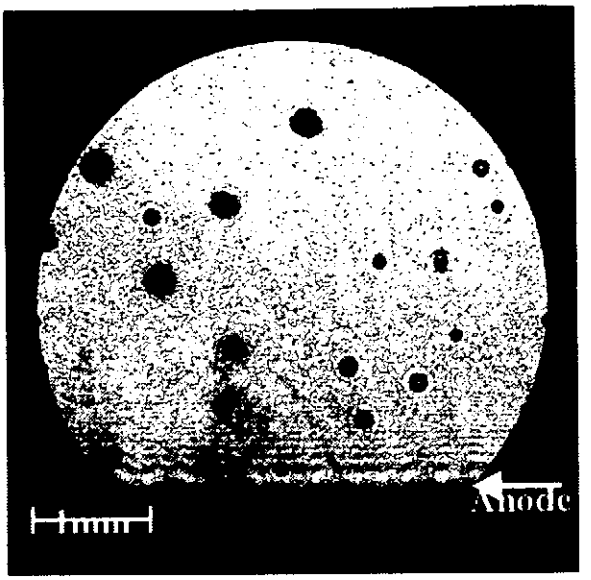

Fig.10 Shadow image of the powder

Fig.10 shows a shadowgraph at the vicinity of the anode in the powder discharge. Three kinds of particle images can be recognized in the picture. The smallest clear black one and the one with fringes are the particles with the original diameter that are not evaporated. Since the depth of focus was shallow, the fringe patterns appeared for the particles in the out of focus. Ones with larger diameter and blurred outer edge correspond to evaporating particles. The recorded diameter for evaporating particles ranges from 1.5 to 3 times that of initial powder, because vapor exists around the particles. At the following phase, the shadowgraph recorded clearly the vapor from the anode of which amount was much larger than that from the particles.

IV. Conclusion

Early stage of discharge with the powder was examined using image-converter cameras and laser shadowgraph with the Nd:YAG laser. The shadowgraph is a useful tool to observe the vaporization process in the powder discharges. The evaporation of powder was occurred only the beginning of discharges. At the following time, plasma creation from the powder was hampered by the development of the anode plasma. It may possible to suppress the anode plasma by reducing the effective surface area of the anode.

References

[1] M.Tatarakis et al.: Phys.of plasmas, vol.5, no.3 (1998) p.682
[2] H.Nozawa et al.: Jpn.J.Appl.Phys., vol.40 (2001) p.1009
[3] L.Dascalescu et al.: IEEE Trans. Ind. Appl., vol.34, no.1 (1998) p.66
[4] A.Y.H.Cho et al.: J.Appl.Phys., vol.35, no.9 (1964) p.2561

Consideration of Scaling Laws in Plasma Focus Devices

Mehrdad Kashani and Tetsu Miyamoto
College of Science and Technology, Nihon University,
Kanda-Surugadai, Chiyoda-ku, Tokyo

Abstract

The scaling laws in plasma focus discharges were studied. In our experimental results that were obtained under the same conditions except for the cathode structure. The scaling laws of the neutron yield in the bar and tubular cathode are different. In order to confirm the difference, the scaling laws and experimental results obtained by many authors and devices were summarized. These results do not seem to support our experimental results. However, they were obtained in different devices with the bar or tubular cathode. Each result deviates from the scaling law by about an order, which is bigger than the difference in both cases. Hence, for a complete comparison it is necessary to investigate scaling laws for both types of cathode in the same device.

Keyword: Plasma Focus, Scaling Laws, Neutron Yields, Cathode Effect, Energy dissipation

1. Introduction

The hot, dense plasma produced in plasma focus is a rich source of phenomena such as the emission of intense radiation, neutron yield, as well as copious nuclear fusion products. One of the important characteristics of plasma focus devices is that the scaling laws hold for emitted neutrons under optimized experimental conditions, independently of the details of devices. The various ways of neutron yield scaling to bank energy or discharge current have been experimentally established or theoretically predicted. Most scaling laws for neutron yield to bank energy or maximum current are $Y \propto E^{\beta}$ with $1.65<\beta<2$ or $Y \propto I^{\alpha}$ with $4<\alpha<5$, respectively[1],[2]. There are a lot of experimental parameters required for optimizing neutron yield, such as length of center electrode and outer electrode, radii of electrode, gas pressure, impurities, insulator material, geometry and so on, but the cathode structure and cathode parameters have been considered to have only a minor influence on the plasma focus discharge. The optimum condition for each device is, roughly speaking, obtained by pinching the plasma in front of the anode at the phase near the current maximum, in other words, by concentrating the discharge energy in the pinch region. When the strong focus occurs, the impedance of the pinch region increases enormously, and the circuit energy is concentrated there. This is the reason why the scaling law holds independently of the details of devices. The scaling laws obtained so far, however, include some ambiguities. There are based on the results of different devices, and give only roughly the tendency data spread around the scaling laws. The results obtained in our previous experiments, that is, the cathode structure dependence, are masked in the scaling laws. The purpose of the present paper is to understand the effect of the cathode in scaling laws.

2. Experimental Result in Nihon University

We summarize the experimental results reported previously[3] (the capacitance 22.5 μF and operating voltage 25 kV) with two types of cathode electrodes: (I) the cathode consisted of sixteen bars arranged cylindrically and (II) the cylindrical copper tube (Figure 1)

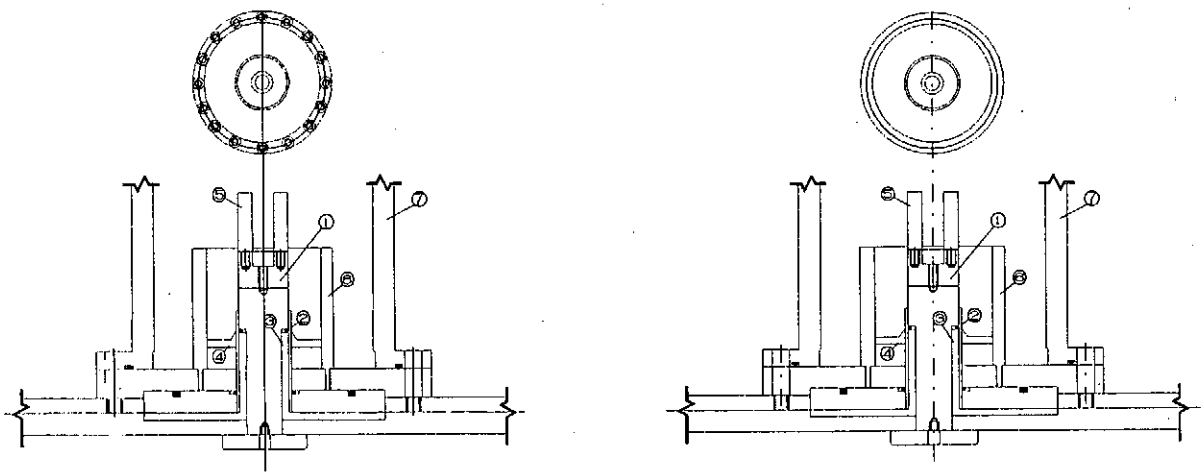

(a) (b)

Figure 1. Schematic diagram of the device, (a) Bar Cathode (B) Tubular Cathode
①Anode,②Pyrex glass,③ Polyethylene,④One part of Cathode,⑤ Cathode and ⑥Vacuum Chamber

The short-circuited current was measured short-circuiting at the top of the anode. The inductance estimated from this current differs from the floating inductance or the zero inductance at the phase of discharge starting. The inductance given in Table 1. (i.e., zero inductance) is obtained subtracting the inductance around the anode.

Table 1. The results of experiments at each optimum condition

Type	Plasma Focus Discharge			Short-Circuited Discharge			I_P/I_M	Neutron Yield per shot
	P (torr)	t_{Pinch} (μs)	I_P(kA)	$t_{1/4}$ (μs)	I_M (kA)	L_o(nH)		
Bar cathode	4.5	1.62	211	1.5	314	48	0.67	1.2×10^9
Tubular cathode	2.5	1.34	168	1.2	350	35	0.48	3.6×10^8

The experimental results are summarized as follows:

(1) The neutron yield is higher in the bar cathode than in the tubular one.
(2) The short-circuited current is lower in the former.
(3) In spite of it, the maximum current in focus discharge (the current just before pinch) is higher in the former.
(4) The optimum pressure is higher in the former.

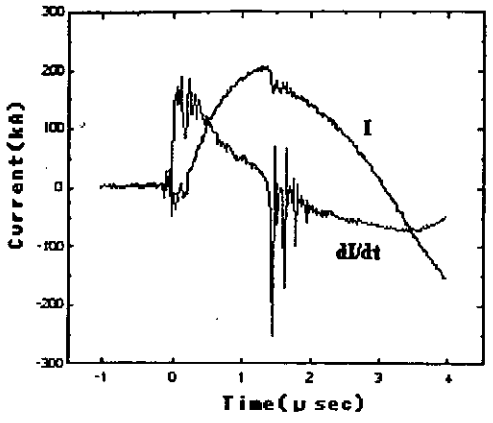

Fig.2 Typical current I and dI/dt signal in the bar cathode

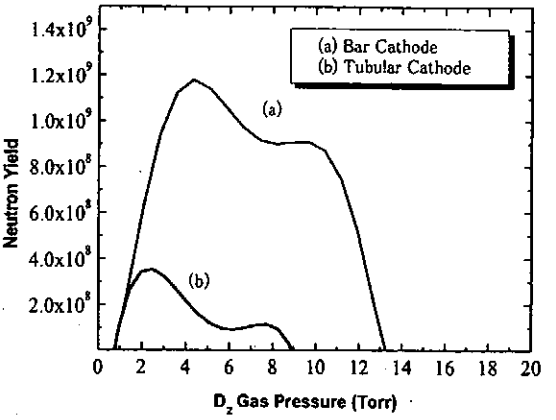

Fig.3 Neutron Yield vs. Gas pressure

The main difference between the bar and tubular cathodes was observed in the neutron yield. The neutron yields were much lower in the tubular cathode than in the bar one. (See Table I and Fig.3).

3. Interpretation of the Experimental Results

Figure 4 shows a simple diagram of the current sheath. In order to compare easily both cathode conditions, the right half of the figure shows the bar cathode condition and the left half the tubular.

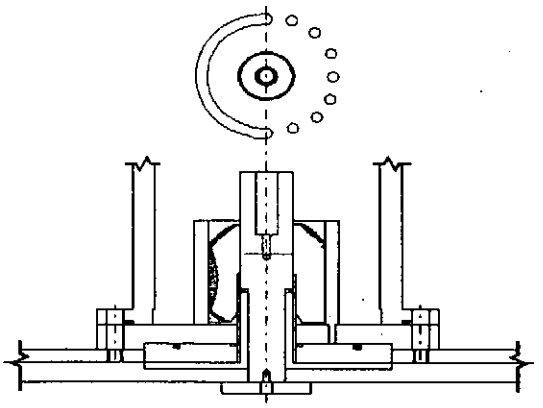

Fig. 4 Current sheath for tubular and bar cathode

This figure shows that most gas around the anode is compressed to the inner surface of the tubular cathode after being ionized and heated, and that the plasma contacts to the cathode in wide region. It seems that most of the energy would be lost due to thermal conduction or due to ablation of the surface material of electrodes. While in the bar case the plasma escapes through bars on the way moving along the axis in this case. The plasma moves to the tip of the anode, forming a thin sheet. Most current flows through this plasma sheet. The contact area and the plasma density near the cathode are smaller. As a result, the energy dissipation smaller and the neutron yield is higher in the bar cathode than in the tubular cathode.

4. Summary of Previous Experimental Results Obtained in Various Devices

Results of various plasma focus devices with bar and tubular cathodes were summarized in Table 2. The scaling laws of the neutron yield to discharge current and stored energy have been re-examined by cathode structure.

In Fig. 5 the plasma discharge current as a function of stored energy is plotted. The slope of the straight line compatible with these points shows that I increase in proportion to $E^{0.4}$. This relation is quite similar to previous results[4].

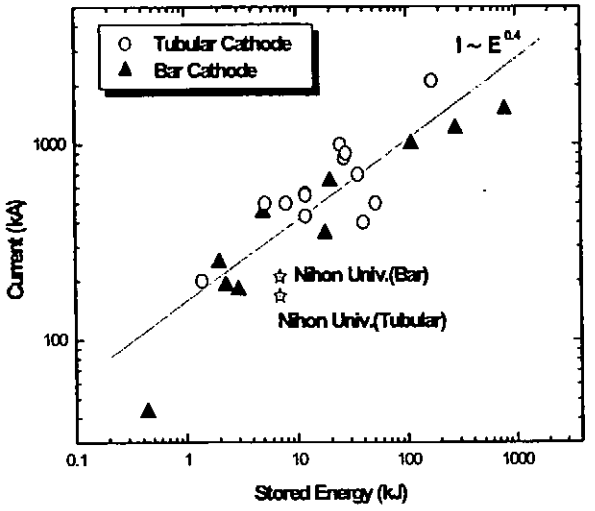

Fig. 5 Stored energy vs. plasma discharge current for various plasma focus devices

The scaling laws of neutron yields to the stored energy and discharge current are shown in Fig. 6 and 7, respectively.

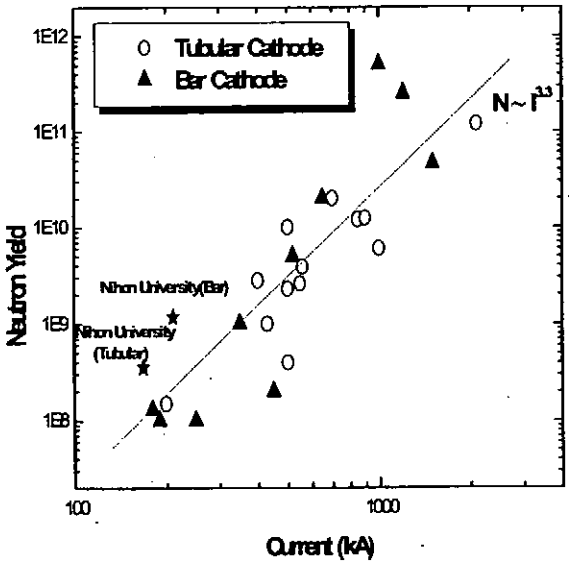

Fig.6 Neutron Yield vs. Discharge Current

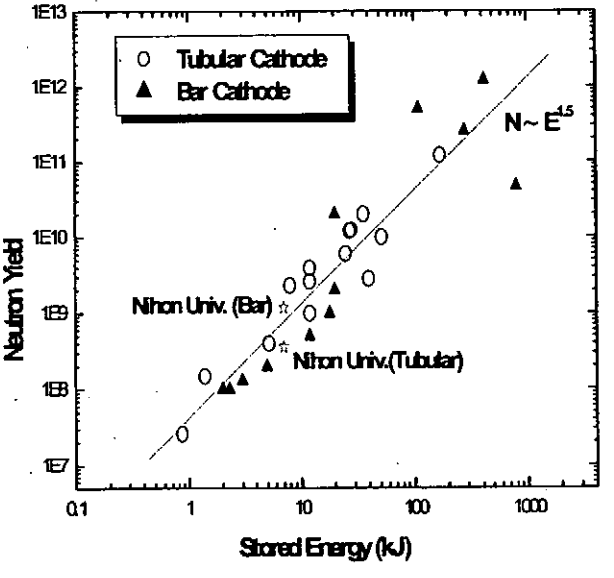

Fig. 7 Neutron Yield vs. Stored Energy

These scaling laws are consistent with previous scaling laws, but fail to show a marked difference between the bar and tubular cathodes.

Table 2. List of characteristic data for various plasma focus devices

Device Name	W_0 (kJ)	V_0 (kV)	I_P (kA)	I_M (kA)	I_p/I_M	L_0 (nH)	r_A (mm)	R_C (mm)	ℓ_{Anode} (mm)	P (Torr)	Neutron Yield
●NESSI[28] Darmstadt	40	16	400	1800	0.22	24	-	-	-	5	2.8×10^{9}
●PF-360[30]	171	36	2100	-	-	-	100	150	300	9	1.2×10^{11}
●MAJA-PF[31]	52	50	500	-	-	-	-	-	-	-	10^{10}
●DGID-AR[9]	0.86	17	-	-	-	-	-	-	-	2.5	2.6×10^{7}
●Burst[10]	5.2	15	500	-	-	-	-	-	-	6	4×10^{8}
●VUNT-USA[11]	25	20	1000	-	-	-	50	100	-	6.5	6×10^{9}
●AERO-CO[12]	27	18	850	-	-	-	39	75	220	4	1.2×10^{10}
●LOS-ALA[13]	36	20	700	-	-	-	-	-	-	4	2×10^{10}
●AFOSR[17]	8	17	500	-	-	-	-	-	-	6	2.3×10^{9}
●DPF-78[18]	28	60	900	-	-	-	-	-	-	4	1.24×10^{10}
●SNL-USA[21]	1.4	20	200	365	0.54	21	12	47	70	4.5	1.5×10^{8}
●MINIFOCUS[1]	12	20	430	585	0.73	70	25	45	212	2	10^{9}
●HV-FOCUS[1]	12	85	560	620	0.90	35	12	30	40	8	3.9×10^{9}
●HYP.-FOCUS[1]	12	20	550	1700	0.32	8.3	12	30	80	8	2.6×10^{9}
●New Mexico[7]	8.9	80	260	585	0.44	116	6.35	50.8	124	-	-
▲Limeil[8]	27	40	520	530	0.98	192	50	100	250	3	5×10^{9}
▲DP-PA[23]	2.3	12	190	-	-	-	-	-	-	2.5	10^{8}
▲DPF-4[24]	18	20	350	-	-	-	-	-	-	3	10^{9}
▲SPEED1[25]	20	160	650	1000	0.65	40	50	150	65	3	2×10^{10}
▲SPEED2[27]	110	230	1000	3800	0.26	15	-	-	-	4	5×10^{11}
▲POSEIDON[29]	280	60	1200	-	-	-	208	272	447	4	2.5×10^{11}
▲IPF-2/20	20	17	-	-	-	-	48	83	-	4	2×10^{9}
▲PACO[14]	2	31	250	292	0.85	47	40	100	140	1	10^{8}
▲CONICET[15]	5	30	450	471	0.95	45	36	72	130	2	2×10^{8}
▲UNU/ICTPPFF	3	14	180	-	-	-	19	32	160	3	1.3×10^{8}
▲PF-1000 (Italy)	800	32.5	1500	-	-	8.9	115	200	600	-	4.6×10^{10}
▲Livermore Lab.	420	46	-	-	-	-	-	-	-	-	1.2×10^{12}
▲DP-UM[22]	12	20	-	-	-	-	-	-	-	6	5×10^{8}

r_a = Anode radius R_C= Cathode radius ℓ_{Anode}= Anode length

●Tubular Cathode ▲ Bar Cathode

5. Conclusion

The experiment in Nihon University showed that the neutron yield was higher in the bar cathode by about three times than in the tubular one. This result is understood as follows.

(1) The dissipated energy increases in relation the contact area between the plasma and the cathode.

(2) The contact area and the plasma density near the contact area are smaller in the bar cathode than in the tubular one.

(3) This results from the fact that the plasma can escape through the bars in the bar cathode.

(4) The result that the optimum pressure is higher in the bar cathode suggests the existence of escaping plasma, and supports the above considerations.

On the other hand, the scaling law on the neutron yield obtained by many researchers shows

that no difference exists between the bar and the tubular cathodes. The contradiction between our experimental result and the previous scaling law is interpreted as follows:

(1) The scaling law having been obtained so far gives only rough estimation with deviation of an on the neutron yield.
(2) The neutron yield depends on various parameters of devices and experimental conditions. We should notice that the optimization in the previous experiments was carried out only for limited parameters and conditions in each different device, and hence was not perfect.
(3) It is suggested from the fact that the experimental results deviate from the scaling law.
(4) The difference of neutron yield in both cathodes showed in our experiments is about three times, and is within the ambiguity of the scaling law. Therefore, our experimental result does not necessarily contradict the scaling law.

If the above interpretation is correct, the cathode effect on the neutron yield is observed only by comparing neutron yield using exactly the same devices except for the cathode structure. Then, the bar cathode will be better than the tubular one.

6. Reference

[1] G. Decker, L. Flemming, H. J. Kaeppeler et al, Plasma Phys., Vol. 22, (1980) 245
[2] M. Milanese and J. Pouzo, "Neutron yield scaling for plasma focus device," in small plasma physics' experiment. London: world scientific, (1987) 66
[3] M.A.M. Kashani, K. Sato, T. Miyamoto, A. Baba, R. Horiuchi, K.Takasugi, S. Sasaki, M. Lu and V. Vikhrev, Proc. of Int. Symposium on Pulsed Power and Plasma Applications (ISPP-2000), Oct. 26-27, 2000, Korea
[4] S. Brant et al, in Plasma Physics and Controlled Nuclear Fusion Research 1998 (Proc. 12th Int. Conf. Nice, 1988) Paper IAEA-CN-50/C-5-17, Vol. 2, IAEA Vienna

DYNAMICS OF CAPILLARY DISCHARGE PLASMAS AND LASING CONDITIONS

N.Sakamoto, G.Niimi, M.Nakajima, E.Hotta and K.Horioka

Department of Energy Sciences, Tokyo Institute of Technology, Nagatsuta 4259 Midori-ku Yokohama, 226-8502, Japan

ABSTRACT

Dependencies of the lasing condition of capillary discharge plasma on the initial gas pressure, rise rate of the feeding current; dI/dt, and the length of the plasma are experimentally investigated. The lasing time lengthens with the increase of the initial gas pressure and decreases with the increase of dI/dt. The lasing output exponentially increases with the plasma length, and it has an optimum condition at proper values of the initial gas pressure and dI/dt. Correlations of the Z-pinch dynamics with the process to lead to the appropriate plasma parameter for lasing are discussed based on the experimental results.

I. Introduction

Generally, the shorter the wavelength is, the more detailed information we can get using the light source. In addition, lasers have remarkable characters; monochromaticity, directivity, high intensity and coherency. In order to utilize these features, it has been looked for the realization of shorter wavelength lasers, with the recent technological advances.

In 1984, groups at Lawrence Livermore National Laboratory and Prinston University succeeded to get lasing at wavelength of about 200 Å. [1,2] They obtained the lasing condition using laser ablation plasma. But, the facilities operated for the lasing experiment were very large, expensive, and the energy efficiency was extremely low (about $10^{-6} \sim 10^{-5}$). Therefore, this lasing method is considered to be difficult to use for practical applications.

On the other hand, J. J. Rocca *et al.* at Colorado State University acquired lasing at 3p-3s transition (~469 Å) of Ne-like argon, by fast capillary Z-discharges. [3] The Z-discharge has possibility to accomplish practical lasing sources compared with the high-power laser system, from the view point of energy efficiency, the size of devices, and so on. Therefore, the fast capillary Z-discharges are paid attention as promising laser sources at soft x-ray region.

In the discharge plasma, the fast pinching effect plays a dominant role to make the high energy density plasma. The fast compression process inevitably accompanies the energy dissipation. If we assume the pressure of compressed plasma is constant, this means that the faster compression process makes hotter and lower density plasmas. In addition, the interaction between the current sheet and the shock wave inside the capillary makes an inner structure with temperature, density and velocity distribution, in the plasma column. [4] All of these parameters affect the gain distribution, refraction of stimulated emission and opacity of the resonance levels. Hence, for realizing larger

energy and shorter wavelength lasers with capillary discharges, it is necessary to understand the formation process of high energy density plasma.

We have experimentally investigated the lasing condition of Ne-like Ar, as a function of initial Ar gas pressure in the capillary and the rising rate of driving current; dI/dt. Based on the results, we discuss the correlation between the plasma dynamics and the lasing condition in fast capillary discharge plasmas.

II. Operational principle of capillary discharge laser

A. Z-pinch process for the formation of lasing plasma

To make a lasing plasma, capillary discharges utilize Z-pinch processes: a high current induced in a capillary compresses the plasma column by Lorentz force caused by the induced magnetic field due to the high current itself. By using a fast discharge with uniform pre-ionization, we can avoid destructive magneto-hydrodynamic (MHD) instabilities. [4] The parameters of compressed plasma are strongly affected by the dynamics of the Z-pinch. The obtained high density and high temperature plasma has a coaxial structure with large volume and high aspect ratio.

B. Z-scaling for lasing plasma

Shorter wavelength lasers can be obtained using isoelectronic sequence such as Ne-like or Ni-like sequences of higher-Z atoms (Z-scaling). [5] A simplified pressure balance; Bennet relation can estimate required current for making the lasing plasma as,

$$n_e kT_e = \frac{\mu_0}{4\pi^2(1+Z)} \cdot \frac{I^2}{r^2}. \quad (1)$$

where I is discharge current, r is the radius of plasma column and Z is the charge state of compressed gas. [6] For this simplified estimation, a stable implosion without MHD instabilities is assumed. Hence, Z-scaling to shorter wavelengths can be made simply by increasing the discharge current. For example, Fig.1 shows an example of the simplified scaling for d=~100 μm which is the diameter of the plasma column at maximum compression. It says that a current of ~10kA is required for Ne-like Ar, and expected laser wavelength is about 500 Å. Also, ~200 kA is desired for Ni-like Xe, whose lasing wave length is about 100 Å. On the other hand, the actual compression processes accompany inertial force effects, therefore it is expected that desired feed currents become lower than the required currents shown in Fig.1.

C. Characteristics of discharge excitation

In case of laser excitations, it is difficult to control the plasma parameters (electron density and electron temperature) to appropriate values for lasing conditions, because the laser plasma is intrinsically formed by expansion process. On the other hand, the discharge excitation utilizes compression process to make the lasing plasma. The parameters of core plasma, here the core means the most compressed state, depend on the numerous operation parameters: density and temperature of the initial gas, the peak value and its rise rate of feed current, and the diameter of a capillary tube. That is to say, we have a possibility to control the compressed plasma conditions, for example by changing the initial Ar gas pressure P_{Ar} and dI/dt. In other words, we can expect a

optimization of the lasing conditions by changing P_{Ar} and dI/dt.

III. Experiment apparatus

A. Discharge devices

We use two types of pulse-power devices for the experiments. One device called "LIMAY" is composed of a Marx generator, a pulse forming line and a transmission line.[4] The maximum output voltage is 600 kV and the characteristic impedance is 3 Ω, hence it can drive a maximum peak current of 200 kA. Another device has a step-up transformer type pulse generator and it can produce sinusoidal waveform with maximum current of 50 kA. [7,8]

B. Capillary load section and diagnostic devices

One of the structures of a capillary load part is shown in Fig.2. The capillary is made of ceramic or pyrex glass, with the diameter of 3 mm, and the maximum capillary length is 150 mm. We can change the capillary length by inserting a molybdenum rod into the capillary. The parameter ranges we have investigated are the initial Ar gas pressure of 100~1000 mTorr and dI/dt of 100~1000 A/ns. We detected the lasing signals by a X-ray diode (XRD) and the current values by a Rogowski coil or a pickup coil. Dividing the current value at lasing by the lasing time, we calculated the rising rate; dI/dt. Here, we define the lasing time as the interval between current starting time and the time when the lasing appears. To observe the pinching process we took photographs by Imacon 648 from the perpendicular direction to the capillary.

IV. Experimental results and discussions

A. Lasing signals and gain coefficient

We obtained lasing signals by adjusting the condition of capillary discharges. Fig.3 is a typical lasing waveform that we got in our experiments. The spike-like waveform in Fig.3 indicates the XRD signal of the lasing. In this figure, "current" means the load current in the capillary.

We examined the directivity of the spike-like waveform by changing the distance of the XRD from the exit of the capillary. Fig.4 shows the XRD signals when the distances from the exit of the capillary to the XRD are 120 mm and 600 mm respectively. As Fig.4 shows, the attenuation of the spike-like waveform is quite less than other parts of the waveform when the distance is increased. This means that the spike waveform has a strong directivity than the other part of XRD signal.

Next, we measured the peak values of spike-like XRD signals as a function of the plasma length. Fig.5 shows the results, which is indicating an exponential enhancement of the spike-like XRD signals when the capillary length was increased. From this result, we can estimate the gain coefficient to be 0.8 cm^{-1}.

We could observe the lasing signal, only when we made pre-ionization discharge with proper current level and timing before the fast main discharge. In order to investigate the pre-ionization effect, we took the fast framing photographs of the

discharge column with (Fig.6) and without (Fig.7) the pre-ionization, from the side direction of the capillary. As shown, obviously the plasma evolution is disturbed by a sausage-like instability without the pre-ionization.

B. Discussion about dynamics of capillary discharge plasmas

We have investigated the lasing times defined above and the peak values of the spike-like XRD lasing signals as a function of P_{Ar} and dI/dt.

Fig.8 shows the lasing times as a function of P_{Ar} with dI/dt as a parameter. The higher the P_{Ar} was, the later the lasing times were; increases of the density of initial enclosed gas delay the pinching speed.

On the other hand, Fig.9 shows the lasing times versus dI/dt with P_{Ar} as a parameter. The higher the value of dI/dt was, the earlier the lasing times were; this means that large values of dI/dt cause strong compression force and accelerate the pinching process.

These results clearly indicate that the lasing conditions depend on the dynamics of Z-pinch and those qualitative behaviors are expected to be extrapolated to the operational range of shorter wavelength, i.e., capillary discharges using heavier gas.

Fig.10 shows the peak values of spike-like XRD signals as a function of P_{Ar} with dI/dt as a parameter. There appeared the distributions that had a peak place. Fig.11 shows a schematic n(density)-T(temperature) diagram of the expected compression processes of the capillary discharge plasmas and the lasing parameter. The solid line in Fig.11 corresponds to an isentropic process from a initial condition expressed by,

$$n_e = n_0 T_e^{\frac{3}{2}} \tag{2}$$

where n_0 is an initial density. The dot-dashed line shows a condition of constant energy density (P), based on the lasing condition of Ne-like Ar. Three dotted lines schematically show the expected compression process for the formation of lasing plasmas. Although these lines on the n-T diagram are drawn only for references, they give us some insights into the plasma process for making the lasing condition. For example when dI/dt was 700~800 A/ns, we got the maximum spike-like XRD signals at P_{Ar} = 500 mTorr. Then, the compression process is considered to correspond to the center line of the three dotted lines because the center dotted line intersects the core of the estimated Ne-like Ar lasing domain. When P_{Ar} is decreased to about 400 mTorr, the compression route is expected to shift to the lower line and when P_{Ar} is increased, for example about 700 mTorr, the process is thought to shift to the upper line.

On the other hand, Fig.12 shows the change of the peak value of the spike-like XRD signals versus dI/dt when P_{Ar} was fixed. The spike-like XRD signals also have the distributions against dI/dt. Dotted lines in Fig 13 also give the anticipated compression processes depending on the change of dI/dt. As shown in Fig.12, at P_{Ar} = 300 mTorr, we obtained the maximum spike-like XRD signals when the dI/dt is around 550 A/ns. Then, the compression route is considered to go through the middle line of the three dotted lines. In this case, when the dI/dt is increased, the compression process is expected to shift to the lower line with smaller inclination shown in Fig.13, because stronger compression is more dissipative during the compression processes.

V. Concluding Remarks

Characterizations of Z-pinch dynamics are crucially important for the optimization and the extrapolation of operational range of capillary discharge lasers. We have experimentally investigated the effect of Z-pinch dynamics on the formation of plasma

appropriate for the lasing action. We can conclude the experimental results by next three points;

1. Lasing by Ne-like Ar was confirmed at discharge condition with proper P_{Ar} and dI/dt;
2. Core plasma parameters depended on the initial gas density and dI/dt of the load current;
3. To lead the plasma parameters to proper conditions for lasings, we have to control the initial conditions and/or the compression process.

References

1) D.L.Matthew *et al.*, Phys. Rev. Lett. **54**, 110 (1985).
2) S.Suckewer *et al.*, Phys. Rev. Lett. **55**, 1753 (1985).
3) J.J.Rocca, V.Shlyaptsev, F.G.Tomasel, O,D,Cortazar, D.Hartshorn, and J.L.A.Chilla, Phys. Rev. Lett. **73**, 2192 (1994).
4) T.Hosokai, M.Nakajima, T.Aoki, M.Ogawa and K.Horioka, Jpn. J. Appl. Phys. **36**, 2327 (1997).
5) T.Hosokai, H.Hanajima, M.Nakajima, T.Aoki, M.Ogawa and K.Horioka, Res. Rep. Natl. Inst. Fusion Sci. (1997) NIFS-PROC-36, 159.
6) M.Yokoyama *et al.*, "Plasma Science and Engineering", Nikkann Kougyou Shinbun, (1988).
7) G.Niimi, Y.Hayashi, A.Okino, M.Watanabe and E.Hotta, J. Plasma Fusion Res. **77**, 1239 (2001).
8) G.Niimi, Y.Hayashi, M.Nakajima, M.Watanabe, A.Okino, K.Horioka and E.Hotta, J. Phys. D.: Appl. Phys. **34**, 2123 (2001)

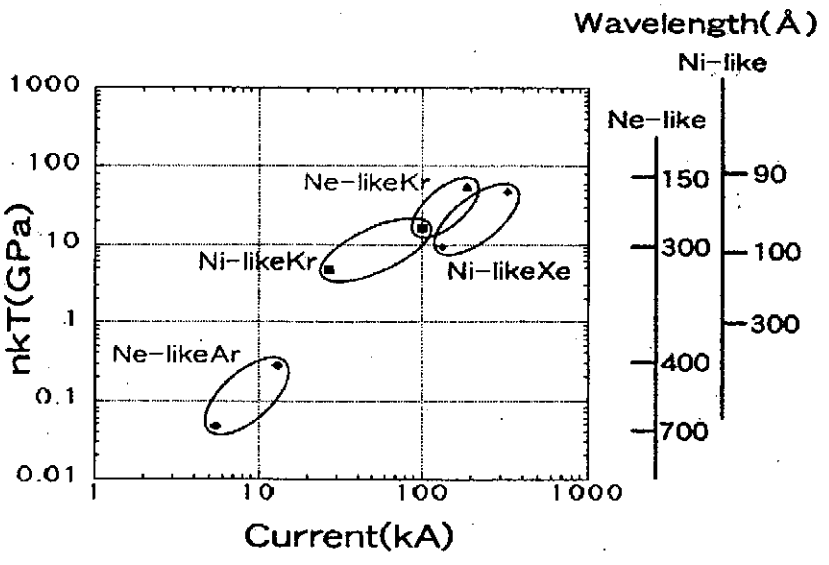

Fig.1 Operational range of discharge pumped lasers. The abscissa indicates discharge currents. The vertical lines show the energy densities of compressed plasmas and expected wavelengths of Ne-like or Ni-like lasers.

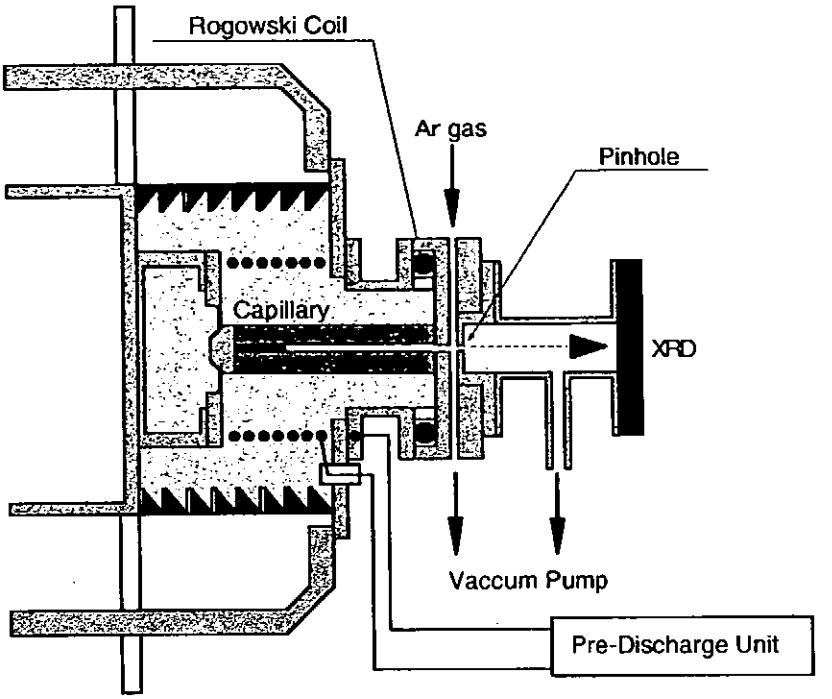

Fig.2 Typical setup of load section for capillary discharge experiments.

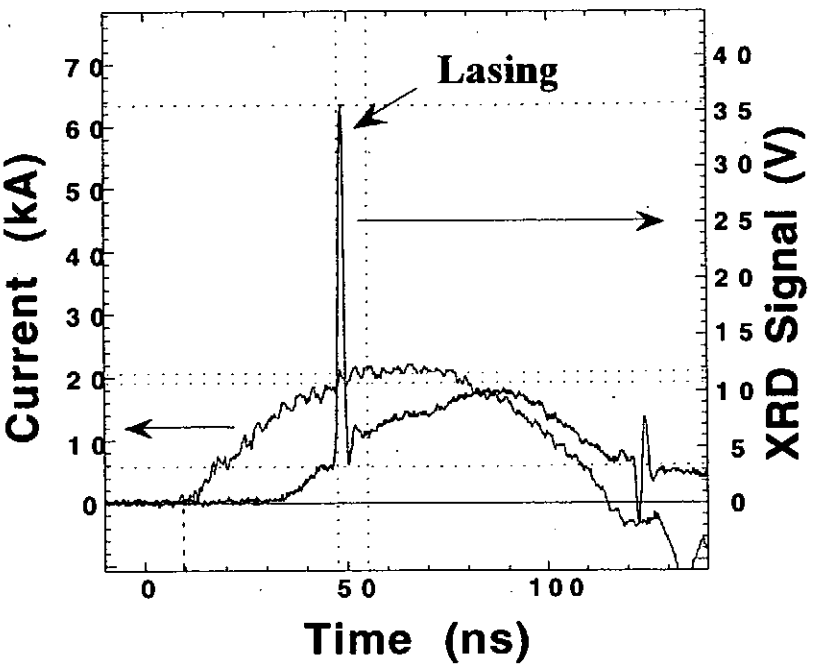

Fig.3 Typical waveforms of load current and XRD signals.

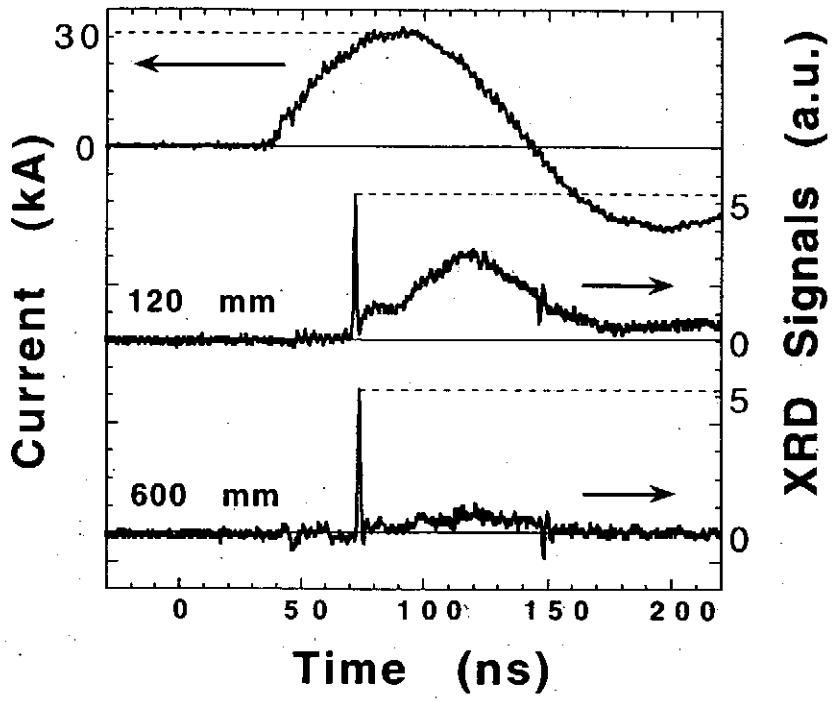

Fig.4 XRD signals at 120 mm and 600 mm from the exit of the capillary.

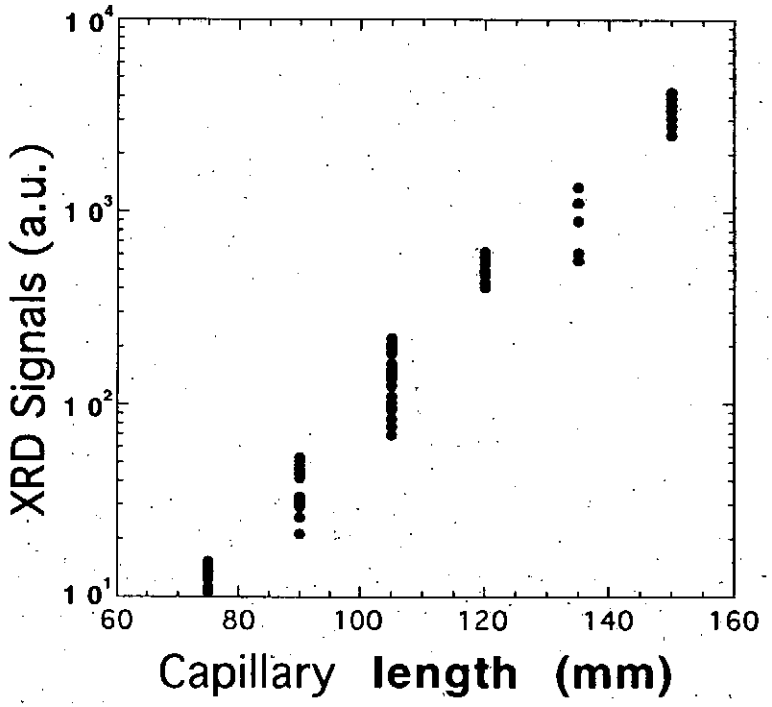

Fig.5 XRD signals versus capillary length.

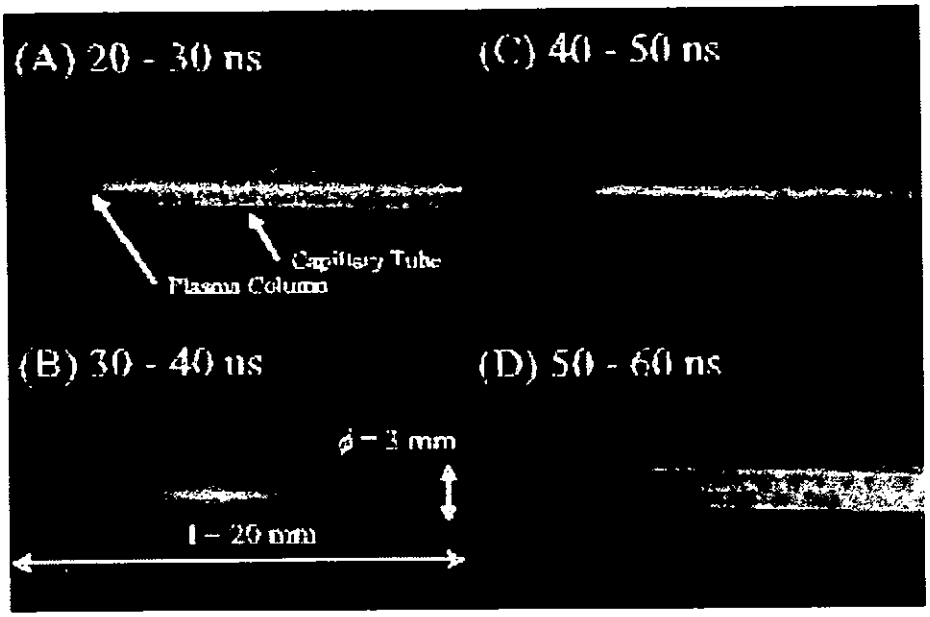

Fig.6 Framing photos of capillary discharge without pre-ionization taken from the perpendicular direction of capillary.

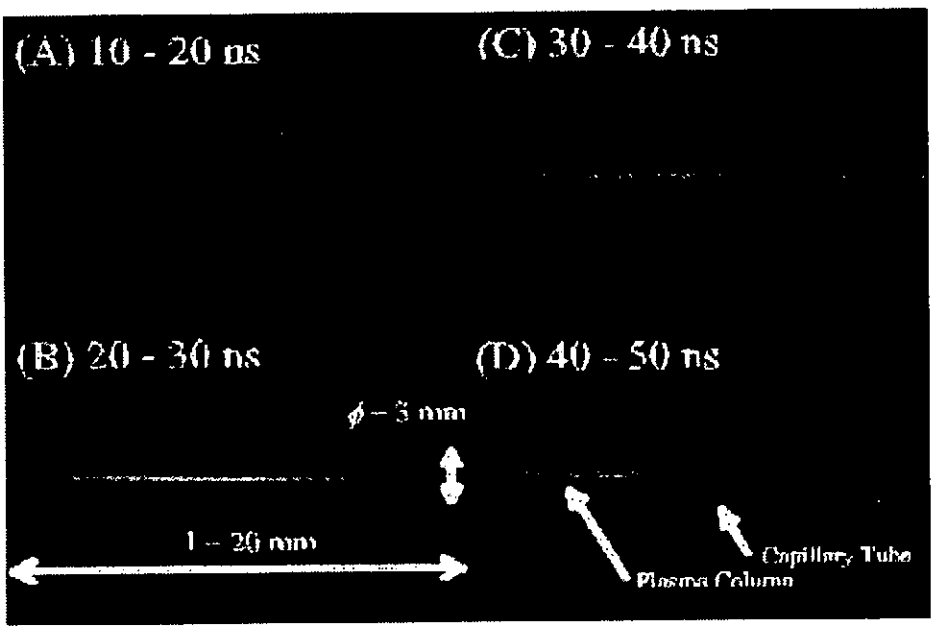

Fig.7 Framing photos of capillary discharge with pre-ionization taken from the perpendicular direction of capillary.

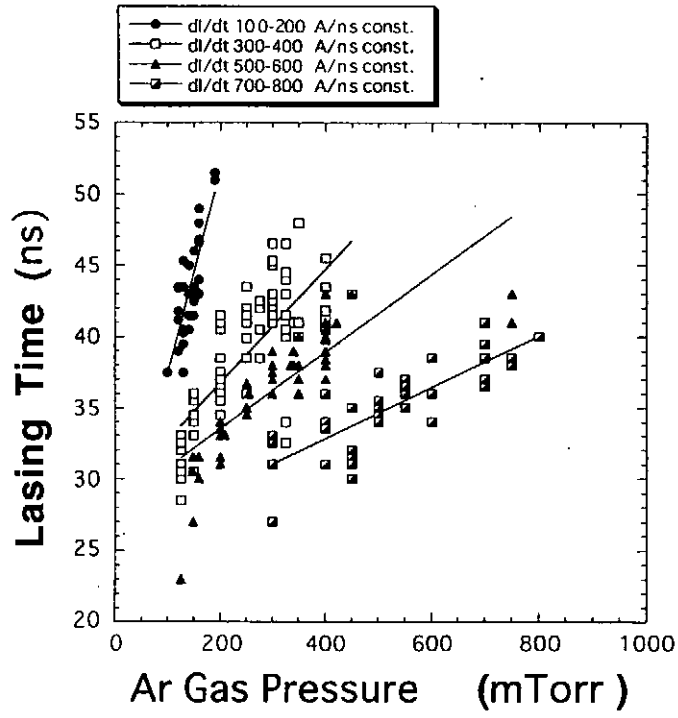

Fig.8 Lasing time as a function of P_{Ar}.

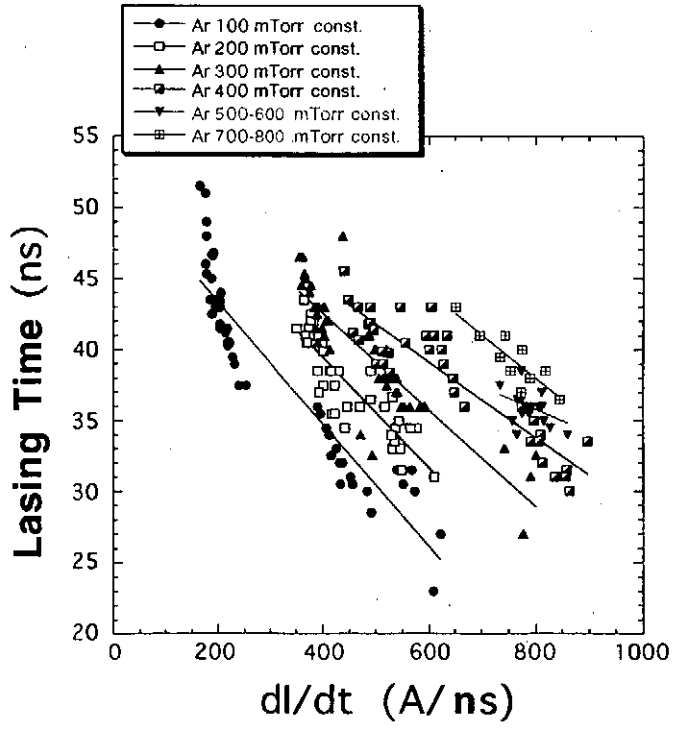

Fig.9 Lasing time as a function of dI/dt.

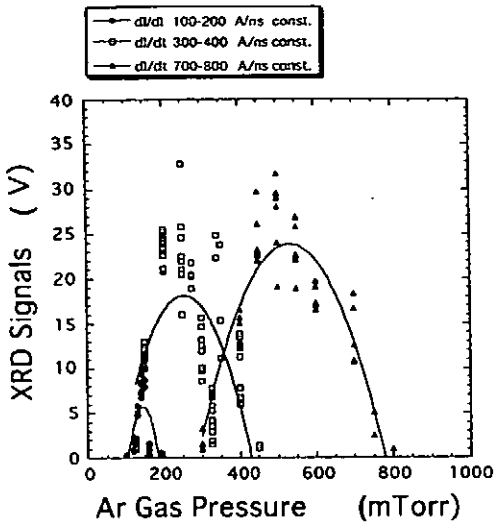

Fig.10 XRD signals as a function of P_{Ar}.

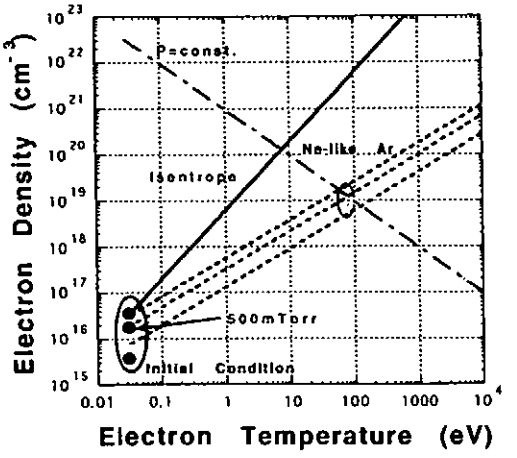

Fig.11 Schematic diagram of the expected compression processes of capillary discharge.

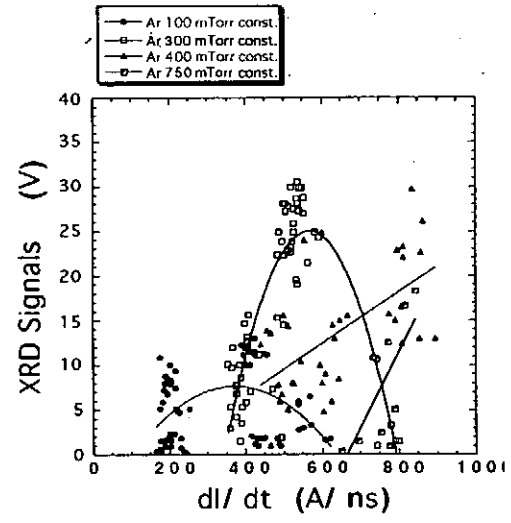

Fig.12 XRD signals as a function of dI/dt.

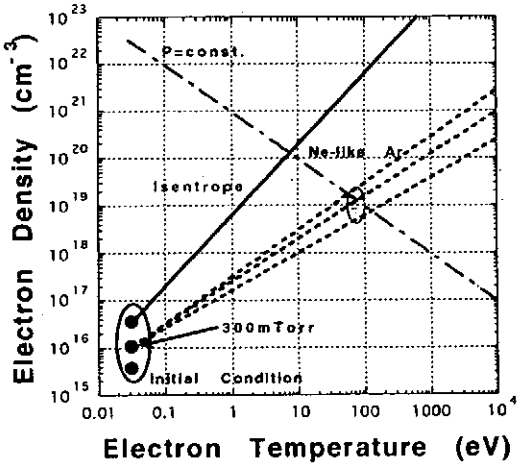

Fig.13 Expected compression processes for change of dI/dt.

A STUDY ON RELATIVE POPULATIONS AND GAIN COEFFICIENTS OF NEON-LIKE KRYPTON FOR FAST MOVING PLASMA IN CAPILLARY DISCHARGES

M. Masnavi, T. Kikuchi, M. Nakajima and K. Horioka

Department of Energy Sciences, Tokyo Institute of Technology, 4259 Nagatsuta, Midori-ku, Yokohama 226, Japan

ABSTRACT

X-ray laser gains and the level populations for collisionally pumped neon (Ne)-like Krypton (KrXXVII) ions have been studied considering the 27 - levels of the $2s^2 2p^6$, $2s^2 2p^5 3s$, $2s^2 2p^5 3p$ and $2s^2 2p^5 3d$ configurations. It was found that large gains on the $3p\ ^1S_0 \rightarrow 3s\ ^3P_1$, $3p\ ^3D_2 \rightarrow 3s\ ^3P_1$, and $3p\ ^3S_1 \rightarrow 3s\ ^1P_1$ transitions are formed for the electron density between 10^{20} and 10^{22} cm^{-3} at the electron temperatures 0.9,1 and 3 keV. The effect of the opacity of the $3d^1P_1 - 2p^6\ ^1S_0$, $3d^3D_1 - 2p^6\ ^1S_0$, $3d^3P_1 - 2p^6\ ^1S_0$, $3s^3P_1 - 2p^6\ ^1S_0$ and $3s^1P_1 - 2p^6\ ^1S_0$ transitions are performed using the escape probability factor approximation, for both the static and dynamic plasmas, which include the effect of the large velocity gradient. In addition, we found some theoretical line-intensity ratios that are sensitive on the electron density, the electron temperature, and also opacity in the interest regime of Ne-like Krypton x-ray laser.

I. Introduction

X-ray lasers using laser plasmas as the active medium have been extensively reported following both the electron collisional and recombination schemes[1]. Since Zherikhin et al.[2] suggested the idea of electron collisional pumping of Ne-like ions for transitions between the $2p^5 3s$ and $2p^5 3p$ energy levels, x-ray laser schemes using transitions between $2p^k 3p$ and $2p^k 3s$ configurations ($0 \le k < 6$) in ionic systems have been studied both theoretically[3-6] and experimentally[7-10]. Vinogradov[11], Vinogradov and Shlyaptsev[12], Palumbo and Elton[13], Feldman et al.[14-16], Goldstein et al.[17] extended the works of Zherikhin et al.[2] and carried out calculations for population inversion and gain in laser-produced plasmas for several ions. Feldman and

co-workers[14] extended the calculation to KrXXVII, and showed that a large number of KrXXVII ions can produce a significant gain in transitions between $2p^5 3p$ and $2p^5 3s$ configurations. Gupta and Sinha[18,19] theoretically estimated the temperature-dependent average ionic charge state and the fraction of KrXXVII ion. Kim et al.[20] have reported x-ray gain coefficients in KrXXVII ion with the effect of opacity using Zemansky escape probability in static plasma. On the other hand, Hosokai et al.[21] experimentally showed that, in capillary discharges, such a high energy density plasma is produced through dynamic processes. These works have motivated us to study the gain characteristics of transitions between $2p^5 3s$ and $2p^5 3p$ configurations of KrXXVII ion, especially the effect of opacity of the fast moving plasma.

In this article, in order to investigate the characteristics of gains in KrXXVII ions, we have calculated the level populations and the gains on various transitions, using the similar model that Feldman et al.[14] have used, for electron density between 10^{18} and 10^{23} cm^{-3} at electron temperatures of 0.9, 1 and 3 keV. These temperature ranges have been considered because the abundance of the Ne-like ionization stage is expected to be highest for an electron temperature near a half the ionization potential.[14] In addition to their results, we have taken into account the effect of velocity gradient using Sobolev escape probability in cylindrically contracting plasma[22], to investigate such an effect on the gain coefficients for some lasing transitions. The Sobolev optical depth estimated for plasma with locally linear velocity profile using two well-known Snowplow[23] and Slug[24] models[25]. Furthermore, some line ratios that are sensitive to the electron density, the electron temperature and also opacity are presented.

A brief description of the theory involved in our calculations is presented in Sec. II: i.e., the quasi-steady-state (QSS) collisional-radiative model for analyzing atomic population kinetics in non-local thermodynamic-equilibrium (non-LTE) plasmas, and the treatment of the opacity. The calculation results presented and discussed, and present a conclusion with our main results in Sec. III.

II. Model for Calculation

The gain coefficient for a Doppler-broadened spectral line on a radiative transition between an upper level u and a lower level l is expressed as[14-16]

$$G_{ul} = \frac{1}{8\pi}\left(\frac{M}{2\pi k T_{ion}}\right)^{1/2} A_{ul}\lambda_{ul}^3 g_u \left(\frac{N_u}{g_u} - \frac{N_l}{g_l}\right) \qquad (1)$$

where λ_{ul} is the wavelength of the transition, A_{ul} the rate of spontaneous emission, N_j the ion population density in the level j having statistical weight g_j, k the

Boltzmann constant, M the atomic mass of the ion and T_{ion} ion temperature. Ion temperature (T_{ion}) was chosen to be equal to the electron temperature (T_e) as assumed by Feldman et al.[14,15]. This assumption generally gives only the lower bound of the gain coefficient. To make a comparison of the present results with the literature[14,15,20], we have used this assumption in the present article.

The rate equation for the population N_l^i of an excited level l in the *ith* ionization stage is given by[26]

$$\frac{dN_l^i}{dt} = \sum_u R_{lu}^i N_u^i - n_e I_l^i N_l^i + n_e Q_l^{i+1} N_l^{i+1} \tag{2}$$

with

$$\begin{aligned} R_{lu}^i &= n_e C_{ul}^e, & l > u \\ &= n_e C_{ul}^d + A_{ul}, & l < u \\ R_{ll}^i &= -\sum_{m<l}(n_e C_{lm}^d + A_{lm}) - \sum_{m>l} n_e C_{lm}^e, & l = u \end{aligned}$$

where n_e is the electron density, $C_{ul}^{e(d)}$ the electron excitation (de-excitation) rate coefficient, and A_{ul} the spontaneous emission rate from an upper state u to a lower state l. The terms I_l^i and Q_l^{i+1} represent the electron collisional ionization rate coefficient from a level l and the total recombination rate coefficient to the level, respectively. Since equilibrium between the excited levels is readily established due to their short relaxation times[26], the quasi-steady-state approximation has been adopted in our calculation. In this study, the 27 levels of the $2s^2 2p^6, 2s^2 2p^5 3s, 2s^2 2p^5 3p$ and $2s^2 2p^5 3d$ configurations in Ne-like Krypton have been considered. We have been taken into account the radiative and collisional processes between all fine-structure transitions including forbidden as well as the radiative transitions. We have used the atomic data presented by Bhatia et al.[27].

The electron excitation rate coefficients are given by[28]

$$C_{ij}(cm^3 \sec^{-1}) = \frac{8.63\times10^{-6}}{g_i (T_e)^{1/2}} \int_{\Delta E_{ij}}^{\infty} \frac{\Omega_{ij}}{kT_e} \exp(-E/kT_e) dE \tag{3}$$

where ΔE_{ij} is the transition energy of the $i \rightarrow j$ transition, and Ω_{ij} the collisional strengths, which were approximated by the data.

The de-excitation rate coefficient is obtained using the detailed-balanced relation[27]

$$C_{ul}^d = \frac{g_l}{g_u} C_{lu}^e \exp(\Delta E_{lu}/kT_e) \tag{4}$$

The populations N_j can be normalized to unity by requiring[14,16]

$$m_j = N_j / N_I; \qquad \sum_j m_j = 1, \tag{5}$$

where m_j is the relative level population in the level j, and N_I the number density of Ne-like ions for all of the levels. Therefore, Eq. (1) can be rewritten as follows

$$\frac{G_{ul}}{N_l} = 1.46\times10^{-31} A_{ul}\lambda_{ul}^3 \frac{1}{T_e^{1/2}} g_u\left(\frac{m_u}{g_u} - \frac{m_l}{g_l}\right), \quad (\mathrm{cm}^{-4}) \tag{6}$$

where λ_{ul} is given in Angstrom, A_{ul} in $\sec^{-1}$, and T_e in eV. The right-hand side of Eq. (6) consists of terms only related to KrXXVII ion. It may be important to note that Eq.(7) of Ref. (20) about gain and corresponding results are incorrect.

Expressing the ion population density N_j in terms of n_e and $N_T(=n_e/\bar{Z})$ of a plasma that consists of ions of only one element with atomic number Z_n as[18]

$$N_j = \left(\frac{N_j}{N_l}\frac{N_l}{N_T}\frac{N_T}{n_e}n_e\right) = \left(\frac{N_j}{N_l}\frac{\delta}{\bar{Z}}n_e\right) \tag{7}$$

where N_j/N_l is the relative level populations calculated from Eq. (2), $\delta(=N_l/N_T)$ the fraction of Ne-like ions, N_T the total ion density, and $\bar{Z}$ the average ionic charge state. Combining Eqs. (6) and (7), the gain is calculated as a function of the relative level population, the electron density and the atomic data, as follows

$$G_{ul} = 1.46\times10^{-31} A_{ul}\lambda_{ul}^3 \frac{1}{T_e^{1/2}} g_u\left(\frac{m_u}{g_u} - \frac{m_l}{g_l}\right)\left(\frac{\delta}{\bar{Z}}\right)n_e, \quad (\mathrm{cm}^{-1}) \tag{8}$$

where n_e is given in units of (cm^{-3}). In this study, the value of gain coefficients evaluated by assuming $\delta = 0.26$ and $\bar{Z} = 27.3$ (This assumption is only optimistic for electron temperature of 3 keV, see Ref. (18) for the detail).

We have investigated the opacity (i.e., re-absorption) effect on gains. The effect of re-absorption of the resonance line radiation increases the populations of the $3s$ levels, which tends to reduce the gains on the $3p-3s$ transitions. Also, in order to the large de-excitation rate from the $3d$ to the $3p$ levels, the $3p$ level population is influenced by the re-absorption of the $2p-3d$ transition, which populates the $3d$ level effectively. This effect tends to enhance gains.

The static optical depth (τ_{mn}) at line center (λ_{mn}) on a radiative transition between the levels m and n is defined by[3]

$$\tau_{mn} = k_{mn}(\lambda_{mn})L \tag{9}$$

where L are the effective length of plasma medium and $k_{mn}(\lambda_{mn})$ the absorption coefficient, which is given by

$$k_{mn}(\lambda_{mn}) = \frac{e^2 f_{mn}}{m_e c}\left(\frac{\pi M}{2kT_{ion}}\right)^{1/2} N_m \lambda_{mn} \tag{10}$$

where f_{mn} is the absorption oscillator strength between the corresponding levels, m_e the electron mass, and e the electron charge. The effect of re-absorption of an emitted photon on the ion level populations in plasma is calculated by reducing the spontaneous emission rate (A) of thick levels by a factor equal to the escape probability $P(\tau)$ that

becomes $P(\tau)A$. In the static case, the following Zemansky escape probability[5] for a given optical depth (τ) is used

for $0 \le \tau \le 4.5$

$$P(\tau) = 0.999003 - 0.697745\tau + 0.266529\tau^2 - 0.061906\tau^3 + 0.008106\tau^4 - 0.000453\tau^5 \quad (11)$$

and for $\tau > 4.5$

$$P(\tau) = \frac{1}{\tau\sqrt{\pi \ln \tau}} . \quad (12)$$

In plasmas with large velocity gradients, escape probability can be accurately calculated using the Sobolev approximation. The large velocity gradient brings about the Doppler shift of wavelength, resulting in the significant reduction of the optical depth of the transition line. In our calculation to estimate this effect, we have used the Sobolev optical depth (τ_s), which is given by[22,29,30]

$$\tau_s = \frac{\overline{X}_{lu}\lambda_{lu}}{\nabla . V_p(r)} \quad (13)$$

where $\nabla . V_p(r)$ is the divergence of plasma velocity at radius r, and $\overline{X}_{lu}$ the frequency integrated line opacity as given by

$$\overline{X}_{lu} = \frac{\pi e^2}{m_e c} f_{lu} \left(N_l - \left(\frac{g_l}{g_u} \right) N_u \right) \quad (14)$$

Note that static optical depth (Eq. (9)) is a globally calculated quantity, while the Sobolev optical depth is a locally defined quantity. The escape factor is calculated by using an approximate expression presented by Shestakov and Eder[21] for cylindrically contracting plasma with locally linear velocity profile. In the present work, the velocity is closely approximated by

$$V_p(r) = \begin{cases} 0 \leftarrow r(t) > R_a \\ \beta(R_a - r(t)) \leftarrow r_{\min} < r(t) \le R_a ; \beta = const. < 0 \\ 0 \leftarrow r(t) \le r_{\min} \end{cases} \quad (15)$$

where R_a is the cylinder radius, $r(t)$ the plasma radius, and $r_{\min}$ minimum of the plasma radius. The time evolution of plasma velocity and radius are estimated using two well-known Snowplow[23] and Slug[24] models.

Solving the quasi-steady-state rate equations, we also found some line ratios. The intensity ratio of two spectral lines is calculated using[31-33]

$$\frac{I_{ij}}{I_{mn}} = \frac{P(\tau_{ij})}{P(\tau_{mn})} \frac{m_j}{m_n} \frac{A_{ji}}{A_{nm}} \frac{\Delta E_{ij}}{\Delta E_{mn}} \quad (16)$$

where I is the intensity, m_k the relative level population, ΔE_{pq} the energy

difference between the levels q and p, and $P(\tau)$ the escape factor of a spectral line ($P(\tau)$=1 for an optically thin transition). In contrast to Ref. (32) we have taken into account the opacity effect on the line ratios.

III. Numerical Results and Discussion

Figure 1 shows the schematic energy level diagram for the 27 levels of KrXXVII, which are taken into account in our study. Lasing is expected in several lines of the $3p-3s$ transitions. The relative sublevel populations per statistical weight (m_j/g_j) for most of the upper laser levels of the $3p$ configuration[27] and two of the lower

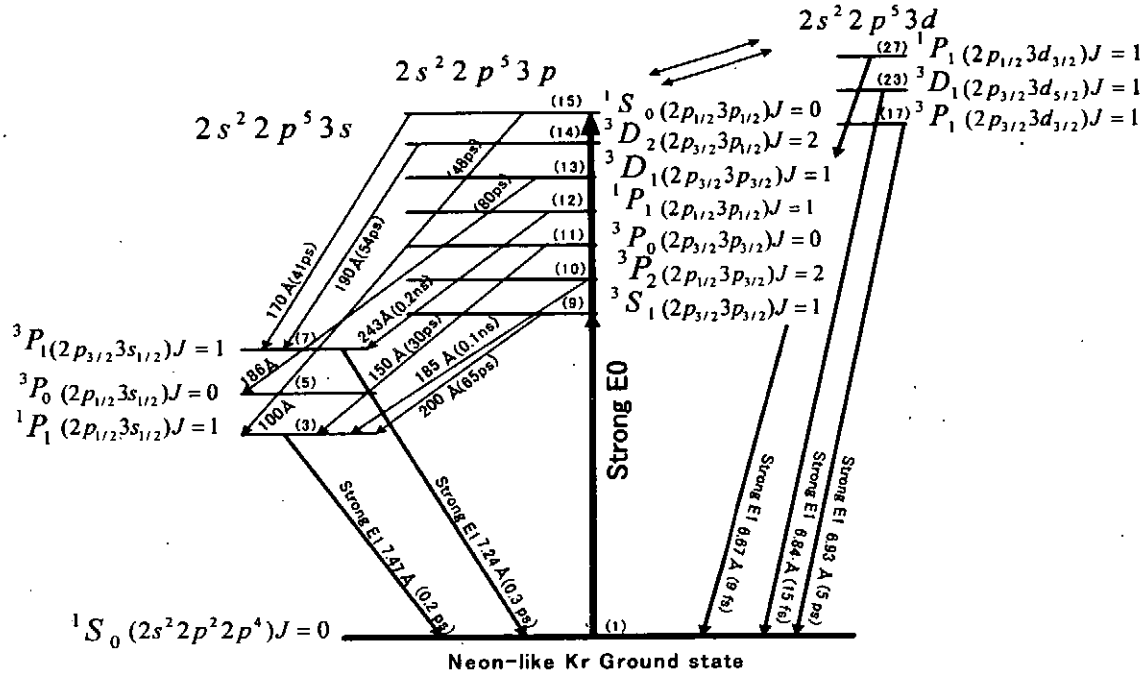

FIG. 1. A schematic diagram for some of the energy levels in KrXXVII (not to scale). The $3p$ laser upper levels are populated by electron monopole collisional excitation E0. The strong dipole transitions E1 have taken into account for opacity effect.

laser levels of the $^1P_1$ and $^3P_1$ in $3s$ configuration are presented in Fig. 2 as functions of electron densities at given two electron temperatures 1 and 3 keV. We focus our attention on the following transitions between $2s^2\,2p^5\,3p$ and $2s^2\,2p^5\,3s$ levels that indicate the large gains

(A) (15→7) $2s^2\,2p^5\,3p\ ^1S_0 \rightarrow 2s^2\,2p^5\,3s\ ^3P_1$

(B) (15→3) $2s^2\,2p^5\,3p\ ^1S_0 \rightarrow 2s^2\,2p^5\,3s\ ^1P_1$

(C) (14→7) $2s^2\,2p^5\,3p\ ^3D_2 \rightarrow 2s^2\,2p^5\,3s\ ^3P_1$

(D) (11→3) $2s^2\,2p^5\,3p\ ^3P_0 \rightarrow 2s^2\,2p^5\,3s\ ^1P_1$

(E) (9→3) $2s^2\,2p^5\,3p\ ^3S_1 \rightarrow 2s^2\,2p^5\,3s\ ^1P_1$

As shown in Fig. 2, the relative sublevel populations grow as functions of the

electron density and the electron temperature due to the increase in the collisional excitation rates. In the region of low electron density and a given temperature, the populations of $3s^3P_1$ and $3s^1P_1$ levels are smaller than other levels due to their strong spontaneous emission rate. The population of $3s^3P_1$ is slightly smaller than $3s^1P_1$ level. At intermediate electron density, collisional de-excitation to either $2p^5 3s$ or

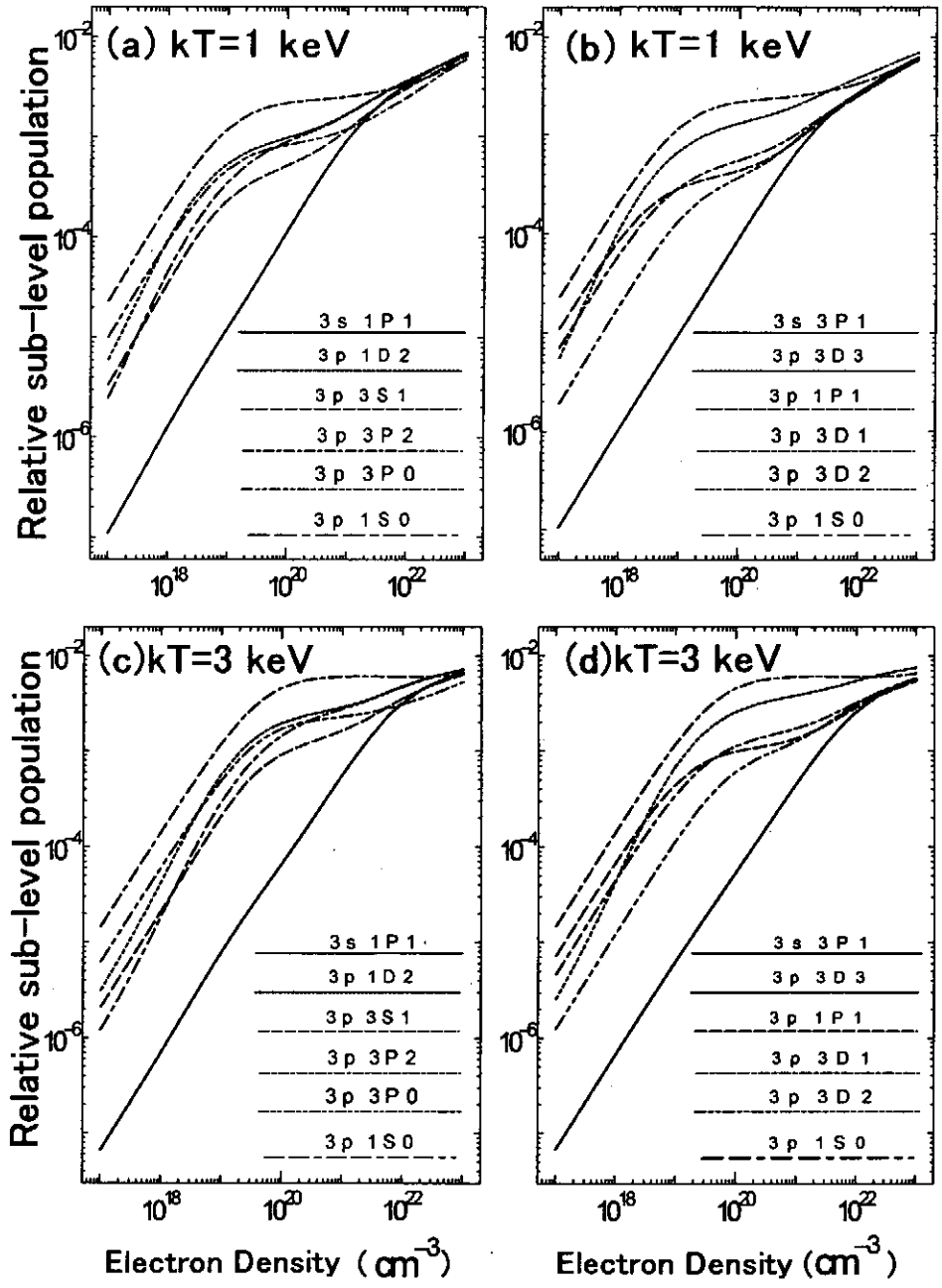

FIG. 2. Relative sublevel populations as a function of electron density for given temperatures: (a) and (b) for 1 keV; (c) and (d) for 3 keV.

$2p^5 3d$ levels are become comparable to spontaneous emission rate for levels belonging to $2p^5 3p$ configurations, and because of collisional de-excitation, the $2p^5 3p$ level populations are increased less rapidly than the electron density. At high electron density; where the collisional de-excitation rates exceed the spontaneous emission rates, the relative sublevel populations are independent of electron density and becomes distributed according to Boltzmann distribution function. The $3p^1S_0$ level is most largely populated due to the close collisional coupling to the ground state; however its population inversion against $3s^1P_1$ level destroyed around electron density of 10^{22} cm^{-3} at electron temperature 1 keV. The populations of $3p^3D_3$ and $^1D_2$ levels are close due to the balance of spontaneous emission rate and collisional processes. An inspection of Fig 2(a) and (b) reveals that the population inversions of $3p^3P_0$, $^3S_1$, $^1P_1$, and $^3D_2$ levels respect to $3s^1P_1$ level are destroyed above the electron density of 10^{21} cm^{-3}. This may be explained by the fact that the collisional coupling of these levels to the ground state is not as strong as that of $3p^1S_0$ level but those decay radiatively faster than other excited levels. Also, the behavior of the populations with variations of temperature between 1 and 3 keV is maintained.

Figure 3 shows the gain coefficients per total Ne-like Kr ion density (Eq.(6)) of the five transitions mentioned above against electron density at two electron temperatures of 1 and 3 keV. The transitions (A), (C) and (E) have potential of high gains. In the electron density less than 10^{20} cm^{-3}, the gains grow approximately with electron density due to the increase of the collisional excitation rates. The gain on the transition (A) is sustained at higher electron density than other transitions. The gains per total Ne-like Kr ion density reach their maximum in the electron density region of between

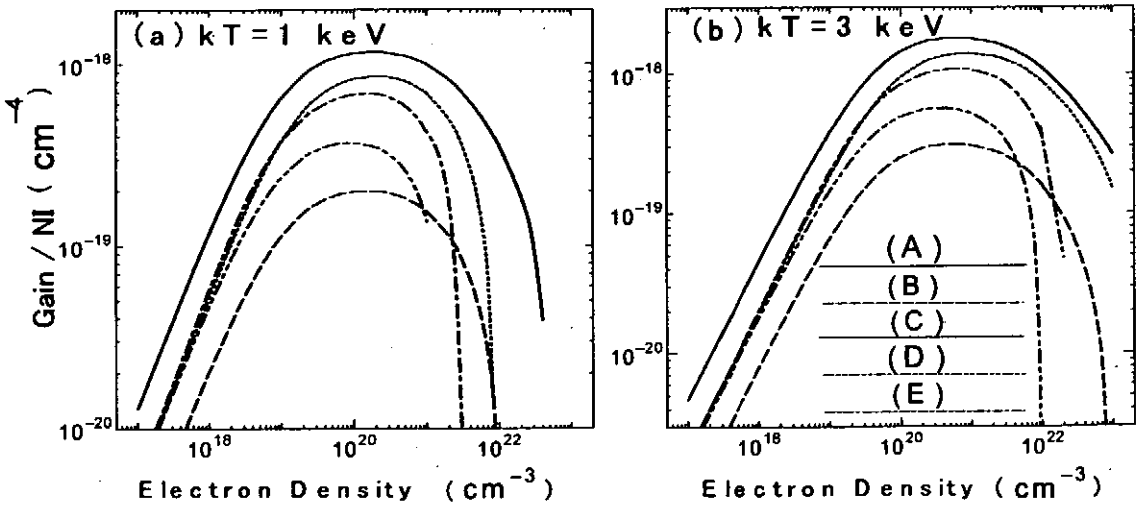

FIG. 3. Gain coefficients per total Ne-like Kr ion density as function of electron density for temperature (a) 1 keV and (b) 3 keV. The designation for transitions are given in the text.

10^{20} and 10^{21} cm^{-3}. Using Eq.(7) for total Ne-like Kr ion density, Fig. 3 indicates that the gains reach their maximum on the electron density region a few times of 10^{20} and $10^{22}\,cm^{-3}$ where the collisional de-excitation rates of the $3p$ level becomes comparable to its spontaneous emission rate. For higher electron density, the gains drastically decrease because the collisional de-excitation rates exceed the spontaneous emission rates and the population of levels approach Boltzmann distribution.

We have also studied the opacity effect. In our study, the effect of opacity of the following fast transitions were taken into account, $3d^1P_1 - 2p^6\,^1S_0$, $3d^3D_1 - 2p^6\,^1S_0$, $3d^3P_1 - 2p^6\,^1S_0$, $3s^3P_1 - 2p^6\,^1S_0$ and $3s^1P_1 - 2p^6\,^1S_0$, since they have strong oscillator strengths.

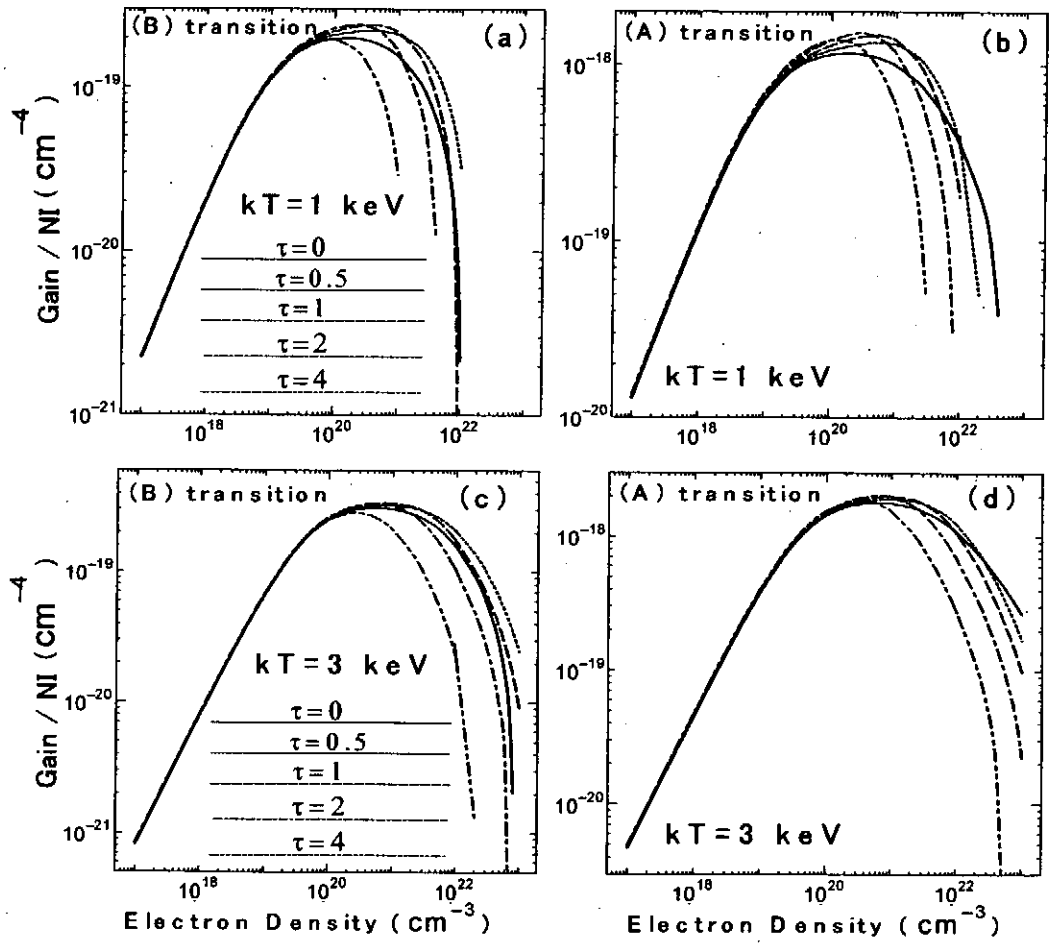

FIG. 4. The opacity effect of five thick levels on gains. The values of τ are for $3s^3P_1 - 2p^6\,^1S_0$ transition. (a) the opacity effect of the (B) transition on gain for temperature of 1 keV; (b) the opacity effect of (A) transition on gain for temperature 1 keV. (c) and (d) same as (a) and (b) but for temperature of 3 keV.

Using Eqs.(9) and (10), for a given static optical depth (τ_α) of a transition α, the

optical depth of another transition β can be related by[5,20]

$$\tau_\beta = \tau_\alpha \left(\frac{\lambda_\beta f_\beta}{\lambda_\alpha f_\alpha} \right) \tag{17}$$

where f_k is the absorption oscillator strength between two levels. The $3s^3P_1 - 2p^6{}^1S_0$ transition was used as a reference, because it has lowest oscillator strength. The optical depths of the other transitions were calculated using Eq.(17) and escape probability was estimated by Zemansky method. Figure 4 gives the opacity effect on the two (A) and (B) transitions at electron temperatures 1 and 3 keV. The values of τ given in the figure are for the reference transition. As can be seen in Fig. 4, the opacity effect on gain is very small for τ up to 4 at electron density regime less than 10^{19} cm^{-3}. The opacity increases gain on (B) transition for τ up to 2, and transition (A) up to 4 for electron density regime about 10^{19} and a few times of 10^{21} cm^{-3} at temperature equal to 1 keV. In high electron density, the gain decreases drastically for high value of the optical depth. No gain on transition (A) is observed for $\tau > 45$[25]. Furthermore, the opacity effect on the gain is larger at the lower temperature.

In the plasma that goes through dynamical changes as in capillary discharges, there may exist a strong velocity gradient that it appears in the behaviors of gain coefficient. A reduction in the optical depth owing to the Doppler-shift-induced decoupling of radiation in the moving plasma leads to an increase in escape probability. To estimate velocity profile, we have performed calculation using two imploding models: Snowplow and Slug models for a set of discharge parameters; maximum plasma current $I_P^{max} = 100$ kA, current rise time $t_{rise} = 40$ ns, initial pressure $P_0 = 132$ Pa, and capillary radius $R_a = 0.15$ cm.[25] The minimum radii are 2.6×10^{-5} , 2×10^{-2} (cm) and corresponding velocity gradient about, 10^{12}, 10^9 sec^{-1}, according to snowplow and slug models, respectively. Figure 5 shows the change of the positions of the plasma boundary and the shock front with respect to time, according to (a) snowplow and (b) slug models.

Using Eq.(8), the gain coefficients are calculated as shown in Fig. 6: (a) for the static plasma, (b) with opacity effect using Zemansky escape probability at plasma radius equal to 0.02 cm, (c) and (d) for contracting plasma made in Sobolev's approximation at corresponding minimum radius of Snowplow and Slug models for electron temperature 0.9 keV, respectively. The plasma radius in Fig 6(b) is chosen equal to minimum radius according to Slug model. As can be seen in Fig 6(a) and (b), the gains on the transitions (A), (B), and (C) are decreased, but on (D) and (E) transitions increased with the opacity effect due to the values of their static optical depths. With the increase of opacity the gain drops drastically, and it comes in the lower

electron density and the smaller opacity.

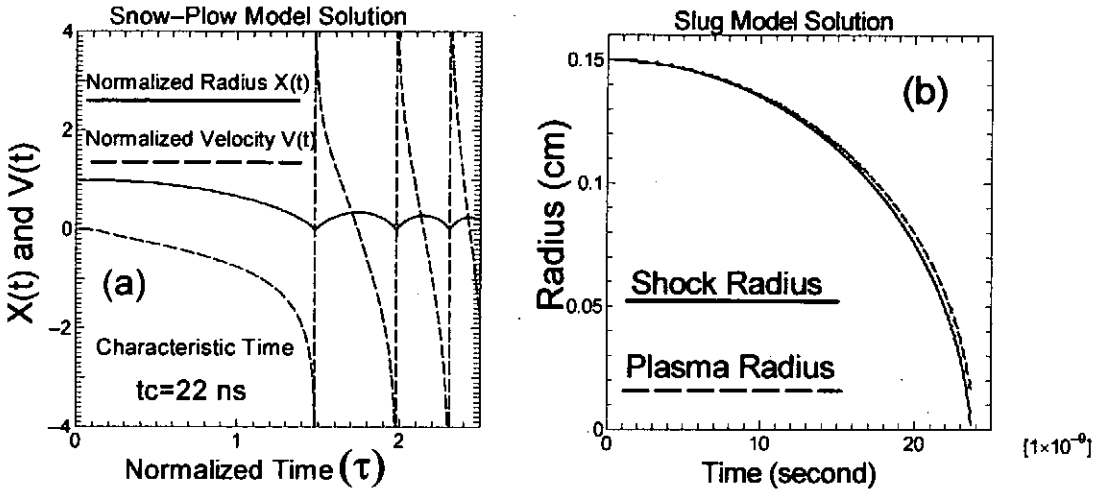

FIG. 5 The change of the positions of the plasma boundary and the shock front with respect to time. Dependencies of normalized radius $X(t) = r(t)/R_a$ and velocity $V(t) = (tc \times v(t))/R_a$ on normalized time $(\tau = t/tc)$ according to (a) snowplow model. (b) Solutions from the slug model for the piston and shock radii as a function of time.

An inspection of Fig. 6(a) and (c) shows that the calculated gains at minimum radius according to Snowplow model is equal to gains without re-absorption effect. As seen from the Fig. 6(b), (c), and (d), the large velocity gradient leads to more transparent laser medium for the resonance transition that allows one to produce inversion over a wider gain region in dense plasmas.

In Fig.7, the effect of velocity gradient on the gains at two electron densities 10^{21} and 10^{22} cm^{-3}, electron temperatures 0.9, and 3 keV is shown. In the limit of the infinite velocity gradient (approximately more than 10^9 and 10^{10} sec^{-1} for set of parameters in Fig. 7 (a) and (b), respectively.), the resonance lines are optically thin, corresponding to no trapping. An inspection of Fig.6 (a) and Fig.7 (a) reveals that for a typical velocity gradient of 7×10^7 sec^{-1}, n_e=10^{21} cm^{-3} and T_e=0.9 keV, the gains on most of transitions are about (1.2-2.5) times of the value at lower velocity gradient and about 0.9 times of the un-trapped value at static plasma. It appears that the velocity gradient has a significant effect in de-trapping of the thick levels and thereby increasing gains in the $3p-3s$ lines.

We have also studied different line ratios that are sensitive to the electron density, the electron temperature and also opacity, which have reasonably high intensities. The advantage of seeking such ratios of lines from a single ionization stage is that they are independent of the stage ionization balance. Using the atomic data, Eqs.(16) and (17), we investigate the density dependence of the line ratio at first.

In Fig.8, we present the electron density-dependent line-intensity ratio of R_1 =

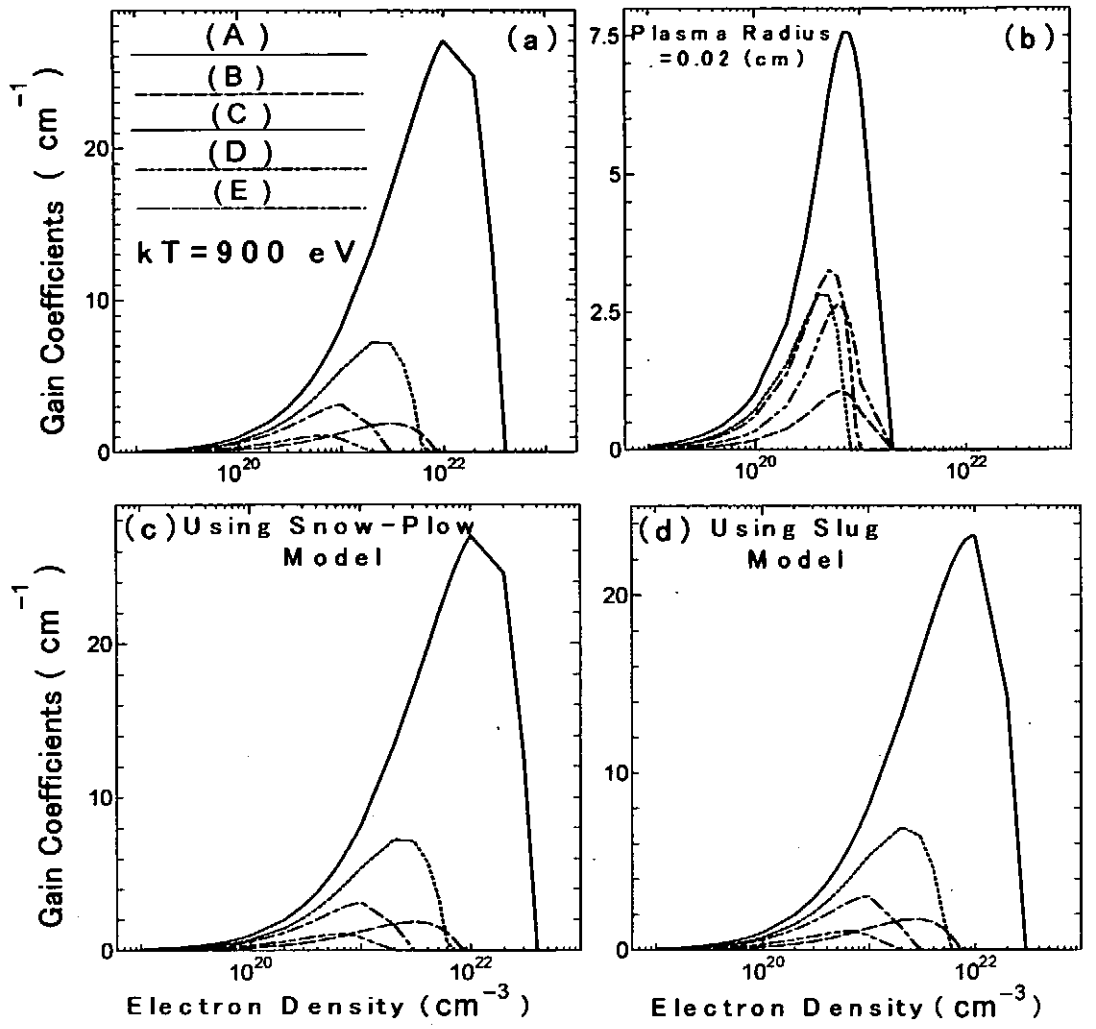

FIG. 6. Gain coefficients of five transitions in Ne-like Kr (a) for static plasma without opacity effect, (b) for static plasma with opacity effect of five thick levels at plasma radius 0.02 cm, (c) and (d) according to Snowplow and Slug models at corresponding pinching radius made in Sobolev' approximation for given electron temperature 0.9 keV.

$I(3d\ ^1F_3 \rightarrow 3p\ ^1D_2)/(3p\ ^3P_1 \rightarrow 3s\ ^3P_2)$ with opacity effect at electron temperature 0.9 keV applicable to Ne-like Kr. The wavelength is given in Angstrom. This ratio depends on the electron density over the range of between 10^{18} and 10^{22} cm^{-3} and approaches the LTE limits at electron density higher than 10^{23} cm^{-3}. There is no density dependence at electron density less than 10^{18} cm^{-3}. The temperature dependence of this ratio is very weak and also the $3p\ ^3P_1$-$3s\ ^3P_2$ transition can not be amplified for electron temperature up to 1 keV.

We next consider the determination of electron temperature-dependent line ratio. Figure 9 shows the temperature-sensitive line-intensity ratio of R_2 = $I(3d\ ^3F_4 \rightarrow 3p$

$^3D_3 + 3d\ ^3P_2 \rightarrow 3p\ ^3P_1)$ / $(3p\ ^3P_1 \rightarrow 3s\ ^3P_2)$ as a function of electron temperature at given electron density 10^{21} cm^{-3}.

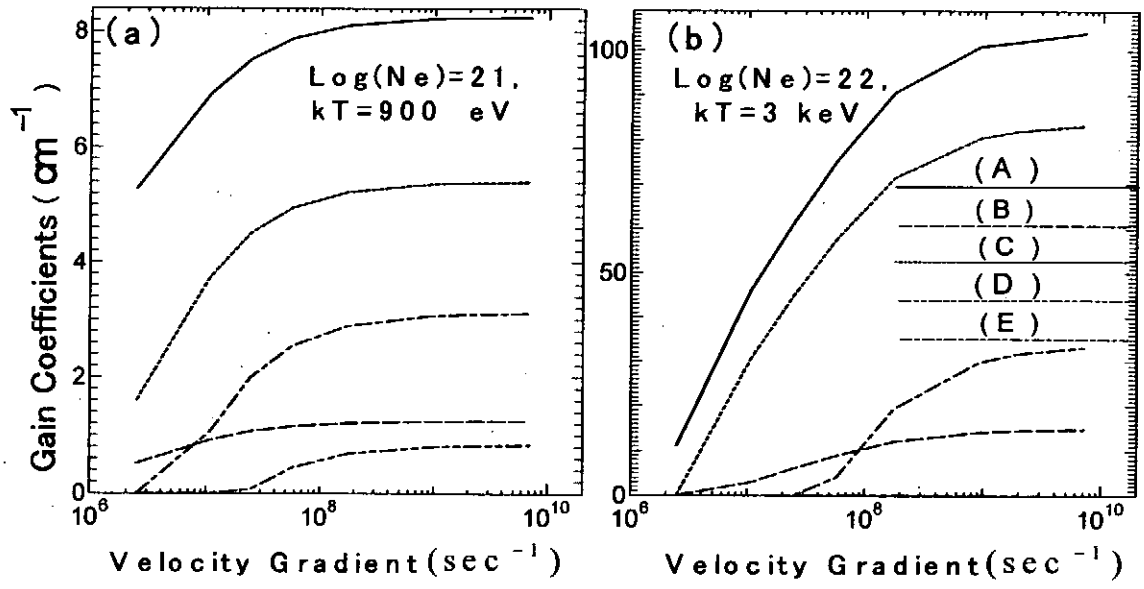

FIG. 7. Gains for the five $3p-3s$ transitions of Ne-like Kr versus velocity gradient; (a) for $n_e = 10^{21} cm^{-3}$, kT=900 eV, and (b) for $n_e = 10^{22} cm^{-3}$, kT=3 keV.

There is no density dependence for this line ratio at density region between 10^{21} and 10^{22} cm^{-3}. Comparison of Figs. 8 and 9 reveal that sensitivity against electron density for R_1 is higher than R_2 on the electron temperature. Also, we see that the effect of opacity on line ratios for the optical depth of reference transition up to 4 is small. Therefore, these line ratios would not be affected by the plasma opacity and might be used for density and temperature diagnostics.

Solving quasi-steady-state rate equations, we might be able to study about optical depth of certain thick levels[31-33] using opacity-sensitive line ratio, if we know electron density and electron temperature. Figure 10 shows the following line ratios between optically thick ($3s\ ^1P_1 \rightarrow 2p^6\ ^1S_0$), ($3d\ ^3P_1 \rightarrow 2p^6\ ^1S_0$) per thin $(3p\ ^1D_2 \rightarrow 2p^6\ ^1S_0)$ and $(3p\ ^1P_1 \rightarrow 3s\ ^3P_0)$ transitions for optical depth of reference transition up to 4, as functions of electron density at given electron temperature of 1 keV.

$$R_3 = \mathrm{I}(\lambda 7.47/\lambda 7.24) = \mathrm{I}(3s\ ^1P_1 \rightarrow 2p^6\ ^1S_0) / (3p\ ^1D_2 \rightarrow 2p^6\ ^1S_0)$$
$$R_4 = \mathrm{I}(\lambda 6.93/\lambda 243) = \mathrm{I}(3d\ ^3P_1 \rightarrow 2p^6\ ^1S_0) / (3p\ ^1P_1 \rightarrow 3s\ ^3P_0)$$

As can be seen from Figs.10 (a) and (b) the sensitivity against opacity effect for R_3

occurs in higher electron density region than R_4. Furthermore, the $(3p\ ^1P_1 \rightarrow 3s\ ^3P_0)$ transition cannot be amplified even for electron temperature of up to 3 keV.

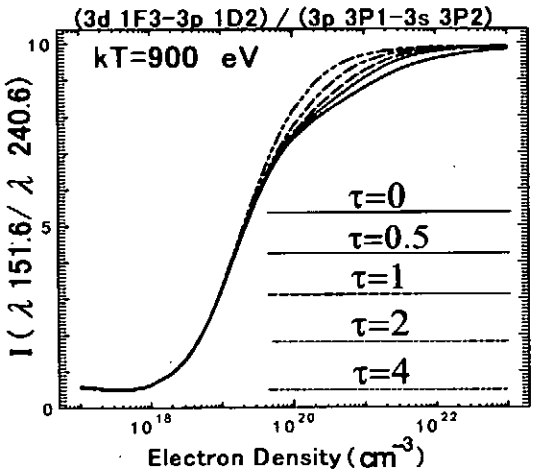

FIG. 8. Density-sensitive spectral-line intensity ratio of Ne-like Kr.

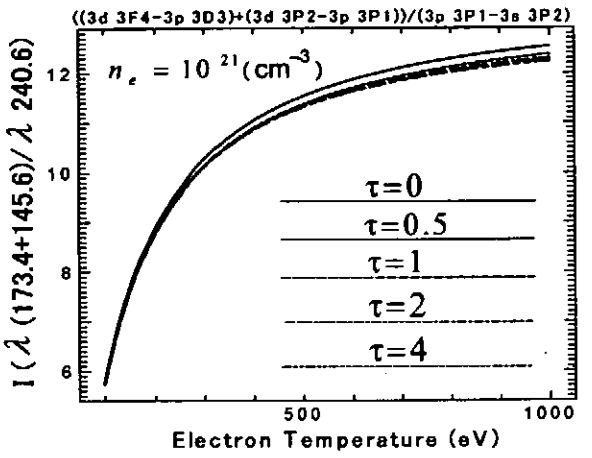

FIG. 9. Temperature-sensitive line ratio of Ne-like Kr.

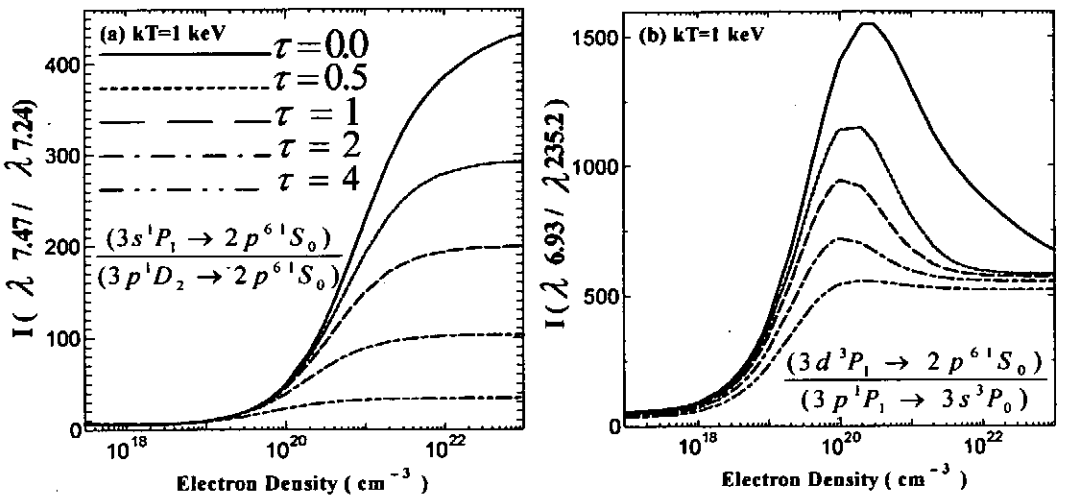

FIG. 10. The opacity-sensitive line ratios of (a) R_3 and (b) R_4 against electron density at given electron temperature of 1 keV.

IV. Conclusions

We have studied the characteristics of the level populations of $2s^2 2p^5 3s$ and $2s^2 2p^5 3p$ configurations in Ne-like Krypton as functions of the electron density and the electron temperature. The gains between the fast transitions are presented with and without opacity effect for both the static and dynamic plasmas. The analysis shows that the $(2p^5 3p\ ^1S_0 \rightarrow 2p^5 3s\ ^3P_1)$, $(2p^5 3p\ ^3D_2 \rightarrow 2p^5 3s\ ^3P_1)$, and $(2p^5 3p\ ^3S_1 \rightarrow 2p^5 3s\ ^1P_1)$ transitions can produce high gains. The maximum gains for transitions occur on the electron density region of between 7×10^{20} and 10^{22} cm^{-3} for the electron temperatures 0.9, 1 and 3 keV. We found that in both the static and dynamic plasmas the effect of opacity on the gains is significantly large in dense region. In the static case, the opacity effect on gains is estimated to be small for optical depth of $(3s^3P_1 - 2p^6\,^1S_0)$ reference transition up to 4 at electron density regime less than 10^{19} cm^{-3}. The opacity increases gains for optical depth of reference transitions up to 2, on the electron density regime between a few times 10^{19} and 10^{22} cm^{-3}. With the increase of opacity the gain drops, and it comes on the lower electron density at the smaller opacity. On the other hand, the large velocity gradient leads to more transparent laser medium for the resonance transitions due to the reduction in the optical depth that allows one to produce a wider gain region in dense plasmas. Also, we presented some line ratios that might be applied to diagnose the electron density, the electron temperature, and opacity effect in the interest regime of Ne-like krypton x-ray laser.

Acknowledgements

The authors would like to thank Professor V. N. Shlyaptsev and Dr. K. Lee for helpful discussions. M. Masnavi gratefully acknowledge financial support from the Ministry of Education, Science, Sports and Culture of Japan.

References

1) D. L. Matthews, '' Review of X-ray Laser", Nucl. Instrum. Methods Phys. Res., **B98**, 91-94 (1995), and references therein.

2) A. Zherikhin, K. Koshelev, and V. Letokhov, " Gain in the Far Vacuum Ultraviolet Region Due to Transitions in Multiply Charged Ions", Sov. J. Quantum Electron., **6**, 82-84 (1976).

3) R. C. Elton, X-ray Laser (Academic press, San Diego, CA, 1990).

4) K. Lan, Y. Zhang, and W. Zheng, '' Theoretical Studies on Discharge-Pumped Soft X-ray Laser in Ne-like Ar", Phys. Plasmas, **6**, 4343-4348 (1999).

5) D. E. Kim, D. S. Kim, and A. L. Osterheld, '' Characteristics of Populations and

Gains in Neon-like Argon (ArIX)", J. Appl. Phys., **84**, 5862-5866 (1998), and references therein.

6) N. A. Bobrova, S. V. Bulanov, D. Farina, R. Pozzoli, T. L. Razinkova, J. I. Sakai, P. V. Sasorov, and I. V. Sokolov, '' MHD Simulations of Plasma Dynamics in Pinch Discharges in Capillary Plasmas", Laser Part. Beams, **18**, 623-635 (2000).

7) B. R. Benware, C. D. Macchietto, C. H. Moreno, and J. J. Rocca," Demonstration of a High Power Tabletop Soft X-ray Laser", Phys. Rev. Lett., **81**, 5804-5807 (1998).

8) J. J. Rocca, Rev. Sci. Instrum., ''Table-top Soft X-ray Lasers, **70**, 3799-3827 (1999).

9) G. Nimi, Y. Hayashi, M. Nakajima, M. Watanabe, A. Okino, K. Horioka, and E. Hotta, '' Observation of Multi-pulse Soft X-ray Lasing in a Fast Capillary Discharge", J. Appl. Phys. D: Appl. Phys., **34**, 2123-2126 (2001).

10) H. Daido, H. Tang, Y. Kato, and K. Murai, '' Review of Collisional Excitation Neon-like and Nickel-like Soft X-ray Lasers Pumped by Multiple Infrared Laser Pulses at the Institute of Laser Engineering, Osaka University", C. R. Acad. Sci. Paris, **t1**, 999-1018 (2000).

11) A. V. Vinogradov, I. I. Sobelman, and E. A. Yukov, '' Population Inversion of Transitions in Neon-like ions", Sov. J. Quantum Electron., **7**, 32-35 (1977).

12) A. V. Vinogradov, and V. N. Shlyaptsev, '' Calculations of Population Inversion Due to Transitions in Multiply Charged Neon-like Ions in the 200-2000 A Range '', Sov. J. Quantum Electron., **10**, 754-756 (1980).

13) L. J. Palumbo and R. C. Elton, '' Short-wavelength Laser Calculations for Electron Pumping in Carbonlike and Heliumlike Ions '', J. Opt. Soc. Am., **67**, 480-488 (1977).

14) U. Feldman, A. K. Bhatia, and S. Suckewer, '' Short Wavelength Laser Calculations for Electron Pumping in Neon-like Krypton (KrXXVII)", J. Appl. Phys., **54**, 2188-2197 (1983).

15) U. Feldman, J. F. Seely, and A. K. Bhatia, '' Scaling of Collisionally Pumped 3s-3p Lasers in the Neon Isoelectronic Sequence", J. Appl. Phys., **56**, 2475-2478 (1984).

16) U. Feldman, G. A. Doschek, J. F. Seely, and A. K. Bhatia, '' Short Wavelength Laser Calculations for Electron Pumping in BeI and BI Isoelectronic Sequences (18<Z<36)", J. Appl. Phys., **58**, 2909-2915 (1985).

17) W. H. Goldstein, B. L. Whitten, A. U. Hazi, and M. H. Chen, '' Mechanism for Creating Population Inversions in Ne-like Ions", Phys. Rev. A , **36**, 3607-3611 (1987).

18) G. P. Gupta and B. K. Sinha, '' Parametric Dependence of X-ray Laser Gain in Laser Plasmas for 3p-3s Transitions in Neon-like Krypton Ions", J. Appl. Phys., **77**,

2287 –2290 (1995).

19) G. P. Gupta and B. K. Sinha, '' Estimation of Optimum Electron Temperature for Maximum X-ray Laser Gain from 3p-3s Transitions of Neonlike Ions in Laser Plasmas", J. Appl. Phys., **79**, 619-624 (1996).

20) D. S. Kim and D. E. Kim, '' The Effect of Radiation Trapping in Gain for Ne-like Kr", Jpn. J. Appl. Phys., Part **1**, 2693-2698 (1998).

21) T. Hosokai, M. Nakajima, T. Aoki, M. Ogawa, and K. Horioka, '' Correlation Between Soft X-ray Emission and Dynamics of Fast Capillary Discharges", Jpn. J. Appl. Phys., Part **1**, 2327-2335 (1997).

22) A. I. Shestakov and D. C. Eder," Escape Probabilities in a Cylindrically Expanding Medium", J. Quant. Spectrosc. Radiat. Transfer, **42**, 483-498 (1989).

23) P. Vrba and M. Vrbova, '' Z-Pinch Evolution in Capillary Discharge", Contrib. Plasma Phys., **40**, 581-595 (2000).

24) D. Potter, '' The Formation of High-Density Z-Pinches", Nuclear Fusion, **18**, 813-829 (1978).

25) M. Masnavi, T. Kikuchi, M. Nakajima, and K. Horioka, ''Characteristics of Energy Trapping in Capillary Discharge Pumped Neon-like Kr Laser", Proc. Second Inter. Conf. on Inertial Fusion Sciences and Applications, (2001), to be publish.

26) Y. T. Lee, '' A Model for Ionization Balance and L-Shell Spectroscopy of Non-LTE Plasmas", J. Quant. Spectrosc. Radiat. Transfer, **38**, 131-145 (1987).

27) A. K. Bhatia, U. Feldman, and J. F. Seely, '' Atomic Data and Spectral Line Intensities for The Neon Isoelectronic Sequence (Si V Through Kr XXVII)", Atom. Data Nucl. Data Tables, **32**, 435-469 (1985).

28) U. Feldman, G. A. Doschek, and J. F. Seely, '' Density Sensitive Line Ratios for Highly Ionized Atoms of the Cu I and Na I Isoelectronic Sequences '', J. Appl. Phys., **68**, 3947 –3952 (1990).

29) Y. T. Lee, R. A. London, and G. B. Zimmerman, '' Application of Escape Probability to Line Transfer in Laser-Produced Plasmas", Phys. Fluids, **B2**, 2731-2740 (1990).

30) J. Plus, U. Springmann, and M. Lennon, '' Radiation Driven Winds of Hot Luminous Stars. XIV. Line Statistics and Radiative Driving", Astron. Astrophys. Suppl. Ser., **141**, 23 –64 (2000).

31) C. F. Maggi, L. D. Horton, G. Corrigon, H. J. Jackel, A. Loarte, R. D. Monk, R. Simonini, M. Stamp, and A. Tarani, '' Modeling of Deuterium Emission in High Density Divertor Plasmas in JET", J. Nucl. Mater., **266-269**, 867-872 (1999).

32) U. Feldman, J. Seely, and A. K. Bhatia, '' Density Sensitive X-ray Line Ratios in

the Be I , BI, and NeI Isoelectronic Sequences", J. Appl. Phys., **58**, 3954-3958 (1985).

33) M. Mathioudakis, J. McKenny, F. P. Keenan, D. R. Williams, and K. J. Phillips, " The Effects of Opacity in the Transition Region of YZ Cmi", Astron. Astrophys., **351**, L23 –L26 (1999).

Observation of Plasma Motion in a Coaxial Plasma Opening Switch With a Chordal Laser Interferometer

Y. Teramoto, S. Kohno*, H. Urakami, S. Katsuki**, and H. Akiyama

Graduate School of Science and Technology, Kumamoto University,
2-39-1 Kurokami, Kumamoto 860-8555, Japan
** Department of Electrical Engineering, Ariake National College of Technology,*
150 Higashihagio-machi, Omuta, Fukuoka 836-8585, Japan
*** Department of Electrical and Computer Engineering, Kumamoto University,*
2-39-1 Kurokami, Kumamoto 860-8555, Japan

ABSTRACT

Electron densities in a coaxial plasma opening switch were measured at many lines-of-sight. In the present experiment, electron density was measured by a He-Ne laser interferometer with chordal lines-of-sight. In order to observe the motion of the POS plasma, the electron density contours during the conduction, opening and post-opening phases were drawn by combining the results of interferometer experiments. The radial and axial motion of POS plasma was investigated from the density contours. As conduction time progressed, the POS plasma moved toward downstream. At 800 ns, which corresponds to the time of opening in the current waveform, low-density region less than 10^{15} cm^{-2} is seen at 10 mm from the cathode. After the opening was completed, the low-density gap disappeared and the shape of the corn-shape-like plasma was distorted.

I. Introduction

A plasma opening switch (POS) is one of the key technology for an inductive-energy storage high-power pulsed power generator system. A long-conduction-time POS can conduct the current above 1 MA during the conduction time up to about 1 μs [1] as a result of MHD motion of the current-conducting plasma which is initially injected into the POS region by an external plasma source. The mechanisms of POS conduction and opening are represented by a snowplow model. The scalings derived from the snowplow model are in good agreement with the experimental results [1]. Also, the numerical calculations have been dedicated to prediction of physics occurring in POSs [2].

On the other hand, an experimental approach to study the mechanism of POS has recently

been done by a laser interferometer technique [3]-[5]. Taking axial-lines-of-sight, the radial behavior of the POS plasma during the conduction phase has been studied. According to the interferometer results, the decrease in the plasma electron density is observed somewhere in the POS region at the time of opening. It must be the vacuum gap creation which is dominant for the current interruption. However, the motion of POS plasma is not only in radial direction but also in axial direction. Therefore, for the further understanding of physics of POS, the axial motion of POS plasma should be studied experimentally.

This paper describes the results of interferometer experiment dedicated to the observation of motion of POS plasma both in axial and radial directions. By modifying the POS coaxial configuration, the many chordal lines-of-sight were taken to measure the plasma electron densities in the wide area of POS region. From the density measurements, the density contours were drawn to understand the behavior of POS plasma.

II. Experimental setup

Fig. 1 shows the POS-to-load configuration indicating measurement positions in the POS region. The inductive voltage adder pulsed power generator ASO-X [6] is placed at the left-hand side in Fig. 1 (a). The generator current provided by ASO-X generator has the rise time of approximately 1.3 μs and amplitude of 200 kA when the capacitors of ASO-X are charged to 30 kV, and is fed directly through the coaxial vacuum transmission line. The POS on ASO-X has the coaxial geometry consisting of 140-mm-diameter outer grounded anode, 60- or 80-mm-diameter inner high-voltage cathode and eight cable plasma guns mounted symmetrically on the outer anode. Each two guns are driven by a 0.7-μF capacitor that is normally charged to 25 kV. The amplitude and quarter period of the current through the plasma gun are 8 kA and 1.6 μs, respectively. However, in this experiment, the two of eight guns mounted on the top and bottom of the outer anode were used to open the diagnostics hole for the probe laser beam. It was confirmed that the decrease in the total amount of POS plasma due to the decrease in the number of plasma guns did not have significant influences on the POS operation and the conduction time could be long enough as approximately 1 μs. The load-end was short-circuited by the copper plate and the inductance of load chamber was estimated to 70 nH. The generator current was measured by a Rogowski coil placed at the output-end of ASO-X and the load current was measured by a B-dot probe placed in the load chamber.

For the electron density measurement in the POS plasma, the He-Ne laser interferometer was employed. The interferometer was arranged in Michelson-type as shown in Fig. 1 (b), having the lines-of-sight as shown in Fig. 1 (c). In order to increase the resolution and to avoid the effect of luminosity of the discharge, a laser beam was focused to the input of the quartz optical fiber by a lens (f=50 mm) through a narrow-band pass filter and a pinhole of 3

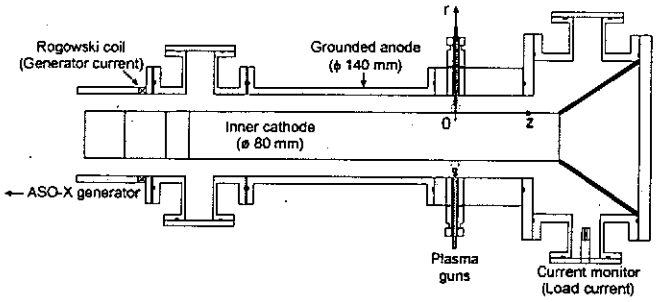

(a)

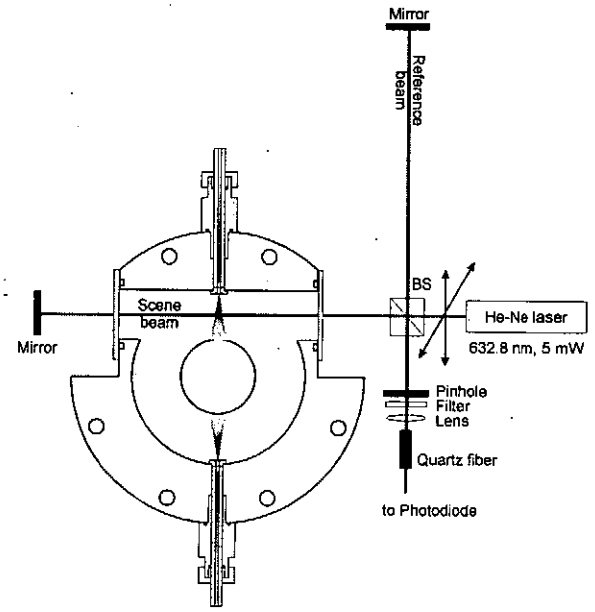

(b)

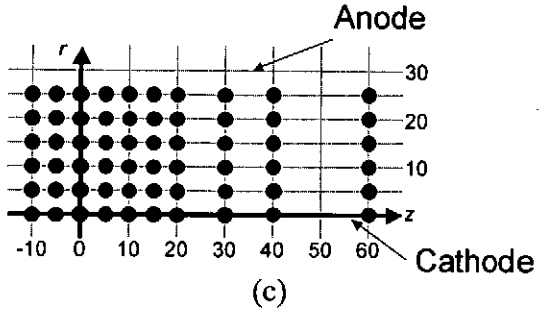

(c)

Fig. 1. POS-to-load configuration on ASO-X (a), interferometer arrangement (b) and lines-of-sight (c).

mm in diameter. A PIN photodiode was used as a detector for the interference signal. The photo detector was placed in the screen room to achieve the noise-free signals. All the signals were recorded by a 4-GSa/s, 1.5-GHz, 4-ch digital oscilloscope (Hewlett Packard, Infinium HP54845A).

The electron densities were measured at the radial positions of r=0, 5, 10, 15, 20, 25 mm for the each axial positions of z=-10, -5, 0, 5, 10, 15, 20, 30, 40, 60 mm as shown in Fig. 1 (c). For the low-density plasma, the electron density was calculated by the following equation;

$$\int_0^L N_e dl = 5.56\times10^{16}\frac{\Delta A}{A} \quad (cm^{-2}) \qquad (1)$$

where, L, N_e, ΔA, A are the length of plasma, electron density, amplitude over the quasi constant level, and amplitude of oscillation of the interference signal due to the mechanical vibration of optical elements, respectively. For the high-density plasma more than p shift, the following equation was used to decide the electron density;

$$\int_0^L N_e dl = 5.56\times10^{16}\phi_p \quad (cm^{-2}) \qquad (2)$$

where, ϕ_p is the phase shift due to the electron density. To increase the sensitivity and make the density calculations easy, a phase tracking system was used to fire the plasma guns and ASO-X when the phase of quasi-sinusoidal interference signal was zero.

III. Experimental Results and Discussions

Fig. 2 shows the typical waveforms of generator (upstream) current I_G, load (downstream) current I_L, and electron density n_e which was measured at 10 mm from the cathode on the gun axis. The load current rose in 80 ns after the conduction time of 850 ns. In this case, the electron density increased at 400 ns after the current onset, then decreased to zero when the opening occurred. Such variations of electron density as Fig. 2 were achieved at each measurement position. All the results were combined and summarized in the density contours as a function of time to observe the motion of POS plasma.

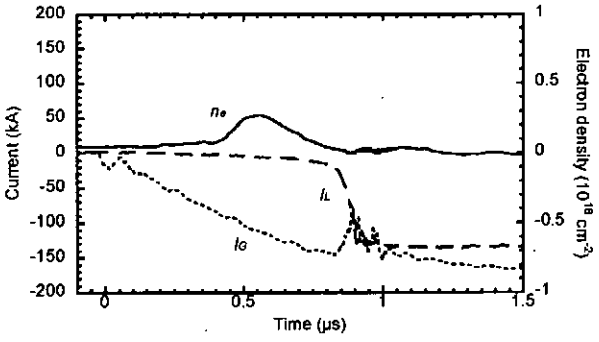

Fig. 2. Typical waveforms of generator current (dotted line), load current (dashed line) and line-integrated plasma electron density (solid line) measured at 10 mm radial position from the cathode along the gun axis.

Fig. 3 shows the density contours at 500 ns (a), 600 ns (b), 700 ns (c), 800 ns (d), 900 ns (e) and 1200 ns (f) after the current onset, respectively. These figures represent the plasma density distribution during conduction, opening and post-opening phases. At 500 ns after the current onset (Fig. 3 (a)), plasma column was seen clearly along the gun axis. Before 500 ns, the plasma column as seen in Fig. 3 (a) was not observed clearly because the electron density was low. The electron density became higher with time due to the further ionization. However, the regions near the both electrodes had relatively high-density even in the earlier phases than 500 ns. In Fig. 3 (a), the upper (anode) side of the plasma seems to be moved 5 mm from the gun axis toward downstream, and shows the highest density in the POS region. On the cathode surface, there was a plasma sheath that had relatively high density and was spreading along the cathode surface. Comparing the contour maps of earlier time, this cathode plasma seems to move downstream with the speed of approximately 13 cm/μs.

Fig. 3 (b) is the contour of 600 ns after the current onset. The density in the anode side of the plasma increased compared with the Fig. 3 (a) and the middle part of the plasma seems to be expanded toward downstream. The plasma sheath on the cathode moved to about 60 mm although that moved to 50 mm in Fig. 3 (a). In the right-up region in Fig. 3 (b), the plasma cluster was seen and likely to be propagating. The reason for this plasma production might be an interaction between the accelerated plasma and the diagnostics window or the edge of electrode. The plasma cluster was located far from the main plasma column which was accompanied with current conduction. Therefore, the effect of the plasma cluster on the POS operation was not significant.

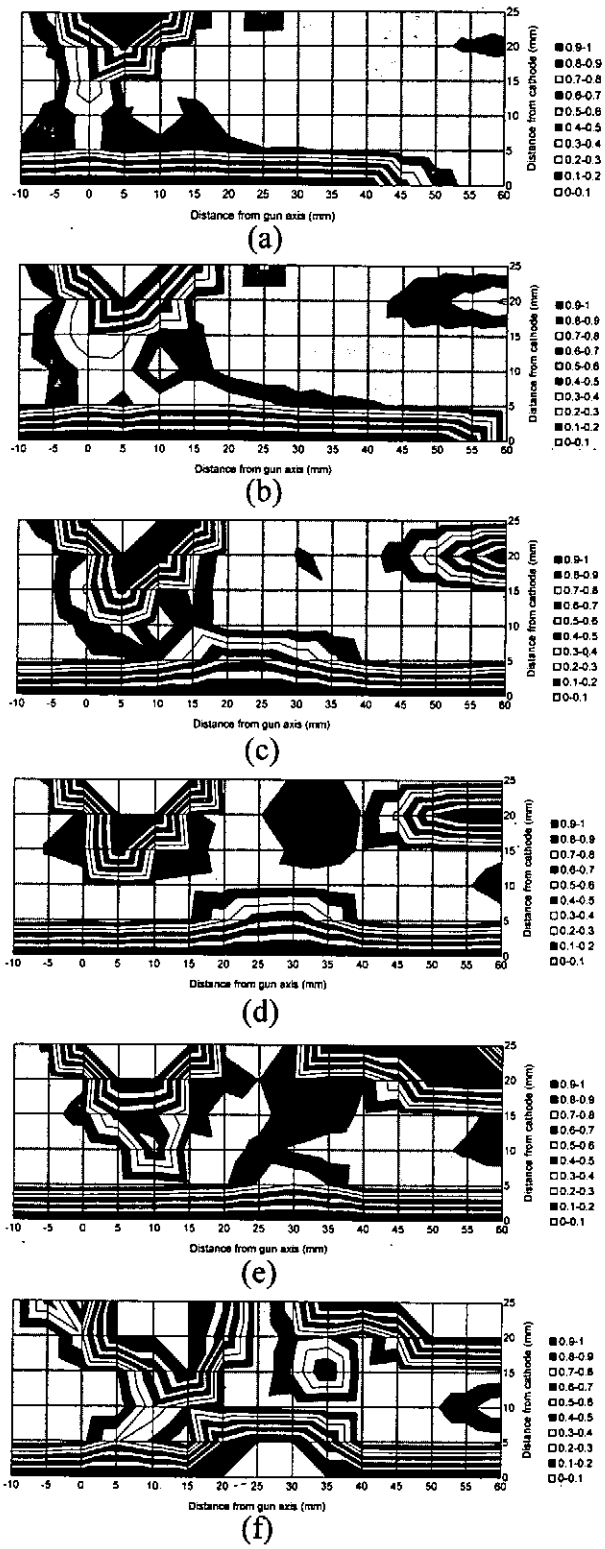

Fig. 3. Iso-density contours in the POS region at 500 ns (a), 600 ns (b), 700 ns (c), 800 ns (d), 900 ns (e) and 1200 ns (f) after the current onset.

Fig. 3 (c) is the contour of 700 ns after the current onset. The plasma on the cathode side was moved about 25 mm downstream and that on the anode side was moved 5 mm downstream. Therefore, the plasma column had a very sharp curvature in the middle of the plasma. Because of the radial magnetic pressure, the plasma was likely to be rarefied.

Fig. 3 (d) is the contour of 800 ns after the current onset that corresponds to the time of opening in the current waveform. It is clearly seen that the plasma moved 5 mm from the gun axis in the region from 10 to 25 mm radial position. On the other hand, the plasma near the cathode moved about 30 mm from the gun axis. These phenomena occur because the plasma with the lighter mass was strongly pushed by a stronger magnetic pressure, resulting in the further motion toward downstream and hence the difference in the speed of motion between the radial positions. Therefore, in Fig. 3 (d), the low-density region less than 10^{15} cm^{-2} was created at the 10 mm from the cathode. It is the vacuum gap where the electrons are magnetized, and current is interrupted. The size of vacuum gap was estimated, in Fig. 3 (d), as several millimeters.

Fig. 3 (e) is the contour of 900 ns after the current onset that is just after the opening in the current waveforms. The low-density gap seen in Fig. 3 (d) was not seen at this time. The main part of the POS plasma is likely to re-close the gap, and the plasma of right-up side and the cathode plasma are bridged. Therefore, after the

opening, a kind of breakdown occurs in the POS region and current flows in the plasma. This is the reason of the damped load current after the very quick rise.

Fig. 3 (f) is the contour of 1200 ns after the current onset. The structure of POS plasma was complicated and the vacuum gap seen in Fig 3 (d) was reconnected completely. The electron density became higher with increasing time since the most of current from the generator was flowing through the POS plasma after the opening. It was understood from the series of contours that the vacuum gap was re-closed immediately after the opening. And the plasma cluster seen in the rght-up region of the contours was also propagating toward the cathode side and likely to be combined with the main plasma column.

In order to estimate the motion of current layer in the POS plasma, the positions having the highest density along each radial position were plotted and shown in Fig. 4 as a function of time. In Fig. 4, the motion of current layer in the region from r=10 to 25 mm is not clearly distinguished. Seeing Fig. 3, since the plasma in that region has the shape like a column consisting of relatively high-density plasma and its motion is tiny, there is a difficulty in the estimation of the current layer. On the contrary, the radial positions of r= 0 and 5 mm have a clear trend of the motion of current layer. The position-of-highest density is moving with time from 10 mm upstream POS to 30 mm downstream POS at the 5 mm radial position. And the speed of the plasma motion is increasing with time during the conduction phase. Moreover, the speed of position-of-highest density at 5 mm radial position is higher compared with both upper (10 mm) and lower (0 mm) positions. This difference in the speed of motion resulted in the curvature of current layer leading to the radial J×B force that has the essential effect on the vacuum gap creation.

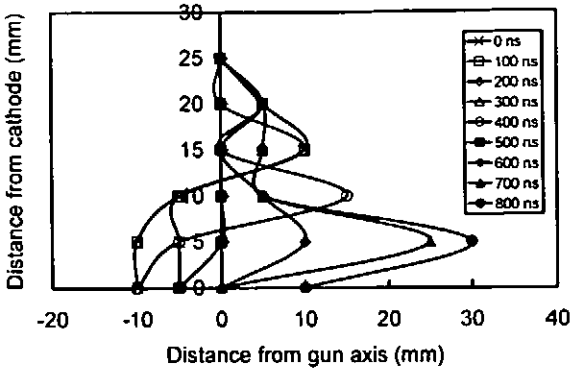

Fig. 4. Positions-of-highest density at each radial position as a function of time.

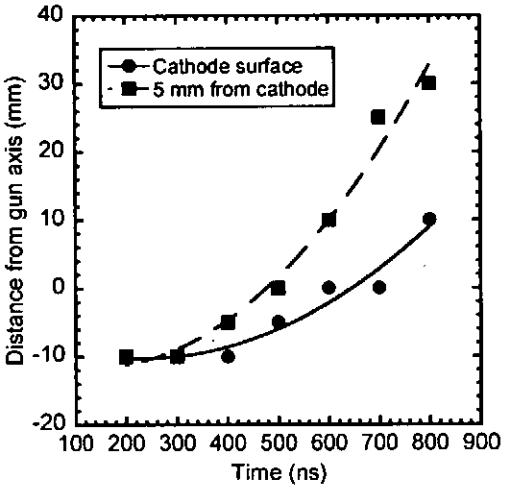

Fig. 5. Variations of the distance of positions-of-highest density in time at the 0 mm (solid line) and 5 mm (dashed line) radial positions from the cathode.

Fig. 5 shows the motions of positions-of-highest density on the r=0 mm and r=5 mm radial positions obtained from Fig. 4. The lines indicate the curve proportional to the time squared. During the early time of the conduction phase, the highest-density-positions were located at the same axial position. Then both moved toward downstream with the different speeds. The distances of axial motions are in proportion to the time squared. Therefore, the positions-of-highest density are thought to move under the constant acceleration and increase their velocities.

Under the assumptions used in the snowplow model, the acceleration of the propagating plasma was estimated using the equation of motion. Assuming that the current through plasma I rises linearly, equation of motion for the current-carrying plasma channel in the POS plasma is

$$I = I_0 t; \tag{3}$$

$$M_i n \frac{d(lv)}{dt} = \frac{\mu I_0^2}{8\pi^2 r^2} t^2. \tag{4}$$

Here l is the variable length of switch changing in the process of the snowplow motion, M_i is the average ion mass, v is the snowplow velocity, n is the plasma density and r is the cathode radius.

Designating

$$C_1 = M_i n; \tag{5}$$

$$C_2 = \frac{\mu I_0^2}{8\pi^2 r^2}, \tag{6}$$

equation (4) becomes

$$C_1 \frac{d(lv)}{dt} = C_2 t^2. \tag{7}$$

Equation (7) can be solved dividing the variables for the channel velocity as

$$C_1 lv = C_2 \frac{t^3}{3}; \tag{8}$$

$$C_1 \frac{l}{t} v = C_2 \frac{t^2}{3}; \tag{9}$$

$$v = \sqrt{\frac{C_2}{3C_1}} \cdot t. \tag{10}$$

Therefore, the current-carrying layer moves with the constant acceleration:

$$a = \sqrt{\frac{\mu I_0^2}{24\pi^2 r^2 M_i n}}, \tag{11}$$

and its velocity linearly rises with time and the distance of motion increases in proportional to

the time squared.

Substituting 1.3×10^{11} [A/s] for I_0, 1×10^{15} [cm^{-3}] for n and 40 [mm] for r in equation (11), which are the values in our experiment, and taking into account the aluminum ion, the magnitude of the acceleration obtained from equation (11) showed the good agreement with the experimental data obtained in Fig. 5. If we take into account the hydrogen ion, the acceleration becomes five times higher than that for aluminum ion. This proposes that, if the conduction time is constant, the lighter ion species give the higher speed of propagating plasma and leads to the good opening. Additionally, the highly-ionized plasma might prevent the breakdown in the vacuum gap and increase the efficiency of the power flow from the generator to the load after the opening.

IV. Summary

The motion of POS plasma throughout the operation was studied by the interferometer and the spectroscopic experiments. From a number of density measurements at many positions, the density contours were drawn. The vacuum gap, which is the low-density region less than 10^{15} cm^{-2}, was observed at 10 mm from the cathode at the time of opening in the current waveform, as a result of downstream propagation of current-conducting POS plasma. The motion of current-front in the POS plasma was estimated by taking positions-of-highest density. The speed of propagation of POS plasma was different at the different radial locations. The consequent curvature of the POS plasma caused the radial separation of plasma resulting in the vacuum gap creation. From the spectroscopic measurement, the emission from the neutral hydrogen was observed in the position where the vacuum gap was created even at the opening time. However, those from ions were not observed. The acceleration of the propagating plasma measured in the experiment is in good agreement with that derived from the theoretical equations.

References

[1] W. Rix, P. Coleman, J. R. Thompson, D. Husovsky, P. Melcher, and R. J. Commisso, "Scaling microsecond-conduction-time plasma opening switch operation from 2 to 5 MA," IEEE Trans. Plasma Sci., **25**, 169 (1997)

[2] J. M. Grossmann, S. B. Swanekamp, R. J. Commisso, P. J. Goodrich, D. D. Hinshelwood, J. D. Huba, P. F. Ottinger, and B. V. Weber, "Conduction phase to opening phase transition in the plasma opening switch," Proc. 10th Int'l Conf. on High Power Particle Beams, San Diego, 1994, Vol. 1, pp. 280-283

[3] B. V. Weber, D. D. Hinshelwood, and R. J. Commisso, "Interferometry of flashboard and cable-gun plasma opening switch," IEEE Trans. Plasma Sci., **25**, 189 (1997)

[4] A. S. Chuvatin, B. Etlicher, N. S. Edison, and C. Rouillé, "A sensitive He-Ne interferometer with passive beam power stabilization for low-density pulsed-plasma measurements," Rev. Sci. Instrum., **64**, 2267 (1993)
[5] S. Kohno, Y. Teramoto, I. V. Lisitsyn, S. Katsuki, and H. Akiyama, "Cable guns as a plasma source in a plasma opening switch," IEEE Trans. Plasma Sci., **27**, 778 (1999)
[6] S. Kohno, Y. Teramoto, I. V. Lisitsyn, S. Katsuki, and H. Akiyama, "High-current pulsed power generator ASO-X using inductive voltage adder and inductive energy storage system," Jpn. J. Appl. Phys., **39**, 2829 (2000)

PROPAGATION OF PULSED STREAMER DISCHARGES IN ATMOSPHERIC AIR

T. Namihira, H. Hori, S. Katsuki and H. Akiyama

The Department of Electrical and Computer Engineering, Kumamoto University, Kurokami 2-39-1, Kumamoto 860-8555, Japan.

ABSTRACT

Pulsed streamer discharges have been extensively used in many applications such as control of NO_X and SO_2 from exhaust gases, treatment of dioxins, removal of VOC (Volatile Organic Compounds), generation of ozone and laser excitation. An operation with a high-energy efficiency is necessary for practical applications. It is very important to know the propagation mechanism of streamer discharges in order to improve the energy efficiency of pulsed discharge systems. The critical conditions of streamer propagation and the electric field of a streamer head or tail have been obtained from the computer simulation about the propagation of streamer discharges. However the propagation of large volume streamer discharges in atmospheric air has not been observed.

In the present work, the emissions from pulsed streamer discharges in the coaxial electrode at atmospheric pressure were observed by a high-speed gated ICCD camera. An electrode configuration of wire to cylindrical was used. A positive pulsed voltage with pulse width of about 100 ns was applied to the central wire electrode. The streamer discharges begin from the inner electrode and reach the outer electrode. The propagation velocity of the streamer discharges was several mm / ns.

I. Introduction

There are several serious environmental problems in the world today. One of them is the acid rain arising from the combustion of fossil fuel produced by thermal power plants, factories and motor vehicles. Several types of electrical discharges, such as surface, silent and corona have been applied to the removal of NO_X and SO_2 from exhaust emissions at the stage of various energy efficiencies. Currently developments in the pulsed power generators have enabled the production of efficient streamer discharges to remove NO_X and SO_2.[1-5]

Since the pulse width of applied voltages has a strong influence on the energy efficiency,[6, 7] the knowledge of the development of streamer discharges using very short

duration pulses is important for practical applications. The most effective condition of streamer discharges might be obtained from the knowledge of streamer propagation phenomenon. H. Raether[8], L.B. Leob[9, 10] and J.M. Meek[11, 12] independently proposed similar mechanisms to explain the streamer discharges. A.A. Kulikovsky[13, 14], F. Tochikubo et al.[15, 16] and K. Durbhakula et al.[17] forecasted the electric fields and the propagation speeds of streamer heads by using computer simulations. K. Yan et al.[18, 19] measured the light emissions from streamer discharges by using the optical fiber and the photomultiplier tube in the vicinity of central wire in the coaxial electrode. E.H.W.M. Smulders et al.[20] observed the images of streamer discharges in 560 torr of air using a high-speed gated camera. W.J. Yi et al.[21] also observed the images of streamer discharges in the tip to plane electrode.

In this work, the emissions from the pulsed streamer discharges in the coaxial electrode at atmospheric pressure were observed with the ICCD camera having a high-speed gate. The coaxial electrodes having the wire diameter of 0.5 mm, the cylinder diameter of 76 or 152 mm and the length of 10 mm were employed. A short length was necessary in order to observe the streamer discharges clearly. A positive pulsed voltage with the pulse width of 100 ns was applied to the central wire. The images of streamer discharges were observed with a frame period of 10 ns and an exposure time of 5 ns. It has been found that the streamer discharges started from the inner electrode and then reached the outer electrode. The propagation velocities of the streamer discharges had dependence on an applied voltage to the central electrode and were several mm / ns.

II. Experimental apparatus and procedure

Figure 1 shows a schematic diagram of the experimental apparatus. The three-staged Blumlein line generator, which has pulse width of 100 ns, was used as a pulsed power source.[2] This generator was charged at 20, 25 and 30 kV. A coaxial electrode having a central rod made of tungsten, 0.5 mm in diameter placed concentrically in a copper cylinder, and a length of 10 mm was employed. A short length of electrode gave clear images of streamer discharges. In this experiment, the copper cylinders having an internal diameter of 76 and 152 mm were used. The coaxial electrode was filled with the air of the atmospheric pressure. The applied voltages of positive polarity from the Blumlein line generator to the coaxial electrode were measured using a voltage divider (1 Ω / 10 kΩ, Ratio 10×10^3), which was connected between the central electrode and the ground. The current to the coaxial electrode was measured using a Rogowski coil (Pearson current monitor, Model 2878, Pearson Electronics, USA), which was located at the wire for the return current to the ground. A high-speed gated ICCD camera (C7972-01, Hamamatsu Photonics, Japan) with a sensitive MCP (Micro Channel Plate, maximum gain = 10,000), was used to observe the images of streamer discharges. The exposure time of this camera was fixed at 5 ns. The delay time from the onset

time of applied voltage was every 10 ns in the range of 0 to 130 ns.

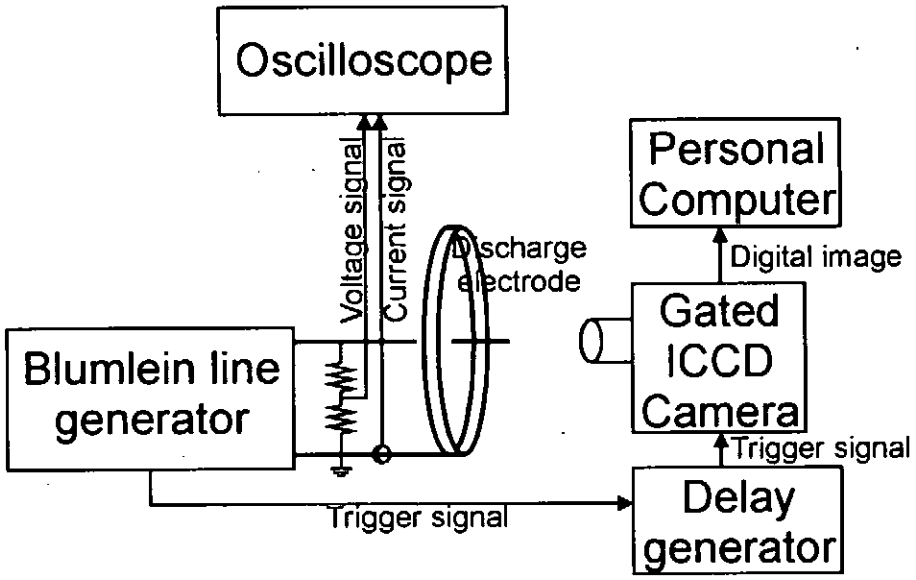

Fig. 1. A schematic diagram of the apparatus

III. Results and discussions

Figure 2 shows typical waveforms of the applied voltage to and the discharge current through the coaxial electrode for the different charging voltages to the generator. The output voltages from the generator were applied to the wire electrode at 0 ns of Fig. 2. The maximum values of the applied voltage and the discharge current increased with the charging voltage.

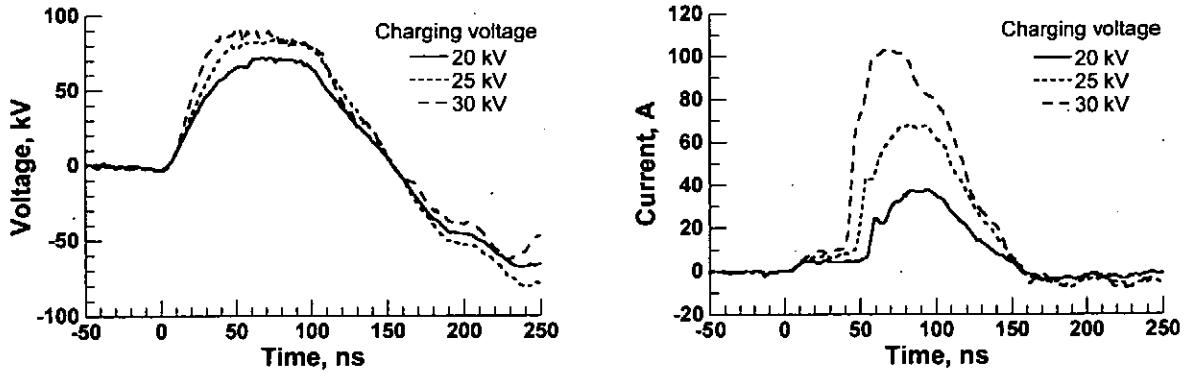

(a) (b)

Fig. 2. (a) Applied voltage to and (b) discharge current in the coaxial electrode for varying charging voltages to the Blumlein generator. Cylinder diameter, 76 mm.

Figure 3 shows the images of emissions from the streamer discharges in the varying delay times of ICCD camera for the charged voltages of 20 kV or 30 kV. The images had the good reappearance when the same experimental conditions. The white areas of these images

show the position of streamer heads in the exposure time (5 ns) because the streamer heads keep high electric fields.[8-17] Major wavelengths of these emissions were considered 337.1 nm and 391.4 nm from 2nd positive band and 1st negative band of N_2, respectively.[22-24]

The electric fields on the surface of the central electrode were constant of 17 MV/m in the different charging voltages when the streamer discharges were formed in the vicinity of center electrode (delay time 10-15 ns in Fig. 3). These electric fields Er,[25] were calculated from

$$E_r = \frac{V}{r\,ln(R_2/R_1)}, \qquad (1)$$

where R_1 (0.25 mm), R_2 (38 mm), r (0.25 mm) and V are the radius of the inner electrode, the radius of outer electrode, the distance from the surface of wire electrode and the applied voltage to the central electrode, respectively.

The electric fields of streamer heads were assumed to keep over 17 MV/m due to the following Meek's criteria[11, 13, 14, 26]

$$E_P = E_r, \qquad (2)$$

where E_P is the electric field by the space charge of electron avalanche.

It is observed from Fig. 3 that the primary streamers[18, 19] propagate from the central electrode to the outer electrode. The reaching time of primary streamer discharges to the outer electrode reduced from 55 to 40 ns with increasing the charging voltages to the generator in the range of 20 to 30 kV. Before the arrival of the primary streamers at the cylinder, the discharge currents were small (in Fig. 2) because the capacitance between the streamer head and the cylinder works as limiting impedance.[20] The fully development of primary streamers between electrodes resulted in the disappearance of the capacitance between the streamer heads and the cylinder electrode. This allows the large discharge currents to flow through the plasma channel of primary streamers (in Fig. 2b).

The secondary streamers[18, 19] appeared from the central electrode at the delay time of 30-35 ns in Fig. 3. The secondary streamer disappeared at middle of electrode because its electric field would be small when the plasma channel of primary streamers reached to the outer cylinder.[15, 16]

After bridging, the emissions from the streamer discharges were observed in the vicinity of a center electrode with a strong electric field by geometrical arrangement of the electrode.[27, 28]

Figures 4 (a) and (b) show the dependences of the applied voltages to the central wire and the velocities of streamer heads on time for the 76 mm and 152 mm diameters of outer cylinder, respectively. Many results of streamer propagation simulations had indicated that the radius of streamer heads was about 100 μm.[14-16] In the images of Fig. 3, the radiuses of the streamer heads can be disregarded because those are enough smaller than the scale of the

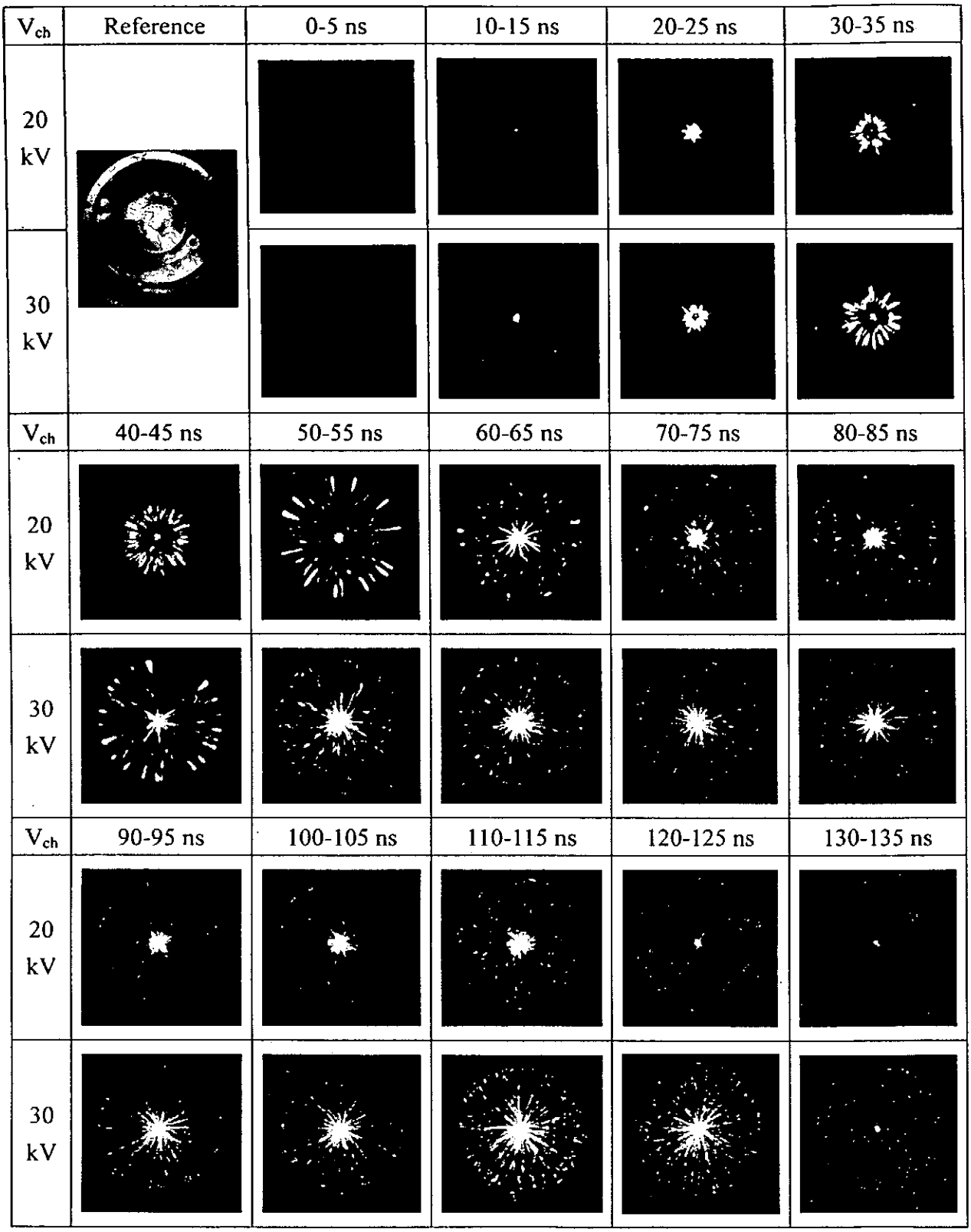

Fig. 3. Images of light emissions from streamer discharges in varying delay times of ICCD camera for the charging voltage of 20 kV or 30 kV. Cylinder diameter, 76 mm.

images. Therefore the velocities of the streamer heads was given by the following equation

$$V_{streamer} = \frac{L}{t_{exposure}}, \qquad (3)$$

where $V_{streamer}$, L, and $t_{exposure}$ (5 ns) are the velocity of the streamer head, the length of emission in the streamer images in Fig. 3 and the exposure time of a ICCD camera, respectively.

It is observed from Fig. 4 that the velocity of streamer heads increases with increasing applied voltages to the wire electrode. The streamer discharges with the speed of the several mm / ns are greatly influenced by the electric field strengths on wire surface.[13-16]

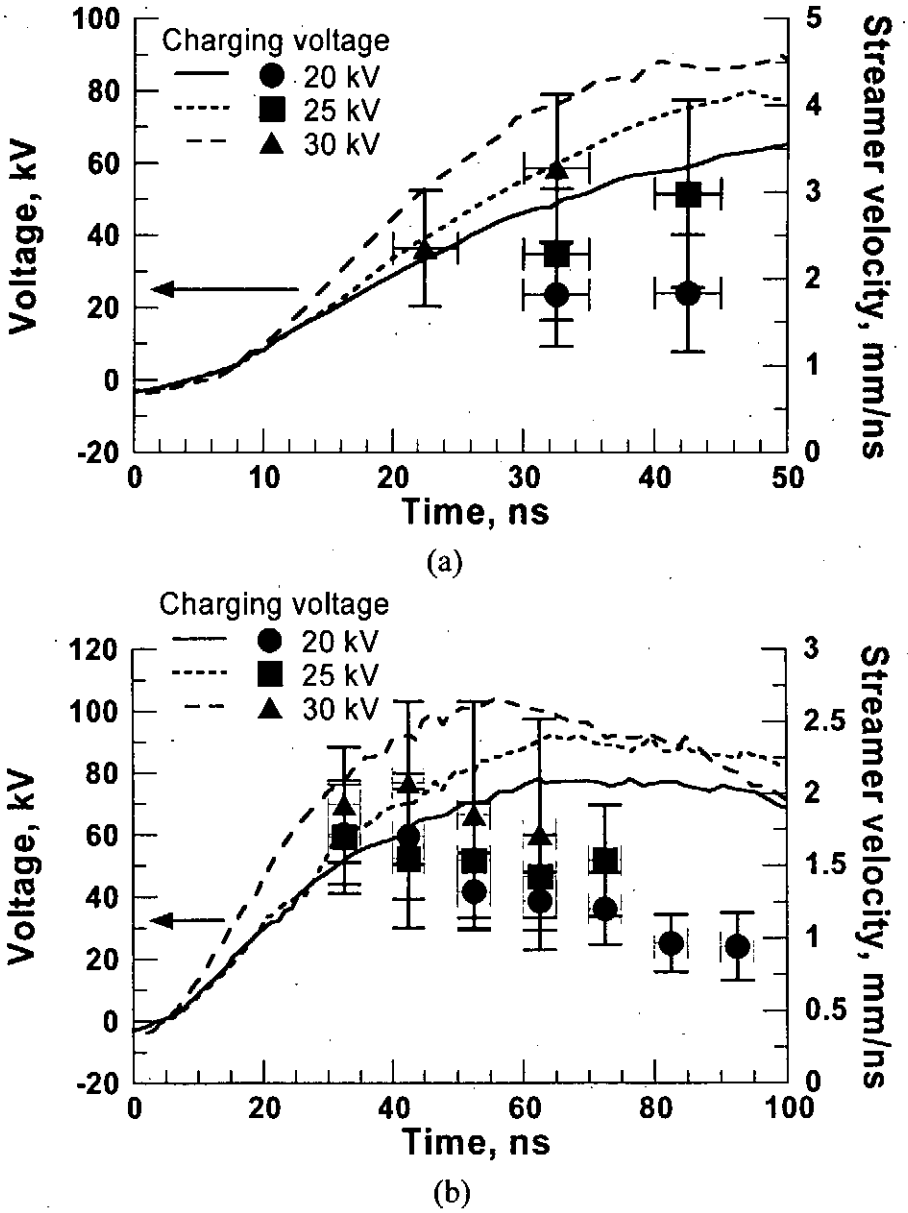

Fig. 4. Dependences of applied voltage to the central wire and the velocity of streamer head on time. Cylinder diameter, (a) 76 mm, (b) 152 mm.

IV. Summary

The images of the streamer discharges in a coaxial electrode at atmospheric pressure have been observed using high-speed gated ICCD camera. The following summaries have been deduced.

1. The heads of the streamer discharges propagate from central rod to outer cylinder.
2. The propagation speeds of the streamer discharges are several mm / ns.
3. The propagation speeds of the streamer discharges are greatly influenced by the electric field strength on the wire surface.

References

1) S. Tsukamoto, T. Namihira, D. Wang, S. Katsuki, R. Hackam, H. Akiyama, A. Sato, Y. Uchida and M. Koike, "Effects of fly ash on NO_X removal by pulsed streamers", IEEE Transactions on Plasma Science, Vol.29, No.1, pp.29-36, 2001.
2) T. Namihira, S. Tsukamoto, D. Wang, H. Hori, S. Katsuki, R. Hackam, H. Akiyama, M. Shimizu and K. Yokoyama, "Influence of gas flow rate and reactor length on NO removal using pulsed power", IEEE Transactions on Plasma Science, Vol.29, No.4, pp.592-598, 2001.
3) Y.S. Mok, S.W. Ham and I.S. Nam, "Evaluation of energy utilization efficiencies for SO_2 and NO removal by pulsed corona discharge process", Plasma Chemistry and Plasma Processing, Vol.18, No.4, pp.535-550, 1998.
4) S. Masuda, S. Hosokawa, X. Tu and Z. Wang, "Novel plasma chemical technologies – PPCP and SPCP for control of gaseous pollutants and air toxics", Journal of Electrostatics, Vol.34, pp.415-438, 1995.
5) B.M. Penetrante, M.C. Hsiao, B.T. Merritt, G.E. Vogtlin and P.H. Wallman, "Comparison of electrical discharge techniques for nonthermal plasma processing of NO in N_2", IEEE Transactions on Plasma Science, Vol.23, No.4, pp.679-687, 1995.
6) T. Namihira, S. Tsukamoto, D. Wang, S. Katsuki, R. Hackam, H. Akiyamma, Y. Uchida and M. Koike, "Improvement of NO_X removal efficiency using short width pulsed power", IEEE Transactions on Plasma Science, Vol.28, No.2, pp.434-442, 2000.
7) V. Puchkarev and M. Gundersen, "Energy efficient plasma processing of gaseous emission using a short pulse discharge", Applied Physics Letter, Vol.71, No.23, pp.3364-3366, 1997.
8) H. Raether, "Electron avalanches and breakdown in gases", London: Butterworth, 1964.
9) L.B. Loeb, "Ionizing waves of potential gradient", Science, Vol.148, p.1417, 1965.
10) L.B. Loeb, "Fundamental processes of electrical discharges in gases", New York: Wiley, 1939.
11) J.M. Meek, "A theory of spark discharges", Physics Review, Vol.57, p.722, 1940.
12) J.M. Meek and J.D. Craggs, "Electrical breakdown of gases", pp.251-290, Oxford,

Clarendon Press, 1953.
13) A.A. Kulikovsky, "Positive streamer in a weak field in air: A moving avalanche-to-streamer transition", Physical Review E, Vol.57, No.6, pp.7066-7074, 1998.
14) A.A. Kulikovsky, "Analytical model of positive streamer in weak field in air: Application to plasma chemical calculations", IEEE Transactions on Plasma Science, Vol.26, No.4, pp.1339-1346, 1998.
15) F. Tochikubo, A. Miyamoto and T. Watanabe, "Simulation of streamer propagation and chemical reaction in pulsed corona discharge", The 11th International Conference on Gas Discharge and Their Applications, Vol.1, pp.168-171, 1995.
16) F. Tochikubo and T. Watanabe, "Use of nonequilibrium plasma for harmful gas treatment", OYO BUTURI, Vol.66, No.6, 576-579, 1997. (In Japanese)
17) K. Durbhakula and S. Dhali, "Computer-generated image of streamer propagation in nitrogen", IEEE Transactions on Plasma Science, Vol.27, No.1, pp.24-25, 1999.
18) K. Yan, H. Hui, M. Cui, J. Miao, X. Wu, C. Bao and R. Li, "Corona induced non-thermal plasma: Fundamental study and industrial applications, Journal of Electrostatics, Vol.44, pp.17-39, 1998.
19) K. Yan, S. Kanazawa, T. Ohkubo and Y. Nomoto, "Evaluation of NO_X removal by corona induces non-thermal plasma", The Transactions of The Institute of Electrical Engineers of Japan, Vol.119-A, No.6, pp.731-737, 1999.
20) E.H.W.M. Smulders, B.E.J.M. van Heesch and S.S.V.B. van Passen, "Pulsed power corona discharges for air pollution control", IEEE Transactions on Plasma Science, Vol.26, No.5, pp.1476-1484, 1998.
21) W.J. Yi, S.J. Hankla and P.F. Williams, "High-temporal-resolution, high-sensitivity imaging of streamers in a long atmospheric pressure gap", IEEE Transactions on Plasma Science, Vol.24, No.1, pp.93-94, 1999.
22) K. Kawamura, S. Tsukamoto, T. Takeshita, S. Katsuki and H. Akiyama, "NO_X removal using inductive pulsed power generator", Transactions IEE of Japan, Vol.117-A, No.9, pp.956-961, 1997. (In Japanese)
23) M. Kosuge, M. Fujiwara and M. Ishida, "Analyses of pulse duration influence on the NO_X removal by a pulsed corona discharge with luminescence measurement", Transactions IEE of Japan, Vol.120-A, No.2, pp.167-173, 2000. (In Japanese)
24) F. Tochikubo and T.H. Teich, "Optical emission from a pulsed corona discharge and its associated reactions", Japan Journal Applied Physics, Vol.39, No.3A, pp.1343-1350, 2000.
25) M. Hara and H. Akiyama, "High-voltage pulsed power engineering", Morikita Syuppan Co., Japan, 1991. (In Japanese)
26) N. Brenning, I. Axnas, J.O. Nilsson and J.E. Eninger, "High-pressure pulsed avalanche

discharges: formulas for required preionization density and rate homogeneity", IEEE Transactions on Plasma Science, vol.25, No.1, pp.83-88. 1997.

27) R. Hackam, "Total secondary ionization coefficient and breakdown potentials of hydrogen, methane, ethylene, carbon monoxide, nitrogen, oxygen and carbon dioxide between mild steel coaxial cylinders", J. Phys. B: Atom. Molec. Phys., vol.2, pp.216-233, 1969.

28) R. Hackam, "Total secondary ionization coefficients and breakdown potentials of monatomic gases between mild steel coaxial cylinders", J. Phys. B: Atom. Molec. Phys., vol.2, pp.201-215, 1969.

SIMULATION OF NON-LINEAR COAXIAL LINE USING FERRITE BEADS

S.Furuya, H.Matsumoto, K.Tachi, S.Takano and J.Irisawa

Nagaoka University of Technology, Niigata, 940-2188, JAPAN

ABSTRACT

A ferrite sharpener is a non-linear coaxial line using ferrite beads, which produces high-voltage, high-dV/dt pulses. We have been examining the characteristics of ferrite sharpeners experimentally, varying various parameters. Also we have made the simulation of the ferrite sharpener and compared the predictions with the experimental results in detail to analyze the characteristics of the sharpener. In this report, calculating the magnetization M of the ferrite bead, we divide the bead into n sections radially instead of adopting M at the average radius in the previous report.

1. Introduction

High-voltage, high-dV/dt pulses are necessary to drive pulsed laser, Pockels cell, pulsed radar and to control electron beam. There are various methods to produce high-dV/dt pulses; non-linear transmission line using ceramic capacitors[1], pn-junction diodes[2] and ferrite[3]. Among them non-linear coaxial line using ferrite beads is superior to the others with respect to low cost and simplicity of structure. Therefore, we have been examining the characteristics of ferrite sharpeners, non-linear coaxial lines using ferrite beads, experimentally, varying various parameters. We have obtained pulses which have high dV/dt of 12kV/ns and open-ended peak voltage of 45kV[4]. Also we have made the simulation of the ferrite sharpener to analyze the characteristics of the sharpener along with Ref.5. Then we compared the predictions with the experimental results in detail. As a result, the results of the simulation are in good agreement with the experimental results[6].

In this report, calculating the magnetization M of the ferrite bead we divide the bead into n sections radially instead of adopting M at the average radius in the previous report[6]. In Sec.2, the experimental setup of the ferrite sharpener is described. In Sec.3, the equivalent circuit of the ferrite sharpener is presented. In Sec.4, the results of the simulation and discussion are described. Finally, the results of this report are summarized in Sec.5.

2. Experimental setup

Fig.1 shows the structure of a ferrite sharpener, which is a non-linear coaxial line using ferrite beads. A peace of ferrite bead is nickel-zinc ferrite bead TDK-HF70BB. The outer and inner diameters of a bead are 5.0mm and 2.0mm, respectively, and its length is 5.0mm. The impedance of the sharpener after ferrite saturation is designed to be approximately 50Ω. The principle of the sharpener is illustrated in Fig.2. As shown in the figure, an input voltage pulse dissipates its front, propagating in the sharpener. Then the input voltage pulse is steepened at the end of the sharpener. The rise time and peak voltage of the input pulse are approximately 40ns and 20kV, respectively. Typical output waveform of open-ended ferrite sharpener is shown in Fig.3. The rise time and peak voltage of the pulse are 2.4ns and 45kV, respectively,

so high dV/dt of 12kV/ns is achieved. Voltages are measured by Tektronix high voltage probe: P6015A and Hewlett Packard digital oscilloscope: HP54510A.

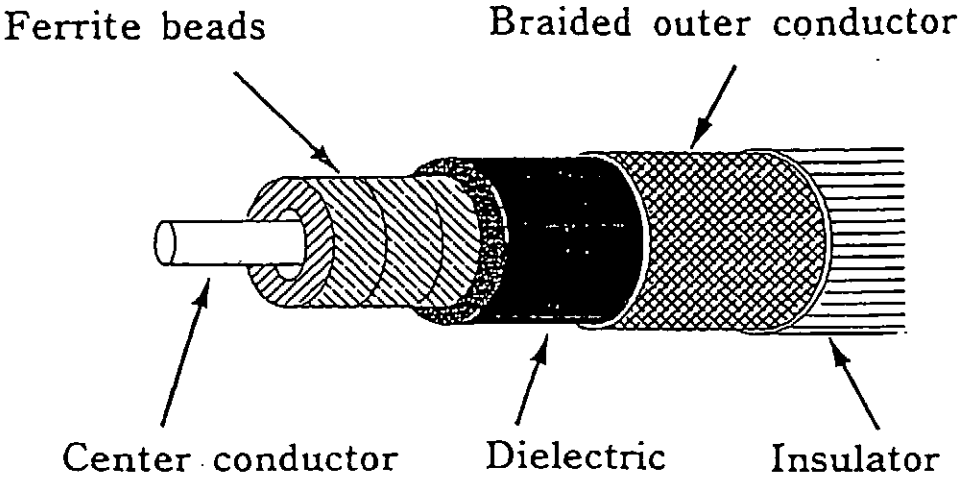

Fig.1 Structure of ferrite sharpener

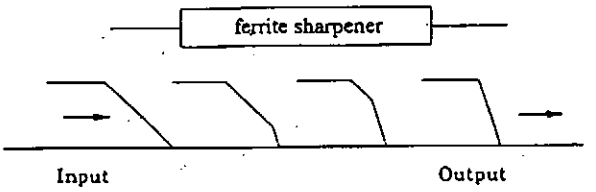

Fig.2 Principle of ferrite sharpener

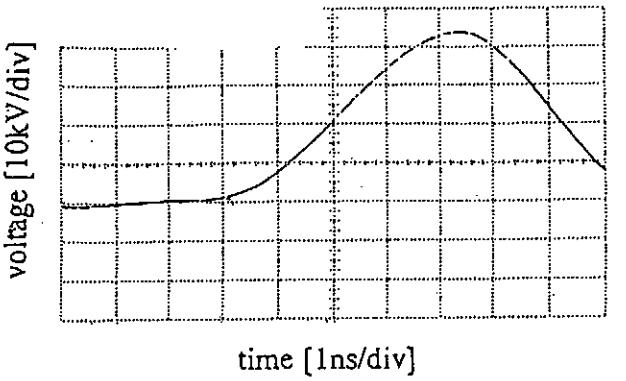

Fig.3 Output waveform of ferrite sharpener

3. Equivalent circuit of ferrite sharpener

Along with Ref.5, we made the simulation of the ferrite sharpener to analyze the characteristics of the sharpener. The equivalent circuit of the sharpener is derived as follows. Current equation of the sharpener is the same as a usual transmission line.

$$\mathrm{d}I/\mathrm{d}z = -C_0 \mathrm{d}V/\mathrm{d}t \tag{1}$$

where C_0 is the capacitance of the sharpener per unit length. The magnetic flux ϕ of the sharpener is

$$\phi = L_0 I + \int_n^{r_m} \mu_0 M(r) dr \tag{2}$$

where L_0 is the inductance of the sharpener per unit length after ferrite saturation. r_m and ri are the outer and inner radius of the ferrite bead, respectively, and M is the magnetization of the bead. In the previous report[6], we assume that M is independent of the radius and is constant;

we adopt M at average radius, i.e. M_{θ_ave} as shown in Fig.4(a), so eq.(2) becomes

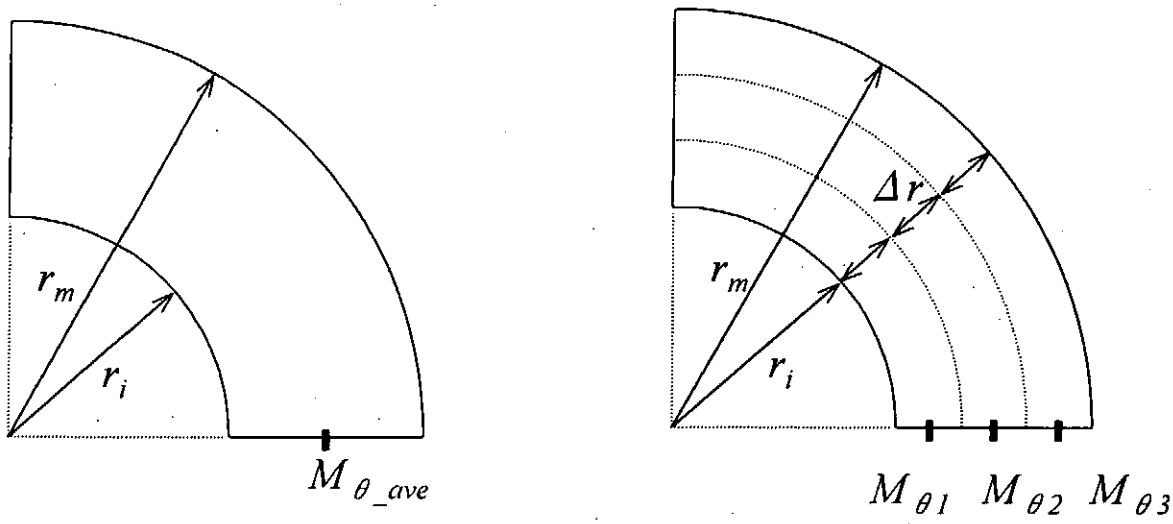

(a) M_{θ_ave} (M at average radius) (b) $M_{\theta i}$ and Δr

Fig.4 Illustration of M_{θ_ave} and $M_{\theta i}$

$$\phi = L_0 I + \mu_0 M_{\theta_ave}(r_m - r_i) \tag{3}$$

Therefore, voltage equation of the transmission line is

$$\mathrm{d}V/\mathrm{d}z = -\mathrm{d}\phi/\mathrm{d}t = L_0 \mathrm{d}I/\mathrm{d}t + \mu_0(r_m - r_i)\mathrm{d}M_{\theta_ave}/\mathrm{d}t \tag{4}$$

In this report, we divide a ferrite bead into n sections radially and take the sum of the products of $M_{\theta i}$ and Δr as shown in Fig.4(b), so eq.(2) becomes

$$\phi = L_0 I + \mu_0 \sum_{i=1}^{n} M_{\theta i} \Delta r \tag{5}$$

Therefore, voltage equation of the transmission line is

$$\mathrm{d}V/\mathrm{d}z = -\mathrm{d}\phi/\mathrm{d}t = L_0 \mathrm{d}I/\mathrm{d}t + \mu_0 \Delta r \sum_{i=1}^{n} \mathrm{d}M_{\theta i}/\mathrm{d}t \tag{6}$$

From eq.(1) and (4) or (6) the equivalent circuit of the sharpener is derived, as shown in Fig.5. Voltage sources in the figure are respond to the product of Δz and the second term of eq.(4) or (6). dM/dt is obtained from Landau-Gilbert equation as below.

$$\frac{\mathrm{d}M}{\mathrm{d}t} = \frac{2}{S_W}\mu_0 H M_S\left(1 - \frac{M^2}{M_S^2}\right) \tag{7}$$

where S_W is a switching coefficient of the ferrite used and H is the magnetic field. M_S is the saturation magnetization of the ferrite used.

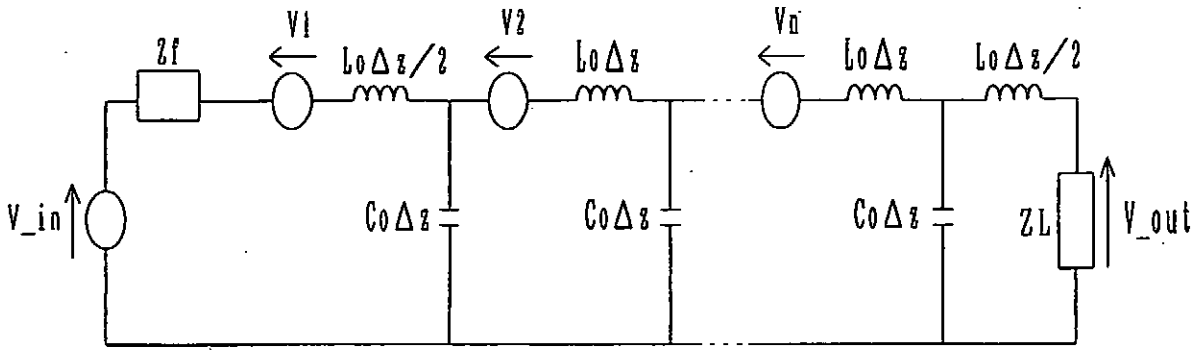

Fig.5 Equivalent circuit of ferrite sharpener

4. Results and discussion

Static B-H curve of the ferrite bead used is shown in Fig.6. From the catalog, relative permeability at H=0 and saturation magnetic flux density are 1500 and 0.28T, respectively. According to Ref.7, the switching coefficient of nickel-zinc ferrite is 0.25 or 0.51 oe·μs. In simulation, time step Δt is 2ps and the sharpener is divided into 200 sections in z direction and 50 sections radially. The input voltage waveform of simulation is fitted to that of experiment. Its peak voltage and rise time are 10kV and 40ns, respectively. The output terminal is loaded with matching impedance, i.e. a 48Ω resistor.

Figure 7 shows the rise time of the output voltage pulse of the sharpener when the length of the sharpener is changed. Figure 8 shows the rise time of the output voltage pulse of the sharpener when the bias current to the ferrite sharpener is changed. The length of the ferrite sharpener is 1m. The direction of the bias current is the same as that of the input pulse. In Fig.7 and 8, the prediction has a similar tendency to the experimental results. In both cases of S_W=0.25 and 0.51, the rise time predicted with summation of the products of $M_{\theta i}$ and Δr is slightly longer than that with M at average radius.

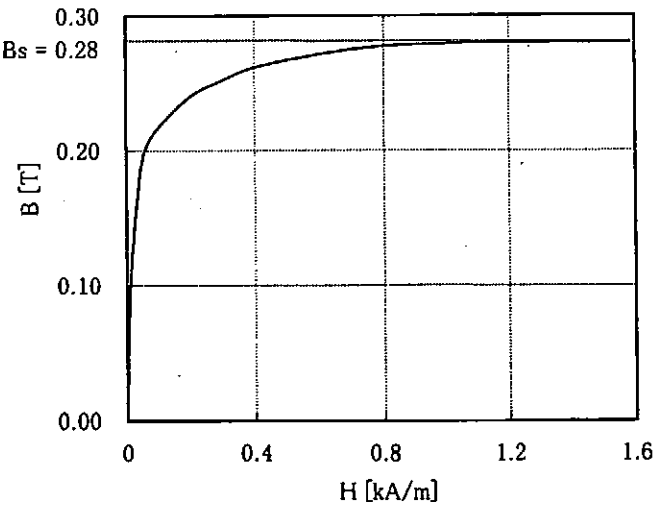

Fig.6 Static B-H curve of the ferrite bead used

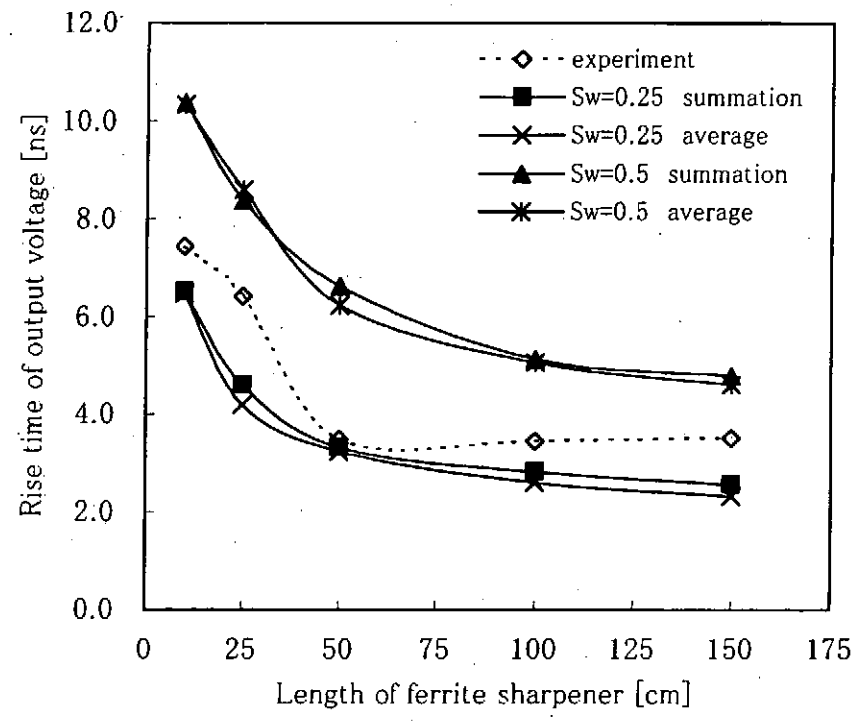

Fig.7 Rise time of output voltage vs. length of ferrite sharpener

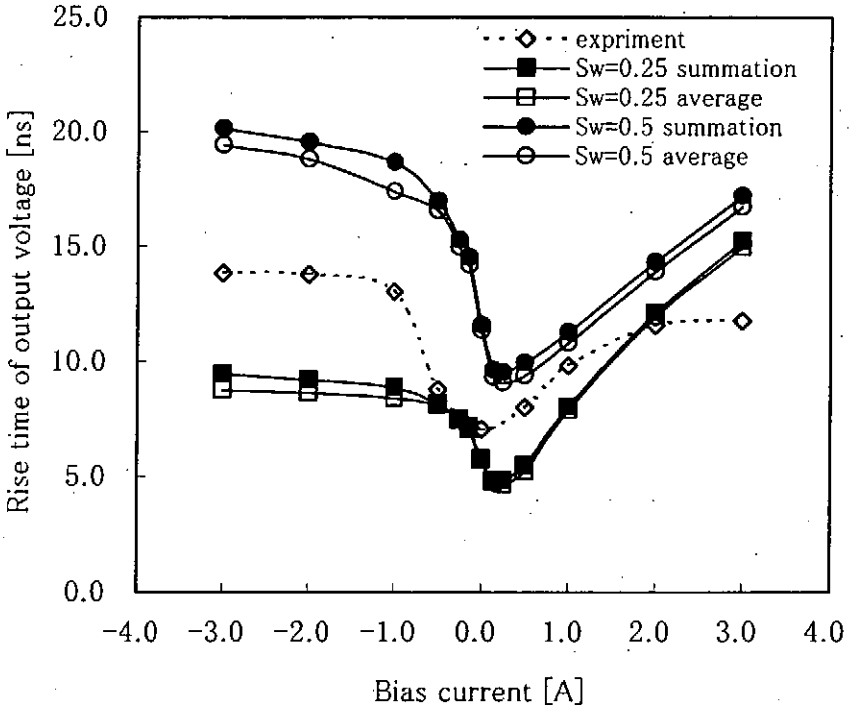

Fig.8 Rise time of output voltage vs. bias current

5. Conclusion

A ferrite sharpener is a non-linear coaxial line using ferrite beads, which produces high-voltage, high-dV/dt pulses. We have been examining the characteristics of ferrite sharpeners experimentally, varying various parameters. Also we have made the simulation of the ferrite sharpener and compared the predictions with the experimental results in detail to analyze the characteristics of the sharpener. In this report, calculating the magnetization M of the ferrite bead, we divide the bead into n sections radially instead of adopting M at the average radius in the previous report. Compared the prediction with experimental results when the length of the ferrite sharpener and the bias current are varied, the prediction has a similar tendency to the experimental results. In both cases of S_W=0.25 and 0.51, the rise time predicted with summation of the products of $M_{\theta i}$ and Δr is slightly longer than that with M at average radius.

Reference

(1) H.Ikezi, J.S.deGrassie and J.Drake, Appl. Phys. Lett., **58**(1988)986

(2) R.J.Baker et al., Meas. Sci. Technol., **4**(1993)893

(3) M.Weiner and L.Silber, IEEE Trans. Magn., **17**(1981)1472

(4) S.Takano et al., NIFS-PROC-26(1996)115

(5) J.E.Dolan, Electronics Lett., **29**(1993)762

(6) S.Furuya et al., NIFS-PROC-50(2001)109

(7) E.M.Gyorgy, J. Appl. Phys., **28**(1957)1011

EXPERIMENTAL SUPPORT FOR A FERRITE-CORE MODEL FOR SUPERTRONS

Hidenori Matsuzawa and Koji Mikami

Faculty of Engineering, Yamanashi University, Kofu 400-8511, Japan

ABSTRACT

Supertrons are a lens of new type for focusing and guiding electron current beams, and are composed of high-T_c superconducting rings into which electron beams are injected. The supertrons are very similar in structure and in functioning to ferrite cores which are composed of the fine magnetic grains (powders) that are electrically insulated each other and are compacted into a configuration required and then sintered. In this report, we review accumulated experimental results on the full-width at half-maximum of the intense electron current pulses that were generated with single or double-layered supertrons. The results are explainable with a ferrite-core model.

I. Introduction

Soon after the discovery of high-T_c superconductors, we proposed a supertron, and have accumulated many experimental results including applications of the supertrons[1] to wigglers for free-electron lasers and electron-beam guiding for an induction accelerator. The supertrons, which are composed of high-T_c superconducting sintered materials (T_c = ~103 K for bismuth (Bi)-based materials), function well for single nanosecond intense electron currents when Bi-based sintered rings are used and do worst when yttrium (Y)-based melt processed ones are used. In order to explain these results, we proposed a ferrite-core model[1, 2] because there exist many similarities between the supertrons and ferrite cores. Supertrons and ferrite cores are both composed of grains of micrometer order and the intergrain connection is weak or insulated to induce not intergrain but intragrain currents. The grain size of the ferrite cores corresponds to the skin depth of magnetic fields at the frequency of operation. Therefore, the grain size should be smaller for the higher frequency operation. Conventionally sintered Bi-based materials are composed of grains of ~10 μm in diameter. To confirm the model, we recently showed[3] that Bi-based powder-pressed rings, which were composed of already sintered grains of ~1 μm in diameter and on which no additional sintering was done, effectively shielded nanosecond magnetic pulses and focused intense electron current pulses of ~340 keV, ~1 kA, and ~10 ns, below the T_c.

In another experiments,[4] a double-layered supertron that consisted of an inner Bi-based sintered tube and an outer Y-based melt-processed tube generated intense electron pulses of

1.4 ns in duration at 80 K. Since generating such a few nanosecond intense electron pulses, we have tried[5, 6] to generate shorter electron pulses using modified double-layered rings. In this report, we describe that the ferrite-core model can explain all the data for these double-layered rings.

2. Experimental devices

Figure 1 shows the experimental setup used. When high voltage pulses were applied to the beam diode consisting of a cold cathode and an anode that is composed of a superconducting ring and a copper heat sink, intense electron current pulses were field emitted from the cathode and were accelerated towards the anode. While propagating through the ring, the electron currents were focused. After emerging from the ring, the electron currents were detected with a collector that was placed in an evacuated atmosphere divided from the diode region with a 20 mm thick titanium foil. Neon gas was introduced[7] into the diode region at pressures of 0.1 Torr order to neutralize space charges of the intense electron currents. The self-magnetic field of the electron currents hit the inner surface of the ring, then diffused through the ring wall and arrived at the Rogowski coil that detects only the azimuthal magnetic field. The temporal behaviors of the signals detected with the collector and Rogowski coil were displayed on a high-speed oscilloscope (Tektonix SCD 1000 or DSA 602A, 1 GHz)

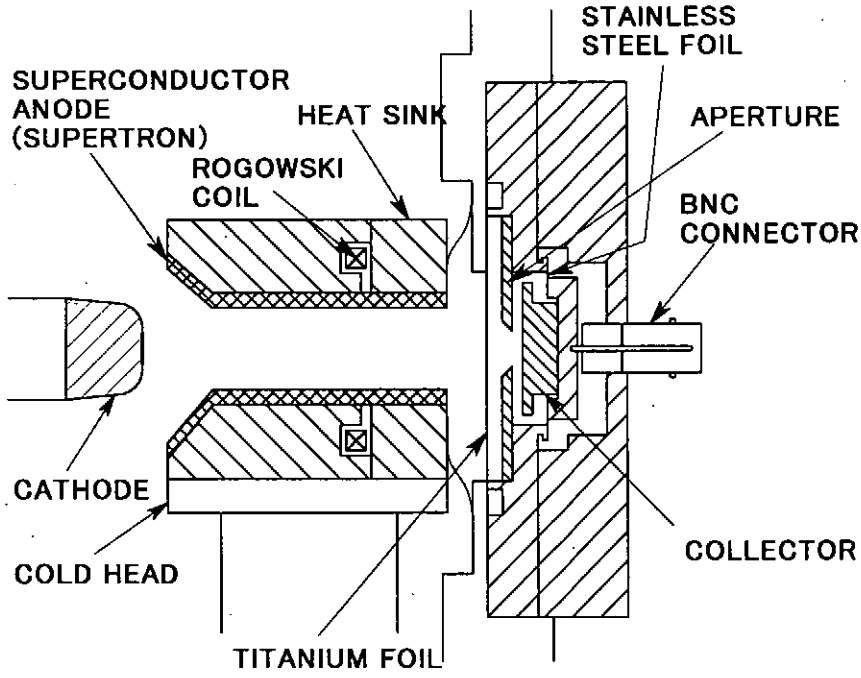

Fig. 1. Experimental setup.

Figure 2 depicts the rings examined. The rings had a 22 mm outer diameter and a 16 mm inner diameter. The Y-based tubes in Fig. 2 were made of Y-based melt-processed materials. The Rogowski coil is not drawn in Figs. 2(b) to 2(d), but was installed in the heat

sink when each ring was examined. Figure 2(a) shows a single layer ring made of 1 μm sized Bi-based powder-pressed tube.[3] Figure 2(b) (Ref. 6) presents a double-layered ring in which the Bi-based tube was made of 1 μm sized powder-pressed materials. Figure 2(c) (Ref. 5) indicates a modified double-layered ring having an inner Bi-based sintered tube. Figure 2(d) illustrates the double-layered ring that had an inner sintered tube and had previously generated 1.4 ns pulses[4] —the shortest ones ever obtained with supertrons.

3. Experimental results

For reference, Fig. 3 presents the shortest electron current waveform with a full-width at half-maximum (FWHM) of 1.4 ns at 80 K, for the ring in Fig. 2(d). After observing time evolutions of the electron currents, we summarized, in Fig. 4, the FWHMs of the waveforms for the rings in Fig. 2.

From Fig. 4, the single, 1 μm sized Bi-based powder-pressed ring generated the longest electron pulses. The second longest pulses were provided by the ring in Fig. 2(b) in which the inner tube was made of the powder-pressed materials. From these results, we can say that a ring made of the powder-pressed materials responds rapidly to external short magnetic pulses. The generation of these long pulses can be explained as follows: When the front of

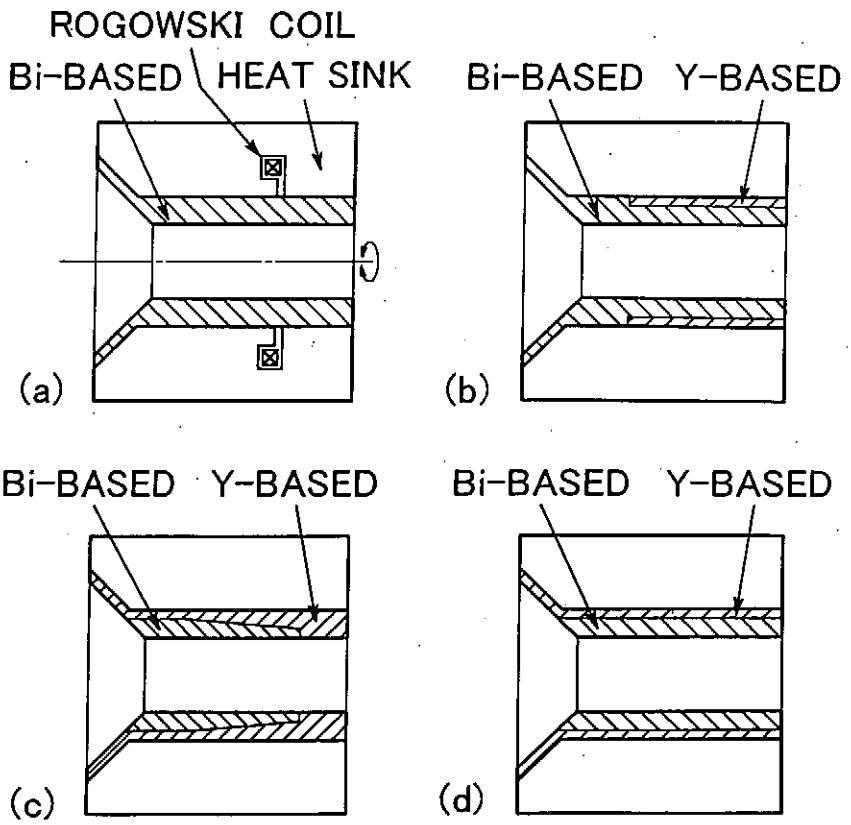

Fig. 2. Supertrons examined. The Y-based tubes were made of melt-processed materials. The Bi-based tubes in (a) and (b) were made of 1 μm sized powder-pressed materials, and those in (c) and (d) were made of sintered materials.

electron current beams enter the powder-pressed ring, the intracurrents (shielding currents) in grains build up rapidly in response to the entrance of the beams. This is because the grain size of the powder is ~1 μm in diameter, and the time constant of the electric circuit along which the intracurrents flow near the surface of the grains is less than 10^{-2} times that of the sintered grains of ~10 μm in diameter and is less than 10^{-6} that of Y-based melt-processed

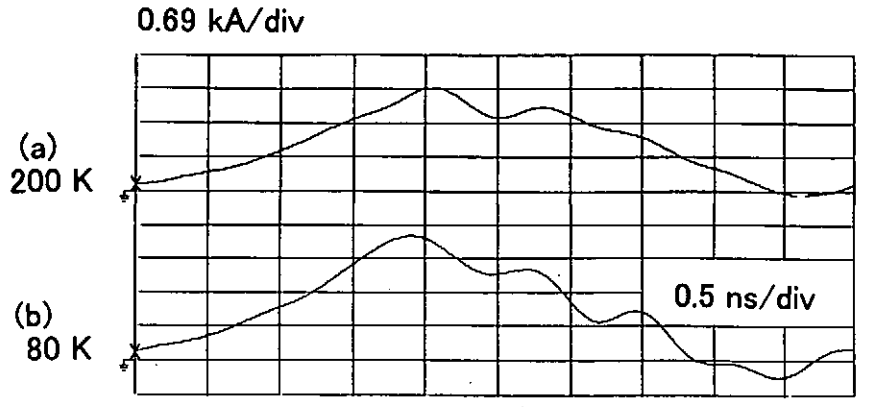

Fig. 3. Waveforms of intense electron current beams for the ring in Fig. 2(d).

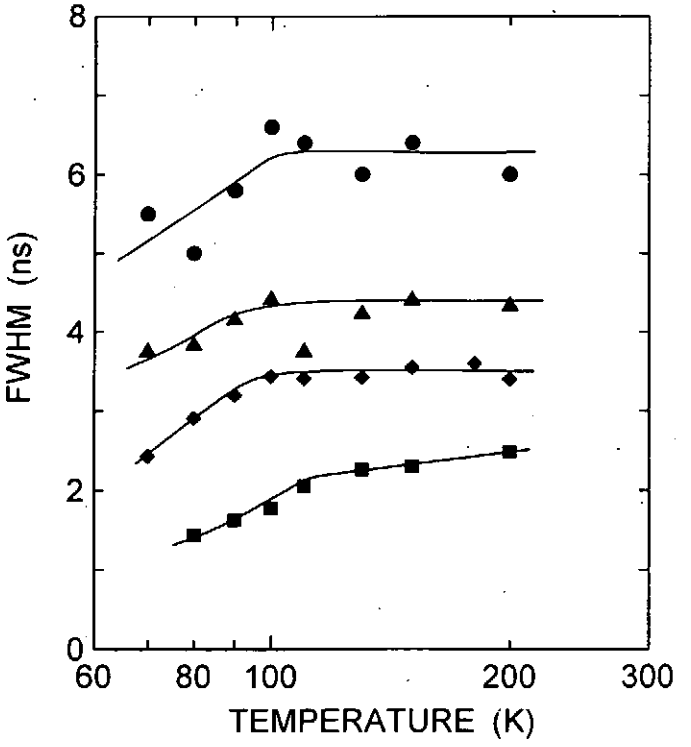

Fig. 4. Full-width at half-maximum (FWHM) of electron currents for the rings in Fig. 2. ●: 1 μm sized Bi-based powder-pressed ring, ▲: double-layered ring with an inner 1 μm sized powder-pressed tube, ◆ and ■: the inner tubes were made of Bi-based sintered materials.

materials of a few millimeters or more in diameter, because of the inductance of the circuit proportional to the squared values of the circuit diameters. Hence, the beam front is pushed back (compressed) owing to the repulsive force between the beam front charges and the rapidly induced intracurrents. By the same reasoning, when the beam tail leaves the ring, the attractive force between the beam tail charges and the intracurrents induced rapidly in opposite direction to that induced on entrance of the beams. Thus, the beam tail is pulled back (stretched). Accordingly, the pulse compression and stretching are to large extent cancelled, and the resulting pulse length do not change so much. Contrary, for the melt-processed materials consisting of much greater grains, when the beam tail leaves the ring, the intracurrents induced on entrance of the beam front cannot reverse their direction of flow and partially sustain the already induced intracurrents yet. Therefore, the repulsive force between the beam tail charges and the still sustaining induced intragrain currents compresses the beam tail. As a result, beam compression is realized. From this modeling, effective compression of pulse widths is probably realized with a ring composed of powder-pressed tube and sintered or melt-processed tube.

4. Conclusions

We explained the experimental results on the compression of intense electron current beams with superconducting rings (supertrons), based on the ferrite-core model. By accumulating further experimental investigations, we aim to realize subnanosecond, intense electron current beams.

References

1) H. Matsuzawa, "Novel magnetic applications of high-T_c bulk superconductors: Lenses for electron beams", J. Appl. Phys., **74**, R111-R131 [Erratum: J. Appl. Phys., **76**, 624 (1994)].

2) H. Matsuzawa, H. Kobayashi, H. Mochizuki, N. Yoneyama, A. Ohshima, S. Hirano, E. Mori, G. Horigome, Y. Ishida, and Y. Chino, "Experimental corroboration for a ferrite-core model of high-T_c bulk superconductor lenses (supertrons)", Jpn. J. Appl. Phys., **33**, 2526-2533 (1994).

3) H. Matsuzawa, K. Mikami, and A. Ibi, "Shielding of pulsed magnetic fields with already sintered 1 mm sized powder-pressed Bi-based superconducting rings", Appl. Phys. Lett., **78**, 3854-3856 (2001).

4) H. Matsuzawa, Y. Watanabe, K. Mikami, and K. Fukasawa, "Double-layered high-T_c superconducting tube lenses (supertrons) for electron beams", Jpn. J. Appl. Phys., **39**, 47-54 (2000); H. Matsuzawa, Y. Watanabe, K. Mikami, and K. Fukasawa, "Supertrons: high-T_c superconducting tube lenses for electron beam—a double-layered tube", Physica C, **335**, 87-91 (2000).

5) H. Matsuzawa, K. Mikami, T. Kibushi, T. Ishihara, and K. Kato, "Focusing characteristics of a modified double-layered high-T_c superconducting tube (Supertron) for charged particle beams", Physica C, **357-360**, 896-898 (2001).

6) H. Matsuzawa and K. Mikami, "Nanosecond generation of intense electron currents with high-T_c superconducting rings", Physica C (2002) (to be published).

7) H. Matsuzawa and T. Akitsu, "High-pressure operation of a beam diode for relativistic electron beams", J. Appl. Phys., **63**, 4388-4391 (1988).

GENERATION OF PULSED ION BEAM BY REPETITIVE PULSED POWER GENERATOR, "ETIGO-IV"

Y. Hayashi, W. Jiang, K. Yatsui

Extreme Energy-Density Research Institute
Nagaoka University of Technology
Nagaoka, Niigata 940-2188, Japan

ABSTRACT

Intense pulsed ion beam has beam successfully applied to various fields, such as magnetic and inertial confinement fusion, ion implantation, and thin film deposition, etc. Practical applications for intense pulsed ion beams require that the beam pulses would be generated at high repetition rate. This paper reports the development of the high repetitive pulsed ion beam by using repetitive pulsed power generator, "ETIGO-IV". It is capable of delivering, to a matched load, an output pulse of 400 kV in peak voltage, 13 kA in peak current, and 120 ns in pulsed length, at the repetition rate of 1Hz.

I. Introduction

The intense pulsed light ion beam has the features[1], of high energy, large current, and short pulse. Moreover, this intense pulsed ion beam has a short range in the solid target. Therefore, generating high temperature and high-density plasma on the target surface by ion beam irradiation on target is relatively easy. The intense pulsed light ion beam has been studied for about 30 years for the application to magnetic and inertial confinement fusion, as well as other applications. Pulse ion beam has also been interesting in the field of material development, such as thin film deposition and ion implantation, etc. In these applications, the repetition rate of the ion beam is a very important factor.

This paper reports initial experimental results of pulsed ion beam generation using pulsed power generator, "ETIGO-IV".

II. Repetitive Pulsed Power Generator, "ETIGO-IV"

In the experiment, repetitive pulsed power generator, "ETIGO-IV",[2] at Nagaoka University

of Technology was used. Figure 1 shows the schematic of "ETIGO-IV". This equipment mainly consists of three units; high-voltage supply unit; pulse forming unit and the central control unit. First, high-voltage pulse generated by the high-voltage supply unit is applied to the first step-up transformer ① and charges the intermediate energy storage capacitor (ESC), which is charged up to 240 kV. The energy accumulated at ESC is pulled out through the magnetic switch ① to a pulse forming line (PFL). Similarly, as the PFL is fully charged, the magnetic switch ② turns on to allow the pulsed power output of PFL to the load, through the second step-up transformer ②. If the load has a matched impedance, the output voltage, current, and pulse length are 400 kV, 13kA and 120 ns.

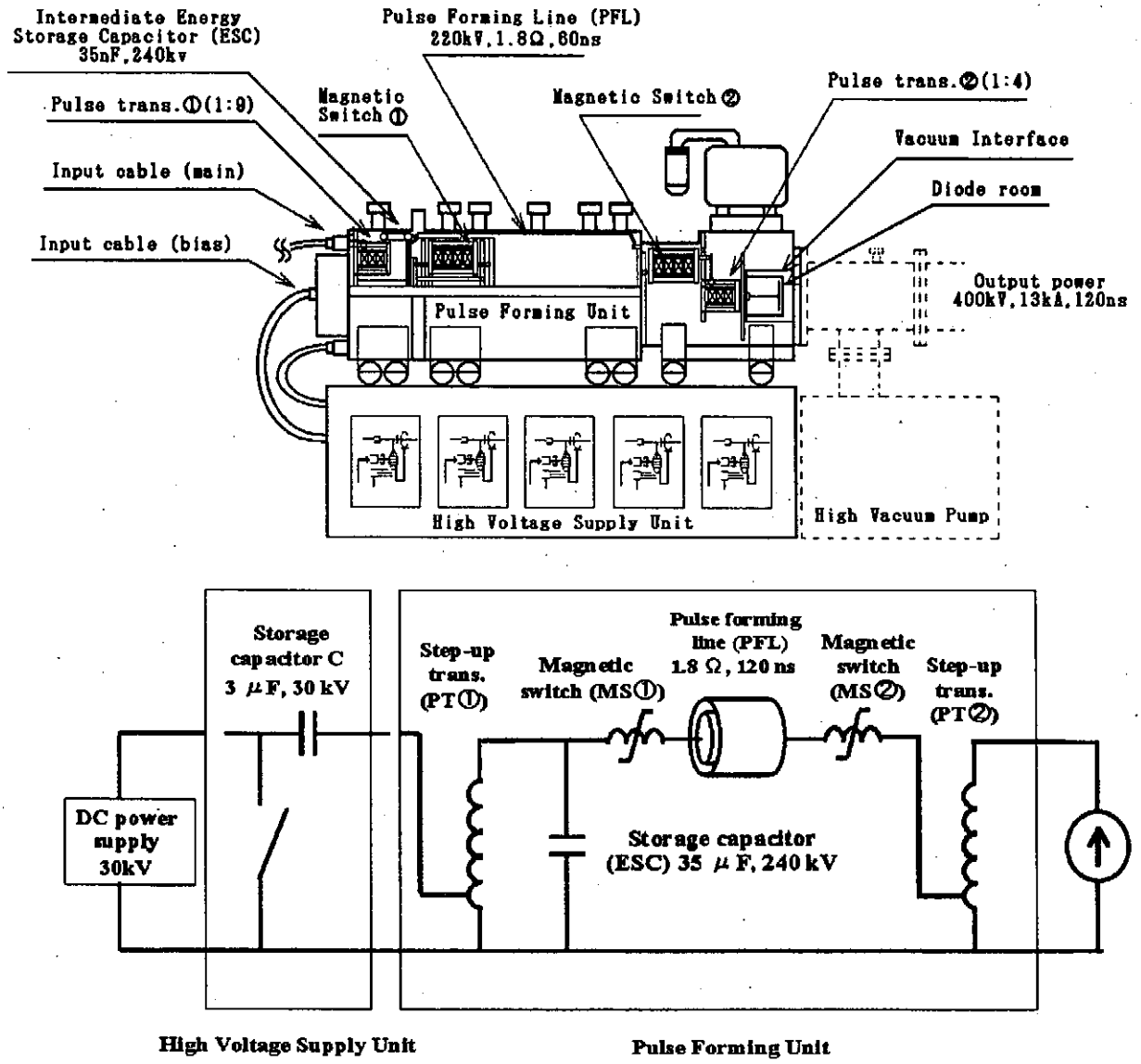

Fig. 1 Schematic of "ETIGO-IV".

Typical diode voltage and current waveforms are shown in Fig. 2. It is seen that the peak voltage 390 kV, peak current 13 kA, and pulse width 140 ns (FWHM) have been obtained.

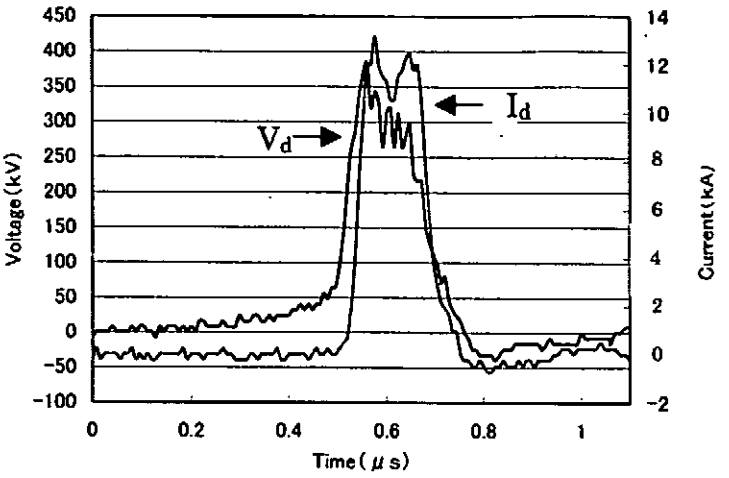

Fig. 2 Typical waveforms of diode voltage and current.

III. Ion Beam Diode

The schematic of the ion-beam diode is shown in Fig. 3. The diode is mounted at the output of "ETIGO-IV." The diode consists of an anode which has epoxy on its surface as ion source, a mesh cathode and intermediate mesh electrode between them. Distance between the anode and cathode (d_{AK}) = 10 ~ 30 mm, that between anode and intermediate electrode (d_{AI}) = 3 mm, and anode radius (r_A) = 80 mm.

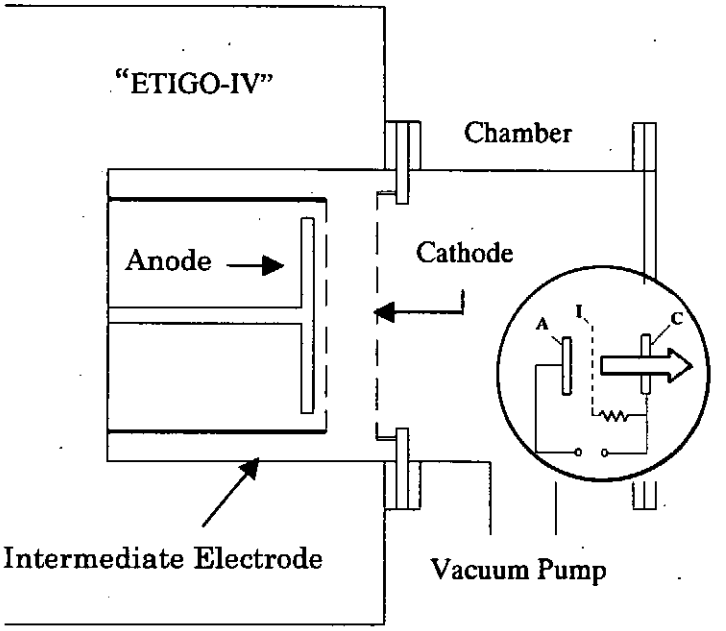

Fig. 3 Schematic of ion beam diode.

The principle of the ion-beam diode operation is shown in Fig. 4. and is explained as follows.

(1) When the high-voltage pulse (400 kV, 120 ns) generated by "ETIGO-IV" is applied between the anode-cathode gap, the electric field is first applied between anode-intermediate electrode, and the anode surface top is then ionized by surface flashover. The anode plasma is thus generated.

(2) The electric field between the intermediate electrode and the cathode accelerates the ions from the anode plasma.

The electrons are accelerated toward the anode from the cathode. Usually, the external magnetic field is applied to suppress electron flow. In this experiment, however, the surface electric field intensity of the cathode was kept as low as possible to reduce the electron emission. Since the plasma is formed on the anode surface, it will increase the ion beam efficiency without external magnetic field.

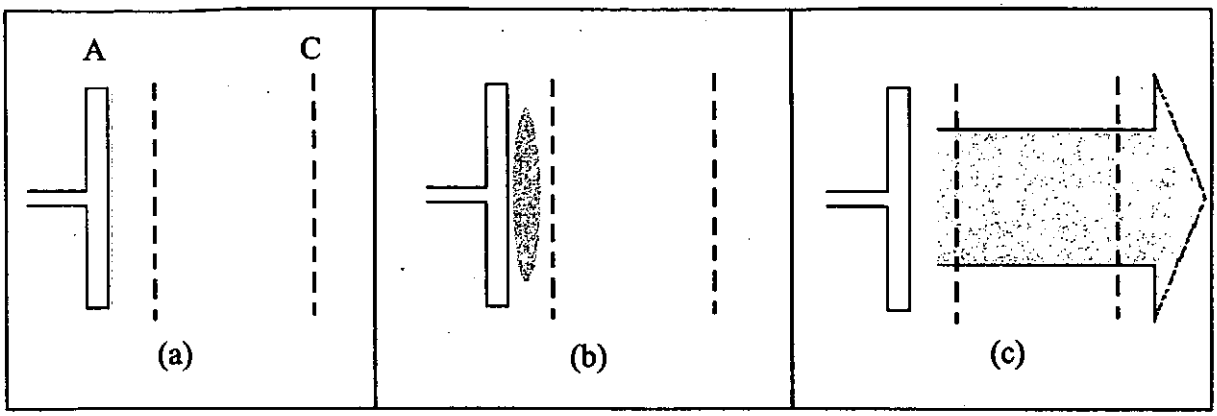

Fig. 4 Principle of ion beam diode : (a) initial state, (b) generation of surface plasma, (c) acceleration of ion beam.

In order to improve uniformity of the plasma formation on anode surface, the anode is splitted as shown in Fig. 5. Each piece of the anode is connected to the positive electrode through a resistor. It is expected that nonuniform anode current may induce different voltages across the resistors that will improve the current uniformity on the anode surface.

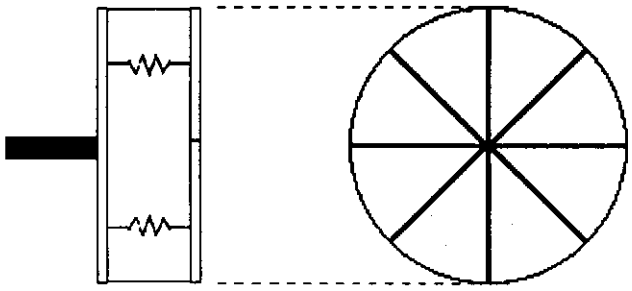

Fig. 5 Splitted anode design : (a) side view, (b) front view.

IV. Experimental Results

Figure 6 shows the diode voltage as a function of anode-cathode gap length. In Fig. 6, V_d goes up and I_d goes down if the anode-cathode gap is increased.

Figure 7 shows the diode impedance and power as a function of A-C gap length. In Fig. 7, the diode power takes the maximum at the gap length of 20 mm.

Figure 8 shows the beam pattern obtained by thermo-sensitive paper. It was settled at 10 mm behind the cathode. We see that nonuniform ion beam is obtained by using a standard anode. The beam size is seen to be approximately 70mm in diameter. On the other hand, when the

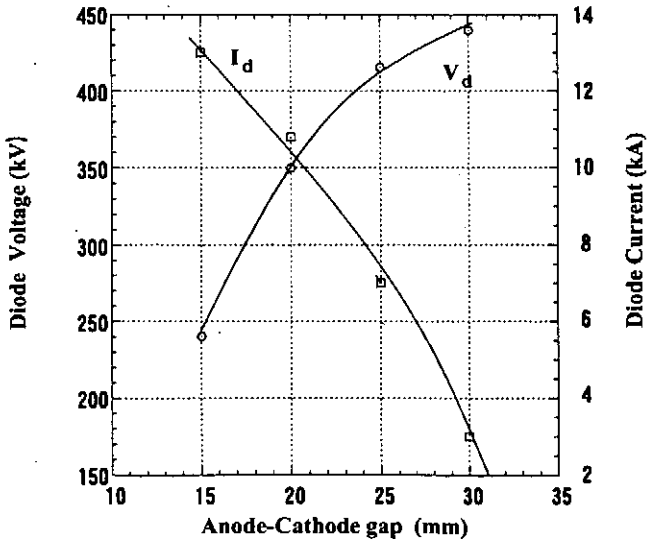

Fig. 6 Diode voltage and current as a function of A-C gap length.

splitted anode is used, relative uniform ion beam pattern is obtained while the ion beam current density is significantly reduced. It is probably caused by the lower plasma density on the anode surface for the splitted anode.

Figure 9 shows the beam energy as a function of anode-intermediate electrode gap length. Beam energy is measured by caloriemeter. At d_{ak} = 15 mm, it turns out that the ion beam energy becomes the maximum when the anode-cathode gap length is 2 mm.

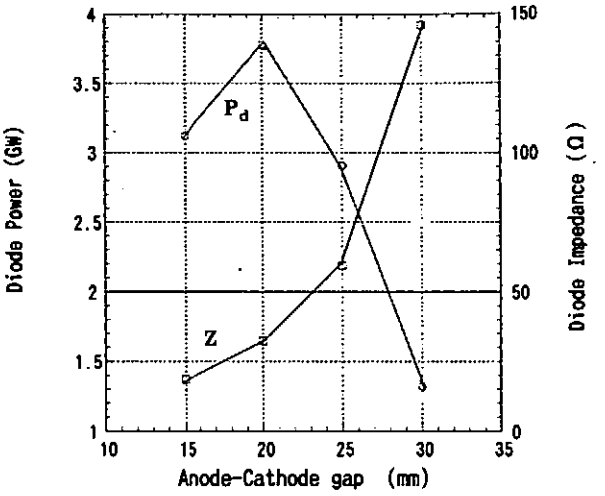

Fig. 7 Diode power and impedance as a function of anode-cathode gap length.

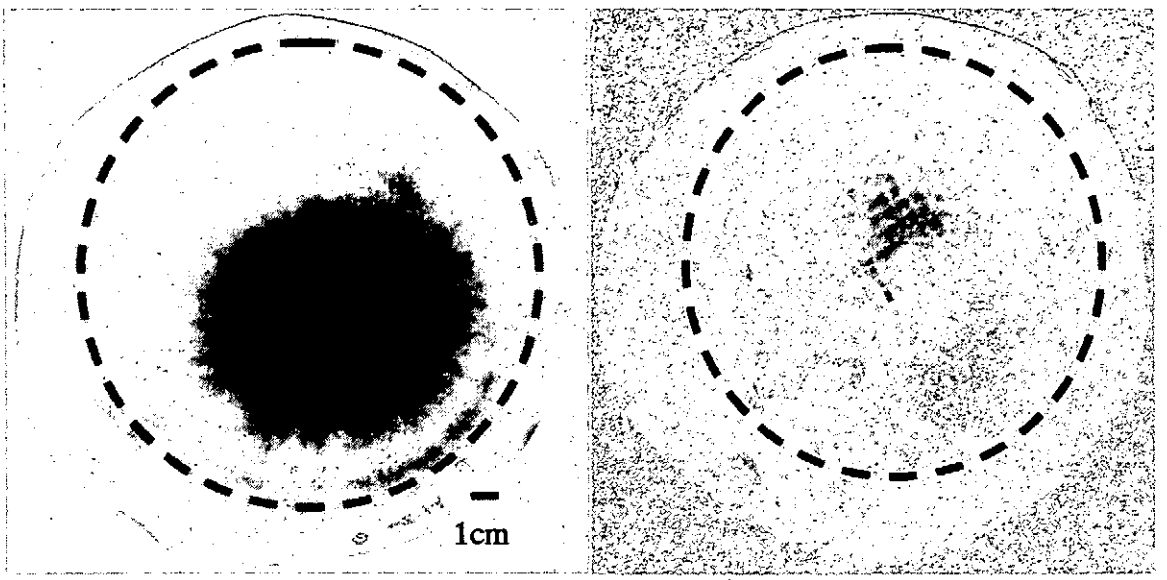

(a) (b)

Fig. 8 Ion beam patterns obtained by thermo-sensitive paper. Dotted line shows the anode size : (a) standard anode, (b) splitted anode.

At d_{ak} = 25 mm, on the other hand, the ion beam energy is obtained when the anode-cathode gap length is less than 1mm.

Figures 10 shows the beam energy as a function of anode-cathode gap. We see that the maximum beam energy of 30 J is achieved. In Figure 11 shows the beam energy and efficiency as a function of anode-cathode gap. We see that the maximum ion beam efficiency is about 9 %.

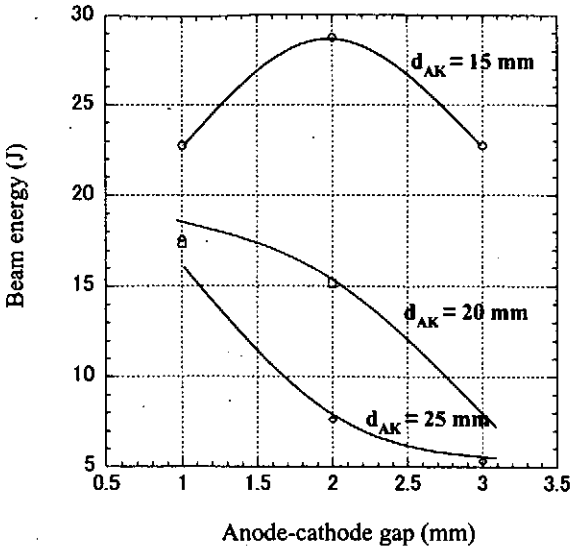

Fig. 9 Ion beam energy as a function of anode-intermediate electrode gap length.

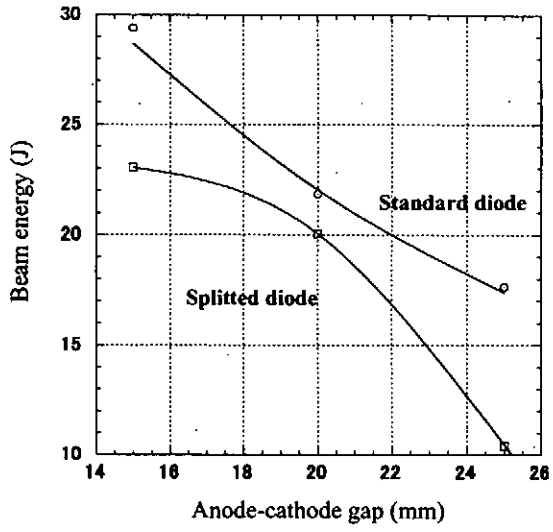

Fig. 10 Ion beam energy as a function of anode-cathode gap length.

V. Conclusions

We have studied the ion beam generation by repetitive pulsed power generator, "ETIGO-IV". We obtained the following conclusions.

1) Pulsed ion beam has been generated by using "ETIGO-IV".

2) At d_{ak} = 15 ~ 25 mm, the beam energy is maximized at d_{ab} = 1 ~ 3 mm.

3) The maximum ion beam energy is about 30 J, yielding the maximum ion beam efficiency of 9 %.

4) The beam size is approximately 70mm in diameter.

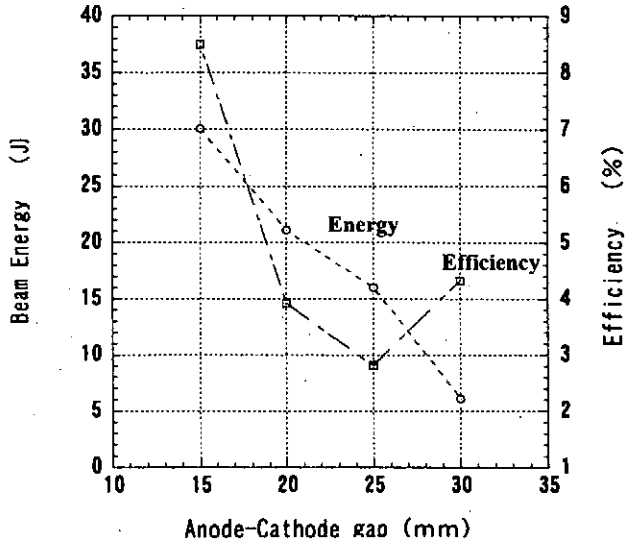

Fig. 11 Ion beam energy and efficiency as a function of anode-cathode gap length.

Refernces

1) S. Humphuries, Jr. : Nucl. Fusion 20 (1980) 1549

2) A. Tokuchi, N.Ninomiya, W. Jiang and K.Yatsui : Repetitive Pulsed-Power Generator "ETIGO-IV" , Proceedings of 13th International Conference on High-Power Particle Beams (BEAMS 2000), Nagaoka, Japan, ed. by K.Yatsui and W.Jiang (2000) 309-312

BEAM EMITTANCE AND OUTPUT WAVEFORMS OF HIGH-FLUX LASER ION SOURCE

M. Nakajima, M. Asahina and K. Horioka

Department of Energy Sciences, Tokyo Institute of Technology
4259 Nagatsuta, Midori-ku, Yokohama, 226-8502, Japan

M. Yoshida, J. Hasegawa and M. Ogawa

Research Laboratory for Nuclear Reactors, Tokyo Institute of Technology
2-12-1 Ookayama, Meguro-ku, Tokyo, 152-8550, Japan

Abstract

A laser ion source with short drift distance has been developed for a driver of heavy ion fusion (HIF). It supplies a copper ion beam of 200 mA (255 mA/cm^2) with duration of 400 ns and beam emittance is about 0.8π mm · mrad. Moreover it has fast rising(30 ns), flat-top current waveform and a potential to deliver pure charge states between $1^+ - 3^+$. Experimental results indicate that the laser ion source is a good candidate for the HIF driver.

1 Introduction

Heavy ion fusion (HIF) requires $< \pi$ mm · mrad emittance and ~A current ion beams with charge state of $1^+ - 3^+$. Generally, a static ion source is in a dilemma; although a good emittance demands low temperature, a high current needs high temperature. Additionally, the ion source must deliver beams with pure species and pure charge states, fast rise and flat top waveforms. [1]

It is difficult to extract such ion beams from gaseous state source because of the difficulty of keeping good vacuum. Thermonic sources offer a high brightness beam with a charge state limited to 1^+, but their ion flux levels are relatively low.

A pulsed solid vapor type like a vacuum arc source or a laser ion source may be a unique solution. The vacuum arc ion source has been overcoming two problems namely beam noise and poor reproducibility. Recently, up to 17 mA/cm^2 of Gd ions were produced with about 85% of the ions in 3^+ state, a pulse rise-time close to 1μs and beam fluctuation level of less than 3% rms. [2]

A laser ion source with short drift length is an attractive candidate. The laser ablation plasma expands spherically from one fixed point and long life of the components is expected owing to high energy efficiency.

To deliver low emittance beam with low charge states, plasma temperature must be low. To avoid prefill of plasma in the extraction gap, the drift distance must be short. For these two reasons, laser flux must be suppressed to the near threshold of plasma ablation. It is known ablation plasmas have high translational kinetic energy up to 100 eV in this region, so a sufficient plasma can be supplied.[3] The laser ion source is free from the above-mentioned dilemma and seems to have many advantages. Moreover, short drift length allows fast turn-on.

This ion source has some specific features;

- The ablation plasma expands spherically at a high rate , so its emitting surface does but its emissive ability decrease with the plasma expansion.
- The ablation plasma is nonstationary and has a density distribution.
- Ions of the laser ablation plasma exceeds sonic speed. Therefore, there is no need for a presheath formation because the Bohm condition is oversatisfied. This means the effective gap width can accommodate itself to balance the space charge limit current $j_{3/2}$ with the supplied one j_i .
- It may encounter three situations depending on the flux balance. If $j_i > j_{3/2}$, the screening potential accelerates electrons and therefore the emission boundary moves faster. If $j_i = j_{3/2}$, a virtual anode vanishes. If $j_i < j_{3/2}$, the plasma is pressured from an applied electric fields.

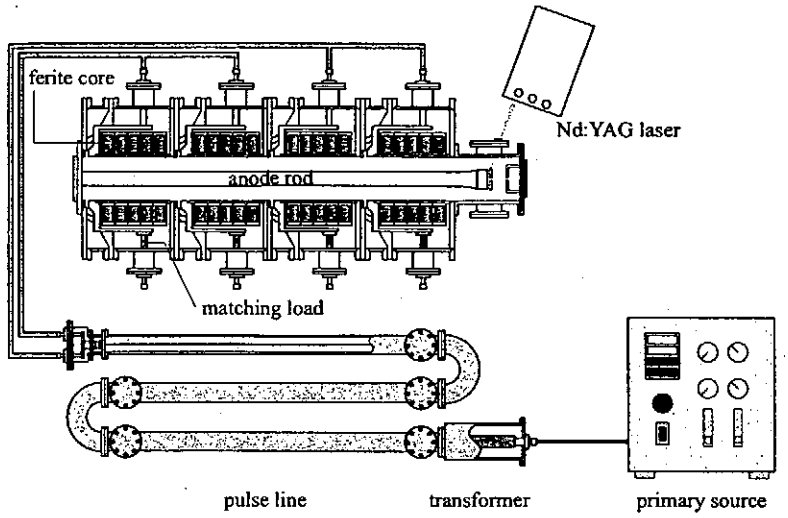

Figure 1: A Schematic view of experimental apparatus.

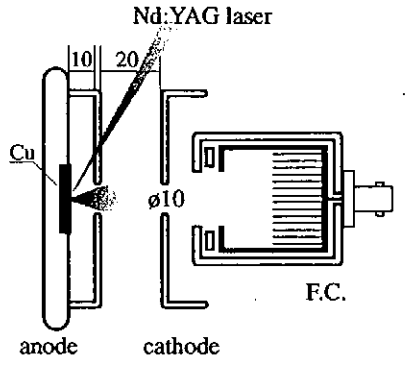

Figure 2: A schemaic view of laser ion source, extractor and Faraday cup.

Then we investigated the meniscus of the emitting surface and the beam waveforms under such temporally changing condition. Charge distributions were also measured as a function of the laser irradiation level.

2 Experimental Setup

A schematic diagram of experimental apparatus is shown in Fig.1. Four induction cavities made of ferrite cores, connected to a pulse forming line, can generate voltages up to 50 kV during 400 ns. Four cavities were stacked in a voltage adder configuration In our experiments, extraction voltage was about 140 kV with 400 ns duration.

Figure 2 shows a schematic view of our ion source. A copper rod was used as the laser target. The laser pulse focused on it with 300 mm focal length and incident angle of 70°. The spot size was 1.6×0.7 mm^2. We used a frequency doubled Nd:YAG laser with pulse duration of 7 nsec. The drift length was 10 mm. Both electrodes are made of plane SUS plates and each extraction hole was 10 mm in diameter. The gap length was 20 mm which was double the extraction hole diameter.

We used a Faraday cup with a honeycomb lattice structure which effectively suppressed the secondary

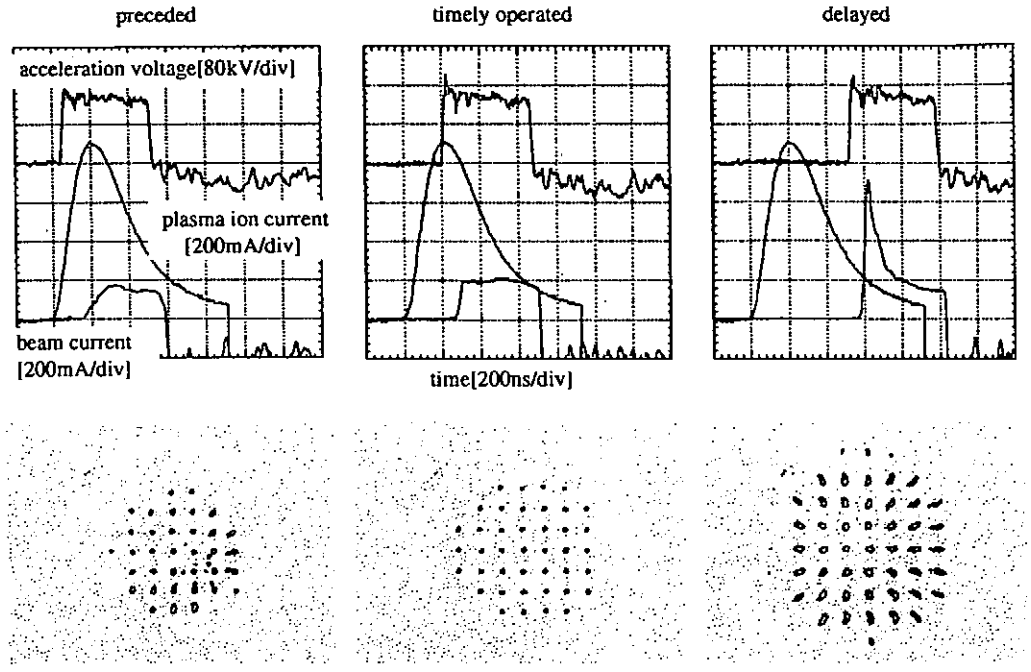

Figure 3: Typical beam waveforms and pepper-pot images at different timings(laser energy 53 mJ).

electrons. Emittance measurements were done using the pepper-pot method. [4] The beam images were amplified by a MCP gated with a 300 ns cable pulser. A tantalum pepper-pot plate with 50 μm thickness has holes of 200 μm in diameter and their interval are 2 mm. We performed the experiments under a background pressure of the order of 10^{-5} torr.

3 Results and Discussion

We measured waveforms and pepper-pot images of ion beams as a function of time duration between laser irradiation and voltage application. Figure 3 shows typical beam waveforms and pepper-pot images at three timings. When the timing of applying gap voltage is delayed, a part of the laser plasma prefills the gap. Thus the beam waveform is similar to that of the plasma opening switch. As shown with the pepper-pot images, ion beam is largely divergent because of strong space charge repulsion and moving emitting surface. When applying voltage preceded, rising of current was slow and waveform was not flat. A slightly divergent pattern which has a center point is overlaid on a medium divergent beam pattern. This pattern was observed whenever $j_i < j_e$. Here j_e shows the extracted ion current.

Surprisingly, when it was timely operated, beam waveform and emittance were close to the ideal; fast rising, flat-top waveform and the emitting surface behaved as if under the matching condition. The meniscus seemed to be very stable, and the emittance was kept small. This timing corresponded to the time when peak of plasma flux enter into the gap.

As shown in fig.5, a slightly divergent pattern could be observed when $j_i < j_e$. This pattern has a center point around the axis and is localized. And this pattern moves intensively as compared with a medium divergent beam pattern. A meniscus of the emitting surface may change when magnitude of relation between j_i and j_e turns. Though plasma flux around the axis is higher than at the periphery, electric field on the axis is stronger.

The divergence angle increases slowly when plasma current exceeds the beam one(see fig.4). The meniscus became to convex shape as laser fluence increasing, but it is insensitive to j_i. Emittance had the minimum value a little above the matching condition.

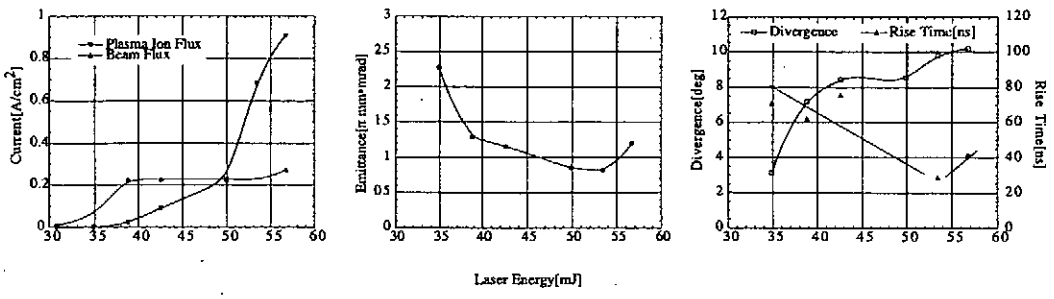

Figure 4: Ion beam current, emittance and rise time versus laser irradiation energy.

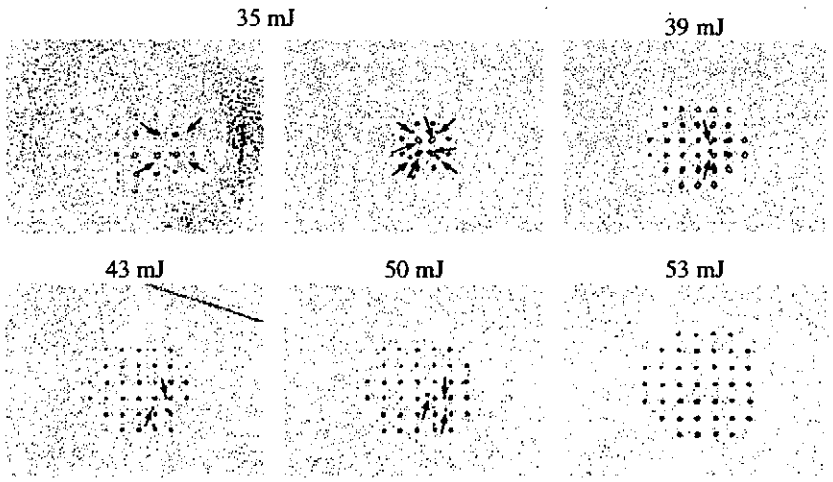

Figure 5: Beam images at timely operated condition.

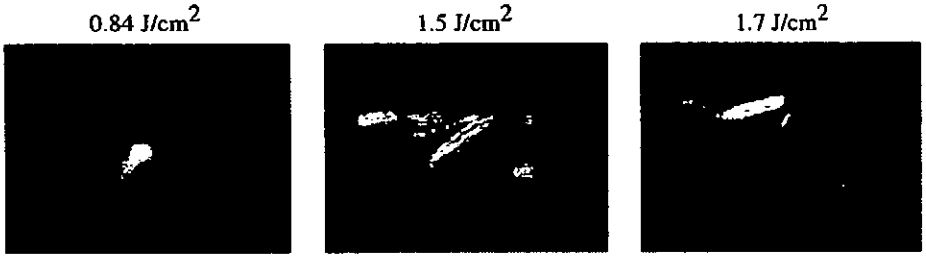

Figure 6: Streak images of magnetically deflected ions as function of laser fluence.

It is unexpected that the extracted beam current was larger than the supplied current (more than 10 times). As shown in fig.4, beam current limited by space charge law could be extracted above the laser energy of 39 mJ. A secondary ionization process, such as field-ionization of excited neutral atoms may be occurred around the anode region. It is noted that the laser intensity was just above the threshold of laser ablation plasma. In this regime the plasma temperature is low. If temperature is around 1 eV, three-body recombination is strong. [5] Rydberg atoms with high principal quantum number have long lifetimes and are expected to be ionized with electric field easily. [6] We don't know whether the stability of emitting surface is linked to these phenomena.

We observed charge distributions of magnetically deflected ions. Figure 6 shows streak images of the ion traces for various laser fluence. As shown, ion abundance depends on the laser fluence; under 1.5 J/cm^2, a major charge state is 1^+, and at the fluence over 1.7 J/cm^2, a charge state of 2^+ dominates.

4 Conclusions

We extracted a copper ion beam of 200 mA(255 mA/cm^2) with flat-top waveform, duration of 400 ns and 30 ns rise time. By adjusting the timing between laser plasma and the voltage application, the effect of temporal change of plasma flux to the meniscus of the emitting surface was not seen during 400 ns. At this operation condition, the beam emittance was about 0.8π mm · mrad.

References

[1] A. Anders, J. W. Kwan, "Arc-discharge ion sources for heavy ion fusion", Nucl. Instr. Meth. **A464**(2001)569-75

[2] N. Qi, et al., "Recent advances in high current vacuum arc ion sources for heavy ion fusion", Nucl. Instr. Meth. **A464**(2001)576-81

[3] G. C. Tyrrell, et al., "Energy-dispersive mass spectrometry of high energy ions generated during KrF excimer and frequency-doubled Nd:YAG laser ablation of metals", Appl. Surface Sci. **96-98** (1996) 227-32

[4] J. G. Wang, et al., "Beam emittance measurement by the pepper-pot method", Nucl. Instr. Meth. **A307**(1991)190-4

[5] R. W.Dreyfus, "Cu^0, Cu^+, andCu_2 from excimer-ablated copper", J.Appl. Phys. 69(1991)1721-9

[6] J. C. S. Kools, et al., "Concentrations and Velocity Distributions of Positive Ions in Laser Ablation of Copper" Appl. Phys. **B53**(1991)125-30

TRANSPORT WINDOW OF HIGH CURRENT HEAVY ION BEAMS IN A FINAL BUNCHER

Takashi Kikuchi, Mitsuo Nakajima and Kazuhiko Horioka

Department of Energy Sciences, Tokyo Institute of Technology, Nagatsuta 4259, Midori-ku, Yokohama, 226-8502, Japan

ABSTRACT

A longitudinal compression is indispensable in a final stage of the driver system for heavy ion inertial fusion. For the beam compression, an induction buncher applies the bunching voltage so as to make a considerable velocity tilt between the head and the tail of the beam bunch. At the first step of the design works for the beam transport line, the initial phase advance is decided to avoid resonance lines on the tune diagram. However, as the phase advance changes by the head-to-tail velocity tilt and the perveance increases during the beam bunching, the beam bunch sometimes reenters into the resonance condition. We estimate the dynamics of the bunching beams using a particle-core model. The stable transport region is discussed using a phase diagram. The transport window is illustrated in the diagram, as a function of the phase advance and the velocity tilt.

I. Introduction

In the field of heavy ion inertial fusion (HIF), an intense-heavy-ion beam is required for a suitable implosion of a fuel pellet.[1-3] In contrast to conventional particle accelerators, the required heavy ion beam has extreme parameters; the particle energy of ~10 GeV, the total beam current of ~100 kA and the pulse duration of ~10 ns. A longitudinal compression is indispensable in the final stage of the heavy-ion driver. In the region, the beam pulse duration must be compressed from ~100 ns to ~10 ns for the effective pellet implosion. For the beam compression, an induction buncher applies the bunching voltage so as to make a considerable velocity tilt between the head and the tail of the beam bunch.[4] Figure 1 shows one unit of the induction buncher system and the schematic of the beam bunching. The induction buncher

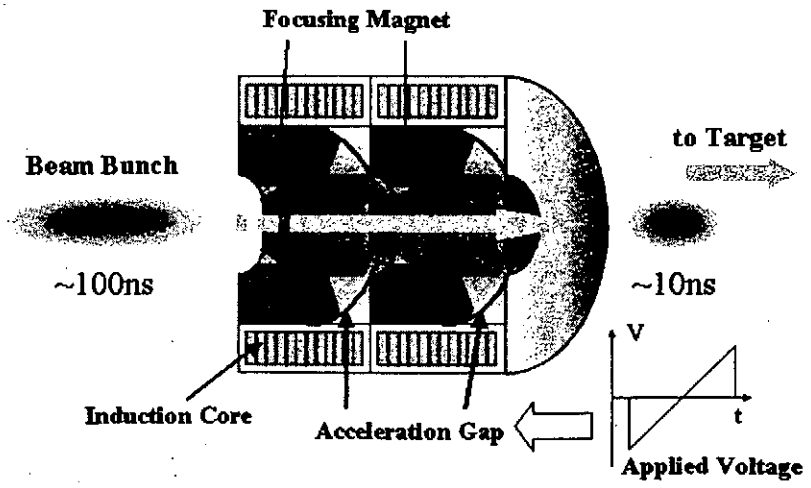

Fig.1: Induction buncher system and schematic of beam bunching.

unit consists of acceleration gaps and a focus-drift-defocus-drift (FODO) configuration lattice. At the first stage of design works for the beam transport line, the initial phase advance is decided to avoid resonance lines on the tune diagram. However, as the phase advance changes by the head-to-tail velocity tilt and the perveance increases during the beam bunching, the beam bunch reenters into resonance conditions. The transverse mismatch induced by those effects may cause a chaotic behavior, a halo formation and an emittance growth of the beam, during the compression process.

In this study, we estimate the dynamics and transport window of the bunching beams using a particle-core model (PCM).[5-7] The stable transport region is discussed on a phase diagram including a consideration about the envelope resonance of the mismatched beam. The transport window is illustrated in the diagram, as a function of the phase advance and the velocity tilt. Finally, we investigate the stability of particles during the bunching process using PCM calculations.

II. Descriptions of Beam Dynamics as Transverse and Longitudinal Envelope

We use beam envelope equations and PCM for the analyses of the bunching beam behavior. In this section, the longitudinal and transverse envelope equations are shown.[8] The transverse envelope dynamics X, Y along transport direction s are calculated by

$$\frac{d^2X}{ds^2} = -\tilde{k}_x X + \frac{2\tilde{K}}{X+Y} + \frac{\varepsilon_x^2}{X^3}, \tag{1a}$$

$$\frac{d^2Y}{ds^2} = -\tilde{k}_y Y + \frac{2\tilde{K}}{X+Y} + \frac{\varepsilon_y^2}{Y^3}, \tag{1b}$$

where ε_x, ε_y are the transverse emittances for the each direction. The K is the transverse modulated perveance expressed by,

$$\tilde{K} = \frac{q^2 N}{4\pi\varepsilon_0 mc^2 \tilde{\beta}^2 \tilde{\gamma}^3} \frac{1}{Z}, \tag{2}$$

where q is the charge of the beam ion, N is the number of the beam ion, ε_0 is the permittivity of free space, m is the mass of the beam ion, c is the speed of light, Z is the longitudinal beam envelope, β is the velocity divided by c and γ is the relativistic factor at the longitudinal beam position, respectively. The $\tilde{}$ indicates the modulated value due to the velocity tilt for the beam bunching. Here, the transverse confinement forces

$$\begin{aligned} \tilde{k}_x &= \tilde{k}h \\ \tilde{k}_y &= -\tilde{k}h \end{aligned}, \tag{3}$$

contain the periodical function h, in the case of FODO lattice which is given by

$$h = \begin{cases} 1 & (0 \le s \le \pi/2) \\ 0 & (\pi/2 < s \le \pi) \\ -1 & (\pi < s \le 3\pi/2) \\ 0 & (3\pi/2 < s \le 2\pi) \end{cases}, \tag{4}$$

and the transverse focusing parameter modulated by the velocity tilt is estimated as:

$$\tilde{k} = \frac{qB}{mc\tilde{\beta}\tilde{\gamma}a_q}, \tag{5}$$

where B is the magnetic force of the FODO lattice, a_q is the inner radius of the FODO magnet coil. Assuming the parabolic line charge density for the longitudinal direction as shown in

Table.1: Parameters for the calculations

Ion Species	Pb^{+1} (207.2 u)
Ion Number	2.5×10^{15}
Total Charge	0.4 mC
Pulse Duration	250 ns ⇒ 10 ns
Total Beam Current	1.6 kA ⇒ 40 kA
Beam Number	4
Current per Beam	400 A ⇒ 10 kA
Particle Energy	10 GeV (β~0.31)
Longitudinal Beam Length	23 m ⇒ 0.9 m
Initial Phase Advance	60 deg
Lattice Period	3 m

Fig.2, the longitudinal beam behavior can be described as:

$$\frac{d^2Z}{ds^2} = -k_z + \frac{K_L}{Z^2}. \tag{6}$$

Here k_z is the applied linear force for the beam bunching, K_L is the longitudinal perveance, which is defined by

$$K_L = \frac{3}{2}\frac{gNr_c}{\beta^2\gamma^5}, \tag{7}$$

g is the geometry factor and r_c is the classical particle radius. By numerically solving the above equations simultaneously, we can calculate the beam envelope dynamics.

Typical calculation results are shown in Figs.3 and 4. The longitudinal beam bunch behaviors are shown in Fig.3. Figure 4 shows the behavior of the transverse envelope along the transport direction at center (a) and at head (b) of the beam bunch. In this case, we use the parameters of Table.1 for the calculation. As shown in Fig.3, the beam bunch length is gradually shortened with the increase of the applied velocity tilt. In Fig.4(a), it is found that the envelope of the beam center is slightly spread due to the perveance increase. However, the envelope of the beam head shows the mismatched oscillation, because of the large head-to-tail velocity tilt, as shown in Fig.4(b). The mismatch oscillation of the beam envelope may induce

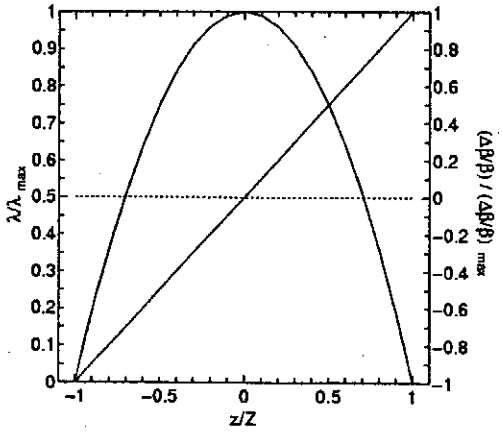

Fig.2: Distributions of longitudinal line charge density and velocity tilt ratio for bunching beam. The above values are normalized by maximum values.

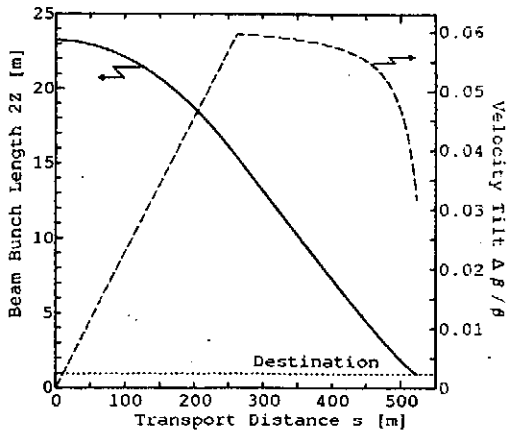

Fig.3: Longitudinal bunch length and velocity tilt during beam compression.

the irreversible emittance growth and the halo formation.[5-7)]

III. Transport Window and Results of PCM Calculation

In this section, we discuss a stably transportable region of the bunching beam on the phase space. It is well known that if the betatron tune of the beam enters to the forbidden values, the beam becomes resonantly unstable.[8)] The phase advance of 60deg is typical value of the resonance conditions. Usually, the initial phase advance (without space charge) σ_0 is depressed by the space charge effect. From this, the space charge depressed phase advance σ is automatically avoided from the resonance line even if the σ_0 is set at the resonance value. However, bunching beams with large compression ratio have inevitably large velocity tilts, and the phase advance is considerably modulated by the velocity tilt. The relations of the FODO lattice parameters and the phase advance are given as;

$$\tilde{k} = \frac{\beta\gamma}{\tilde{\beta}\tilde{\gamma}} k , \tag{8}$$

$$\cos\sigma_0 = \cos\theta\cosh\theta + \frac{L}{\ell}\theta(\cos\theta\sinh\theta - \sin\theta\cosh\theta) - \frac{1}{2}\left(\frac{L}{\ell}\right)^2 \theta^2 \sin\theta\sinh\theta , \tag{9}$$

$$k = \left(\frac{\theta}{\ell}\right)^2 , \tag{10}$$

where ℓ is the length of the focusing space (F or D in FODO), L is the length of the drift space (O in FODO) and θ is the focusing strength of the magnetic lens.

The modulated phase advance by the velocity tilt is shown in Fig.5. Figure 5(a) shows the modulated phase advance as functions of the velocity tilt, at the head and the tail of the bunching beam. As Fig.5(a) shows, the phase advance at the beam head is increased with the velocity tilt. As mentioned previously, the phase advance is depressed by the space charge due to the velocity tilt, and the phase advance increased may cause the resonance reentrance. Consequently, the stable transport region is restricted by the resonance reentrance condition as a function of the velocity tilt. Figure 5(b) shows the transport window derived in this study. As expected, the beam transport with the initial phase advance of 60deg tends to cause the beam instability. In contrast to the case of the σ_0=60deg, the beam is expected to be transported with stable condition in the case of σ_0=56deg and $\Delta\beta/\beta \leqq 0.1$.

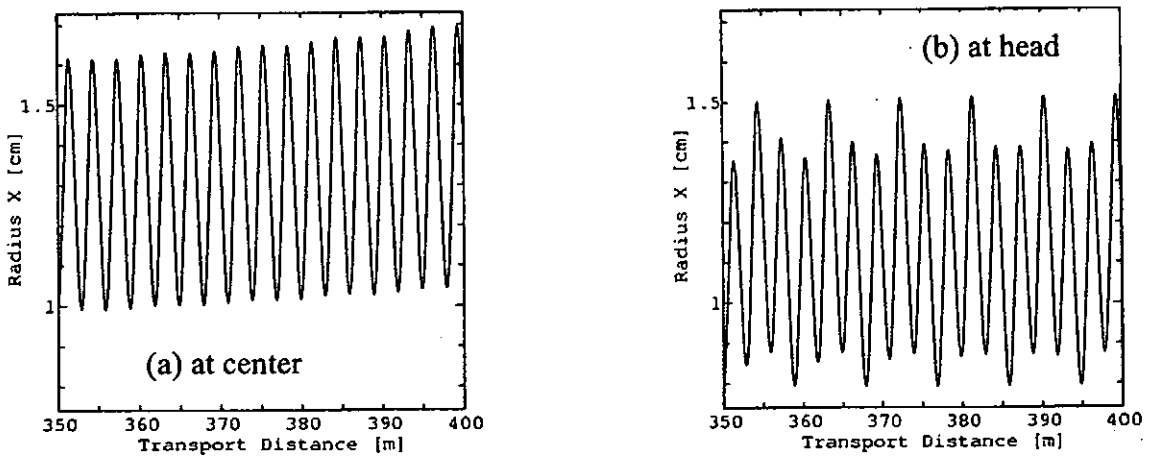

Fig.4: Typical results for transverse mismatch of bunching beam envelope. (a) shows beam envelope at the center, and (b) shows beam envelope at the head.

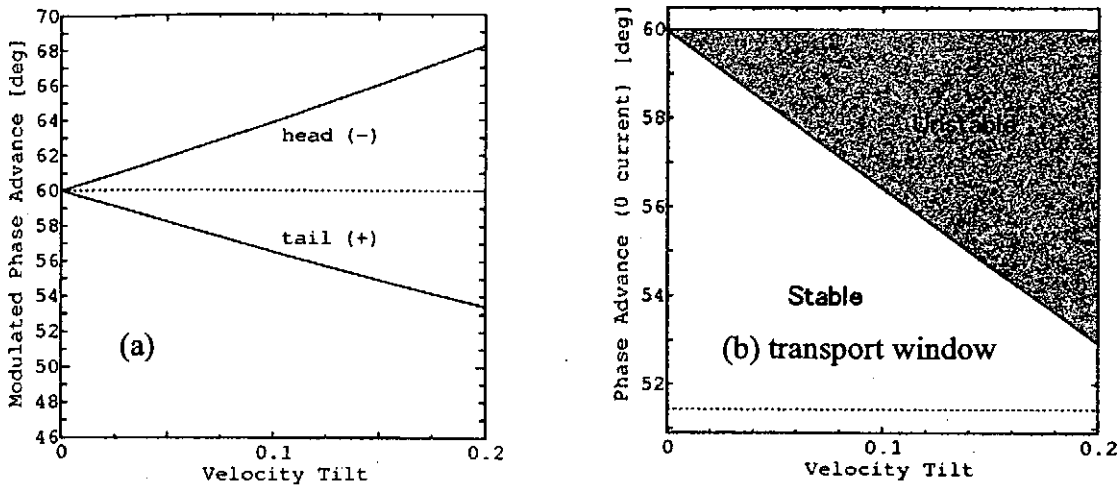

Fig.5: Expected phase advance modulated by velocity tilt (a) and transport window as a function velocity tilt (b).

Based on the above consideration, we carried out the PCM calculation. We investigate the stability of the beam particles on the phase space. For example, the test particle equations of x-direction are written by

$$\frac{d^2x}{ds^2} = -\tilde{k}_x x + \begin{cases} \dfrac{2\tilde{K}}{X(X+Y)}x & (|x| \le X) \\ \dfrac{\mathrm{sgn}(x)\cdot 2\tilde{K}}{|x| + \sqrt{x^2 + Y^2 - X^2}} & (|x| > X) \end{cases}, \tag{11}$$

where x is the position of a beam particle and

$$\mathrm{sgn}(x) = \begin{cases} +1 & (x > 0) \\ -1 & (x < 0) \end{cases}. \tag{12}$$

We can also calculate about y in the same manner, which is the position of a test particle along the y-direction. Using the above relations, we can investigate the particle evolutions of the bunching beam within the framework of PCM approximation. The beam instability is indicated by the scattering of test particles on the phase space. In this study, the perveance and

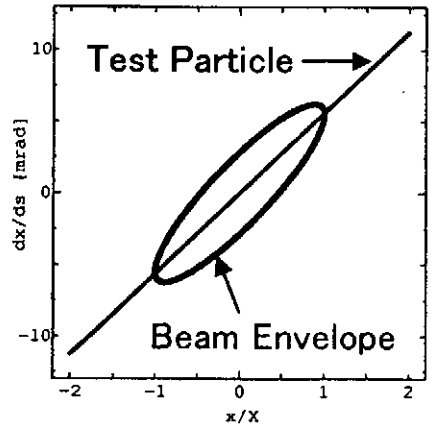

Fig.6: Initial distribution of beam envelope and test particles on phase space for x-direction.

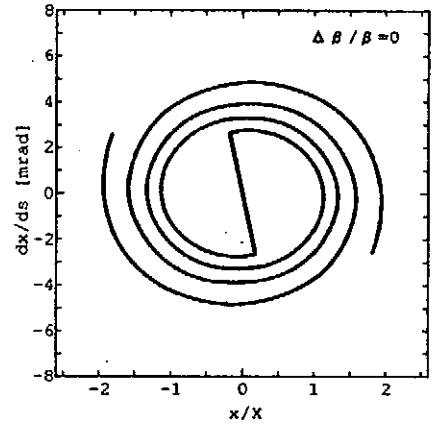

Fig.7: Typical example of test particle distribution on phase space in the case of matching beam after 150 lattice periods.

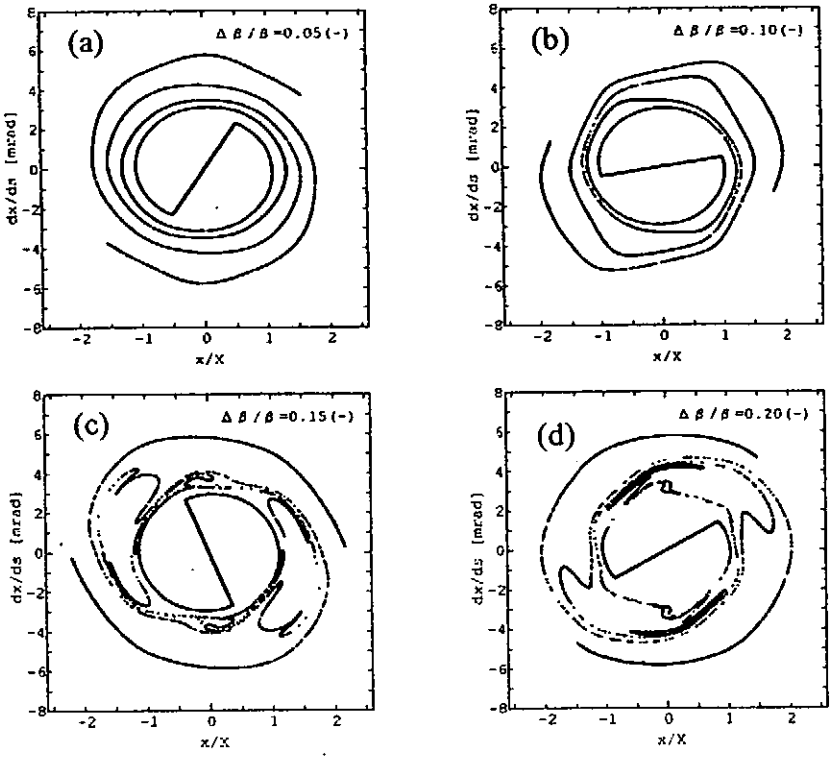

Fig.8: PCM calculation results after 150 lattice periods in the case of σ_0=60deg at the beam head. $\Delta\beta/\beta$ are (a) at 0.05, (b) at 0.10, (c) at 0.15 and (d) at 0.20, respectively.

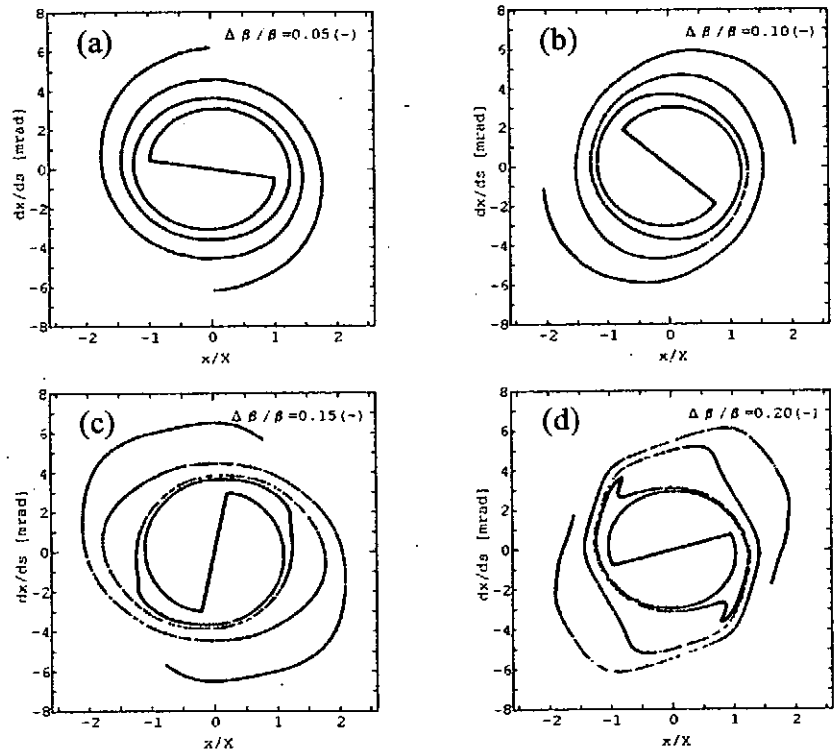

Fig.9: PCM calculation results after 150 lattice periods in the case of σ_0=56deg at the beam head. $\Delta\beta/\beta$ are (a) at 0.05, (b) at 0.10, (c) at 0.15 and (d) at 0.20, respectively.

the velocity tilt are assumed as constant during the beam transport for the clarification of the velocity tilt effect. Figure 6 shows the initial test particle distribution and beam envelope on the x-x' phase space. In the case of matched beam, the test particles are periodically evolved on the phase space as shown in Fig.7. However, as mentioned earlier, the velocity tilt causes the resonance reentrance, and the interaction between the resonance effect and the envelope mismatch due to the large velocity tilt induces the irregularity of the particle behaviors as shown in Fig.8. On the other hand, the bunching beam with σ_0=56deg can be stably transported as Fig.9 shows, in contrast to the case of σ_0=60deg. Although, detailed behaviors of the intense and highly bunched beam including the emittance growth must be investigated by more sophisticated models, these results indicate that the transport window as shown in Fig.8 can predict the bunching beam stability on the phase space.

IV. Conclusion

We investigated the transport window of the high current bunching beam using the beam envelope and PCM calculations. The stable transport region was estimated on the phase diagram, with a consideration about the envelope mismatch by the resonance. The transport window was illustrated in the diagram as a function of the phase advance and the velocity tilt. Using PCM calculations, we demonstrated the beam particle stability. As a result, it is found that those criterions can practically predict the transportability of the bunching beam. We believe that the criterion based on the transport window is useful as the first step evaluation of the transport line design for the final buncher in HIF.

References

1) J.J. Barnard, *et al.*, "Recirculating Induction Accelerators as Drivers for Heavy Ion Fusion", Phys. Fluids B, Vol.5 No.7, pp.2698-2706. (1993).
2) M. Reiser, "Physics of Intense Charged Particle Beams for Heavy Ion Inertial Fusion", Fusion Eng. Design, Vol.32-33, pp.133-140. (1996).
3) I. Hofmann, "Recent Developments in Heavy Ion Driver Studies at GSI", Proc. First Int. Conf. on Inertial Fusion Sci. and Applications, Bordeaux, pp.12-17. (1999).
4) M. Watanabe, M. Nakajima and K. Horioka, "Voltage Modulation and Repetitive Operation of Induction Ion Accelerator", Nucl. Instrum. Methods A464, pp.440-444. (2001).
5) J.-M. Lagniel, "Chaotic Behaviour and Halo Formation from 2D Space-Charge Dominated Beams", Nucl. Instrum. Methods A345 pp.405-410. (1994).
6) Q. Qian, R.C. Davidson and C. Chen, "Halo Formation Induced by Density Nonuniformities in Intense Ion Beams", Phys. Rev. E Vol.51 No.6 pp.5216-5219. (1995).
7) M. Ikegami, "Particle-Core Analysis of Mismatched Beams in a Periodic Focusing Channel", Phys. Rev. E Vol.59 No.2 pp.2330-2338. (1999).
8) M. Reiser, *Theory and Design of Charged Particle Beams*, Wiley, New York, (1994).

CHARACTERISTICS OF ENERGTIC IONS PRODUCED IN PLASMA FOCUS

M.Shiotani, K.Takao, T.Honda, I.Kitamura, T.Takahashi, and K.Masugata

Faculty of Engineering, Toyama University, 3190, Gofuku, Toyama, 930-8555, Japan

ABSTRACT

Characteristics of ion beams produced in the Mather type plasma focus (P.F) were studied experimentally to apply the beam to materials processing. The plasma focus was pre-filled with H_2 of 250 Pa, or mixture of H_2 (180 Pa) and N_2 (20 Pa). At 400 mm downstream from the top of the anode on the electrode axis, ion beam of current density ≈ 650 A/cm^2, pulse width ≈ 200 ns (FWHM) was observed when filling gas of H_2 was used. The ion species and energy spectra were evaluated by a Thomson parabola spectrometer (TPS). For protons of energy in the range of 0.1 - 1 MeV are observed when P.F was filled with H_2, where as protons and variety of nitrogen ions ($N^{(1-5)+}$) of energy in the range of 0.4 - 6 MeV are observed when using mixture gas. From the evaluation of the energy spectrum of nitrogen ions we see that the spectrum has a peak on 1 or 2 MeV. To evaluate the irradiation effect on materials, amorphous silicon films were irradiated by the ion beam and we see that amorphous silicon layers are crystallized by the irradiation.

I. Introduction

Strong emission of energetic ions, electrons, and x-ray are known to be emitted from the pinch plasma produced in plasma focus (P.F.). Especially, the energetic ions have following characteristics and expected to be applied to materials processing. [1-5]

a) High energy ions of energy ranging from 100 keV to several MeV are produced
b) Ion beam is obtained by relatively low voltage pulsed power systems.[6]
c) The power density and the brightness of the beams are very high. [1]
d) The ion species can be controlled by changing the filling gas.

To apply the ion beam to materials processing we have evaluated the characteristic of the ion beam. In addition, amorphous silicon films were irradiated by the ion beam to evaluate the irradiation effect on materials.

Ⅱ. Experimental apparatus

Figure 1 shows a schematic of the Mather type P.F. was used in the experiment. The P.F. consists of an anode, a rod cathode, and a glass insulator. The anode is a cylindrical copper electrode and the length and the diameter are 300 mm and 50 mm, respectively. To reduce the production of impurity ions and to reduce the damage of the electrode, the anode has a hollow shape top.

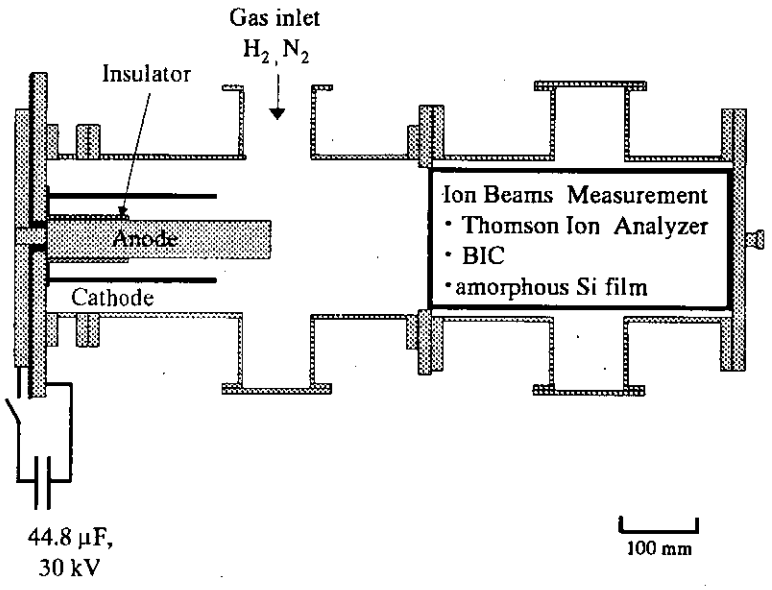

Fig. 1. Schematic of the experimental system.

The cathode consists of 24 copper rods of diameter 10 mm, length 230 mm and the effective inner diameter of the cathode is 100 mm. The insulator is made of glass and the length and the outer diameter are 125 mm and 55 mm, respectively.

To drive the P.F. a capacitor bank of capacitance 44.8 μF, maximum charging voltage 80 kV was used, which is connected to the P.F. through 28 of coaxial cables. In the experiment the charging voltage of the capacitor bank was fixed to 30 kV. The vacuum chamber was once evacuated to $< 7\text{x}10^{-3}$ Pa and after that filling gas was introduced. In the experiment pure hydrogen (250 Pa), and mixture gas of hydrogen (180 Pa) and nitrogen (20 Pa) were used as the filling gases.

To evaluate ion current density of the beam (J_i), biased ion collector (BIC) was used, which was placed in the gas filled vacuum chamber. The BIC has a cup electrode inside the grounded body and the ions are injected into the cup electrode through an aperture of diameter = 0.3 mm . The electrode was biased to -1 kV to remove commoving electrons.

For the measurement the species of ions and their energy spectra, Thomson parabola spectrometer (TPS) was used. The TPS is constructed of a first pinhole, a second pinhole, a magnetic deflector, an electrostatic deflector, and a ion track detecting film of CR-39, the detail of which is shown in the leterature[1].

Ⅲ. Experimental results

Figure 2 shows typical waveforms of the discharge current (I_d) measured by a Rogowski coil, and J_i measured at z = 400 mm downstream from the top of the anode on the electrodes axis. In the experiment the P.F. was pre-filled with pure hydrogen. As seen in the figure, I_d has a peak of 600 kA at t = 1.55 μs and after that 100 kA of current dip is observed, which suggest the strong pinch of the plasma. Ion current density rises sharply at t = 1.6 μs and a peak value of 650 A/cm^2 is observed with pulse width of 200 ns (FWHM).

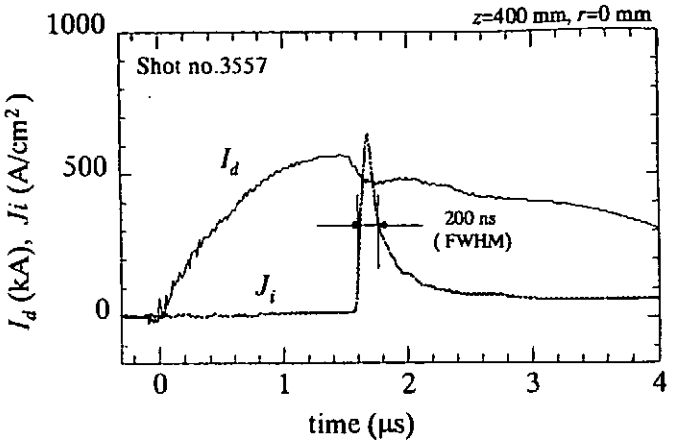

Fig. 2 Typical waveforms of I_d and J_i .

Figure 3 shows the distribution of the peak value of J_i obtained by BIC. As seen in the figure, at z = 200 mm, very large value of J_i = 3600 A/cm^2 is observed on the axis (r = 0).

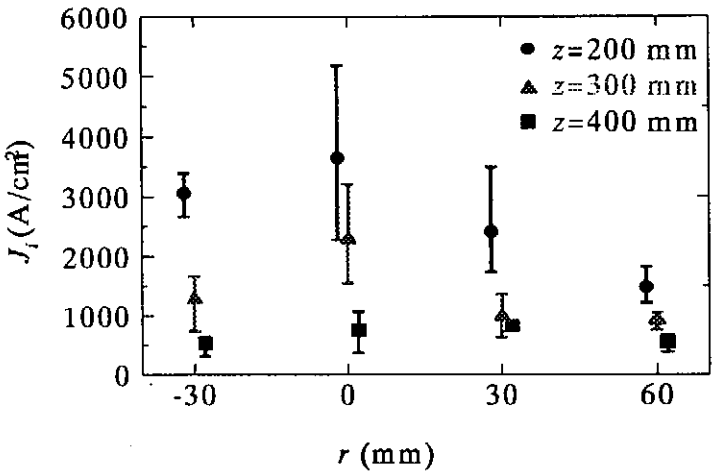

Fig. 3 Space distribution of J_i.

Figure 4 shows the ion track pattern obtained by TPS. As seen in the figure, strong

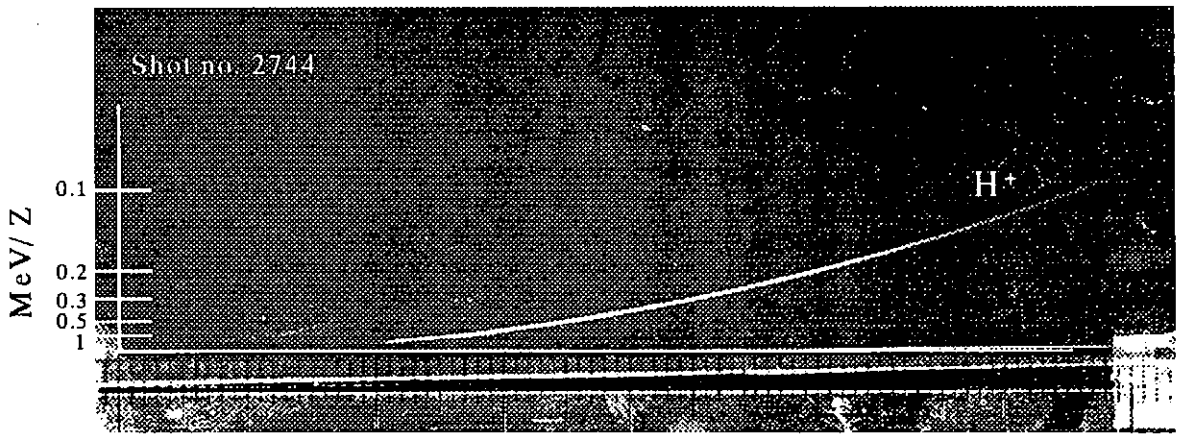

Fig. 4. The track pattern obtained by TPS. The filling gas was H_2 250 Pa.

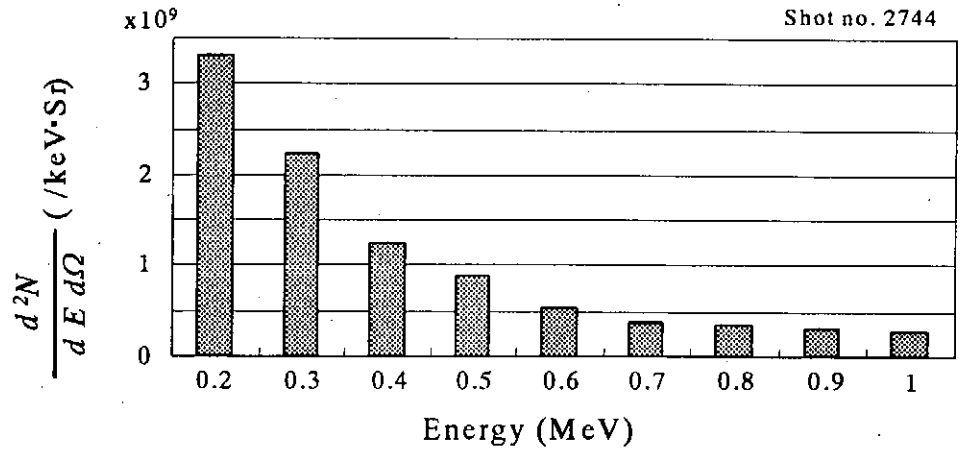

Fig. 5. Energy spectrum of protons evaluated from Fig. 4.

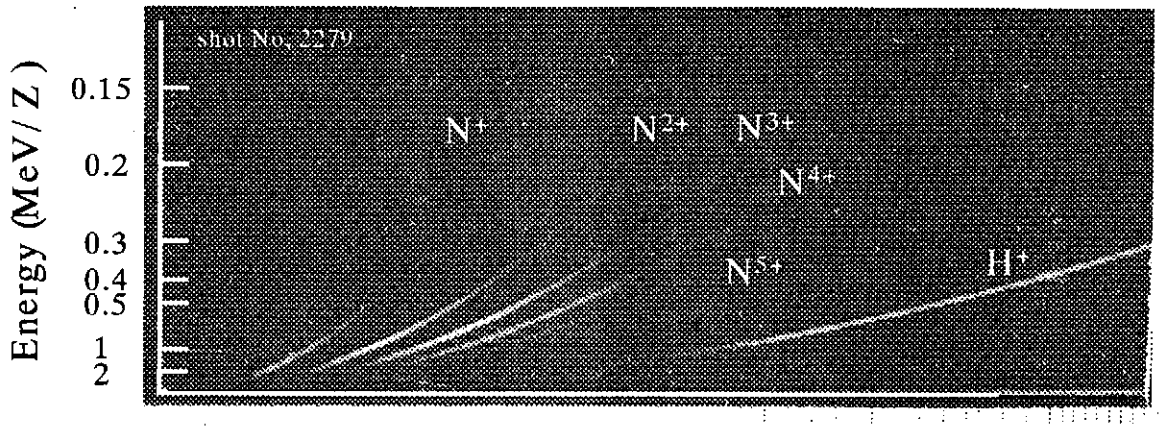

Fig. 6. The track pattern obtained with the TPS at mixture gas.

trace of protons is observed with weak trace of impurities. The energy of the protons is in the range of 0.1 - 1 MeV.

From the evaluation of ion track densities in Fig. 4, we have evaluated the energy spectrum of protons, which is shown in Fig. 5. From the figure, we see that proton flux decreases with increasing energy.

Figure 6 shows the track pattern obtained with TPS when mixture of H_2 and N_2 was used. As seen in the figure, variety of nitrogen ions ($N^{(1-5)+}$) are observed with protons. The energy of nitrogen ion is in the range of 0.4 - 6 MeV. In addition, no impurity ions was observed in the condition.

Figure 7 shows the energy spectra of nitrogen ions obtained from Fig. 6. As seen in the figure the each energy spectrum has a peak around 1 or 2 MeV. In addition we see that the average energy tend to be higher for highly ionized ions.

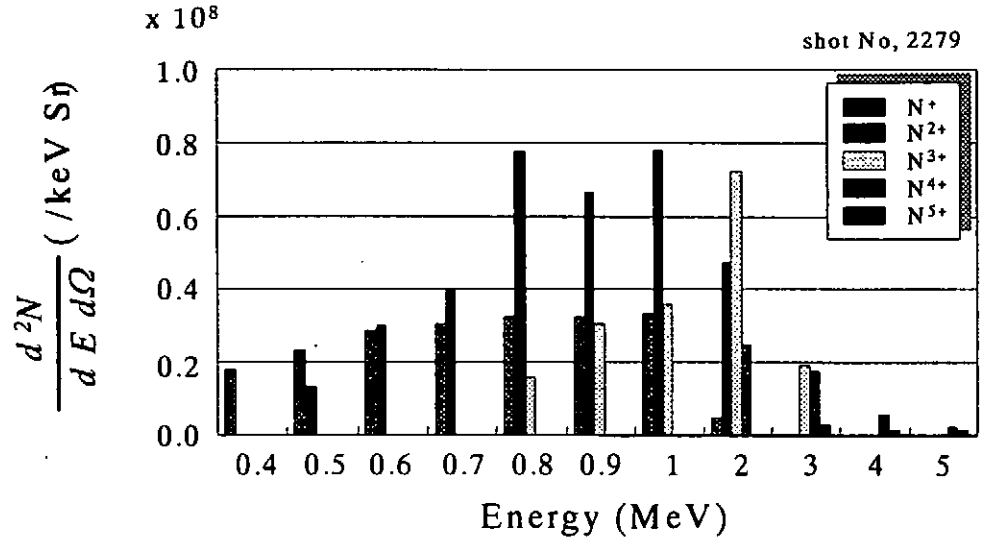

Fig. 7. Energy spectrum of nitrogen ion when mixture gas is used.

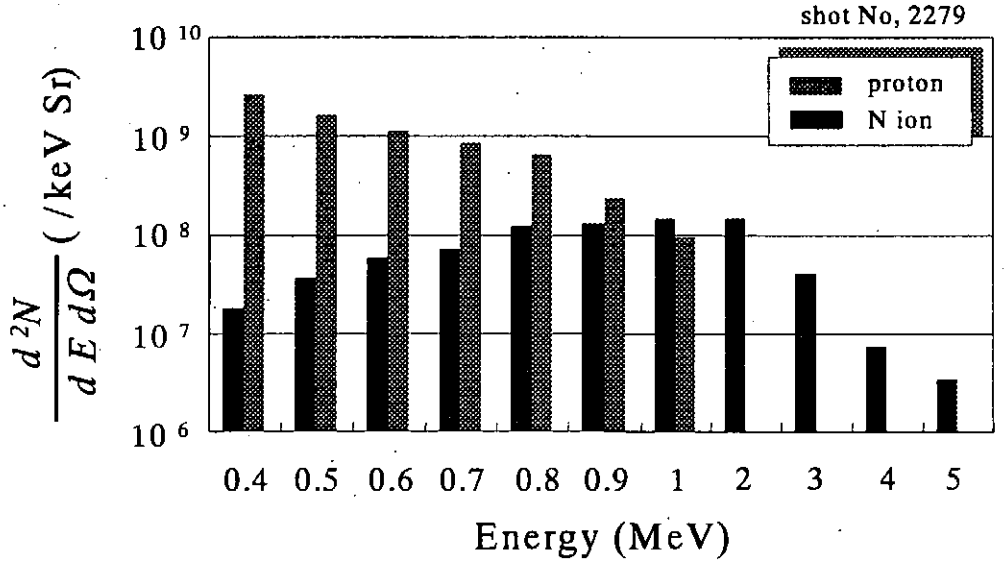

Fig. 8. Energy spectra of protons and nitrogen ions.

Figure 8 shows the energy spectrum of protons and nitrogen ions. As seen in the figure we found a clear difference between them. For protons the spectrum decrease monotonically with energy, whereas clear peak is observed in the spectrum of nitrogen.

IV. Irradiation Experiment

By the irradiation of intense pulsed ion beam to materials, the surface will pulse heated to extremely high temperature and the crystal structure is expected to be modified. To demonstrate the modification effect, amorphous silicon films were irradiated by the ion beam produced in P.F. The films were deposited on soda glass substrates by a vacuum evaporation technique. The size and the sickness of the targets are, 10 × 10 mm and 800 nm, respectively.

In the experimental P.F was operated on the same condition as that shown in Fig. 2-5 to irradiate proton beam. Figure 9 shows the positions of the targets in the experiment. The targes were placed at z = 400 mm and different radial positions. The ion current densities of each position can be estimated from Fig. 3.

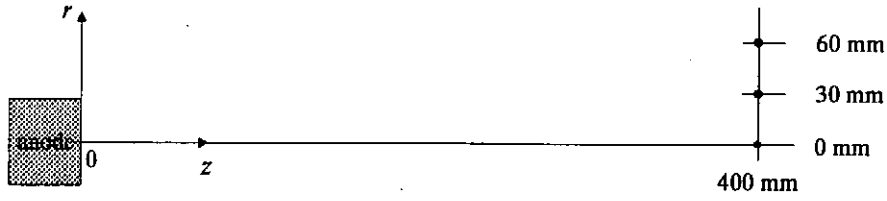

Fig. 9. The target positions in the irradiation experiment.

Figure 10 shows the x-ray diffraction patterns of the films before and after one shot of beam irradiation. Here, the peaks correspond to Al are due to that Al holder is used in the diffraction measurement. From the figure we see that there is no crystal stricture in the target before irradiation. In contrast, in the diffraction patterns for the targets irradiated at r = 0 and 30 mm, we clearly see the peaks corresponding to Si (111) and Si (220), which indicate that amorphous silicon layer was crystallized by the irradiation of the beam. The target irradiated at r = 60 mm was not crystallized. This seems to be due to the insufficient beam intensity since it is much lower in that position.

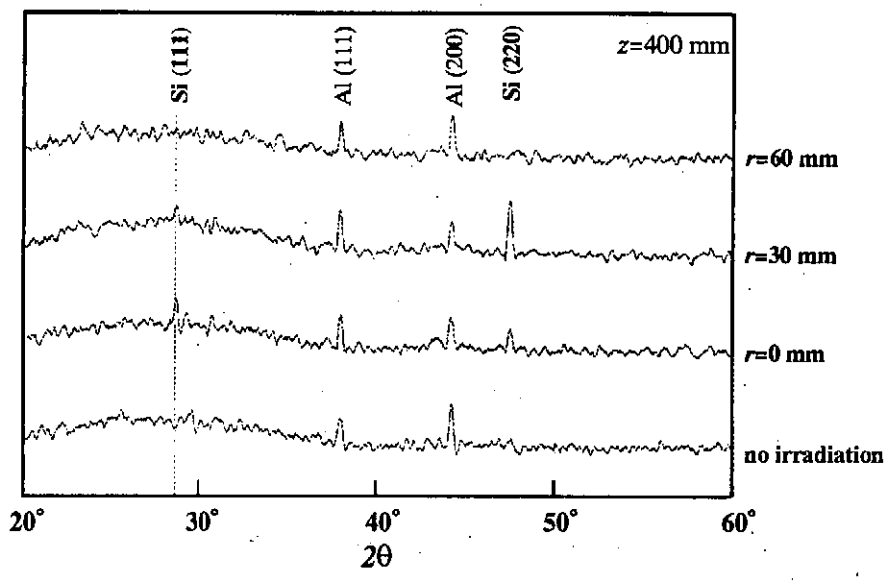

Fig. 10 X-ray diffraction patterns of amorphous Si thin films irradiated by pulsed proton beam.

Ⅳ. Conclusion

Characteristics of ion beams produced in the Mather type P.F were studied experimentally to apply the beam to materials processing. The P.F was pre-filled with H_2 of 250 Pa, or mixture of H_2 (180 Pa) and N_2 (20 Pa). At 400 mm downstream from the top of the anode on the electrode axis, ion beam of current density ≈ 650 A/cm^2, pulse width ≈ 200 ns

(FWHM) was observed when filling gas of H_2 was used. The ion species and energy spectra were evaluated by a Thomson parabola spectrometer (TPS). For protons of energy in the range of 0.1 - 1 MeV are observed when P.F was filled with H_2, where as protons and variety of nitrogen ions ($N^{(1-5)+}$) of energy in the range of 0.4 - 6 MeV are observed when using mixture gas. From the evaluation of the energy spectrum of nitrogen ions we see that the spectrum has a peak on 1 or 2 MeV. To evaluate the irradiation effect on materials, amorphous silicon films were irradiated by the ion beam and we see that amorphous silicon layers are crystallized by the irradiation.

References

1) K. Takao, Y. Doi, S. Hirata, M. Shiotani, I. Kitamura, T: Takahashi and K. Masugata, Jpn. J. Appl. Phys., **40**, Part 1 (2000) pp. 1013-1015

2) T. Takao, M. Shiotani, T. Honda, I. Kitamura, T. Takahashi, K. Masugata, Characteristics of the Nitrogen Ion Beam Produced in a Plasma Focus Device, Proc. 28th IEEE Int'l Conf. on Plasma Science and 13th IEEE Int'l Pulsed Power Conf., Las Vegas, Nevada, June 17-22, 2001, P1C01 (2001)

4) J. N. Feugeas, E. C. Llonch, C. O. de Gonzalez and G. Galambos, J. Appl. Phys., **64** (1988) 2648

5) H. Kelly, A. Lepone, A. Marquez, D. Lamas and C. Oviedo, Plasma Sources Sci. Technol. **5** (1996) 704

6) R.L. Gullickson and H.L. Sahlin, J. Appl. Phys., **49**, (1978) 1099

DEVELOPMENT OF BIPOLAR PULSE ACCELERATOR

K.Kawahara, Y.Doi, I.Maetubo, C.Mitsui, I.Kitamura, T.Takahasi, K.Masugata,
Y.Tanaka*, H.Tanoue*, and K.Arai*

Faculty of Eng., Toyama Univ., 930-8555 Japan
*Industrial technical Laboratory, 1-1-4, Tsukuba, Ibaragi, 305-8568 Japan

ABSTRACT

Intense pulsed heavy ion beams (PHIB) are expected to be applied to the implantation technology for semiconductor materials. In the application it is very important to purify the ion beam. To produce a pure PHIB a new type of pulsed power ion accelerator using bipolar pulse is proposed, which is called as "bipolar pulse accelerator (BPA)". As the first step of the development of BPA, a test system was constructed to confirm the principle of the acceleration. The system consists of an anode with an ion source of gas puff plasma gun, a B_r type magnetically insulated acceleration gap, and a drift tube. In the experiment the gas puff plasma gun generates a nitrogen ion flux of current density 50 A/cm^2. The ions are successfully accelerated in the gap by applying negative pulse of voltage 210 kV to the drift tube. The accelerated ions are detected by a shadow box and the divergence angles of r and θ directions of the beam were estimated to be 0.1 rad and 0.2 rad, respectively.

I. Introduction

Intense pulsed ion beams (PIB) of carbon, nitrogen or aluminum, have a wide area of applications including nuclear fusion, materials science, etc. PIB can easily be generated in a conventional pulsed power ion diode using flashboard ion source. However, since many kinds of ions are produced in the same time, the purity of the beam is usually very poor. For example, in a point pinch ion diode we found that produced PIB contains protons, multiply ionized carbons, organic ions, etc. Hence an application of the PIB has been limited. To improve the purity a new type of pulsed power PIB accelerator named "bipolar pulse accelerator (BPA)" was proposed[1-3]. As the first step of the development of BPA, an experimental system was constructed to confirm the principle of the acceleration. In the paper the preliminary result of the experiment is shown.

II. Principle

Figure 1 shows conceptual drawing of the bipolar pulse accelerator. A conventional PIB diode is also shown for comparison. The proposed ion diode shown in Fig.1 (b) consists of a grounded ion source, a drift tube and a grounded cathode. In the diode, bipolar pulse (V_1) is applied to the drift tube. At first the negative voltage pulse of duration τ_p is applied to the drift tube, and ions on the grounded ion source is accelerated towered the drift tube. If τ_p is adjusted to the time of flight delay of the ions to pass the drift tube, the pulse is reversed and the positive voltage of duration τ_p is applied to the drift tube when top of the ion beam reaches the 2nd gap. In the case ions are again accelerated in the 2nd gap toward the grounded cathode.

As seen in Fig.1 (a), in the conventional PIB diode, ion source is placed on the anode where a high voltage pulse is applied, while in the proposed ion diode, ion source is on the grounded anode. This seems to be favorable for the active ion sources where ion source is powered by an external power supply.

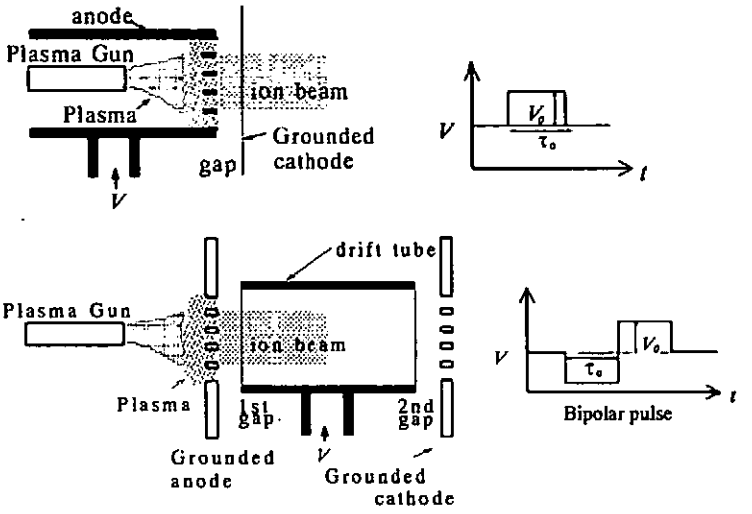

Fig.1 (a) Conceptual drawing of the conventional ion beam accelerator and (b) the proposed bipolar pulse accelerator

Here considering the acceleration of ions in the case that ion source contains N^+ ions and impurity ions of H^+ in the proposed diode (see Fig.2). In the case, ions of N^+ and H^+ are accelerated in the first gap toward the drift tube when negative voltage is applied. In Fig.2, N^+ and H^+ beams are schematically described and as seen in the figure, due to the deference of the velocity the length of the beams is much longer for H^+. Here assuming that the length of the drift tube is designed to be same as the beam length of N^+ of duration τ_p at acceleration voltage V_p. It is, for example calculated to be 0.19 m when V_p = 1 MV, τ_p = 50 ns. When N^+ beam of length 0.19 m is in the drift tube ($t = t_1$) the voltage is reversed and positive voltage is applied to the drift tube, which accelerate N^+ beam in the 2nd gap. Since length of H^+ beam at V_p = 1 MV, τ_p = 50 ns is 0.71 m, ≈ 73 % of the beam is out of the drift tube at $t = t_1$ and not accelerated in the 2nd gap. Hence ≈ 73 % of H^+ beam is removed in the accelerator.

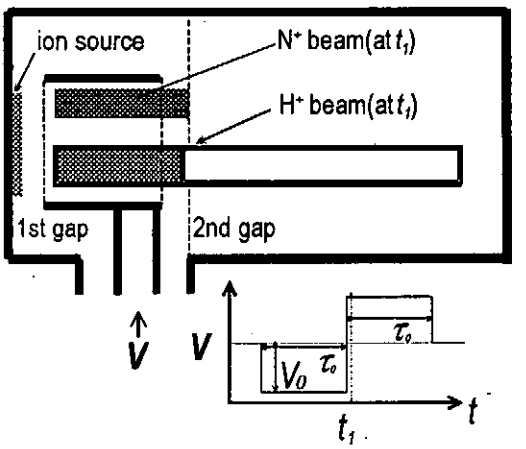

Fig. 2. Principle of the improvement of the purity of the ion beam.

II. Experimental Apparatus

As the first step of the development of BPA, a test system was constructed to confirm the principle of the acceleration. Figure 3 shows the cross-sectional view of the system and the electrical configurations. The system consists of a grounded anode (copper), a drift tube (stainless steel) and a magnetically insulated acceleration gap (MIG). The drift tube is connected to the high voltage terminal of the pulse forming line (PFL, designed output is 300 kV, 48 kA, 60 ns) and by applying negative pulse, ions on the anode are accelerated toward the drift tube.

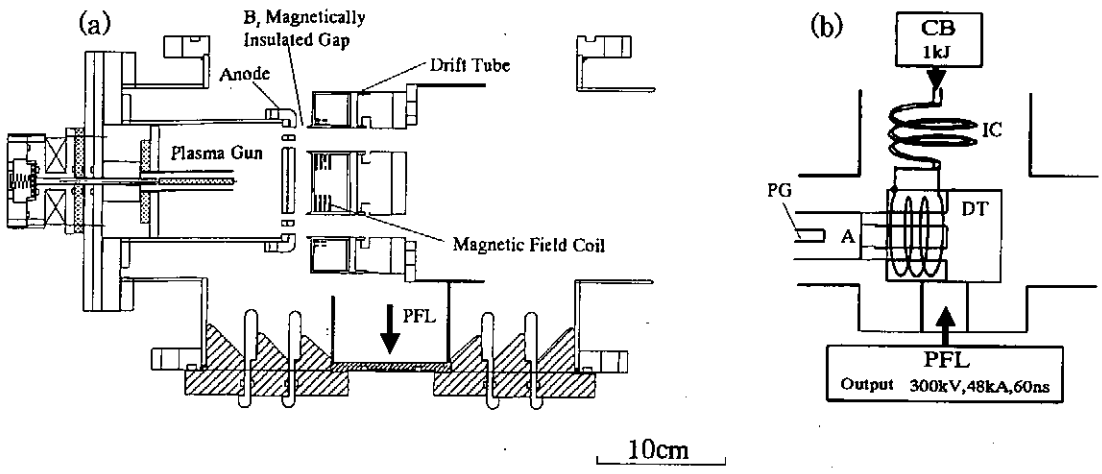

Fig.3 (a) Cross-sectional view of the experimental system. (b) Schematic of electrical configuration to apply the current to the magnetic coils.

The MIG is the B_r type and an inner coil and an outer coil are installed on the end of the drift tube and B_r magnetic field is produced in the gap. The coils are designed to produce B_r magnetic field of the field line to be parallel to the anode surface. The rise time and the strength of the B_r field were measured to be 150 μs and 0.4 T, respectively. Since high voltage is applied to the drift tube, pulsed current produced in the capacitor bank (CB) is applied to the coils through an inductively isolated current feeder (IC) (see Fig. 3 (b)). The IC is the helically winded coaxial cable and the outer conductor of the IC connects the grounded vacuum chamber and the drift tube with inductance of 4.6 μH. The gap length, inner diameter and outer diameter of the effective gap area are 10 mm, 53 mm, and 93 mm, respectively. To produce anode plasma (source plasma of the ion beam) gas puff plasma gun is used, which is placed behind the anode. The anode has two coaxial slits of width 6 and inner diameter 54 mm, and width 6.5 mm and inner diameter 76 mm, to pass through the source plasma.

Figure 4 shows the cross sectional view of the gas puff plasma gun used in the experiment. The plasma gun consists of a high-speed gas puff valve and a coaxial plasma gun. The gas puff valve consists of a nylon vessel, an aluminum valve and a drive coil and the vessel is pre-filled with N_2 gas. By applying pulse current to the magnetic coil magnetic stress and the gas expand with a supersonic velocity and reach the gas nozzles on the inner electrode of the plasma gun. The plasma gun has coaxial electrodes of inner electrode diameter 4 mm, outer electrode diameter 10 mm, and length 100 mm. Since it takes about a hundred μs to open the valve and several tens μs for N_2 gas to expand to reach the gas nozzle of the plasma gun, the capacitor bank of the plasma gun is discharged with a delay time

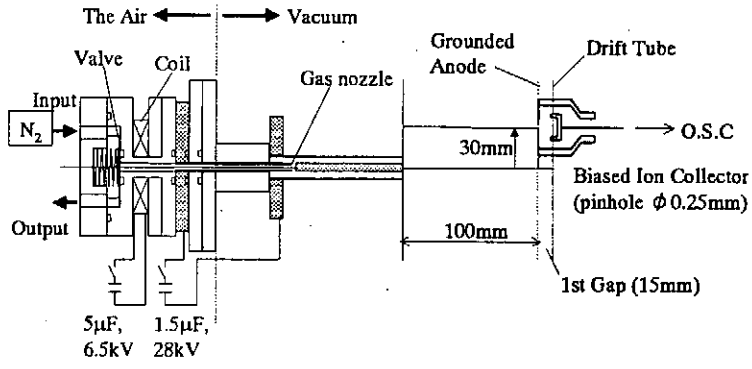

Fig.4 Cross-sectional view of the gas puff plasma gun.

of τ_d. To apply pulsed current to the gas puff coil and the plasma gun capacitor banks of 5 μF and 1.5 μF are used, respectively. Both of the capacitors were usually charged to 6.5 kV, and 28 kV, respectively.

To measure the ion current density of the produced plasma, a biased ion collector (BIC) was used which was placed as shown in the figure.

IV. Experimental Results

Figure 5 shows the wave forms of the discharge current of the plasma gun ($I_{P.G}$) and the ion current density (J_i) obtained by BIC when τ_d = 213 μs. As seen in the figure $I_{P.G}$ rises in 2.75 μs and have a peak value of 23 kA. The peak value of J_i of 50 A/cm^2 is obtained at 100 mm downstream from the plasma gun at t = 5 μs after the rise of $I_{P.G}$.

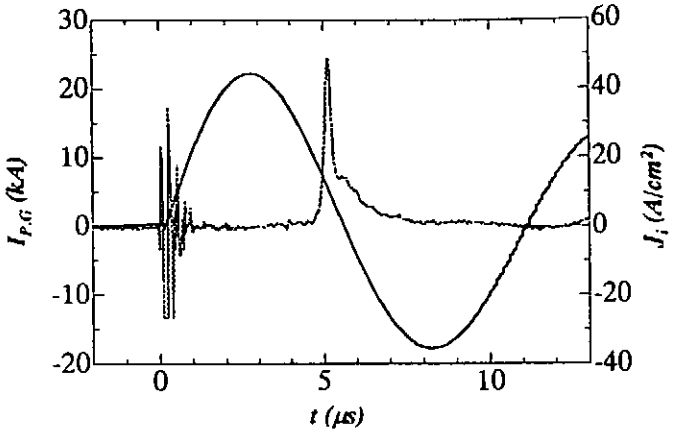

Fig. 5 Typical waveforms of the discharge current of the plasma gun ($I_{P.G}$) and the ion current density (J_i) obtained by BIC.

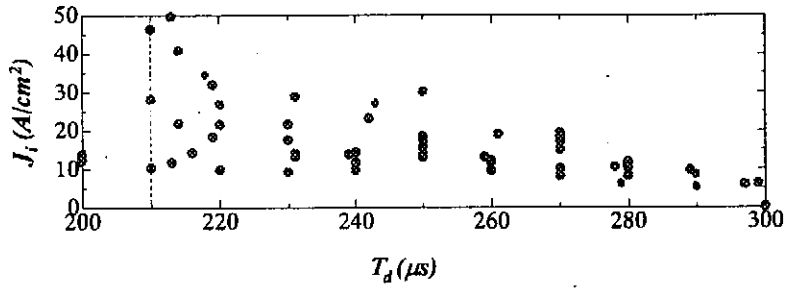

Fig. 6 The dependence of J_i on τ_d.

Figure 6 shows the dependence of J_i on τ_d. As seen in the figure J_i rises at $\tau_d \approx 210$ μs, which suggest that it takes 210 μs to injection gas from the nozzles. After the rise of J_i, J_i gradually decreases with increasing τ_d. This seems to be due to that the degree of ionization decreases with increase of the quantity of the gas.

To confirm the acceleration of the ions in the MIG the test system was operated at 70 % of the full charge condition of the PFL. The plasma gun was operated at $\tau_d \approx 215$ μs and high voltage negative pulse was applied to the drift tube at 6.2 μs after the rise of the $I_{P.G}$.

Figure 7 shows the typical waveforms of applied voltage to the drift tube (V_d) and the current (I_d). The leak current through IC (I_{IC}) is also shown in the figure, which is calculated from V_d assuming the inductance of IC to be

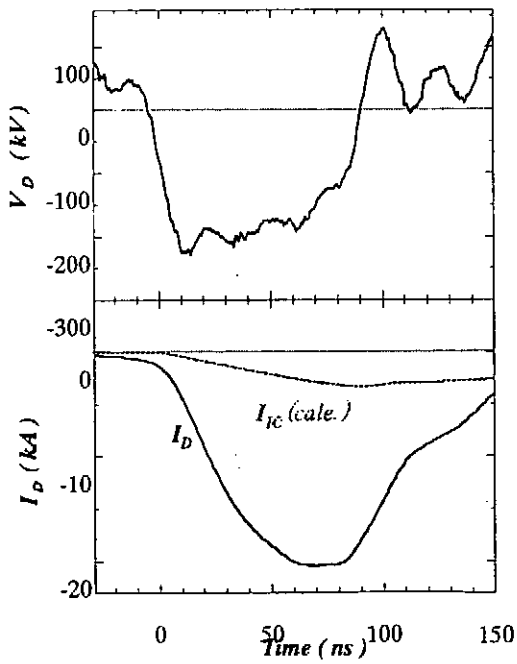

Fig. 7 Typical waveforms of V_d and I_d.

4.6 μH. As seen in the figure V_d rises in 15 ns and have a peak value of - 210 kV, whereas I_d rises in 50 ns and have a peak of 20 kA. Considering the I_{IC}, the effective current through MIG seems to be less than 17 kA.

Figure 8 shows the pinhole image obtained by the shadow box. The shadow box consists of a pinhole plate placed 92 mm downstream from the anode and an ion track detecting plastic of CR–39 placed 10 mm downstream from the pinhole plate. The pinhole plate has 15 pinholes of diameter 0.2 mm each.

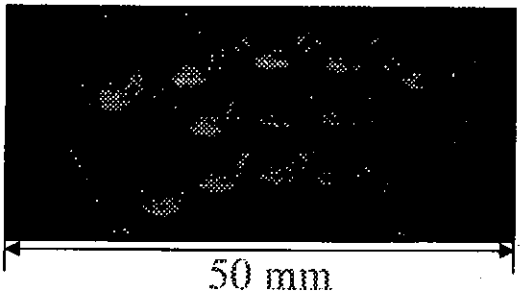

Fig. 8. Ion pinhole images obtained by the shadow box.

As seen in the figure ion pinhole images are observed, each of which corresponds to the pinholes, suggesting uniform production of ion beam. From the track images the divergence angles of r and θ directions of the beam were estimated to be 0.1 rad and 0.2 rad, respectively.

V. Conclusion

To produce a pure PHIB a new type of pulsed power ion accelerator using bipolar pulse is proposed, which is called as "bipolar pulse accelerator (BPA)". As the first step of the development of BPA, an experimental system was constructed to confirm the principle of the acceleration. The system consists of a anode with ion source of gas puff plasma gun, a Br type magnetically insulated acceleration gap, and a drift tube. In the experiment the gas puff plasma gun generates a nitrogen ion flux of current density 50 A/cm^2. The ions are successfully accelerated in the gap by applying negative pulse of voltage 210 kV to the drift tube. The accelerated ions are detected by a shadow box and

Reference

1) K. Masugata, "High current pulsed ion beam accelerators using bi-directional pulses" Nuclear Instruments & Methods in Physics Research, Section **A 411** pp.205-209 (1998)
2) K. Masugata, K. Kinbara, T. Atsumura, Y. Kawahara, T. Takao, I. Kitamura, and T. Takahashi, "Generation and purification of high current pulsed heavy ion beam using bi-directional pulses", Proc. 12th Symp. on High Current Electronics (1st Int'l Congress on Radiation Physics, High Current Electronics, and Modification of Materials, Tomsk, Russia, 24-29 September 2000), pp.111-114 (2000)
3) K. Masugata, I. Kitamura, T. Takahashi, Y. Tanaka, H. Tanoue, K. Arai, "Intense heavy ion beam acceleration using bipolar pulse for implantation to semiconductor", Proc. 28th IEEE Int'l Conf. on Plasma Science and 13th IEEE Int'l Pulsed Power Conf., Las Vegas, Nevada, June 17-22 2001, O3C3 (2001)

MEASUREMENT OF THE ELECTRON ENERGY DISTRIBUTION USING AN ELECTROSTATIC ANALYZER IN THE PLASMA DISTURBED BY AN INTENSE RELATIVISTIC ELECTRON BEAM

Hiromasa Morishita, Mitsuhiro Nitta, Haruhisa Koguchi, Ritoku Ando[1], Keiichi Kamada

Faculty of Science, Kanazawa University
Kakuma, Kanazawa City, 920-1192, JAPAN

ABSTRACT

The interaction between an intense relativistic electron beam (IREB) and a plasma excites many nonlinear phenomena. The energy distribution function of the plasma electron is very important to know the physics. An electrostatic analyzer with multi grids is newly developed to measure the electron distribution function of the plasma in the interaction region. The signal from the analyzer is obtained just after the IREB injection. The temperature is estimated to be about 15 eV, which roughly coincides with the temperature measured by spectroscopy. The temperature increases strongly when the original plasma density becomes comparable to the IREB density.

I. Introduction

The electron-electron collision rate decreases as the beam energy increases. Nevertheless the energy transfer rate from intense relativistic electron beam (IREB) to plasma stays in constant because of another mechanism, the two-stream instability. The energy transfer to the Langmuir wave through the instability can reach several 10 %. In this situation, strong Langmuire wave can be excited. It is well known that the stochastic heating and the transit-time-dumping heating by the turbulence field are expected to occur for the plasma electrons. Heating of the plasma has been observed in our experiment also, and the electron temperature, T_e, raised from 1 eV to 35 eV by an IREB injection, which was measured spectroscopically by filling up with helium gas.[1)] Electron temperature is a very important parameter especially in the Langmuir turbulence. It changes the

[1] Author of this paper: ando@plasma.s.kanazawa-u.ac.jp

Debye-length and the strength of interaction between the localized Langmuir wave packets and electrons. Moreover the energy distribution function has a lot of information. For example, the turbulence field produces a high-energy tail in the distribution through the burnout of "caviton". So the characteristic behavior of the energy distribution of the plasma electron can be one of the important parameters for the IREB-plasma interaction. An electrostatic analyzer is developed to measure the energy distribution function of electrons disturbed by the IREB propagation..

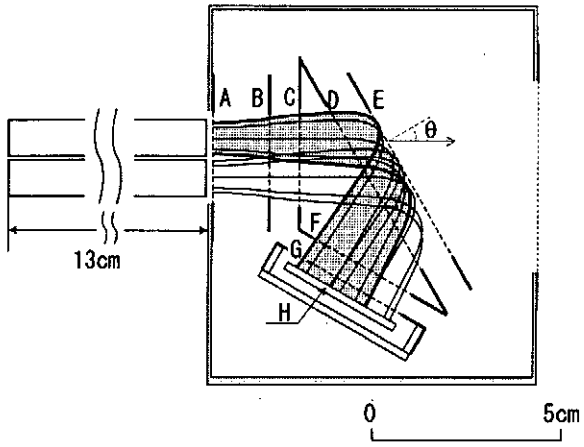

Fig.1 The differential-spectrum electron-energy analyzer.

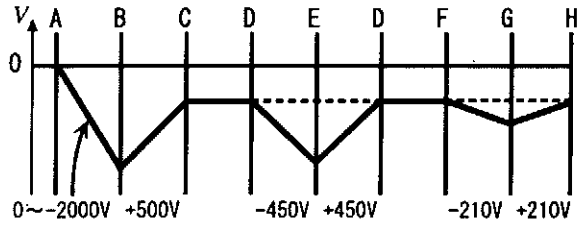

Fig.2 Potential of the grids and electrodes. The potential differences from the grid-A to H are given in the figure. The voltage of B is variable from 0 to - 2000V. Other potentials change with B, simultaneously.

II. Experimental Apparatus

We developed an electrostatic analyzer for the plasma electrons. The analyzer should work for the plasma electrons with low energy, under no influence of the high-energy electrons of the IREB. For this reason, the "differential-spectrum" operation is chosen instead of the "energy-integrated" operation for the electrostatic analyzer. The original design comes from an ion-energy-analyzer.[2] The design and the potentials of the grids were determined after analysis of electron trajectories. The analyzer is composed of multi grids as shown in Fig.1. All the potentials of the grids are shown in Fig.2. The primary grid A and the case are grounded. The primary-repeller grid-B is biased negatively with the voltage V_B. The grids C, D, and F are biased with the same voltage of V_C. Therefore no electric field exists inside of the triangle with the grids C, D, and F. The grid-E and D are tilted against the incidence ray of electron with an angle θ. The grid-E is the secondary-repeller grid. The grid-E is biased negatively with the potential of V_E. The electrode-H is a collector, which is biased at the same voltage of V_C. One more repellar grid is placed in front of the collector, to push back the secondary electrons that are

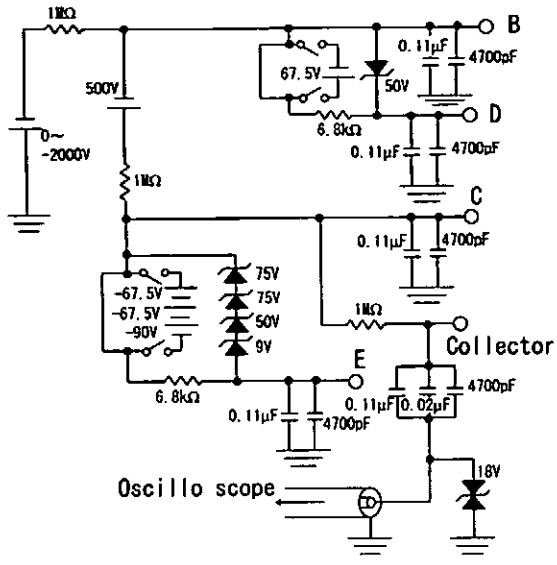

Fig.3 Electrical circuit for the electrostatic analyzer

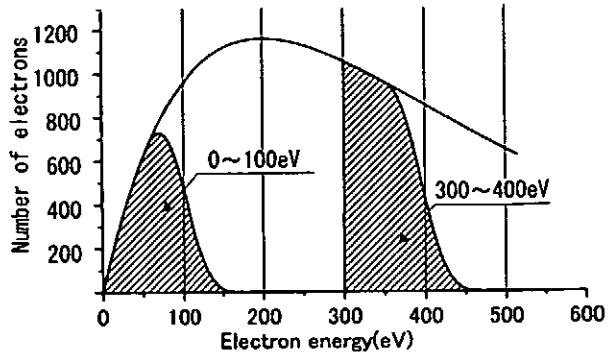

Fig.4 The energy bands are shown for two bias voltages, V_B= 0 V and 300 V. The maximum incidence angle and the angle of the grids D and E is fixed at 3.5 deg and θ = 30 deg, respectively. The electron temperature and the electron density are 200 eV and 1 x10^{18} m^{-3}, respectively. The energy bandwidth is fixed at 100 V through the experiments.

emitted from the grid-F and the electrode-H. The electrons with the lower energy than $-eV_B$ are reflected between A and B. The electrons with the higher energy, $-eV_B < E$, can pass through the grid-B, and then accelerated between B and C. The secondary-repeller grid-E reflects the electrons with the energy lower than $-e(V_E - V_C)\cos^2\theta$. Eventually the electrons with energy between $-eV_B < E < -e(V_E - V_C)\cos^2\theta$ are reflected between D and E and hit the electrode-H. The higher-energy electron can pass through the analyzer without contribution. The angle θ of the secondary-repeller grid is 30 degree. The V_B is changed with keeping the relative voltages, V_C = 500 V +V_B, V_E = 50 V +V_B. The energy band is fixed at the constant width of 100 eV for any V_B by the relation. The repellar grid-G is biased with the voltage of – 210 V +V_C. The V_B, which gives the lower-energy end, is changed between 0 ~ – 2000 V. The upper threshold energy not depends only on the $-e(V_E - V_C)\cos^2\theta$, but on the incident angle to the grids-D and E. To avoid that the incident electrons have large angle spread, a bunch of the stainless steel pipes, with 130 mm length and 8 mm diameter, is placed in front of the analyzer. It limits the incidence angle less than 3.5deg. The voltage difference between the grids-B and C, 500 V, was introduced also to reduce the incidence angle into the space between D and E. The bias circuit is shown in Fig.3. All the grids and electrode, are electrically connected each other by the circuit. For example, when the V_B, is changed between 0 ~ – 2000 V, the potential of the electrode-H is changed from + 500 V to – 1500 V in the same time. The electrodes and oscilloscope are isolated by capacitors. For example, the capacitor with 0.14 μF is

employed to cut the dc voltage. The signal is monitored with a termination of 50 ohm in front of the oscilloscope. Then the capacitor and the resister works as a high-pass filter with the time constant of 7 μs. A serge-absorber is inserted to the each channel for safety. Because the time response has to be improved, the serge-absorber with minimum capacitance is employed. The breakdown voltage of the serge-absorber is ±18 V and the capacitance is 360 pF (Ishizuka Electronics Corp. *VRD Z1018*). The entrance area is restricted to the upper half for the purpose to reduce the secondary electrons emitted from the grid-E.

Number of the electrons collected by the analyzer is estimated and is shown in Fig.4 against its kinetic energy. Maxwellian distribution function with temperature of 200 eV and the density of 1 x10^{18} m^{-3} is assumed for the calculation. The energy bands for $V_B = 0$ V and – 300 V, *i.e.* E = 0 - 100 eV and E = 300 - 400 eV are shown by hatches. The high-energy side of each energy band is broadened due to the spread of the incidence angle, as mentioned above. The current is estimated by the integration of the hatched region. It is about 30 mA for $V_B = -300$ V. The width of the energy band is fixed at 100 eV with any V_B through the experiment.

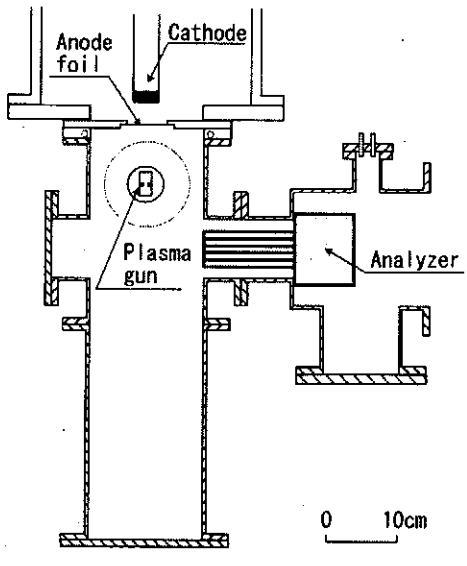

Fig.5 The experimental setup with the IREB injection. The analyzer is placed at the periphery of the main chamber.

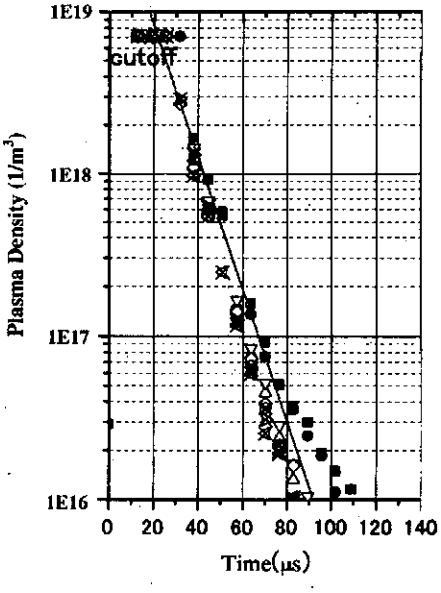

Fig.6 The original plasma density, n_{p0}, is measured by an interferometer. z=17.5 cm

III. Experiment

The experimental setup is shown in Fig.5. No external magnetic field is applied in this experiment . The two rail-type plasma-guns are located at z= 10 cm downstream from the anode. A 36 mm diam. cathode and an anode of titanium foil with thickness 20 μm are employed. The IREB with beam energy of 1.5 MeV, diode current of 27 kA, and pulse-length of 30 ns, is injected to the plasma. The analyzer is placed at z= 17.5 cm at the periphery of chamber to avoid damages from the IREB. The kinetic energy to the radial direction is measured. The plasma density on the axis at the z= 17.5 cm, n_{p0}, increases from the start of discharge to 15 μs, and has the maximum density about 4 x10^{19} m^{-3}. Then the n_{p0} decreases with time as shown in Fig.6. The n_{p0} was measured at the time until 100 μs by an interferometer. The plasma density has a slow peak on the axis at the middle of chamber after 40 μs. Because the pulse length of the IREB, 30 ns, is short enough compared to the characteristic time of the variation of n_{p0}, the injection time of IREB from start of the gun-firing, τ, is used as a parameter of the plasma density for the interaction.

The collector signal appears just after the IREB injection, as shown in Fig.7. The δ is the time from the IREB injection. The IREB pulse finishes at δ=30 ns in the figure. The collector signal becomes largest at the lowest voltage V_B = 0 V, and decreases with the bias voltage. High frequency noise is observed, and is smoothed out by a FFT filtering procedure, with a cut-off frequency = 10 MHz. The signal with amplitude from 1 mV to 100 mV is observed typically. It corresponds to the current influx of 0.02 mA and 2 mA.

The noise was checked by masking the full entrance of analyzer using a brass plate with 3 mm thickness. Figure 8 shows the normal signal (a), and the noise signal (b). A large noise with a peak around δ= 200 ns appears as shown in Fig.8. We can understand that the first peak of the collector signal is strongly contaminated by the noise. Because the noise decrease with time, we assumed the signal at moderately later time from the injection, δ > 500 ns, is not contaminated by the noise. We concentrate and analyze the signal after the time δ> 500ns.

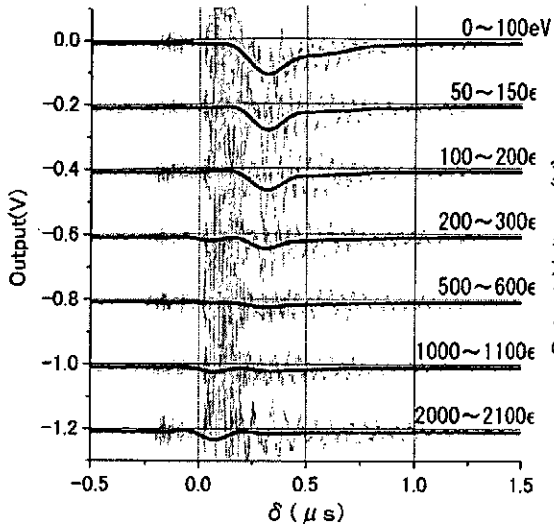

Fig.7 Signal waveform when an IREB is injected. The signals for $V_B = 0 \sim -2000$ V are obtained shot by shot. The high frequency noise is smoothed out by a FFT filtering procedure. $\tau = 150$ μs.

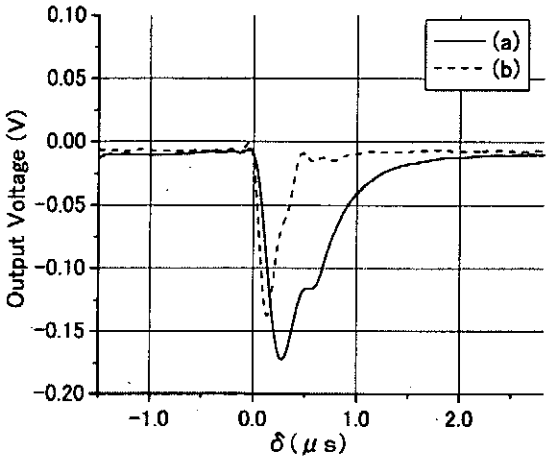

Fig.8 The typical signal is shown by a solid line (a). The noise signal is shown by a dotted line (b). $z = 305$ cm, $V_B = 0$ V, $\tau = 150$ μs.

The V_B-dependence of the collector current is traced in detail in the two ranges, *i.e.* from 0 V to – 2000 V with 100 V step (Fig.9 (a)), and from 0 V to – 100 V with 10 V step (Fig.9 (b)). Figure 9 (b) shows the detail of the sharp peak around 0 V in Fig.9 (a). Maxwellian distribution of the electrons is assumed for the energy distribution for fitting of the V_B-dependence. As shown in the Fig.9, at least two Maxwellian components are necessarily for the fitting. First the noise component about 0.068 mA is subtracted from the both curves. Next, the high-temperature component is determined using Fig.9 (a). Finally the low-temperature component is determined from Fig.9 (b). The temperature and the density of the low-temperature component are 15eV and 2.1×10^{16} m^{-3}. The temperature and the density of the high-temperature component are 196 eV and 0.64×10^{16} m^{-3}. The temperature of the low-temperature component is comparable to the value, 35 eV, that was obtained from spectroscopy. The difference is probably due to the influence of high-energy component. The low-temperature component always has higher density than the high-temperature component. And they are called as the bulk-component and the tail-component. Temperature and density of the tail-component will be strongly affected by the way of analysis, *i.e.* the subtraction of constant current. Only the relative change is meaningful.

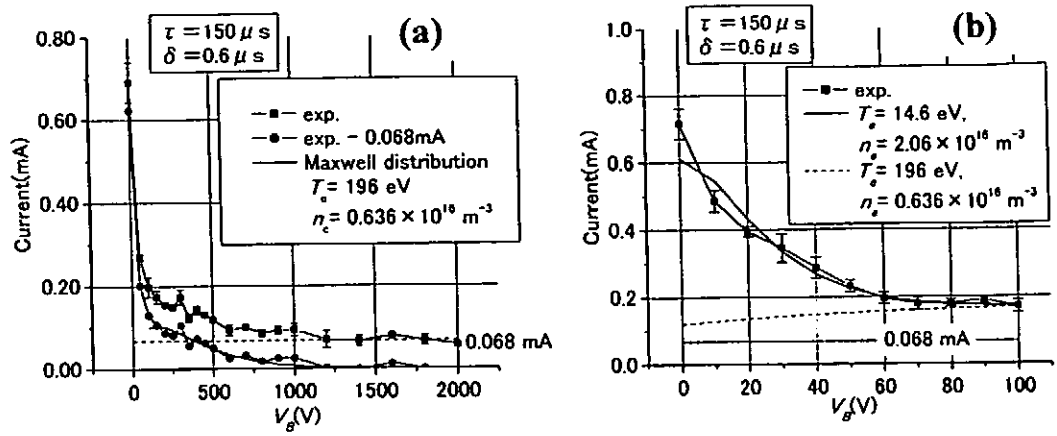

Fig.9 V_B dependence of the collector current can be fitted using two thermal components. The fitting curves are shown by a solid line and a dotted line. The temperature and the density are 14.6 eV and 2.06 x10^{16} m^{-3} for the bulk, and 196 eV and 0.636 x10^{16} m^{-3} for the tail. τ = 150 μs, δ= 600 ns

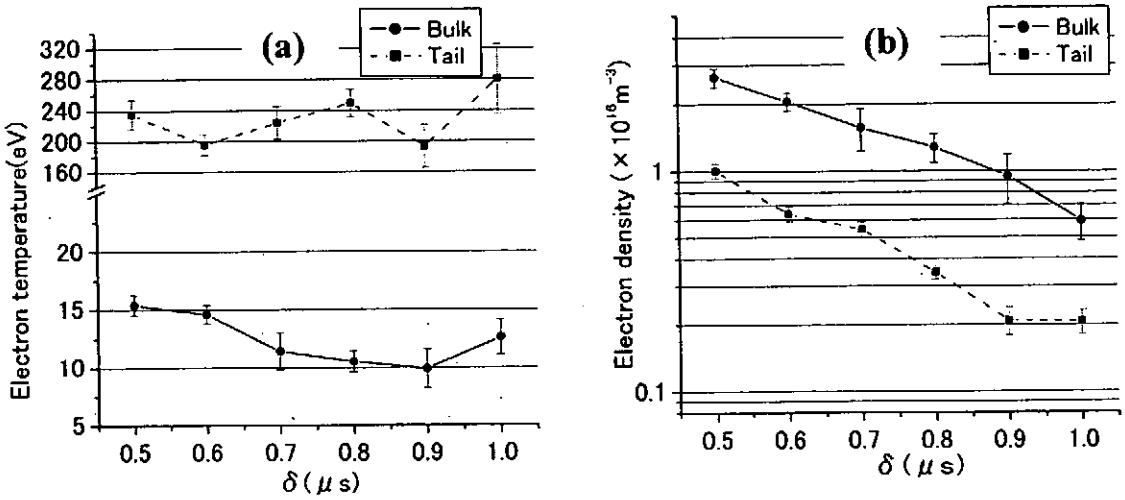

Fig.10 Time behaviors of the temperature and density after the IREB injection. τ = 150 μs.

Figure 10 shows the time behavior of the temperatures and densities of the bulk- and tail-components after 500 ns from the IREB injection. The temperature of the bulk component keeps constant, which is much higher than the temperature of the original plasma. On the other hand, the density decays quickly. Probably the change of the signal intensity comes from the change in the density.

The signal intensity strongly depends on the τ, *i.e.* original density, n_{p0}. The temperature and the density of bulk and tail components are estimated at δ= 700 ns. The IREB density n_{b0} is about 4 ×10^{16} m^{-3}, is comparable to the plasma density of τ= 70 μs. The plasma density n_{p0} is shown by triangle dots in the Fig.11 (b). The density that

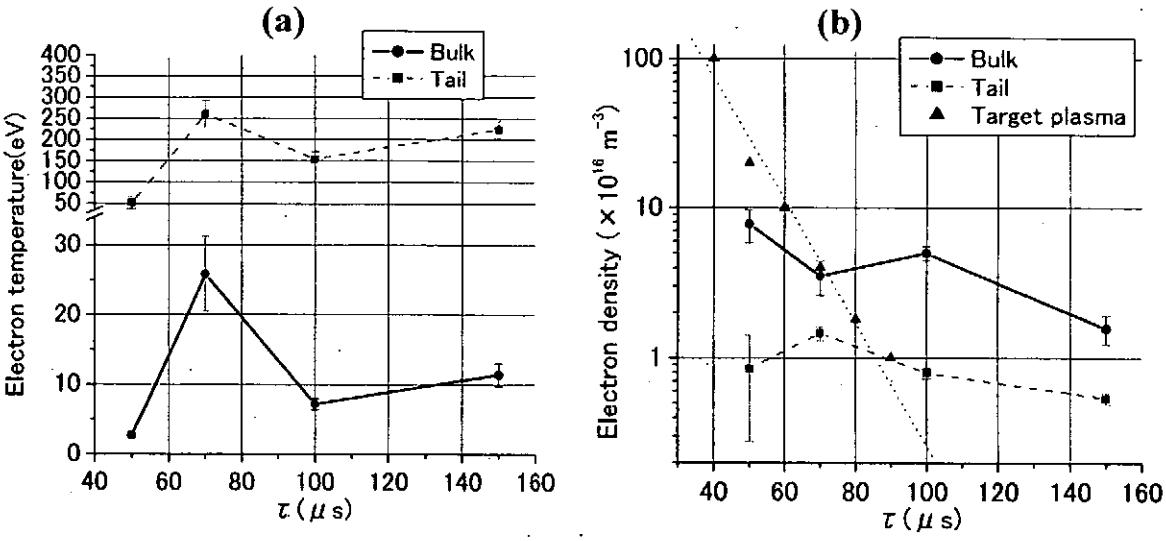

Fig.11 n_{p0} dependences. The temperature and the density at δ= 700 ns are shown in (a) and (b) respectively. The n_{p0} is showed by triangle dots in (b).

measured by the analyzer does not change like the n_{p0} (as shown in Fig.11 (b)). It is constant compare to the n_{p0}. The densities change the position at $\tau\sim$ 70 μs. On the other hand, the electron temperature has a sharp peak at τ= 70 μs. The temperature becomes smaller but keep constant around 10 eV at $\tau > 70$ μs. It becomes small quickly at $\tau < 40$ μs.

IV. Discussion

Difference between the n_{p0} and the density from the analyzer was observed. We consider that the density detected by the analyzer is the electron density of the flux that escapes from interaction region. Then it is strange that the flux density exceeds the original plasma density. In that case, we think that the real density may be larger than the n_{p0} due to the plasma production by an IREB injection.

The stochastic heating is considered to take place, if large amplitude standing wave exists. Theoretically when the parameter, p, exceeds 0.473, the stochastic heating start, where $p = eE_0k_0 / m_e\omega_0^2$, E_0 is the wave amplitude, k_0 is the wave number, and ω_0 is the angular frequency.[3] Here, the amplitude of Langmuir wave can be estimated from the two-stream instability theory.[4] In our case, the condition for the parameter p can be satisfied in a relatively thin plasma, if the IREB density is constant. The threshold density for the heating is estimated to be n_{p0}= 5 $\times 10^{16}$ m^{-3}. It corresponds to the plasma of $\tau > 70$ μs. In the experiment, the similar tendency was observed at $\tau > 70$ μs where the temperature increased.

The heating by cavitons, *i.e.* the localized Langmuir wave packets, is expected around δ= 600-1200 ns, at which the caviton-like patterns on the beam shadowgraph

shrink and disappear. [5] Strong temperature rise was not observed clearly in the experiment. It might mean that the heating by cavitons is not so strong as the stochastic heating. We need more data for precise discussions, and our experiment will be continued.

References

1) M. Yoshikawa, *et al.*, J. Phys. Soc. Jpn., *Vol.*65, *pp.*2081-2086, 1996.
2) Y. Sakamoto, *et al.*, Rev. Sci. Instrum., *Vol.*66, *pp.*4928-4936, 1995.
3) Y. Hsu, *et al.*, Phys. Rev. Lett., *Vol.*43, *pp.* 203-206, 1979.
4) L.E. Thode and R.N. Sudan, Phys. Fluids., *Vol.*18, *pp.*1552-1563, 1975.
5) R. Ando, *et al.*, Research Report NIFS-PROC-50, *pp.*163-172, 2001.

Trains of electron pulses generation using multi-stage cavities

Masaki Kamada, Michiya Mori, Kazuyoshi Sugawara,Yoko Yamada, Kazuteru Kurihara, Haruki Shirasaka, Takashi Nishiguchi, Ritoku Ando and Keiichi Kamada

Department of Physics, Faculty of Science, Kanazawa University, Kanazawa 920-1192, Japan

ABSTRACT

Automodulation of an intense relativistic electron beam was reexamined experimentally to obtain trains of subnanosecond electron bunches. Sufficient beam modulation with frequency larger than 1 GHz was expected for the trains of subnanosecond bunches. It was obtained when a short pulse electron beam with energy of 550 keV, current of 4 kA, pulse duration of 12 ns and current rise time of 2ns was injected to a series of four coaxial cavities with the length of 75 mm. However, only a poor modulation was observed when a long pulse electron beam of 700 keV, 4 kA, 175 ns with current rise time of 20 ns was injected to the same cavities. Transmission line theory as well PIC code simulation suggested that the round trip time for the electromagnetic wave in the cavity must be longer than the rise time of the beam current to obtain the high level current modulation. Therefore, we studied experimentally how the ratio between the beam current rise time and the length of the cavity affects on the level of current modulation. Single cavity experiments were carried out with the short pulse beam. Single cavity with the length of 75, 150 or 300 mm was utilized. The round trip times for 75 and 150 mm cavities are shorter than the current rise time of 2 ns. The experiments with a 75 or 150 mm cavity resulted in suppression of the modulation amplitude. In the case of a 300mm cavity, the high level modulation was obtained. The simulation results showed good agreements with the experimental results. We employed a series of cavities with decreasing lengths to improve the current rise time. For the short pulse beam, the high level current 1 GHz modulation was obtained when two 75 mm cavities were set at the downstream side of cavities with lengths of 300 mm and 150mm.

1 Introduction

The physics of propagation of an intense relativistic electron beam (IREB) with strong self- and induced field was not only interesting but also important for many applications. Typical IREB machine consists of a Marx generator and a pulse forming line that applies a high voltage pulse to a diode. A typical diode consists of a cold, field emission cathode and a thin foil or an aperture anode. The typical IREB parameters are electron energy of 0.5-10 MeV, electron current of 1 kA-1 MA, pulse duration of 10-100 ns and beam radius

of 1-10 cm. These parameters yield electron densities in the range of $10^{11} - 10^{13}$ cm^{-3}. However, it is technically difficult for the above systems to generate an IREB not only with electron energy larger than 10 MeV but also with pulse duration of less than 10 ns. Autoacceleration and automodulation processes were demonstrated [1], [2] as a potentially simple and inexpensive approach to obtain high energy and/or ultrashort electron beams. The energy of an IREB increases twice in the expense of its duration to the half using only a coaxial passive cavity [3] in the single-stage autoacceleration. The autoacceleration process compresses the IREB pulse. The pulse length of the autoaccelerated IREB depends on the cavity length. We reported that an IREB with duration of less than 1 ns was attainable from 10 ns IREB with multi-stage autoacceleration using decreasing length cavities [4] [5]. The autoacceleration process can be applied repeatedly on the long pulse IREB. While the multi-stage autoacceleration was useful to generate a single subnanosecond electron bunch using a short pulse IREB, automodulation is a potential approach to generate trains of subnanosecond electron bunches using a long pulse IREB. An IREB with subnanosecond duration is an interesting subject of study for an application to high power, short pulse millimeter wave generation called superradiance [6]. Trains of subnanosecond IREB should expand the abilities of IREB's.

Automodulation was intensively studied by M. Friedman, et al. [7]. They reported that electron beams with voltage varying from 0.25 to 1 MeV, current from 1 to 8 kA, and pulse duration from 20 to 300 ns were modulated to a depth of nearly 100 %. In our experiment, the final goal is to obtain high level 1 GHz modulation with a long pulse IREB with 175 ns duration. However, only a poorly modulated electron beam was observed with the long pulse IREB when four cavities with length of 75 mm were utilized in accordance with the results reported in [7]. In this case, the current rise time of 20 ns was much longer than the round trip time for electromagnetic wave in the cavity. When we used a short pulse IREB of 12 ns duration with 2 ns current rise time, high level current fluctuations with 1 GHz frequency were observed with the same four cavities [8]. Therefore, we report here how the ratio between the beam current rise time and the round trip time of the cavity for electromagnetic wave affects on the level of current modulation. And a potential approach for the long pulse IREB automodulation is proposed.

2 Experimental Setup

Two IREB sources were utilized to generate a short and a long IREB's. Pulserad 105A was utilized to generate a short pulse IREB of 550 keV, 4kA,12 ns with rise time 2 ns. Pulserad 220G was utilized to generate a long IREB of 700 keV, 4kA, 175 ns with rise time 20 ns. Both IREB sources are produced by Physics International.

Typical waveforms of the diode voltage and the beam current for the short and long IREB's are shown in Fig. 1(a) and (b), respectively. For both IREB's, foilless diode consisted of carbon cathode with hollow knife edge of 20 mm diameter and a carbon anode with 29 mm diameter aperture. The anode-cathode spacing in the diode was 5-15 mm. An annular electron beam with diameter of 20 mm and thickness of 1 mm was

injected from the diode into a conducting drift tube with inner diameter of 31 mm and a series of coaxial cavities. The system was immersed in axial magnetic field of 1 T applied by solenoid coils.

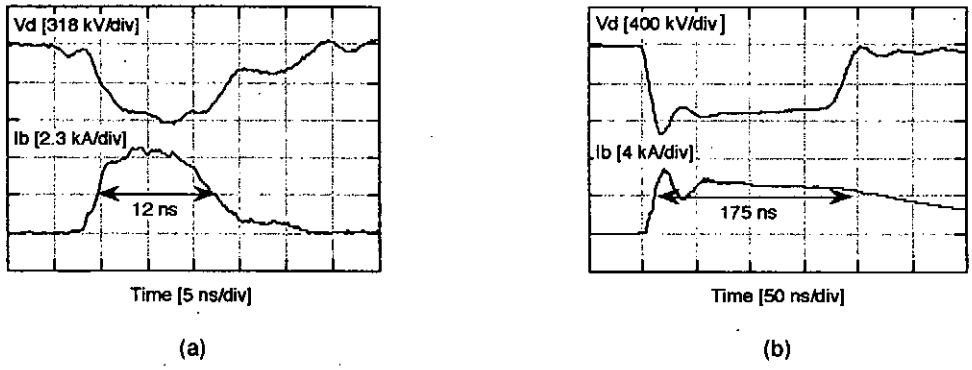

Figure 1: Typical waveforms of the diode voltage and the beam current. (a) The short pulse IREB. (b) The long pulse IREB.

Three type arrangements of coaxial cavities were utilized in the experiments. At first, a series of four cavities with length of 75 mm was utilized to obtain 1 GHz automodulation with both the short and the long IREB's. At the second, a single cavity was utilized to examine how the relation between rise time of beam current and cavity length affected the modulation level. And the third, a series of cavities with decreasing length adjusted 300-150-75-75 mm was utilized. The second and the third experiments were carried out for only the short pulse IREB.

In any experiments, the first cavity was connected to the drift tube via gap at $z = 16$ cm, where z is the distance from the anode. The gap spacing in any cavity was 2.5 cm and the impedance of any cavity was 76 Ω. The base pressure in the system was maintained below 1×10^{-5} Torr.

A Faraday cup was used to measure the beam current at various locations along the axis in the drift tube and to estimate the kinetic energy of beam electrons. Aluminum foils of various thicknesses were placed in front of the Faraday cup and a transmitted current through aluminum foils was measured. Using the ratio of the transmitted current to the current detected without foil and the range-energy relations [9], the kinetic energy of beam electrons was estimated. A magnetic analyzer located at the end of the drift tube was used to check the electron kinetic energy obtained by the range-energy relations. And the measured energy was in good agreement with the estimated one.

Magnetic probes were also used to measure the beam current and the current at the end of cavity. The differentiated currents detected by magnetic probes were integrated numerically.

The signals were monitored by Tektronix TDS 684A digitizing oscilloscope (1 GHz, 5 GS/s).

3 Experimental Results and Discussion

3.1 Four cavities experiment

Following the experimental results of M. Friedman [7], we employed a series of four cavities with the same lengths to obtain highly modulated IREB's. A schematic diagram of the four cavities experiment is shown in Fig. 2. The length of each cavity is 75 mm.

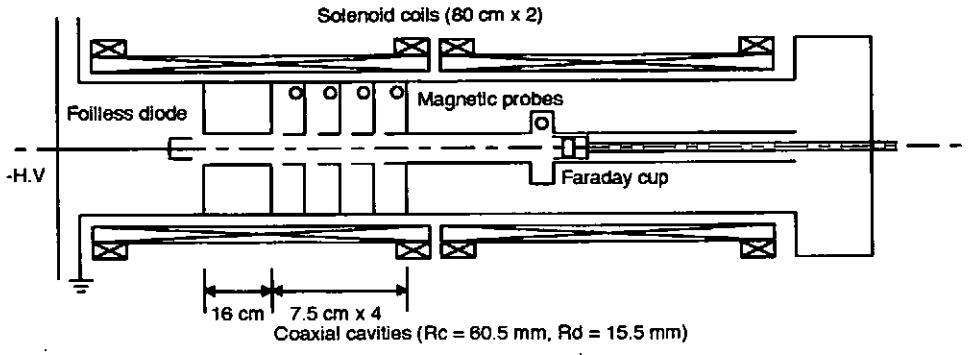

Figure 2: A schematic of the four cavities experiment.

The round trip time of electromagnetic wave for the cavity is 0.5 ns. The beam decelerated and accelerated with 0.5 ns intervals at the gaps was expected to result in the trains of 0.5 ns electron bunches, i.e. 1 GHz modulation. The experimental results are shown in Fig. 3 for the short and the long pulse IREB's. High level current modulations with 1 GHz frequency were observed by the short pulse IREB. The electron energy of the accelerated part increased to 900 keV was observed with less than 1 ns duration as shown in Fig. 4. However, only a weakly modulated electron beam was observed with the same four cavities for the long pulse IREB. We noticed the difference of the current rise time between the short and the long pulse IREB. The current rise time of 20 ns for the long pulse IREB was considered to be too long for the high level automodulation in comparison with the round trip time of the cavity of 0.5 ns. So that we investigated how the ratio between the beam current rise time and the round trip time of the cavity for electromagnetic wave affected on the level of current modulation.

3.2 Single cavity experiment

A single cavity whose length was changeable was utilized for the short pulse IREB. The cavity length was adjusted to 75, 150, 300 mm. The Faraday cup waveforms detected at $z = 50$ cm for each cavity length are shown in Fig. 5. No fluctuation in beam current was observed for IREB propagation through a smooth drift tube [Fig.5 (a)]. The round trip times for 75 and 150 mm cavities are shorter than the current rise time of 2 ns. The experiments with a 75 mm cavity resulted in suppression of the modulation amplitude.

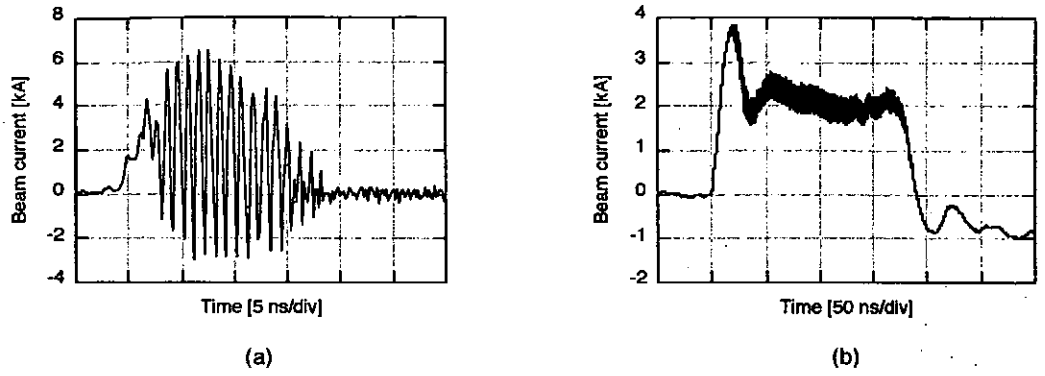

Figure 3: Waveforms of the beam current after four cavities. (a) The short pulse IREB. (b) The long pulse IREB.

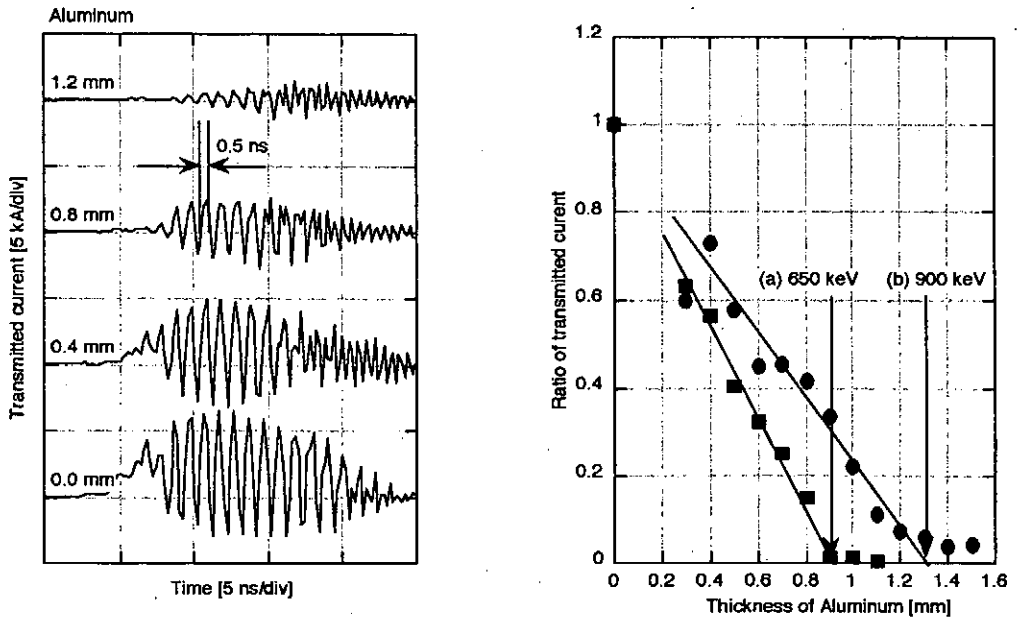

Figure 4: The estimation of the electron energy. (left) The current after aluminum foil. (right) The ratio of the transmitted current to the current without foil.

With a 150 mm cavity, we observed current modulation. In the case of a 300 mm cavity, the highest level of modulation was obtained. The Fast Fourier transform of the Faraday cup waveforms showed that the fundamental frequencies of fluctuations were 0.5 and 0.25 GHz for 150 and 300 mm cavities, respectively. These frequencies corresponded to the round trip times for electromagnetic wave in each cavity. However, the expected frequency of 1 GHz for the 75 mm cavity was not observed clearly because of its low level fluctuations. The waveforms of the magnetic probes in the cavity corresponded to those of the Faraday cup. Poor fluctuations were also observed with frequency of 1 GHz by the magnetic probe in the 75 mm cavity, though high level fluctuations were detected in the150 and 300 mm cavities.

Electron energies after the single cavity were measured by the Faraday cup with aluminum foils. Though the electron energy with the 75 mm cavity was observed to be 650 keV, i.e. no energy increase, electron energies increased to 700 keV and 800 keV for 150 mm and 300 mm cavities, respectively.

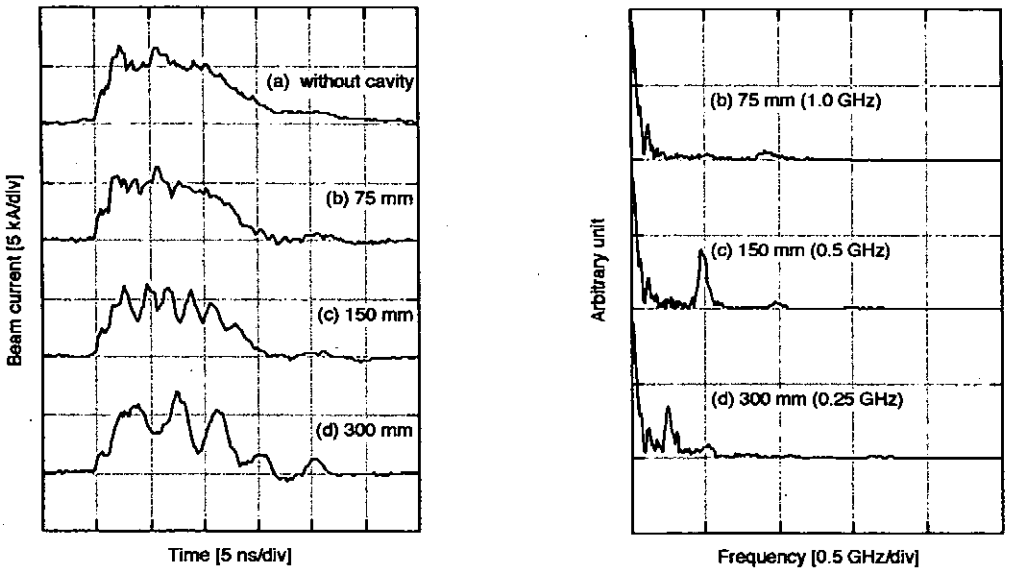

Figure 5: Waveforms of the faraday cup. (left) The beam current after single cavity. (right) The Fourier transforms of the beam current.

The energy increase should be related to the induced voltage across the gap. The gap voltage, $V_g(t)$ was expressed as the equation below by transmission line theory.

$$V_g(t) = Z \times (I(t) - 2I(t - T) + \cdots,), \tag{1}$$

where Z is the impedance of the cavity, I is the beam current and T is the round trip time for electromagnetic wave in the cavity. In Fig. 6, the energy increases were estimated by the calculated gap voltage and the experimental results are plotted. They agreed qualitatively. The presence of the beam was not included in the transmission line theory.

So that we employed a simulation code KARAT [10] based on the particle-in-cell method [11]. The results of the simulation showed good agreement with experiments as shown in Fig. 6.

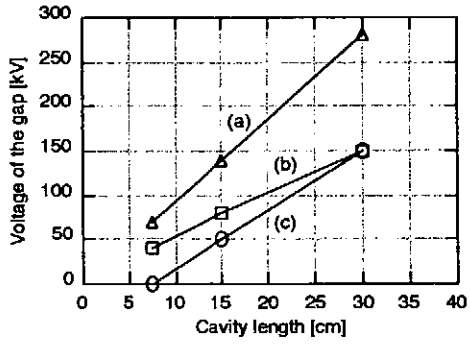

Figure 6: The gap voltage or the increase of the energy.(a) Transmission line theory. (b) Simulation. (c) Experiment.

The current waveforms passing through the gap obtained by the simulation are comparable to those detected by the Faraday cup as shown in Fig. 7. KARAT was also able to simulate the four cavities experiments with a short and a long pulse IREB. We concluded that KARAT was useful to simulate our experiments.

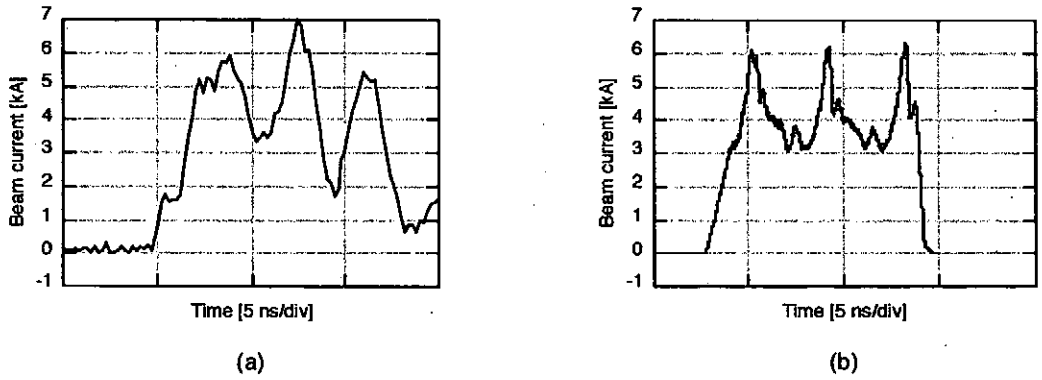

Figure 7: Waveforms of the beam current after 300 mm cavity. (a) Experiment. (b) Simulation.

Now, it becomes clear that the rise time of the current should be shorter than the round trip time of the cavity to obtain high level current modulation. However, it is impossible to modify the machine to decrease the rise time of the long pulse IREB. We noticed that the rise time of the beam current was improved by cavity modulation. Therefore, we tried to utilize the 150 and/or 300 mm cavities in front of 75 mm cavity to decrease the rise time.

3.3 Decreasing length cavities experiment

A series of cavities with lengths of 300-150-75-75 mm was utilized to obtain high level current fluctuations with frequency of 1 GHz for the short pulse IREB. The Faraday cup waveforms as shown in Fig.8 indicated that the levels of current fluctuations were increased. The level of current fluctuations of the 300-150-75-75 mm cavities was higher than those of the 75-75 mm cavities. The fundamental frequencies of the current fluctuations were about 1 GHz. The energy increase of the accelerated part was 250 keV. The appropriate numbers and lengths of the cavities at each stage for high level current fluctuations must be examined. The use of decreasing length cavities should make high frequency and high level current fluctuations possible for the IREB with slow rise time.

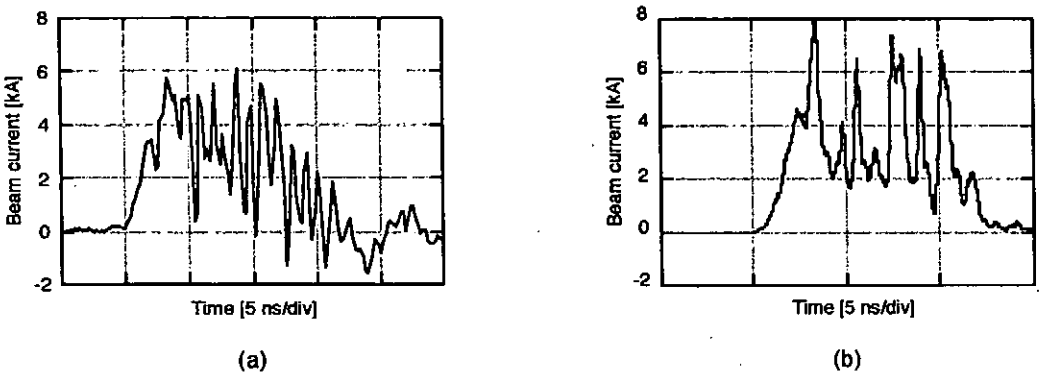

Figure 8: Waveforms of the beam current after the decreasing length cavities for the short pulse IREB. (a) Experiment. (b) Simulation.

The results of the simulation showed good agreement with the experimental results as shown in Fig. 8. And the simulation suggested that the level of modulation should increase as shown in Fig. 9 when the decreasing length cavities were applied to the long pulse IREB. The experiments should be continued to obtain subnanosecond trains of electron bunches from the long pulse IREB with decreasing length cavities.

4 Conclusion

In the experiments and the simulations in this paper, it becomes clear that the current rise time of IREB's should be shorter than the round trip time for electromagnetic wave in the cavity for high level automodulation. A series of cavities with decreasing length was found to be effective to obtain trains of subnanosecond electron bunches by the automodulation scheme using IREB's with slow rise time. Developments of cavity structure and arrangements of the cavities had just started experimentally to obtain higher level current fluctuations and shorter bunch duration.

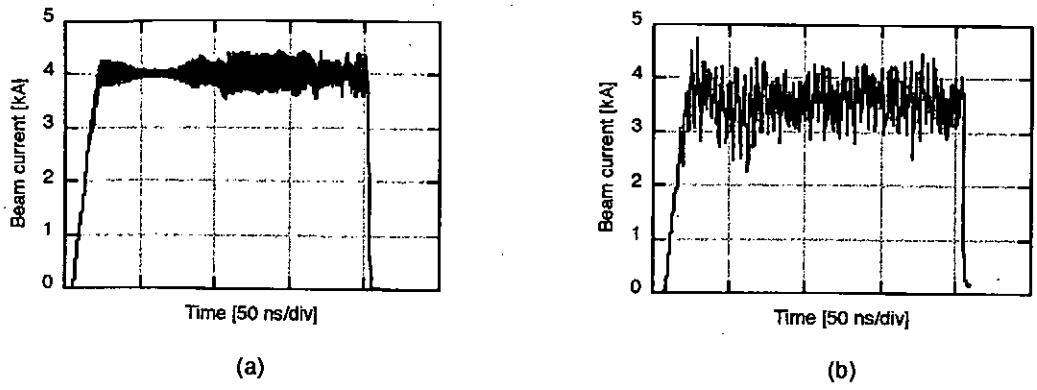

Figure 9: Waveforms of the beam current in simulation for the long pulse. (a) 75-75 mm. (b) 300-150-75-75 mm.

Acknowledgement

A part of this work is supported by a Grant-in-Aid for Scientific Research from Ministry of Education, Science, Sports and Culture, Japan

References

[1] A. Kisletsov, L. N. Kazanski and A. N. Lebedev, "Selfacceleration in intense electron beams," *At. Energ.*, vol. 30, pp. 27–31, 1971.

[2] M. Friedman, "Automodulation of an intense relativistic electron beam," *Phys. Rev. Lett.*, vol. 32, pp. 92–940, 1974.

[3] M. Friedman, "Autoacceleration of an intense relativistic electron beam," *Phys. Rev. Lett.*, vol. 31, pp. 1107–1110, 1973.

[4] K. Kamada, D. Hasegawa, K. Shimizu, R. Andou and M. Masuzaki, "Two-stage autoacceleration using decreasing length cavities," *IEEE Trans. Plasma Sci.*, vol. 27, pp. 1609–1610, 1999.

[5] D. Hasegawa, K. Kamada, K. Shimizu, R. Andou and M. Masuzaki, "Four-stage autoacceleration for a subnanosecond intense relativistic electron beam," *IEEE Trans. Plasma Sci.*, vol. 28, pp. 1648–1651, 2000.

[6] N. S. Gintburg, I. V. Zotovan A. S . Sergeev I. V. Konoplev A. D. R. Phelps A. W. Cross S. J. Cooke, V. G. Shpak, M. I. Yalandin, S. A. Shunalinov, and M. R. Ulmaskulov, "Experimental observation of cyclotron superradiance under group synchronism conditions," *Phys. Rev. Lett.*, vol. 78, pp. 2365–23680, 1997.

[7] M. Friedmn, V. Serlin, A. Drobot and L. Seftor, "Self-modulation of an intense relativistic electron beam," *J. Appl. Phys.*, vol. 56, pp. 2459–2474, 1984.

[8] M. Kamada, M. Mori, K. Kamada, R. Ando, C. Y. Lee and M. Masuzaki, "Auto-modulation of an intense relativistic electron beam using decreasing length cavities," *NIFS-PROC-50.*, pp. 42–51, 2001.

[9] H. H. Seliger, "Transmission of positrons and electrons," *Phys. Rev.*, vol. 100, pp. 1029–1037, 1955.

[10] V. P. Tarakanov, "Users manual for code KARAT," vor. 7.09, 1999.

[11] C. K. Birdsall, A. B. Langdon, "Plasma physics via computer simulation," McGraw-Hill Co., 1985.

Generation of nanosecond S band microwave pulses based on superradiance

N. S. Ginzburg, I. V. Zotova, R. M. Rozental, A. S. Sergeev, M. Kamada[a)], K. Sugawara[a)], K. Kurihara[a)], H. Shirasaka[a)], R. Ando[a)], K. Kamada[a)]

Institute of Applied Physics, Russian Academy of Science, Nizhny Novgorod, Russia
[a)]Department of Physics, Faculty of Science, Kanazawa University, Kanazawa, Japan

Abstract

Modeling carried out demonstrates possibility of generation of gigawatt power level S band microwave pulse with duration of several nanoseconds using superradiation of short electron beam moving along slow-wave periodical structure. A 10 ns / 500 keV / 5 kA accelerator of Kanazawa University can be used in such experiments. It is shown that significant increasing peak power can be obtained by optimization of voltage and current pulses waveforms. Required increasing of electron energy and current by the end of electron pulse can be achieved by using self-acceleration of a short beam passing through a system of passive cavities.

1. Introduction

One attractive method of generating ultrashort electromagnetic pulses is stimulated emission from a spatially localized ensemble (bunches) of electrons. Radiation from such bunches may be considered as a classical analogue of an effect in the quantum electronics known as Dicke's superradiance [1-3]. In this process incoherent emission induces a small macroscopic polarization in the inverted medium which gives rise to the growth of an electric field and consequently an increasing polarization in space and time. After a delay a highly directional pulse of peak output power proportional to N^2 is emitted, where N is the number of emitters. In the classical region, a similar effect is involved in the process of stimulated emission in spatially localized ensembles of electrons. Naturally, superradiance of classical electrons may be associated with different mechanisms of stimulated emission (bremshstrahlung, Cherenkov, cyclotron etc [4-17]). Different types of SR were studied theoretically [4-12] and were recently observed experimentally [13-18] at infrared and millimeter wavelength bands. RADAN accelerator producing intense subnanosecond electron bunches (250-300 KeV, 1-2 kA, 0.3-1 ns) has been used in these experiments [19].

The maximal peak power of SR pulses was associated with Cherenkov emission from an electron bunches moving through a periodical slow-wave structure and interacting with

backward wave. Based on these mechanisms, generations of SR pulses have been observed experimentally at all millimeter waveband through the frequencies 35-150 GHz. For example, at central frequency 39 GHz (K band) peak power exceeded 200 MW with pulse duration less then 300 ns. Obviously, theoretical and experimental studies of superradiance should be continued in different directions. Expanding frequency range including short and long wavelengths bands is one of the interesting applications. In the case of generation of SR pulse at centimeter (X and S) wave bands, an electron pulse duration should be increased in correspondence with increasing wavelength. As a result, nanosecond accelerators can be used for production of driving electron pulse. In Section 1 of this paper planning experiments on observation of SR at the S band based on 10 ns high-current accelerator of Kanazawa University are discussed. According to simulations carried out 10 ns, 500 keV, 5 kA electron beam from this accelerator can be used for Cherenkov type SR emission to produce powerful 2-3 ns S band microwave pulses. Section 2 of present work devoted to problem of increasing peak power of SR pulses. In the previous theoretical works it was assumed that the electron pulses with a top plate waveform are the most suitable for SR as the case of steady state generation. It is shown in this paper that an accelerating voltage and current amplitude should increase over electron pulse duration to enhance peak amplitude of microwave pulse due to nonstationary nature of SR emission. One of the effective ways to realize such pulse variation it is using self-acceleration of a short beam passing through a system of passive cavities [20].

2. Simulation of S band Superradiative Emission of 10 ns Electron Beam Moving in Periodical BWO Structure

For planning experiments on observation of S band SR emission a high current accelerator (5 kA, 500 keV, 10 ns) of Kanazawa University should be exploited. The typical voltage and current pulses waveforms are shown in Fig. 1. Presently the accelerator equipped with a cold emission cathode of 2.4 cm diameter forming a tubular electron beam. For discussed experiments cathode diameter will be increased up to 5 cm. The electron beam will be transported in homogeneous 1 T magnetic field of pulsed solenoid. Electrons moving along rectilinear trajectories will interact with synchronous spatial harmonic of backward wave propagating in a periodical waveguide. The synchronism condition can be presented in the from

$$\omega = (-h + h_c)V_0, \qquad (1)$$

where ω and h are the wave frequency and longitudinal wave number of fundamental harmonic respectively, $h_c = 2\pi/\lambda_c$,

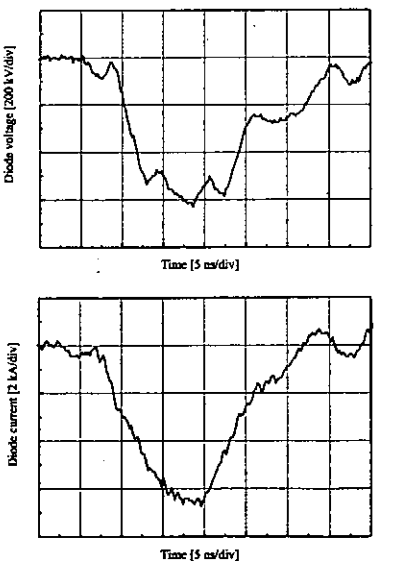

Fig. 1 Voltage and current waveforms

and λ_c is the corrugation period, $V_0 = \beta_0 c$ is the electron velocity.

Dispersion diagram presented in Fig. 2 demonstrates that radiation frequency of 4.6 GHz (S band) is expected for electron energy of 500 keV and the corrugation period of 3 cm and mean waveguide diameter of 3.2 cm.

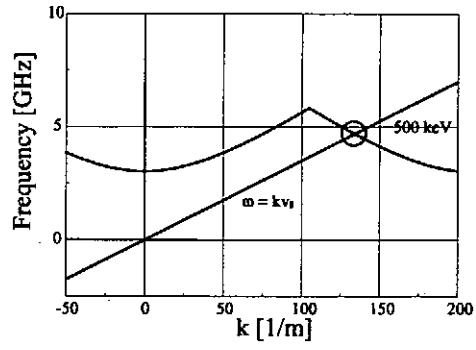

Fig 2 Dispersion diagram

Because emitted wave has negative group velocity under condition (1), cut-off narrowing should be used at cathode side of slow-wave structure to reflect wave in the positive direction where output window is installed. Meander-like corrugation should be performed using set of rings of variable internal diameter. The depth of corrugation is about 0.6 cm. At the right end corrugation depth decreases adiabatically for matching with output waveguide.

Simulation of S band superradiatiative emission of 10 nanosecond electron beam passing through the periodic waveguide structures was carried out using the particle in cell code KARAT. The number of macroparticles involved in the simulation was about 5000. The mesh used consisted of 100x1200 points.

The system geometry (all sizes in centimeters) and the positions of electrons 5 ns after the beam injection are shown in Fig. 3. The piecewise approximation was used to describe the voltage pulse with total duration 12 ns. Note that we used a model with self-consistent emission that includes simulation of electron beam formation. In the example presented the peak current was 4 kA. The phase planes (p_z, z) (Fig. 4) show a development of modulation of the electron longitudinal momentum. This modulation results in visible modulation of bunch density (Fig. 3) at moment of time 5 ns. The dependence of RF output power on time is presented in Fig. 5a. The main spike of peak power 400 MW corresponds to the expected backward wave emission. Its central frequency of 4.6 GHz (see, the spectrum in Fig. 5b) corresponds to the frequency that can be found from the synchronism condition (1).

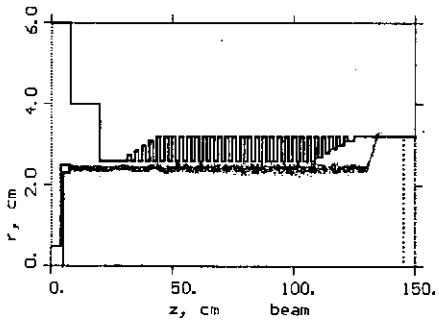

Fig. 3 Geometry of interaction space and positions of electrons at time t = 5 ns

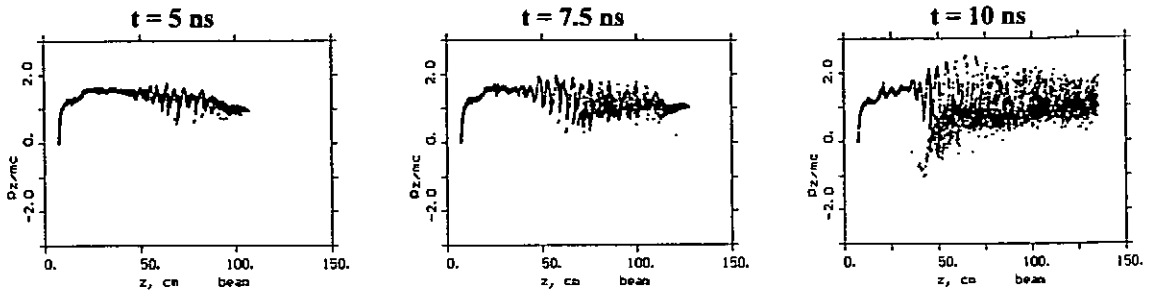

Fig 4 Evolution of positions of electrons at phase plane (p_z, z)

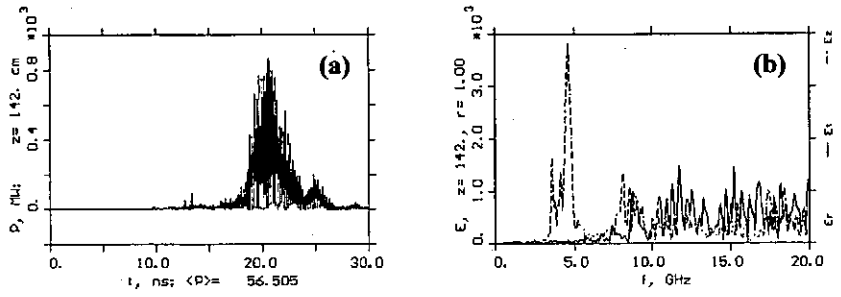

Fig 5a Microwave pulse (a) and its spectrum (b)

3. Increasing of peak power of superradiation pulse by variation of acceleration voltage and current amplitude

In the previous theoretical works [4-12] it was assumed that the electron pulses with a top plate waveform are the most suitable for SR (similar to the case of steady state generation). It is shown in this section that due to nonstationary nature of SR emission to enhance peak amplitude of microwave pulse an accelerating voltage should change over electron pulse duration. In the case of SR from an electron bunch moving through a periodical slow-wave structure and interacting with backward wave, a mechanism of this enhancement can be explained by following way. When a short SR pulse occurs inside interaction space and propagates towards a gun side, it is appropriate to feed this pulse by electrons with longitudinal velocities more and more exceeding phase velocity of the wave. Due to increasing in time SR pulse amplitude, the SR pulse can effectively extract energy from electrons with velocities strongly different from a synchronous value. Based on average time-domain model and PIC code simulations it is shown that optimization of profile of voltage

and current pulses provides possibility for increasing peak power of SR pulses in several times.

We start consideration with a model based on equation for wave amplitude and averaged motion equations of relativistic electrons. The longitudinal electric field of the synchronous wave can be presented in the form

$$E_z = Re\left[E_z^s(\mathbf{r}_\perp)A(z,t)exp(i\omega(t-z/V_0))\right]$$

where $E_z^s(\mathbf{r}_\perp)$ describes the transverse distribution and $A(z,t)$ describes a temporal evolution of the longitudinal distribution. The interaction of the electrons with radiation can be described by the following equations

$$\frac{\partial a}{\partial \tau} - \frac{\partial a}{\partial \zeta} = -f(\tau)\frac{GI}{\pi}\int_0^{2\pi} e^{-i\theta}d\theta_0 \qquad (2)$$

$$\frac{\partial \theta}{\partial \zeta} = \frac{1}{\sqrt{1-\gamma^{-2}}} - \frac{1}{\sqrt{1-\gamma_0^{-2}}} \qquad (3)$$

$$\frac{\partial \gamma}{\partial \zeta} = Re\left(a(\zeta,\tau)e^{i\theta}\right). \qquad (4)$$

Here we are using dimensionless variables:

$a = eE_z^s(r_b)A/(mc\omega)$, $\tau = \omega(t-z/V_0)\left(1/\beta_0 + 1/\beta_{gr}\right)^{-1}$, $\zeta = \omega z/c$, $\theta = \omega t - h_s z$ is the electron phase with respect to the synchronous wave, $h_s = hc - h$, $G = Zc/2\beta_0^2$, Z is the coupling impedance of the TM_{01} mode, $I = eJ_0/mc^3$, J_0 is the electron current, $\gamma = \left(1-\beta_0^2\right)^{-1/2}$ is relativistic mass factor, $V_{gr} = \beta_{gr}c$ is the electromagnetic wave group velocity. The function $f(\tau)$ describes the unperturbed electron density $f(\tau) = 1, \tau \in [0,T]$, where T is the dimensionless duration of the electron bunch.

$$T_e = \omega t_{e.pulse}\left(1/\beta_0 + 1/\beta_{gr}\right)^{-1}. \qquad (5)$$

When emission start up related with electron density fluctuations, it is described by parameter $q \ll 1$ and the boundary conditions can be presented in the form

$$\begin{aligned} &\theta|_{\zeta=0} = \theta_0 + q\cos\theta_0, \theta_0 \in [0,2\pi], \gamma|_{\zeta=0} = \gamma_0 \\ &a|_{\zeta=L} = 0, a|_{\tau=0} = 0 \end{aligned} \qquad (6)$$

where $L = \omega l/c$ is the dimensionless length of the interaction region.

Peak power of radiation can be defined as

$$P = \frac{m^2c^5}{e^2}\frac{|a|^2}{4G} \qquad (7)$$

In fig. 6, temporal dependence of radiation power in the case of voltage and current pulses of constant amplitude (top plate pulses) is shown by curve 1. Curve 2 corresponds to

the situation when accelerating pulse amplitude grows from 300 keV to 900 keV. Curve 3 correponds to the case when electron current also grows in time from 4 kA to 12 kA. We see that for the last case a peak power of SR pulse increases in 2 times in comparison with SR pulse generating from top plate electron pulse with current 8 kA and electron energy 600 keV. Note that total energy in the both electron pulses is approximately the same. It is also seen that optimization of driving electron pulse results in shortening of microwave pulse.

In Fig. 7 it is presented that instant efficiency of energy extraction $\eta = 1 - <\gamma> / \gamma_0$ in the case of top plate and optimal electron pulses. We see that efficiency increases in the case of variable accelerating voltage. It is resulted in even more remarkable increase of SR pulse amplitude because higher efficiency corresponds to part of electon pulse with higher current.

Fig. 8 demonstrates evolution over Z axis position of electons at phase plane (γ, θ) for electon fraction injected at $\tau = 25$. We see that the most of electons are decelerated at the end of interaction space.

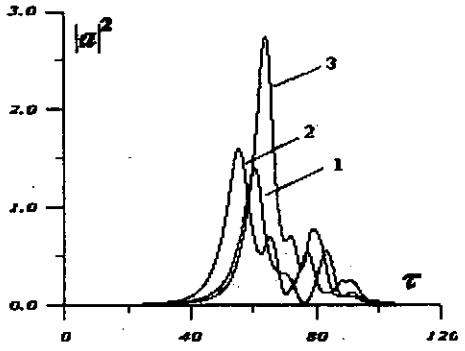

Fig. 6 Dependence of normalized radiation power on time for rectangle electron pulse curve 1, for electron pulse with only voltage variation curve 2, for pulse with variable both voltage and current curve3.

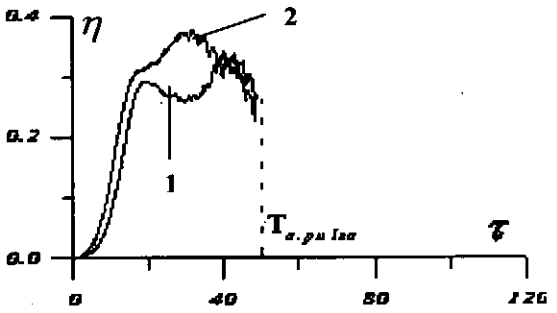

Fig. 7 instant efficiency of energy extraction in the case of rectangle (curve 1) and optimal (curve2) electron pulses

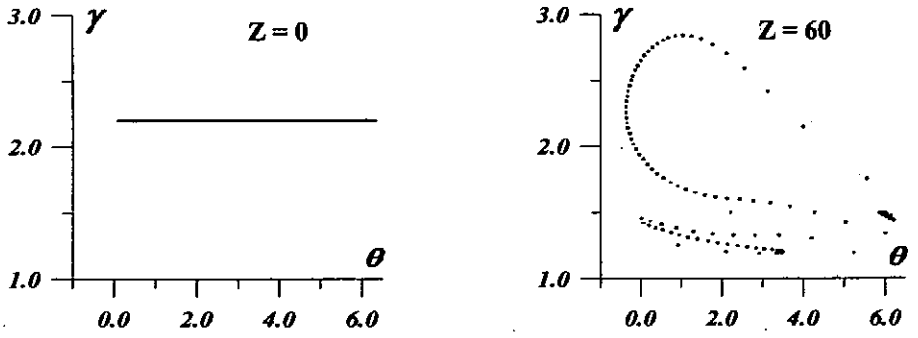

Fig. 8 Evolution of phase plane for electron fraction injected at time $\tau = 25$

4. PIC code simulation of SR from electron pulse with variable voltage and current

The results on enhancement of amplitude of SR pulse obtained in the frame of the model based on averaged equations agree with result of PIC code simulation. In this Section in difference with Sect. 2 we consider simple model that not includes beam formation. In Fig. 10a SR pulse presented in the case of voltage and current pulse variation corresponding to Fig. 1. Maximal power amounts 4 GW for average power of electron beam 4.8 GW that corresponds to instant efficiency > 80%. For comparison, Fig. 10b corresponds to SR pulse emitted by top plate electron pulse with mean voltage 6 kV and current 8 kA (the kinetic energy in such a beam equal to optimal one). We see that the gain in the SR pulse peak power exceeds factor of 2. It is also observed that pulse became much shorter than in the case of top plate electron beam. The pulse duration at the half of pulse amplitude is less then 1.5 ns. In Fig. 12 shown dependence on time several electrons injected in consecutive moments. We see that the most of electrons are decelerated in the case of the pulse of optimal waveform.

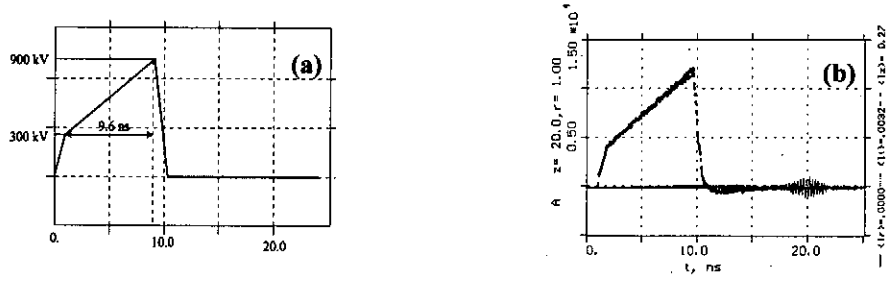

Fig. 9 Optimal accelerating voltage (a) and current (b) pulse profiles

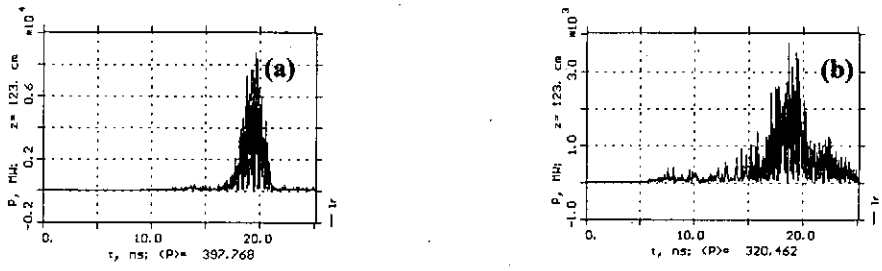

Fig. 10 (a) SR pulse for the case of optimal electron pulse (b) SR pulse for the case of rectangle electron pulse with the same energy

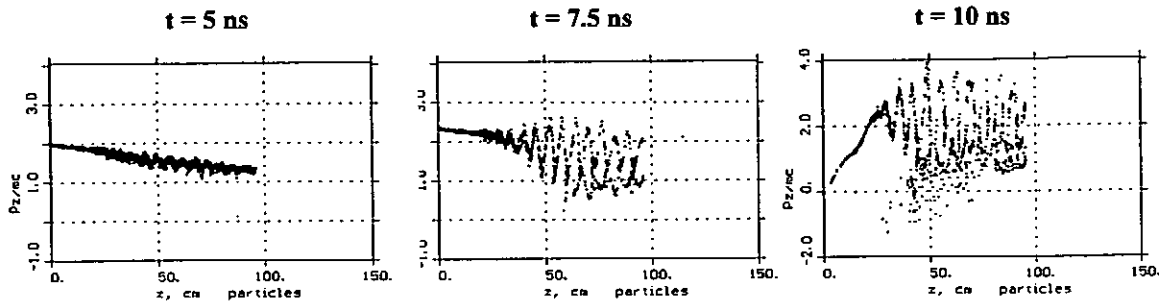

Fig 11 Evolution of positions of electrons at phase plane (p_z, z) in the case of optimal electron pulse

5. Conclusion

Modeling carried out in this paper demonstrates possibility of generation of gigawatt power level S band microwave pulse with duration of several nanoseconds using superradiation of short electron beam moving along slow-wave periodical structure. A 10 ns. 500 keV, 5 kA accelerator of Kanazawa University can be used in such experiments. It is shown that significant increasing peak power can be obtained by optimization of voltage and current waveforms. Note that required increasing of electron energy and current by the end of electron pulse can be achieved by using self-acceleration of a short beam passing through a system of passive cavities [20].

References

[1] R.H. Dicke, Phys. Rev. **93**, 99 (1954).

[2] J.C. MacGillirvay and M.S. Feld, Phys. Rev. A **14**, 1169 (1976).

[3] N. Scribanowitz, H.P. Herman, J.C. MacGillirvay and M.S. Feld, Phys. Rev. Lett. **30**, 309 (1973).

[4] R.H. Bonifacio, C. Maroli and N. Piovella, Opt.Commun, **68**, 369 (1988).

[5] R.H. Bonifacio, B.W.J. McNeil and P. Pierini, Phys. Rev. A **40**, 4467 (1989).

[6] R.H. Bonifacio, N. Piovella and B.W.J. McNeil, Phys. Rev. A **44**, 3441 (1991).

[7] N.S. Ginzburg, Sov. Tech. Phys. Lett. **14**, 197 (1988).

[8] N.S. Ginzburg, I.V. Zotova and A.S. Sergeev, Pis'ma ZhTF **15(14)**, **83** (1989)

[9] N.S.Ginzburg, Yu.V.Novozhilova, and A.S.Sergeev, Sov.Tech.Phys.Lett. 22, 359 (1996)

[10] N. Piovella, P. Chaix, G. Shvets and D.A. Jaroszynski, Phys. Rev. E **52**, 5470 (1995).

[11] G. R. M. Robb, N. S. Ginzburg, A. S. Sergeev, A. D. R. Phelps, Phys. Rev. Lett. **77**, 1492 (1996).

[12] N. S. Ginzburg, I. V. Zotova and A. S. Sergeev, Sov. Phys. JETP Lett. **60**, 513 (1994).

[13] D. A. Jaroszynski, P. Chaix, N. D. Oepts, G. M. H. Knippels, A. F. G. Van Der Meer and H. H. Weits, Phys. Rev. Lett. **78**, 1699 (1997).

[14] N. S. Ginzburg, I. V. Zotova, A. S. Sergeev, I. V. Konoplev, A. D. R. Phelps, A. W. Cross, S. J. Cooke, P. Aitken, V. G. Shpak, M. I. Yalandin, S. A. Shunailov and M. R. Ulmaskulov, Phys. Rev. Lett. **78**, 2365 (1997).

[15] N. S. Ginzburg, I. V. Zotova, A. S. Sergeev, A. D. R. Phelps, A. W. Cross, S. J. Cooke, V. G. Shpak, S. A. Shunailov, M. R. Ulmaskulov, M. I. Yalandin and V. P. Tarakanov, IEEE Plasma Science **27**, 462 (1999)

[16] N. S. Ginzburg, I. V. Zotova, Yu. V. Novozhilova, A. S. Sergeev, A. D. R. Phelps, A. W. Cross, S. J. Cooke, P. Aitken, V. G. Shpak, M. I. Yalandin, S. A. Shunailov and M. R. Ulmaskulov, Nucl. Instr. and Meth. in Phys. Rev. A **393**, 352 (1997)

[17] N. S. Ginzburg, N. Yu. Novozhilova, I. V. Zotova, A. S. Sergeev, N. Yu. Peskov, A. D. R. Phelps, S. M. Wiggins, A. W. Cross, K. Ronald, W. He, V. G. Shpak, M. I. Yalandin, S. A. Shunailov and M. R. Ulmaskulov, Phys. Rev. E **60**, 3297 (1999).

[18] M. I. Yalandin, V. G. Shpak, S. A. Shunailov, M. R. Ulmaskulov, N. S. Ginzburg, I. V .Zotova, A. S. Sergeev, A. D. R. Phelps, A .W .Cross, K. Ronald, S. M. Wiggins, 'IEEE, **28**,1615 (2000)

[19] M. I. Yalandin, V. G. Shpak, S. A. Shunailov, and M. R. Ulmaskulov, Proc.SPIE **2557**, 289 (1995)

[20] D. Hasegawa, K. Kamada, K. Shimizu, R. Ando and M. Masuzaki, IEEE trans. Plasma Sci., **28**, 2275 (2000)

STUDY ON ION INDUCED SECONDARY EMISSION ELECTRON GUN

P. R. Chalise, M. Watanabe, A. Okino and E. Hotta

Department of Energy Sciences, Tokyo Institute of Technology, Nagatsuta, Midori-ku, Yokohama, 226-8502, Japan.

ABSTRACT

A low energy (<100 keV) secondary emission electron gun has been designed, fabricated and tested. The gun is set beside a pulsed glow discharge wire ion plasma source (WIPS). Positive helium ions extracted from the WIPS are accelerated in vacuum towards the cathode surface, which is set oblique to the ion loci. By collision of ions, secondary electrons emitted from this cathode surface are then accelerated towards an electron window and form a wide electron beam. The electron window is set orthogonal to an ion extraction window and is on earth potential. In order to design a structure of cathode, which can inject the electron beam perpendicular to the electron window, the ion and electron trajectories were numerically simulated for several conditions. A wide and uniform electron beam with current density of 15 mA/cm^2 is obtained in pulse width duration of 20 μs over an area of 64.5 cm^2 at cathode voltage of 100 kV. The achieved combination of parameters (effective secondary emission coefficient $\gamma' = 6.36$, foil window transparency $\tau = 0.49$, gun efficiency $\eta = 33\%$ and average power $P_{av} = 230$ W) are attractive to use the gun in various applications requiring a large cross-section electron beam. The utilization of the gun in the electron beam induced flue gas (NO_X) treatment is underway.

1. Introduction

Secondary emission electron gun (SEEG) has been extensively used in the area requiring large cross section high-energy electron beams. The device developed in this concept have been reportedly applied in areas such as pre-ionization and excitation of laser [1,2,3,4], electron beam processing[5] etc. This paper reports a study on the fundamental characteristics of the SEEG and its possible application in electron induced irradiation of flue gas (NOx). The application of pulsed low energy (<200 keV) electron beam for the treatment of flue gases from power plants, waste incinerators and combustion boilers have been investigated using different types of electron beam sources[6,7,8]. We believe that this is the

first attempt to investigate the potential application of SEEG in flue gas treatment.

The SEEG uses a thin wire pulsed glow discharge ion source called wire ion plasma source (WIPS). The energetic positive helium ions extracted from the WIPS are accelerated in vacuum towards a negatively biased cathode. When the accelerated ions collide with nearly free electrons at the cathode surface, a kinetic emission of secondary electrons takes place. The emitted electrons are then accelerated towards an electron window and form a very wide electron beam. This configuration, where the electron window is kept on the side orthogonal to the ion extraction window is referred to as side extraction type (SET). The conventional design is referred to as vertical incident type[1,3], in which the emitted electrons are accelerated again towards the low pressure discharge region and experiencing collisions before passing to the electron window. The main advantage of this SET electron gun over the vertical incident type is that it avoids the interaction between the WIPS and the electron beam.

The SEEG offers several inherent advantages such as compact size, control from ground potential and long life. Since the ion beam controls the intensity and time response of the emerging electron beam, the gun is suitable for both a continuous and a high repetition rate operation. Besides, it provides a nearly mono-energic electron beam[3]. Any wide and uniform electron beam characterized by high efficiency, low foil attenuation and high current density is expected to offer an efficient flue gas treatment. The SEEG has demonstrated that a steady operation with electron beam current density of 15 mA/cm^2 in pulse width duration of 20 μs over an area of 64.5 cm^2 at a cathode voltage of 100 kV ensures an efficient irradiation of electron beam to the NO_X gas.

2. Device and Experiment

The details of schematic cross-section and discharge characteristics of WIPS have already been reported[9,10,11]. The experimental conditions were: charging voltage of capacitor (anode voltage) = 10 kV, helium gas pressure = 3×10^{-4} Torr, wire discharge current = 268A, pulse width (FWHM) of discharge current = 770 ns. A schematic view of side-extraction-type (SET) SEEG is shown in Fig. 1. The SET SEEG basically consists of two regions: extraction region, where ions are extracted from WIPS and the high voltage acceleration region where the ions are accelerated to the cathode plate. The extraction region basically consists of an ion extraction window, which is located between the WIPS and the electron gun. The window is a metal mesh having the dimension of 1 x 200 mm and the ion extraction efficiency (β) of such grid is 81%[11]. A flat stainless steel plate and an ion transmission window define the high voltage acceleration region. The wide electron beams are accelerated towards the electron window on their way to a gas treatment chamber through an aluminum foil (15 μm thick) supported by an aluminum honeycomb structure. The gas treatment chamber is the device where the irradiation of flue gas is supposed to take place. The entire electron gun structure

including gas treatment chamber was evacuated to the pressure of 3 x 10^{-4} Torr during the experiment.

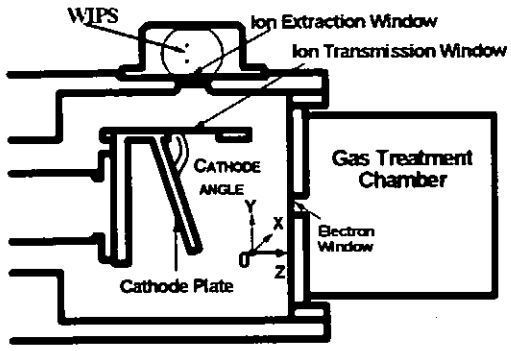

Fig. 1 SEEG gun

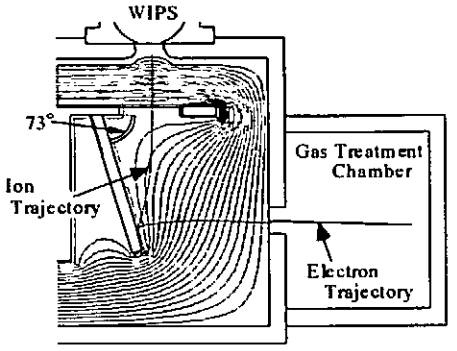

Fig.2 Numerical simulation

3. Results and discussions

The experimental results are discussed together with a numerical simulation to establish a relative understanding of particle trajectories as well as potential distribution inside the gun geometry. The numerical simulation is based on finite element method with following assumptions: Initial energy of ion is considered as 0 eV, a secondary electron is emitted without initial velocity from the ion collision position on the cathode surface.

The equipotential line, electron and ion trajectories obtained from the numerical simulation are shown in Fig. 2. The numerical simulation is also carried out to determine the optimal cathode angle in order to inject the beam perpendicularly to the electron window. The simulation gives the cathode angle of 73 degree as the optimal cathode angle[9].

3.1 V-I characteristics of Electron Gun

The voltage–current (V-I) characteristics of the SEEG have been studied on the basis of V-I curve shown in Fig. 3. The experimental values of cathode current (I_t), ion beam current (I_i) and electron beam current (I_e) are plotted against cathode voltage (V_d) up to 100 kV, a value limited by the power supply. I_t gives the total ion and electron currents impinging on the cathode surface, which was measured with a current transformer while I_e was measured using an aluminum plate collector (21 x 305 mm). I_i is calculated by subtracting I_e from I_t.

It is noticed that I_i increases linearly at lower V_d but saturates at higher V_d, the threshold value being 60 kV under the given experimental condition. The limiting values of I_i and I_e under the influence of respective space charges have been estimated using Child-Langmuir law for the planar diode. Under the following condition (d = 50 mm, V_d =100 kV) the space charge limited ion current $I_{i\,\text{Child Langmuir}}$ = 0.138 A while experimental ion current I_i =0.19 A. The authors think that following reasons are responsible for I_i being higher

than $I_{i\ \text{Child Langmuir}}$: 1) In the classical treatment of space charge limited current, zero initial velocity is assumed while the ions extracted from the WIPS contains initial velocities 2) Besides, the numerical simulation result shows a largely curved equipotential lines at the ion extraction grid, which is expected to increase the number of extracted ions.

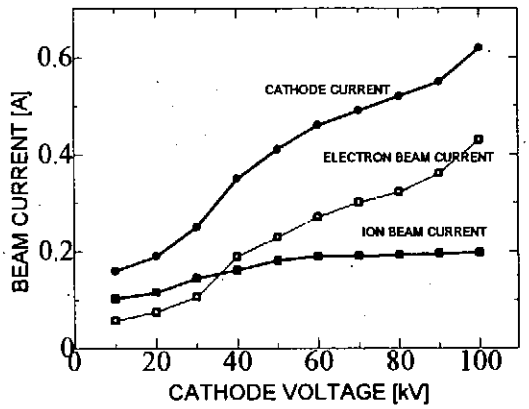

Fig. 3 Dependence of I_t, I_i and I_e *on* V_d

It is shown that I_e gradually increases with V_d, on contrary to the case of I_i. I_e depends on the secondary electron yield, which ultimately increases with V_d. Under the following condition (d=150 mm, V_d=100 kV) the space charge limited electron current $I_{e\ \text{Child-Langmuir}}$ =7.36 A while I_e=0.47 A. It is seen that I_e is well within the limiting value of $I_{e\ \text{Child-Langmuir}}$. This is due to the weak and non-uniform electric field on the cathode plate surface. (Fig. 2)

Secondary electron emission coefficient γ defined as the number of electrons emitted per incident ion has been calculated as γ=2.51 at V_d=100 kV using the following relationship.

$$\gamma = \frac{I_e}{I_i} = \frac{I_e}{I_t - I_e} \quad \text{----------(1)}$$

When the extracted helium ion collides with natural helium atoms in acceleration region, it produces energetic neutral and slow speed helium ions. Since the momentum and energy of such neutrals are approximately equal to those of the original ion, the helium particle flux incident on the cathode is larger than the ion current. It has been reported that total current of the secondary electrons due to the neutral is 1.1 times the combined current of the positive ions and positive ion secondaries[12]. Hence the value of γ has been corrected accordingly to 6.36 and referred to as effective secondary coefficient (γ').

3.2 Foil transparency

As electron beam passes through the thin foil material, the elastic scattering of electron with the foil atom leads to the attenuation of electron in both numbers and energy. The scattering of electron beam produces backscattered electrons and transmitted electrons. The transparency (τ), which is defined as the ratio of incident to the transmitted electrons, has been determined by the ratio of I_e measured before and after passing the foil window. The experiments were carried out first in the open electron window in absence of the foil and then in presence of Al foil supported by honeycomb structure. Figure 4 shows V_d dependence of I_e in an open window and in a foil window condition. The variation of τ on V_d is also shown. Almost a linear dependence of τ on V_d is noted with τ =0.49 at V_d =100 kV. Besides, τ depends on foil material and thickness. It is seen that the cut-off V_d of the 15 μm thick aluminum foil is about 40 kV under the given experimental conditions.

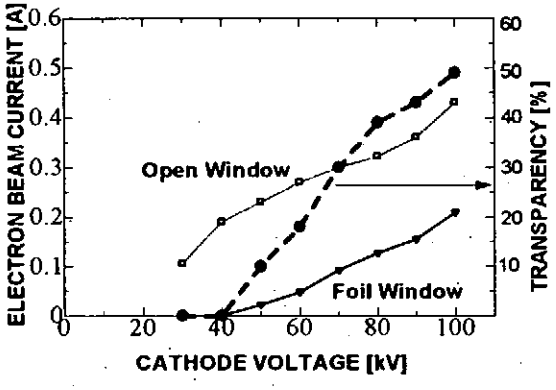

Fig.4 Dependence of I_e and τ on V_d

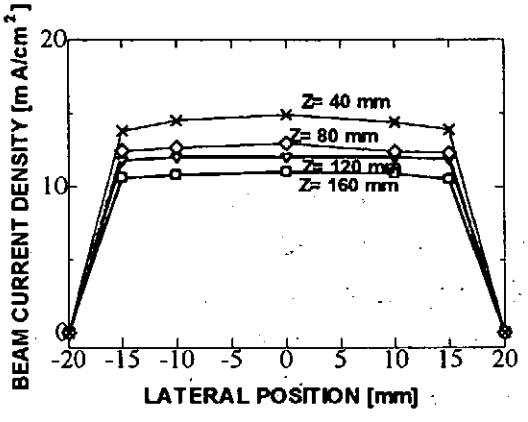

Fig. 5 Beam current density distribution

3.3 Beam Uniformity

The spatial uniformity of output electron beam has been estimated by measuring the electron beam current density distribution inside the gas treatment chamber. A number of fixed current probes (300 x 4 mm) are mounted in four acrylic plates each placed at the distances of 40 mm, 80 mm, 120 mm and 160 mm upstream of the foil. Figure 5 shows the axial resolution of the electron beam current density (axis ref. Fig. 1) inside the gas treatment chamber.

It is noted that the electron beam current density is nearly uniform around 15 mm in both the directions from the center of the electron window along X-axis. However, the electron beam current density is reduced when measured away from the center of electron window along Z-axis. The electron beam current density of 15 mA/cm^2 in pulse width duration of 20 μs has been measured at the reference point (X-axis = center of the electron window, Y-axis = 40 mm from the electron window) decided by the device consideration.

3.4 Gun Efficiency

The electrical efficiency (η) of the SEEG is defined by the ratio of power delivered by the electron beam after foil attenuation to the total power delivered to ions and electrons by high voltage supply. Since the power needed to drive the WIPS is small compared to high voltage acceleration, following equation has been derived for η neglecting the input power to the WIPS.

$$\eta = \frac{\gamma'}{\gamma'+1} \cdot \beta \cdot \tau \quad \text{---------- (2)}$$

It is noted that the efficiency is dependent on the parameters such as γ', β and τ, which are largely dependent on the quantities such as V_d, materials of ion and electron extraction. Using equation (1), at V_d = 100 kV, η is calculated as 33 % (γ'= 6.36, β = 0.8 and τ = 0.49). The available peak power at the gas treatment chamber is estimated as 23 kW (V_d=100 kV, I_e=0.47 A and τ =49%). The calculated average power of about 230 W (pulse width =10 μs, repetition rate = 1 kHz) can assure the effective NOx removal[6,13].

4. Summary

The fundamental characteristics of side-extraction-type ion induced secondary emission electron gun using wire ion plasma source have been evaluated. A wide and uniform electron beam with current density of 15 mA/cm^2 is obtained in pulse width duration of 20 μs over an area of 64.5 cm^2 at cathode voltage of 100 kV. The combination of achieved parameters (effective secondary emission coefficient γ'= 6.36, foil window transparency τ =49%, gun efficiency η =33% and average power P_{av}=230 W) with number of advantages over other types of high-energy electron gun suggest that the SET secondary emission electron gun is a desirable device for the NO_X gas treatment.

5. Acknowledgement

This work is supported in part by the Ministry of Education, Sports, Science and Technology, Japan under Grant-in-Aid for Scientific Research (No.10555088).

References

1. D. Pigache et. al., J. Vac. Sci. Technol., **12** (6) 1197 (1975)
2. C. Wu, T. Kamia, H. Sunami, E. Hotta and K. Kasuya, Fusion Engineering and Design, **44**, 365-370 (1999)
3. W. M. Clark and G. J. Dunning, IEEE J. of Quantum Electron., **QE-14** (2) 126-129 (1978)
4. N. N. Ustinovskii et.al., Rev. Sci. Instrum., **65**(9) 2941-2945 (1994)

5. H. Suezawa et.al., Vacuum, **47** (6-8) 613-616 (1996)
6. Y. Nakagawa, S. Adachi, A. Kohchi and J. Nagasawa, Jpn. J. Appl. Phys., **34**, 793-796 (1995)
7. A.V. Ignat'ev, D.L. Kuznetsov, G. A. Mesyats and Y. N. Novoselov, Sov. Tech. Phys. Lett., **18** (11) 745 (1992)
8. G. A. Mesyats and Yu. N. Novoselov: Proc. 10 th Int'l Conf. High Power Particle Beams (San Diego, 1994), p. 207
9. P. R. Chalise, M. Ishikawa, M. Watanabe, A Okino, K.C. Ko and E. Hotta, Jpn. J. Appl. Phys., **40**, 1118-1121 (2001)
10. H. Urai, E. Hotta, M.S. Maeyama, H.Yasui and T. Tamagawa, Jpn. J. Appl. Phys., **33**, 4243-4246 (1994).
11. H. Urai, T. Kurosawa, A. Okino, E. Hotta, H. Yasui, T. Tamagawa and K. C. Ko, Rev. Sci. Instrum., **68** (9) 3346 (1997)
12. G. W. Mclure, Phy. Rev., **124**(4) 969-980 (1961)
13. B. M. Penetrante, M.C.Hsiao and J.N.Bardsley, Jpn. J. Appl. Phys., **36**, 5007-5015 (1998)

Modification of BSCCO surface by excimer laser annealing

A. Ibi, T. Akitsu, and H. Matsuzawa

Faculty of Engineering, Yamanashi University, 4-3-11 Takeda, Kofu 400-8511, Japan

ABSTRACT

Irradiation of Kr-F excimer laser onto the BSCCO calcined pellets changed their surface to be amorphous. SEM micrographs showed that sintering of the irradiated pellets recrystallized the surface layer and much reduced the intergrain gaps as compared with only sintered pellets, whereas the internal structure of the irradiated pellets remained unchanged. This processing made the surface-layer grains be tightly connected, resulting in the higher critical temperatures than the conventionally sintered samples. We can say that excimer laser annealing process is a novel scheme to reduce the surface weak-link of the high-T_C superconductors.

I. Introduction

The cylindrical beam guide, Supertron [1, 2], has increasingly attracted attention for their application to magnetic flux containers for self-magnetic field pinch of plasma as well as for free-electron laser wigglers. The best performance has been demonstrated using a double-layered tube [2] consisting of a sintered layer of powder-pressed materials and a crystalline layer made from melt-processed monolith. If such a single tube is available as its wall structure is graded in grain size from small sintered to large melt-processed crystals continuously as one of functionally graded materials, or if the double-layered tube is readily prepared instead of the two-pipe configuration, then this tube would replace the double-layered tube. Therefore, we tried to irradiate Kr-F excimer laser (wavelength $\lambda = 248$ nm) onto the one side of BSCCO calcined pellets. The process of excimer laser irradiation onto the pellets and then conventional sintering is called excimer laser annealing (ELA) process. The experimental results showed that the pellets that were ELA processed had a structure similar to that of the double-layered tube. In this paper, we describe this novel method for the production of a double-layered BSCCO sample.

II. Experimental procedure

The $Bi_{1.85}Pb_{0.35}Sr_{1.90}Ca_{2.05}Cu_{3.05}O_X$ calcined powder was cold isostatic pressed into a configuration of pellets of 16 mm in diameter and 1.2 mm in thickness. After Kr-F excimer laser was irradiated onto the pellets with step-and-repeat process, they were sintered in air at 850°C for 48h, followed by slow cooling to room temperature.

Figure 1(a) shows a typical X-ray diffraction pattern of the ELA processed sample with a peak at $2\theta = 4.7°$ of 110-K phase. Figure 1(b) indicates a pattern of

excessively laser irradiated and then conventionally sintered sample, with two peaks at 4.7° and 5.7° corresponding to the 110- and 80-K phases, respectively. Thus, from Fig. 1, we determined the optimal condition for the energy density to be 0.3 ~ 0.4 J/cm^2 for realizing the samples consisting of only high-T_C phase.

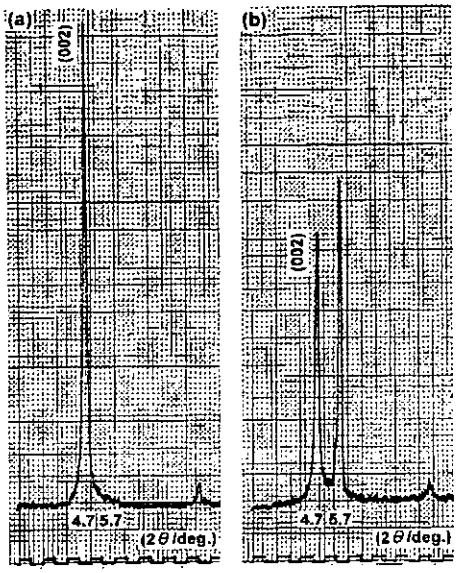

Fig. 1. X-ray diffraction patterns of (a) optimally excimer laser irradiated and then conventionally sintered sample and (b) excessively excimer laser irradiated and then sintered sample.

To evaluate the effect of overlapping of excimer laser spots, we exposed the pellets to the laser with step-and-repeat process for the following three different conditions of separation of the adjacent laser spots, with the optimized energy density. The condition tried are as follows: a separation of d = 0.19 mm of the spots, no separation, and an overlapping of d' = 0.19 mm in width of the spots. Figures 2(a)-2(c) schematically show the three different arrangements just mentioned.

Figures 3(a)-3(d) present optical micrographs of the surfaces of (a) the sample

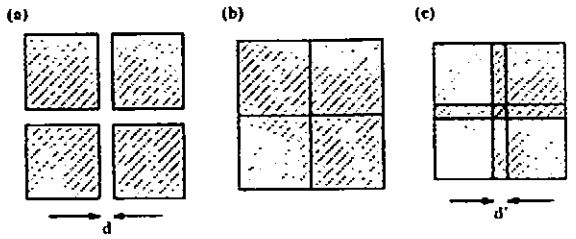

Fig. 2. Schematic visualization of three different conditions for the arrangement of (a) a separation, d, of 0.19 mm of the adjacent laser spot edges, (b) neither separation nor overlapping, and (c) an overlapped width, d', of 0.19 mm of the adjacent laser spot edges.

only cold isostatic pressed, in which the scratched marks were caused by the end surface of a press jig, (b) the laser irradiated sample with a separation of 0.19 mm of the adjacent laser spot edges, (c) the laser irradiated sample with no separation and no overlapping of the spots, and (d) the laser irradiated sample with an overlap of 0.19 mm of the adjacent laser spot edges.

Figure 4 plots the dependence of the T_Cs on the separation and overlapping between the adjacent laser spot edges for the applied DC current of 500 mA. A conventionally sintered sample had the lowest T_C as indicated at the left-bottom of Fig. 4. All the ELA processed samples had higher T_Cs than the conventionally sintered sample. In addition, the highest T_C was obtained for the exposure with no overlapping and no separation of the adjacent laser spots—the optimal condition. The decrease in T_C of the laser irradiated samples with either overlapping of or separation of the adjacent laser spots is probably caused by the deviation from the optimal condition; For the samples with overlapping of the laser spots, the narrow twice-irradiated areas would have been changed to non-Bi(2223) phase; For the samples with separations of the laser irradiated areas, the narrow unirradiated area would have had weak intergrain boundaries.

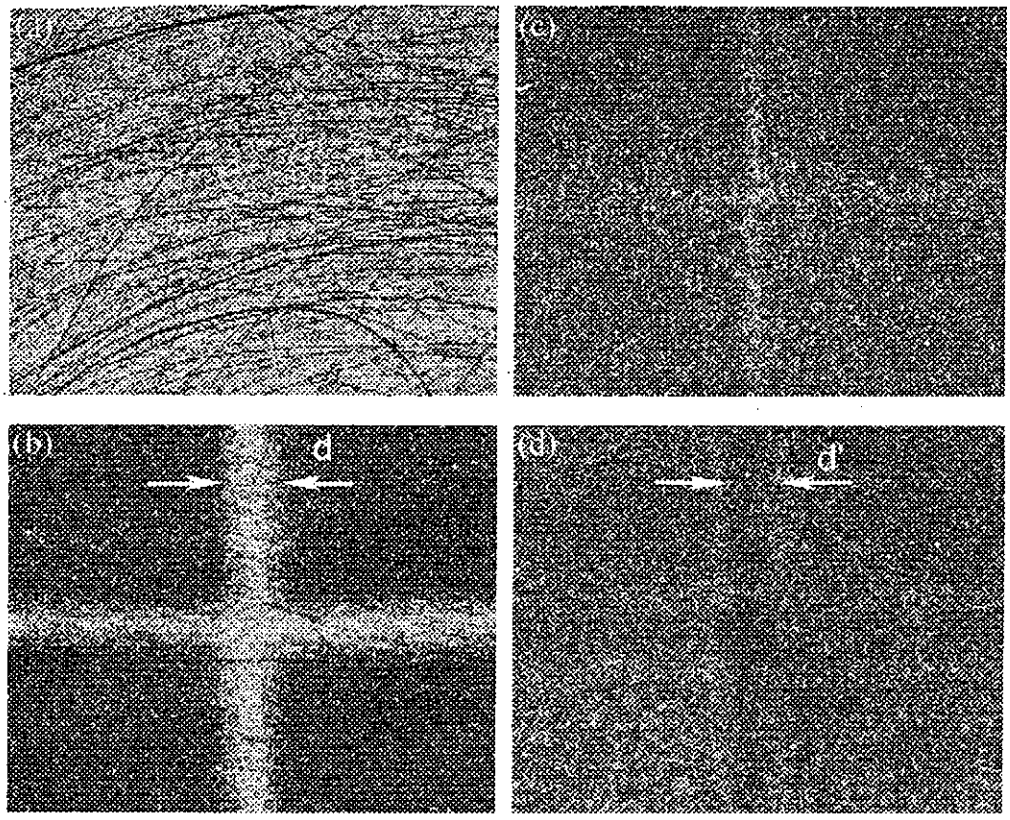

Fig. 3. Optical micrographs of the surface of (a) the cold isostatic pressed sample, (b) the laser exposed sample with a separation, d, of 0.19 mm of the adjacent laser spot edges, (c) the laser irradiated sample with neither separation nor overlapping, and (d) the laser irradiated sample with an overlapped width, d', of 0.19 mm of the adjacent laser spot edges.

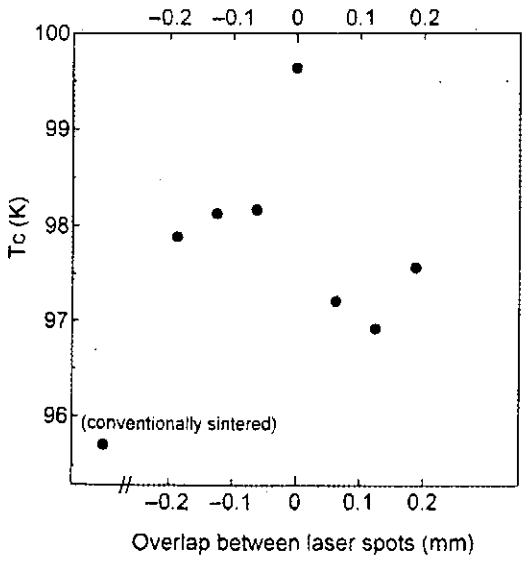

Fig. 4. T_Cs as a function of the overlapped width between the adjacent laser spots. The highest T_C was obtained for the laser exposure with neither overlapping nor separation of the adjacent laser spots.

III. Experimental results

Figures 5(a)-5(c) show SEM micrographs of the surfaces and cross-sections of the samples. Figure 5(a) shows the sample sintered in air without ELA. Figures 5(b) and (b*) indicate the excimer laser irradiated sample. The surface layer was amorphous and was a few micrometers in thickness. From Fig. 5(b*), the internal structure of the sample remained unchanged. Therefore, ELA seems to be effective for realizing a double-layered structure of the samples. Figure 5(c) shows the sample surface recrystallized by sintering in air after the ELA. When Fig. 5(c) is compared with Fig. 5(a), the ELA processed sample (Fig. 5(c)) seems to be more highly compacted than the conventionally sintered one (Fig. 5(a)).

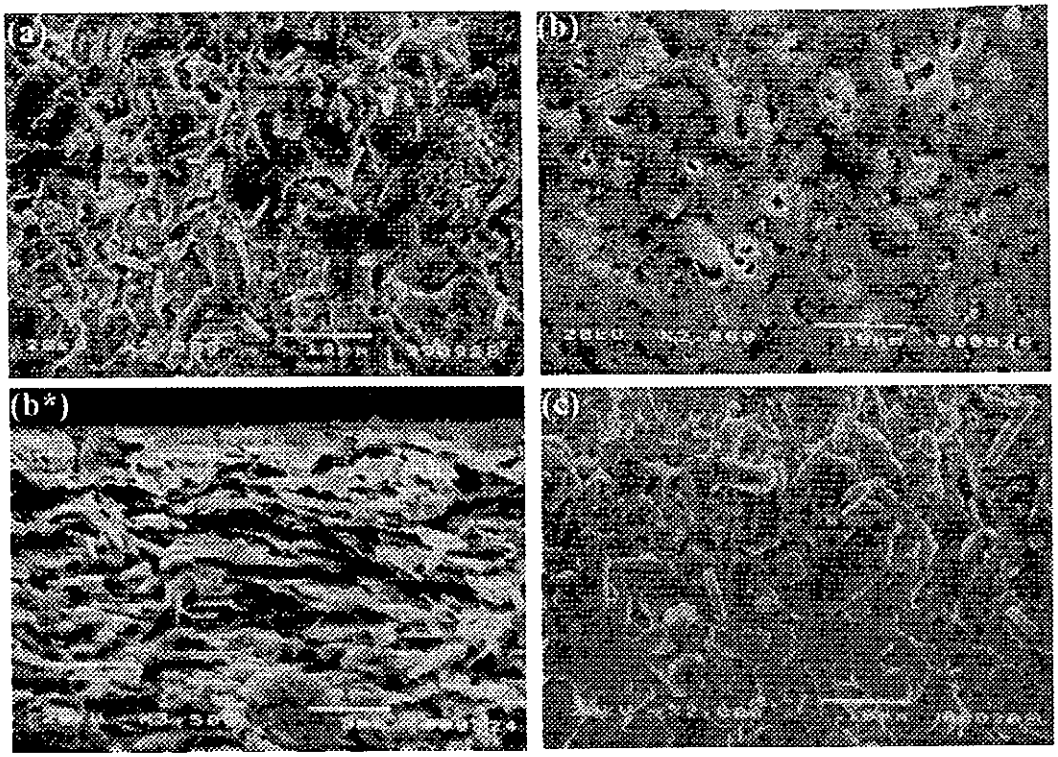

Fig. 5. SEM micrographs of the surfaces of sample (a) sintered in air without ELA, sample (b) excimer laser irradiated before sintering in air, and sample (c) recrystallized by sintering after ELA. Fig. (b*) shows the cross-section of the sample (b). Sample (c) seems to have better grain contact than sample (a).

Figure 6 shows R-T characteristics for the samples in Figs. 5(a) and 5(c) for the measuring DC current of 500 mA. The critical temperatures T_Cs for the ELA processed samples were higher than those for the conventionally sintered samples [3].

The dependence of T_Cs of the samples in Figs. 5(a) and 5(c) on the measuring currents up to 500 mA is plotted in Fig. 7. The T_Cs decreased with increasing measuring currents. These results can be explained by the following model that self-magnetic field of the measuring currents, imposed on the samples, suppressed the critical temperatures. The T_Cs of the ELA processed samples less decreased than those of the conventionally sintered ones, indicating that the intergrain gaps were more tightly connected by the additional processing of ELA and that the self-magnetic field of the measuring currents, consequently, less penetrated the ELA processed samples [3].

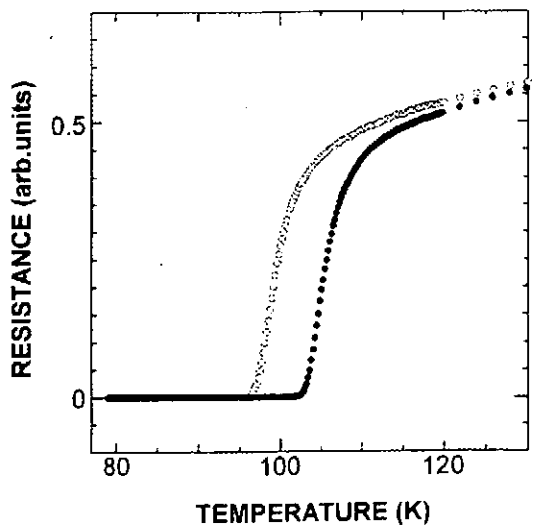

Fig. 6. Temperature dependence of resistance at 500 mA for sample (a) (open symbols) and sample (c) (closed symbols) in Fig. 5. Higher T_Cs were obtained for the ELA processed samples.

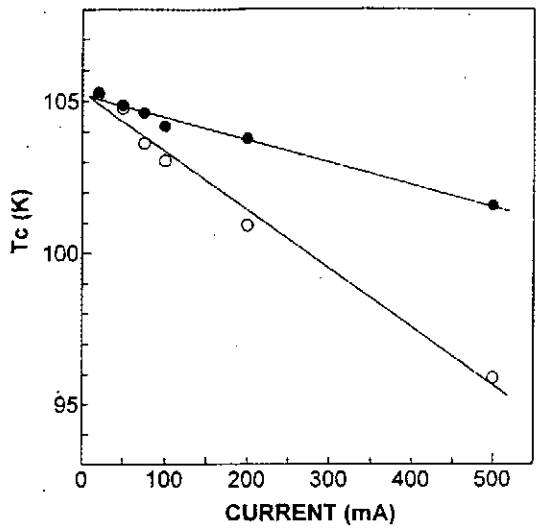

Fig. 7. Measuring direct-current dependence of T_cs for sample (a) (open symbols) and sample (c) (closed symbols) in Fig. 5.

IV. Conclusion

We have developed a novel method for synthesizing a multilayered structure of BSCCO bulk superconductors using Kr-F excimer laser annealing process. This processing made the surface-layer grains be tightly connected, resulting in the higher critical temperatures than the conventionally sintered samples.

References

1) H. Matsuzawa, J. Appl. Phys. **74** (1993) R111 [Erratum: **76** (1994) 624].
2) H. Matsuzawa, Y. Watanabe, K. Mikami, and K. Fukasawa, Jpn. J. Appl. Phys. **39** (2000) 47.
3) A. Ibi, M. Fujii, T. Akitsu, Y. Saito, and H. Matsuzawa, Physica **C 357-360** (2001) 730.

NO_X REMOVAL IN DISTANT GAS CHAMBER BY PULSED, INTENSE RELATIVISTIC ELECTRON BEAM

Go IMADA*, Tomoki SAKURAI, Nobuaki OHSHIMA, and Kiyoshi YATSUI

Extreme Energy-Density Research Institute, Nagaoka University of Technology, Nagaoka, Niigata 940-2188, JAPAN

*e-mail: imada@nagaokaut.ac.jp

ABSTRACT

Treatment of NO_X has been studied using a pulsed, intense, relativistic electron beam (PIREB). The dependence of NO_X concentration and the removal efficiency of NO_X on the number of PIREB shots have been investigated within a chamber spatially isolated from the electron beam source. The isolated chamber is filled up with a dry-air-balanced NO gas mixture with the pressure of 270 kPa, and is irradiated by the PIREB (2 MeV, 2.2 kA, 35 ns) passing through a 1.6-m-long atmosphere. With the initial NO concentration of 88 ppm, ~ 70 % of NO_X is removed by firing 10 shots of PIREB. The NO_X removal efficiency has been found to be 0.2-1 μmol/J.

I. Introduction

The flue gases produced by the electric power plants, ironworks and diesel engines have caused serious environmental problems in the earth. For example, a large amount of NO_X may result in the acid rain and/or the photochemical smog. The injection of a pulsed, intense, relativistic electron beam (PIREB) into a flue gas is expected to be effective for pollutant removal. In the removal of NO_X by PIREB, NO_X reacts with the radicals, such as O, N, OH, HO_2 and so on. The radicals are formed by the collision of the electrons with the atoms or molecules in the flue gas. The PIREB is able to produce a lot of radicals simultaneously due to the high current density. It is reported that the removal efficiency of NO_X can be improved by utilizing a pulsed electron beam.[1-4] The electrons of PIREB have large kinetic energy, resulting in long *range* in the gas. For example, the *range* of PIREB at 2 MeV is calculated to be ~ 9 m in an atmosphere.[5] Therefore, the PIREB irradiation is believed to be a promising candidate for NO_X removal in the elongate chimney at electric power plants and in

the tunnels for automobiles.

We have studied the NO_X removal by PIREB of the beam energy of the order of 1 MeV using a pulsed power generator, "ETIGO-III" (8 MV, 5 kA, 50 ns). In this study, the dependence of NO_X concentration and the removal efficiency of NO_X on the number of PIREB shots have been investigated within a chamber spatially isolated from the electron beam source. The spatially isolated chamber is filled up with a dry-air-balanced NO gas mixture with the pressure of 270 kPa, and is irradiated by the PIREB passing through a 1.6-m-long atmosphere.

II. Experimental Setup

Figure 1 shows the schematic diagram of the PIREB generator, "ETIGO-III".[6] It consists of a Marx generator, a pulse forming line, and induction acceleration cells of four stages. The Marx generator is charged up to 680 kV with the stored energy of 3 kJ. The output voltage of the pulse forming line is ~ 670 kV, which is fed to the four acceleration cells through the transmission lines in parallel. Three amorphous-metallic magnetic cores are installed in each cell, producing approximately 2 MV per cell (670 kV×3). The magnetic cores are characterized by the following properties; B_S (saturated magnetic-flux density) > 1 T, ΔB (flux swing) ~ 2.1 T, and Vt product ~ 0.034 Vs. The electron beam with the energy up to 2 MeV is generated by an electron-beam diode placed at the first acceleration cell. The field-emission foilless diode with a hollow cathode is used to generate the electron beam. The inner and outer diameters of the cathode are 59.5 mm and 60 mm, respectively. This electron beam is accelerated by each acceleration cell, and the maximum energy of the PIREB increases up to ~ 8 MeV.[7]

Figure 2 shows the schematic of the experimental apparatus. It consists of an electron-beam diode, drift tube, PIREB-gas interaction chamber, external magnetic field, gas mixer,

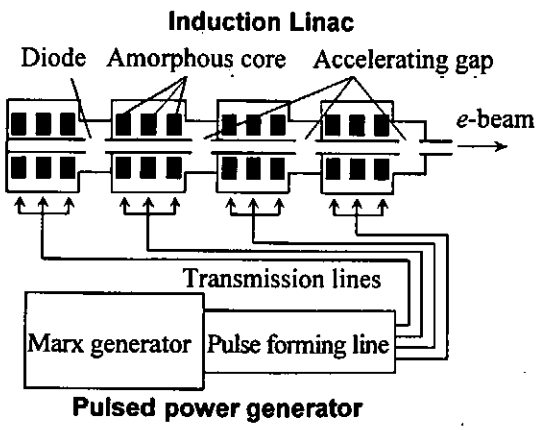

Fig. 1 Schematic of "ETIGO-III".

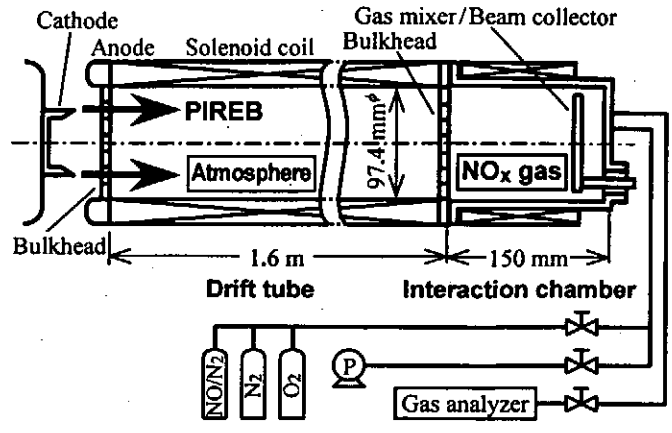

Fig. 2 Schematic of experimental apparatus.

and gas system. The PIREB generated by "ETIGO-III" is injected into the interaction chamber through not only the two bulkheads but also the 1.6-m-long drift tube filled up with air. The bulkheads consist of a titanium foil with a thickness of 40 μm and a stainless-steel honeycomb flange with the optical transparency of ~ 50 %. At the PIREB energy of 2 MeV, the energy loss of the electron through the titanium foil and the 1.6-m-long atmosphere are calculated to be ~ 26 keV and ~ 330 keV, respectively.[5] The PIREB is guided by an external magnetic field (~ 0.5 T) through the drift tube and the interaction chamber. The PIREB-gas interaction chamber is made of a stainless-steel pipe. After the interaction chamber is evacuated to ~ 20 Pa by the rotary vacuum pump, it is filled up with a dry-N_2/O_2-balanced NO gas mixture with the total pressure of 270 kPa to simulate the flue gas. The concentrations of NO, NO_2, and NO_x (= NO + NO_2) are measured by a controlled potential-electrolysis gas analyzer after mixing up the gas mixture for 3 minutes.

III. Results and Discussion

a) Propagation of PIREB in drift tube and interaction chamber

Figure 3 typically shows the time evolution of the electron beam diode voltage (V_d) and PIREB current (I_d and I_c), where I_d and I_c are measured by a Faraday cup with a pick-up coil placed at the inlet of the drift tube and the end of the interaction chamber, respectively. The peak currents of I_d and I_c are observed to be ~ 2.2 kA and ~ 30 A at V_d ~ 2 MV, respectively. The pulse width of I_d and I_c is approximately 100 and 35 ns (full width at half maximum), respectively. The injected PIREB energy into the interaction chamber (ε) is estimated to be ~ 1.5 J from the time integral of the product of V_d^* and I_c, where V_d^* is the reduced PIREB voltage (V_d^* = V_d - 382 kV).

Figure 4 shows PIREB damage patterns recorded on an acrylic plate (thickness = 10 mm). It is found that the PIREB propagates up to the interaction chamber. The profile of PIREB seems to be circle according to the shape of the cathode of electron beam diode. The diameter of PIREB is estimated to be ~ 60 mm at z = 0.8 m.

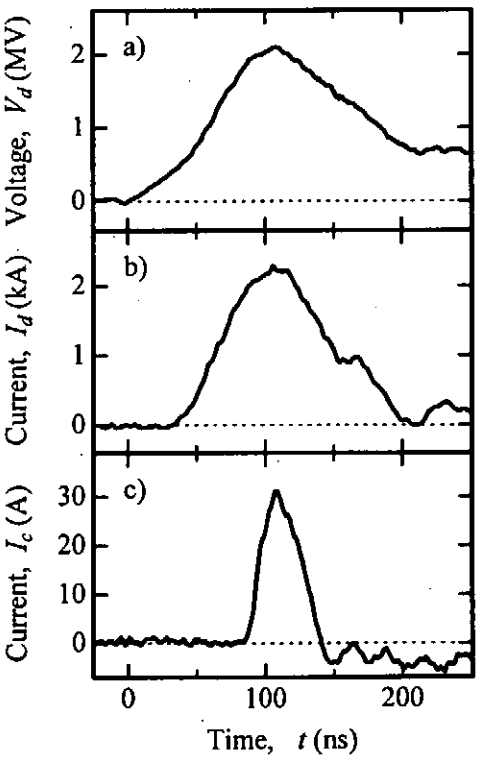

Fig. 3 Time evolution of diode voltage and PIREB current: a) voltage, b) current at inlet of drift tube, c) current at end of interaction chamber.

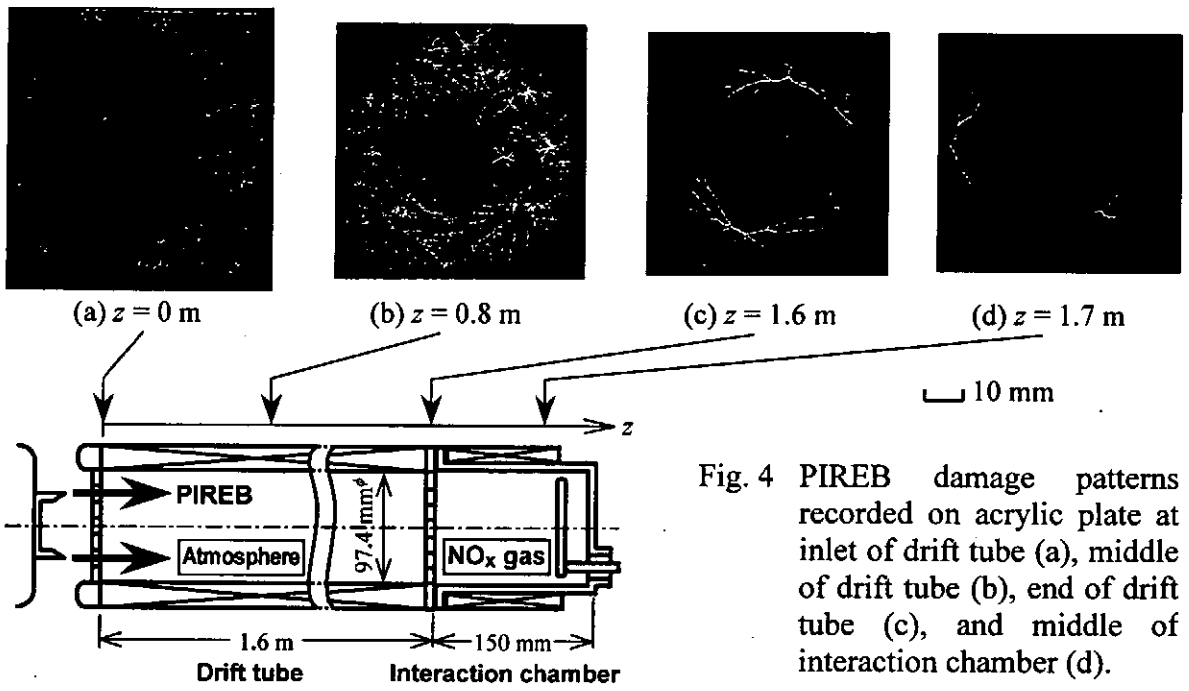

Fig. 4 PIREB damage patterns recorded on acrylic plate at inlet of drift tube (a), middle of drift tube (b), end of drift tube (c), and middle of interaction chamber (d).

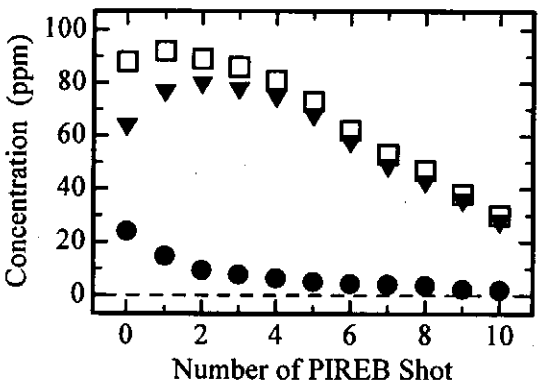

Fig. 5 NO, NO_2, and NO_X concentrations as a function of number of PIREB shots: ● NO, ▼ NO_2, □ NO_X.

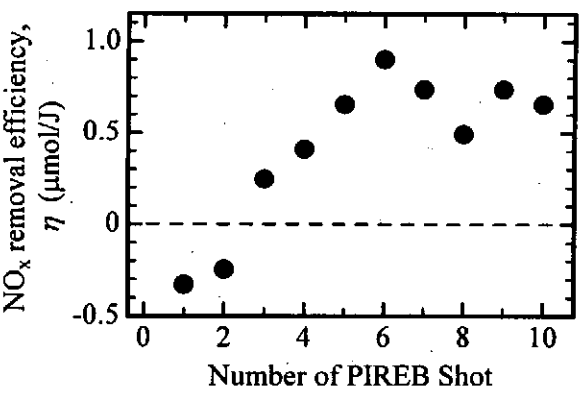

Fig. 6 NO_X removal efficiency as a function of number of PIREB shots.

b) NO_x removal in distant chamber by PIREB

Figure 5 shows the NO, NO_2, and NO_X concentration as a function of the number of PIREB shots for the initial NO concentration of 88 ppm in the dry-N_2/O_2-balanced NO gas mixture with the composition of $N_2:O_2$ = 8:2, where the NO_X concentration is defined as the sum of NO and NO_2 concentrations. A certain amount of NO is oxidized by ambient O_2 without firing the PIREB, and therefore, the NO concentration equilibrates to ~ 24 ppm, and

then ~ 64 ppm of NO_2 is produced. It is found from Fig. 5 that the NO is removed by the irradiation of PIREB. Until the second shot of PIREB, on the other hand, NO_2 is generated by the irradiation of PIREB because of high NO concentration. The NO_2 concentration decreases in proportion to the number of PIREB shots after the third shot of PIREB when the reduction of NO_2 may exceed the oxidation of NO. We found that ~ 70 % of NO_x is removed by firing 10 shots of PIREB. Thus, NO has been almost treated by the irradiation of PIREB.

Figure 6 shows the NO_x removal efficiency (η) as a function of the number of PIREB shots, where the experimental conditions are the same as those in Fig. 5. Here, η is defined as $\eta = q/\varepsilon$, where q is the amount of NO_x removal in each shot. Until the second shot of PIREB, η is negative because of the generation of NO_2. It is seen from Fig. 6 that η is estimated to be 0.2-1 μmol/J. It is found that η tends to increase with decreasing the NO_x concentration in the gas mixture (cf. Fig. 5).

IV. Conclusions

Nitrogen oxide within the interaction chamber spatially isolated from the electron beam source has been successfully removed by the irradiation of PIREB. The following results can be drawn from the present investigation.

1) With the initial NO concentration of 88 ppm in the dry-N_2/O_2-balanced NO gas mixture with the pressure of 270 kPa, ~ 70 % of NO_x is removed by firing 10 shots of PIREB.
2) The NO_x removal efficiency of 0.2-1 μmol/J is obtained.

Acknowledgements

This work was partly supported by Grant-in-Aid for Encouragement of Young Scientists from the Ministry of Education, Culture, Sports, Science, and Technology in Japan. The authors would like to thank Mr. Y. Sekimoto for help with the mechanical design and experiment.

References

1) B. Penetrante: "Removal of NO_x from Diesel Generator Exhaust by Pulsed Electron Beams", *Digest of Technical Papers on 11th IEEE Int'l Pulsed Power Conf.*, **I**, 91-96 (1997).
2) Y. Nakagawa and H. Kawauchi: "Pulse Intense Electron Beam Irradiation on the Atmospheric Pressure N_2 Containing 200 ppm of NO", *Jpn. J. Appl. Phys.*, **37**, 5082-5087 (1998).

3) T. Ikegaki, S. Seino, Y. Oda, T. Matsuda, G. Imada, W. Jiang, and K. Yatsui: "Flue Gas Treatment by Pulsed Relativistic Electron Beam", *Proc. 13th Int'l Conf. on High-Power Particle Beams*, **2**, 934-937 (2001).
4) T. Ikegaki, S. Seino, Y. Oda, T. Matsuda, G. Imada, W. Jiang, and K. Yatsui: "Flue Gas Treatment by Intense Pulsed Relativistic Electron Beam", *Jpn. J. Appl. Phys.*, **40**, 1104-1107 (2001).
5) M. Berger, S. Coursey, and A. Zucker: *ESTAR: Computer Programs for Calculating Stopping-Power and Range Tables for Electrons* (ver. 1.21), [Online available]: http://physics.nist.gov/Star [2001, July 19], National Institute of Standards and Technology, USA.
6) A. Tokuchi, N. Ninomiya, K. Yatsui, G. Imada, Q. Zhu, W. Jiang, and K. Masugata: "Development of High Energy Induction Accelerator, "ETIGO-III"", *Proc. 12th Int'l Conf. on High-Power Particle Beams*, **1**, 175-178 (1998).
7) Y. Oda, T. Matsuda, S. Seino, T. Ikegaki, G. Imada, W. Jiang, and K. Yatsui: "Electron Energy Measurement for Induction Linear Accelerator "ETIGO-III"", *Proc. 13th Int'l Conf. on High-Power Particle Beams*, **2**, 544-547 (2001).

CHARACTERISTICS OF DEPOSITION PROCESS OF THIN FILMS BY ION-BEAM EVAPORATION

Shinji Kitayama, Fumito Endo, Tsuneo Suzuki, Hisayuki Suematsu, Weihua Jiang, and Kiyoshi Yatsui

Extreme Energy-Density Research Institute, Nagaoka University of Technology
Nagaoka, Niigata 940-2188

ABSTRACT

Intense pulsed ion-beam evaporation (IBE) has been proposed as one of the new techniques for the preparation of thin films. To understand the basic process of thin film deposition, the energy deposition on the substrate surface by ablation plasma was measured by using calorimetric technique. The characteristics of prepared thin films were studied with deposition energy. In addition, the substrate temperature was calculated, based on the experimental results, by using one-dimensional simulations only considering heat conduction.

I. Introduction

When an intense pulsed light ion beam (LIB) is irradiated onto a solid target, high-temperature, high-density ablation plasma is produced by the energy deposition of the ion beam. Intense pulsed ion-beam evaporation (IBE)[1-3], which deposits thin films on the substrate by utilizing the above plasma, has been proposed for preparing thin films as a new technique. After that, various kinds of thin films have been prepared successfully[4-9]. On the other hand, in order to prepare each thin film, considerable understanding of the deposition process is required. We have investigated the energy density deposited on the substrate and the characteristics of the thin films prepared by IBE. In addition, based on the results of deposited energy and the existing time of the ablation plasma by high-speed photography, time evolution of the substrate temperature was calculated by using one-dimensional heat conduction model.

When a charged particle beam is irradiated onto a solid target, the target gains thermal energy in a volume between the surface and the range of ions which depends on the initial ion energy and the target material. When a very short pulsed ion beam is utilized, the part of the surface within the ion range is heated rapidly. Since the range of LIB is very short (for

example the range of 1 MeV proton (H^+) ion ~ 10 μm), the energy of the ion beam is deposited in a very thin layer near the surface. When its energy is deposited, the layer can be heated, melted, vaporized and ionized. As a result, high-density ablation plasma is produced. Solid materials such as ceramic, metal or alloys, can be used as the targets for IBE.

The ablated plasma that is produced near the surface of the target expands in vacuum, resulting in a plasma flow in a direction perpendicular to the target. When the ablation plasma reaches the substrate which is located near the target, a thin film is deposited by the solidification of the ablation plasma.

The features of IBE method are summarized as follows.

1) Since the temperature of the target surface is heated up to higher than several thousands of degrees, materials with high melting point can be easily ablated.[5)]
2) Due to the high-density plasma, the instantaneous deposition rate exceeds more than a few cm/s. For the same reason, mask-side deposition (MS/IBE) and backside deposition (BS/IBE)[9, 10)] are also available, where the substrate is placed by the target holder and the reverse side of the holder, respectively.
3) Since the pulse width is short compared with the conduction time of heat, there is no need to heat the substrate during preparation of the thin films.[4)]

II. Experiment Setup

The experiment was carried out by using intense pulsed power machine, "ETIGO-II".[11)] Figure 1 shows the schematic of the experimental arrangement for the preparation of thin films by IBE. The left-hand side is the ion-beam diode chamber that produces the LIB, while the right-hand side shows the thin-film preparation chamber. The LIB is produced by a magnetically insulated diode (MID)[12)] with a geometrically focused configuration. In this experiment, the target was tilted at 30 degrees to the beam axis. The vacuum chamber was evacuated to ~ 10^{-4} Torr.

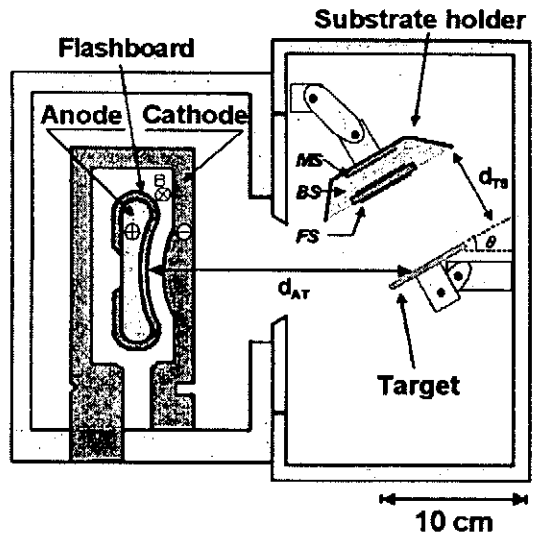

Fig. 1 Schematic of experimental setup for IBE.

The energy density deposited on substrate by ablation plasma was measured by using calorimeter. Figure 2 shows the schematic of setting for calorimeter. Cu plate which has a

good thermal conductivity, was used for measuring the temperature variation at the substrate, where its temperature was measured by a thermistor installed behind it. An acryl resin was placed to the front and the rear of the substrate as a mask and the heat insulating material. To check the plasma life-time near the substrate surface, the behavior of ablation plasma was observed by high-speed photography, where high-speed camera (Ultra NAC FS501) was separated at a distance (3m) from the preparation chamber to avoid the noise generated by "ETIGO-II".

Table 1 summarizes the experimental conditions. In this investigation, Ag was used as target and Si wafers were used as substrate. The thin films were characterized by scanning electron microscopy (SEM) and X-ray diffraction (XRD).

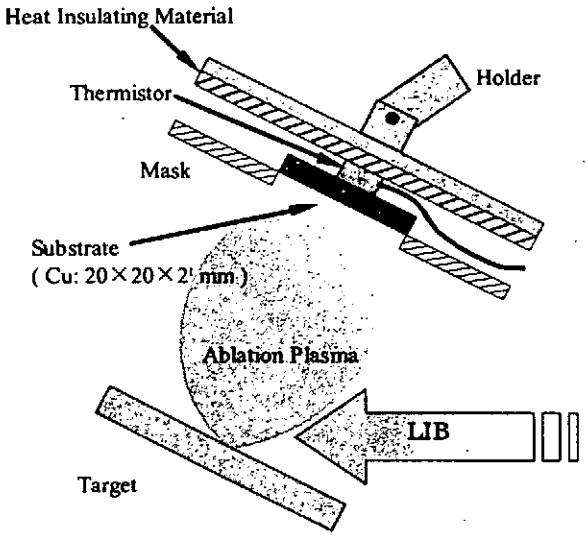

Fig. 2 Schematic of calorimetric technique.

Table 1 Experimental conditions.

Ion species	mostly H^+ (>70%)
Maxmum ion energy	1 MeV
Pulse width (FWHM)	70 ns
Ambient pressure	2×10^{-4} Torr
Target	Ag
Energy density	40 J/cm^2
d_{AT}	200 mm
d_{TS}	50~130 mm
Substrate	Cu, Si (100)
Substrate temperature	R. T.

III. Numerical simulations

It is important to know the surface temperature in preparing thin films. So, the temperature of substrate surface was calculated by the numerical simulation using one-dimensional thermal conduction model. This calculation was carried out by using the energy density deposited on substrate and the plasma life-time of the ablation plasma on the substrate. In this simulation, it was assumed that substrate surface has received a constant heat flux from the ablation plasma.

Figure 3 shows the schematic of the one-dimensional simulation. The substrate has a surface area of S (cm^2) and is assumed to have a semi-infinite thickness which is divided into small length of Δz (cm). Here, thermal conductivity K_n (W/cm^2 K) and specific heat c_n (J/g K) were used as a function of the variation of temperature. Density of substrate ρ (g/cm^3) was

assumed constant. Then, the mean temperature ΔT_n of each small volume (A_1, A_2, A_3, ... ,A_{n-1}, A_n) is obtained by Eq. (1).

$$\Delta T_n = c_n \cdot \rho \cdot \Delta z \cdot S \cdot \Delta E_n \quad \text{(K)} \tag{1}$$

where ΔE_n is the thermal energy (J) deposited into the volume.

In addition, if the temperatures of two consecutive regions A_{n-1} and A_n are T_{n-1} and T_n respectively, then the flow of thermal energy in time Δt (s) can be expressed as

$$\Delta E = K \cdot S \frac{\Delta t}{\Delta z}(T_{n-1} - T_n) \quad \text{(J)} \tag{2}$$

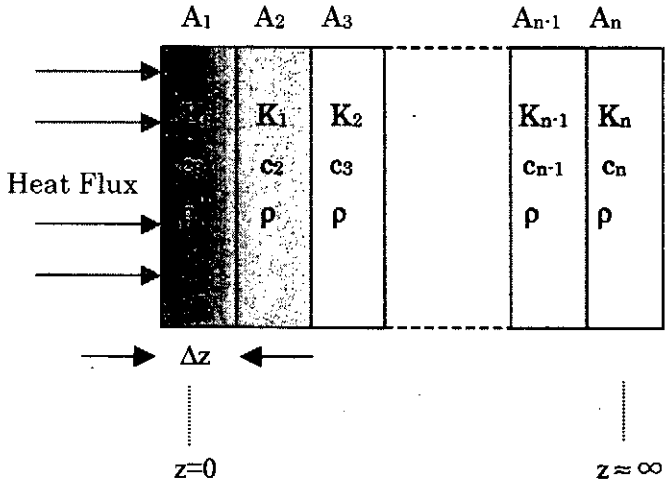

Fig. 3 Schematic of one-dimensional heat conduction simulation.

IV. Results and discussion

Figure 3 shows high-speed photographs of Ag target. It is seen that, the ablation plasma instantly expands toward the direction of the substrate holder. In addition, the plasma exists near the substrate holder for nearly μs.[13)]

Figure 4 shows energy density deposited on the substrate by ablation plasma, where it was measured by using a calorimeter. From this figure, it is seen that the energy density deposited on the substrate decreases as the d_{TS} (distance between target and substrate) increases. The main reason is due to the decrease in the ablation plasma density and temperature. The energy density obtained at d_{TS}=130 mm drops to about 25 % at 50 mm.

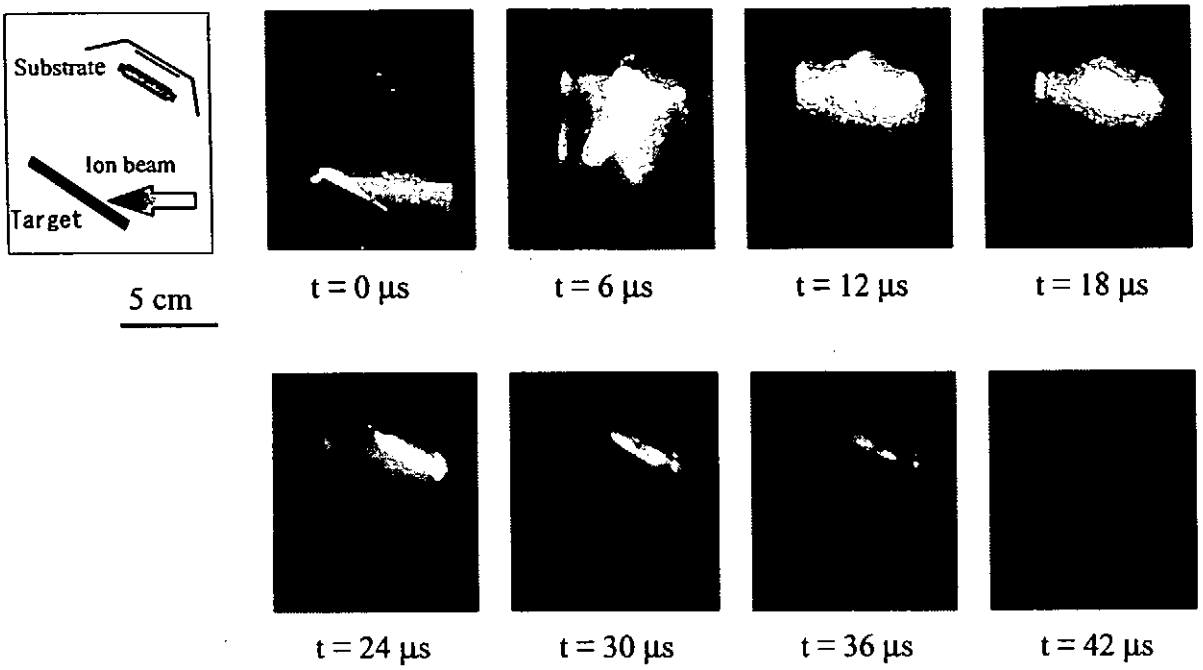

Fig. 3 High-speed photographs for Ag target.
d_{TS} = 70 mm

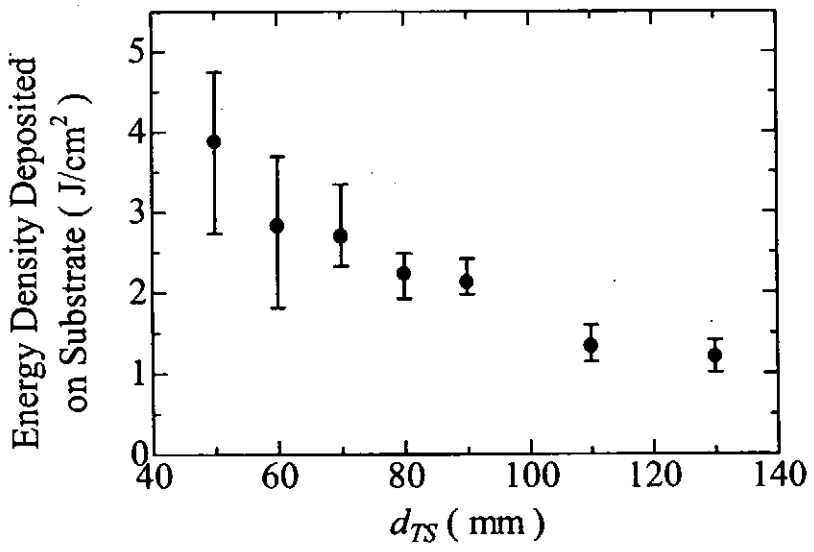

Fig. 4 Energy density deposited on substrate by the ablation plasma of Ag as a function of d_{TS}.

Since it was reported that the energy density depends on the substrate position, Ag films were deposited on the Si substrate at the positions of d_{TS}=50, 90 and 130 mm. For the thin films prepared, Fig. 5 and Fig. 6 show XRD patterns and sectional SEM images, respectively. From Fig. 5, we can see that the crystallized films of Ag are produced on Si substrate without substrate heating. From Fig. 6, it is seen that the thickness of films decreases with increasing d_{TS}, but surface states are observed to become smoother. Thus, it is found that characteristics of thin films widely vary by the difference of the energy density deposited on substrate.

Figure 7 shows cross-sectional SEM images for Ag films prepared by multiple shot at the position of d_{TS}=130 mm. In these thin films, there are good smooth and flat surface states. As the number of shots increases, it is clear that the thickness of thin films favorably increases.

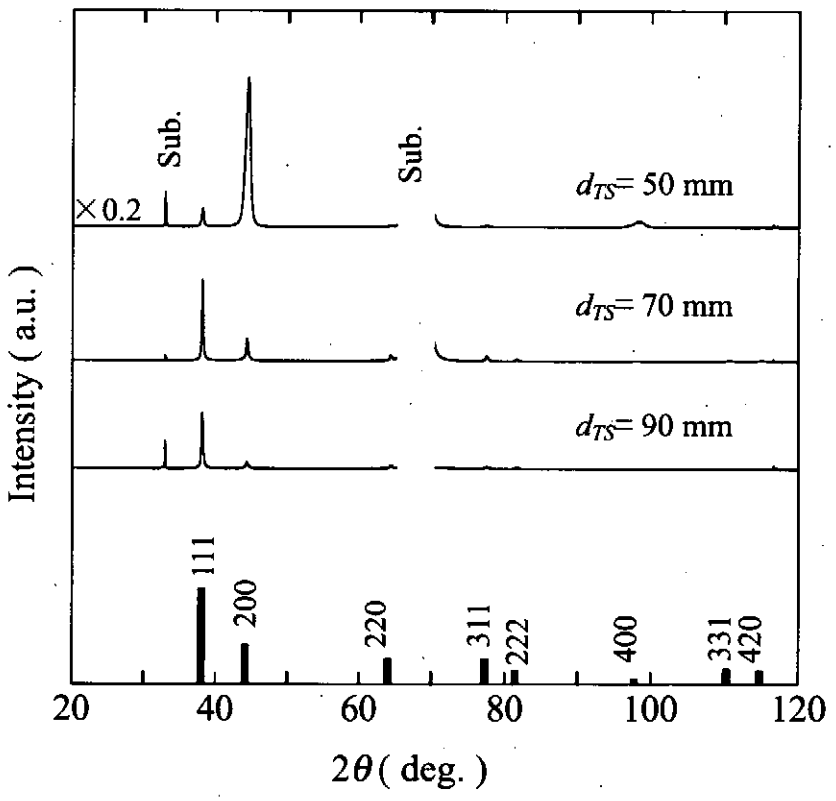

Fig. 5 XRD pattern of Ag films with d_{TS} as a parameter.

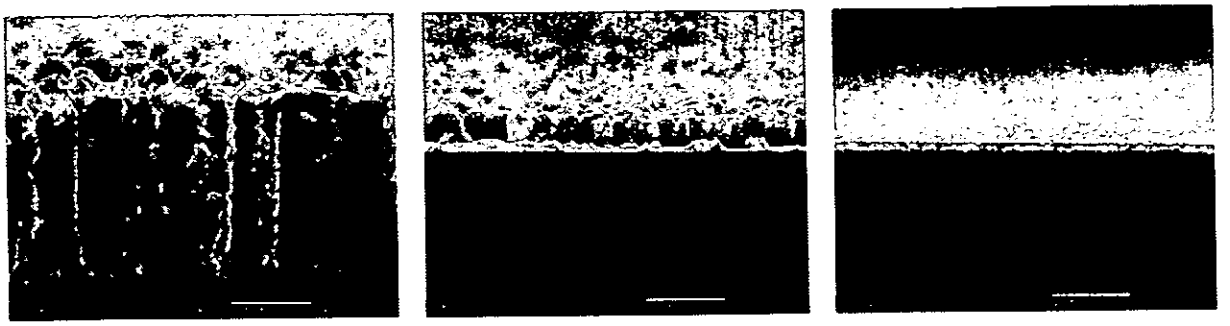

(a) d_{TS} = 50 mm (b) d_{TS} = 90 mm (c) d_{TS} = 130 mm

Fig. 6 SEM micrographs of the cross sectional view of Ag films prepared by one shot.

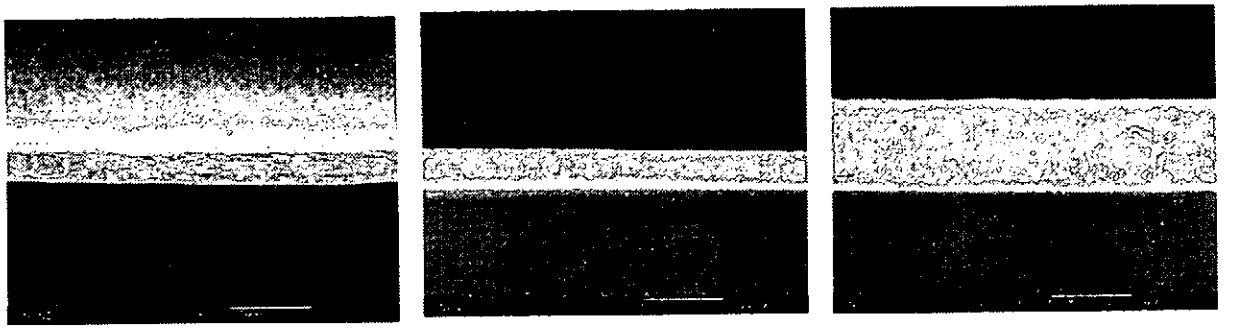

(a) 5 Shots (b) 10 Shots (c) 20 Shots

Fig. 7 SEM micrographs of the cross sectional view of Ag films prepared by multiple shot. d_{TS}=130 mm

From the above results, it seems that difference of the substrate surface temperature is main cause for the change of crystallinity and the surface state. Thus, substrate temperature was calculated by numerical simulation for one dimensional thermal conduction model. Here, to set up constant heat flux in the simulation, the existing time of ablation plasma on the substrate surface was taken to be 30 μs from the high-speed photographs (cf. Fig. 3), and the diagnostic results of the energy densities deposited on substrate were utilized (cf. Fig. 4).

Figure 8 shows the time variation of surface temperature of substrate at each d_{TS} obtained by one-dimensional simulation. As can be seen from Fig. 8, the surface temperature at d_{TS} =50 mm rapidly rises to higher than 800 ℃ within 30 μs. In addition, the maximum surface temperature of the substrate decreases as the d_{TS} increases. The main cause of the different characteristics in the thin films prepared at different positions is thought to be due to the temperature variation of the substrate surface.

Figure 9 shows the calculation results of temperature distributions of the substrate at the position of d_{TS}=50 mm. It is seen from Fig. 8 that while the ablation plasma exists, only thin layer on the substrate surface is instantaneously and adiabatically heated. After that, the surface temperature abruptly decreases.

From the above results, it is understood that only a certain thin layer of the substrate surface is instantaneously and adiabatically heated by the energy of ablation plasma. Thus, it can be considered that the growth of crystallized thin films is promoted in such a shallow area by IBE technique.

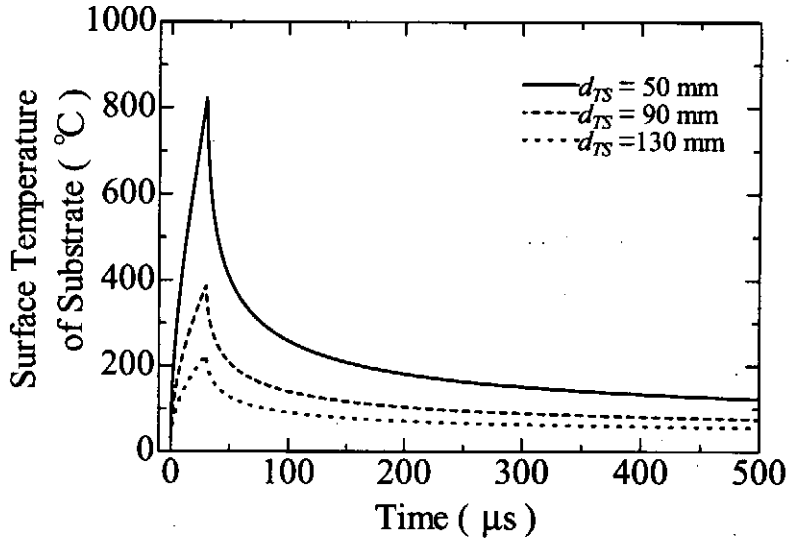

Fig. 8 Surface temperature of substrate as a function of time history.

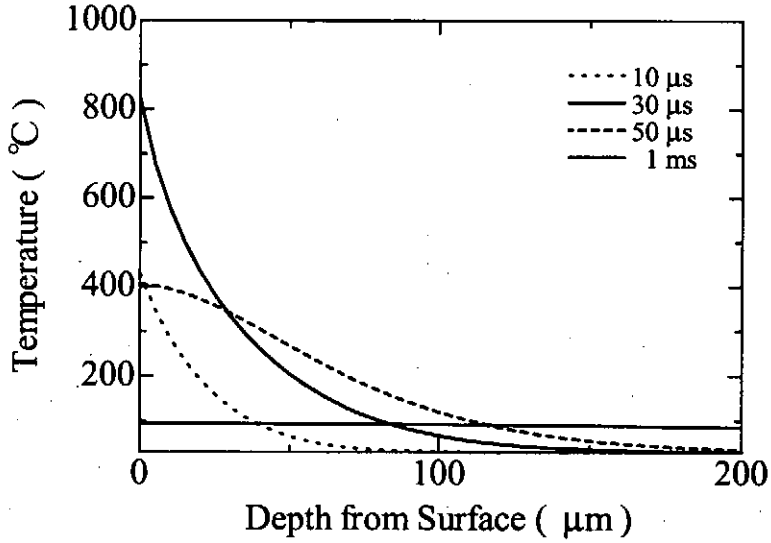

Fig. 9 Substrate temperature in Si as a function of depth from substrate surface.

V. Conclusions

From the results on characteristics of the ablation plasma and the thin films, the following conclusions have been obtained.

1) The energy density deposited on substrate decreases as the d_{TS} increases.

2) When d_{TS} is increased, the thickness of deposited thin films per shot is decreased, and crystallized thin films with relatively flat surface state were obtained.

3) The thickness of films is decreased with increasing d_{TS}, however surface states were observed to be much smoother.

4) Only a thin layer of the substrate surface is instantaneously and adiabatically heated by the ablation plasma.

References

1) Y. Shimotori, M. Yokoyama, H. Isobe, S. Harada, K. Masugata and K. Yatsui, "Preparation and Characteristics of ZnS Thin Films by Intense Pulsed Ion Beam", J. Appl. Phys., **63**, 968-970 (1988).
2) K. Yatsui, "Industrial Applications of Pulse Power and Particle Beams", Laser & Particle Beams, **7**, 733-741 (1989).
3) Y. Shimotori, M. Yokoyama, H. Isobe, S. Harada, K. Masugata and K. Yatsui, "Quick Deposition of ZnS:Mn Electroluminesent Thin Films by Intense, Pulsed, Ion Beam Evaporation", Jpn. J. Appl. Phys., **28**, 468-472 (1989).
4) K. Yatsui, X. D. Kang, T. Satoh, S. Furuuchi, Y. Ohuchi, T. Takeshita, and H. Yamamoto, "Applications of Intense Pulsed Ion Beam to Material Science", Phys. Plasmas, **1**, 1730-1737 (1994).
5) K. Kitajima, T. Suzuki, W. Jiang and K. Yatsui, "Preparation of B_4C Thin Film by Intense Pulsed Ion-Beam Evaporation", Jpn. J. Appl. Phys., **40**, 1030-1034 (2001).
6) M. Sengiku, Y. Oda, W. Jiang, K. Yatsui, Y. Ogura, K. Kato, K. Shinbo and F. Kaneko, "Preparation of $SrAl_2O_4$:Eu Phosphor Thin Films by Intense Pulsed Ion-Beam Evaporation", Jpn. J. Appl. Phys., **40**, 1035-1037 (2001).
7) T. Suzuki, M. Kishima, W. Jiang and K. Yatsui, "Synthesis of Ti-Al Intermetallic Compound Films by Intense Pulsed Ion Beam Evaporation", Jpn. J. Appl. Phys., **40**, 1042-1044 (2001).

8) T. Suzuki, K. Shioiri, W. Jiang and K. Yatsui, "Preparation and Characterization of C-N-H-O Thin Film by Ion Beam Evaporation", Jpn. J. Appl. Phys., **40**, 1045-1048 (2001).

9) T. Sonegawa, T. Arakaki, T. Maehama, W. Jiang and K. Yatsui, "Ferroelectric Thin Films Prepared by Backside Pulsed Ion-Beam Evaporation", Jpn. J. Appl. Phys., **40**, 1049-1051 (2001).

10) T. Sonegawa, C. Grigoriu, K. Masugata, K. Yatsui, Y. Shimotori, S. Furuuchi and H. Yamamoto, "Preparation of $BaTiO_3$ Thin Films by Backside Pulsed Ion-Beam Evaporation", Appl. Phys. Lett., **69**, 2193-2195 (1996).

11) A. Tokuchi, N. Nakamura, T. Kunimatsu, N. Ninomiya, M. Den, Y. Araki, K. Masugata and K. Yatsui, "3MV Pulse-Power Generator at the Technological University of Nagaoka", Proc. 2nd Int'l Top. Symp. on ICF Res. by High-Power Particle Beams, ed. K. Yatsui, 430-439 (1986).

12) K. Yatsui, A. Tokuchi, H. Tanaka, H. Ishizuka, A. Kawai, E. Sai, K. Masugata, M. Ito and M. Matsui, Geometric Focusing of Intense Pulsed Ion Beams from Racetrack Type Magnetically Insulated Diode", Laser & Particle Beams, **3**, 119-155 (1985).

13) W. Jiang, K. Ide, S. Kitayama, T. Suzuki and K. Yatsui, "Pulsed Ion-Beam Evaporation for Thin-Film Deposition", Jpn. J. Appl. Phys., **40**, 1026-1029 (2001).

SUBSTRATE BIAS EFFECT ON CRYSTALLINITY OF POLYCRYSTALLINE SILICON THIN FILMS PREPARED BY PULSED ION-BEAM EVAPORATION METHOD

Fazlat Ali, Michiharu Gunji, Sung-Chae Yang, Tsuneo Suzuki,
Hisayuki Suematsu, Weihua Jiang and Kiyoshi Yatsui

Extreme Energy-Density Research Institute, Nagaoka University of Technology
1603-1 Kamitomioka, Nagaoka, Niigata 940-2188, Japan

ABSTRACT

The deposition of polycrystalline silicon thin films has been tried by a pulsed ion-beam evaporation method, where high crystallinity and deposition rate have been achieved without heating the substrate. The crystallinity and the deposition rate were improved by applying bias voltage to the substrate, where instantaneous substrate heating might have occurred by ion-bombardment.

1. Introduction

Polycrystalline silicon (poly-Si) thin films are widely used in various electronic devices such as thin film transistors, solar cells, peripheral circuits of liquid-crystal displays and electrodes in silicon integrated circuits because of high optical absorption and high carrier mobility. [1-3] Generally, these thin films have been fabricated by a plasma-enhanced chemical vapor deposition (PECVD) method using highly hydrogen-diluted SiH_4. It is well known that poly-Si thin films deposited by PECVD need post annealing or substrate heating, and that the deposition of these thin films are desired at low temperatures.

In practical application such as solar cells, the very low deposition rate is a serious problem for achieving higher throughput of the devices. For this purpose, several types of low-pressure and high-density plasma sources have been applied to increase the crystallinity and the deposition rate of poly-Si thin films. They are represented such as inductively coupled plasma (ICP), surface wave plasma (SWP), ultra high-frequency plasma (UHF) and electron cyclotron resonance plasma (ECR). [4-7]

A novel thin film preparation method called pulsed ion-beam evaporation (IBE) has been proposed by one of the authors, where various thin films have been prepared successfully. [8-9] By IBE, crystallized thin films, such as B_4C, $BaTiO_3$, BN, SiC, $SrAl_2O_4$ and TiFe were

prepared without heating substrates. [8-9] Only preliminary results were reported on the preparation of poly-Si thin films by IBE. [14]

In the previous paper, [14] we have reported about substrate bias effect on the crystallinity of poly-Si thin films. It was found that a large-area, high crystallinity poly-Si thin film could be achieved by applying bias voltage to the substrate. In this paper, we report the deposition of poly-Si thin films at room temperature, i.e., without substrate heating or annealing, by using the intense, pulsed, ion-beam evaporation (IBE) technique. To investigate the crystallization and deposition rate, the substrate was placed at r=10mm away from the plasma center. Furthermore, to study the crystallinity, bias voltage was applied to the substrate.

2. Experimental Apparatus and Method

Figure 1 shows the schematic of the experimental arrangement. An intense, pulsed, light ion-beam (LIB) generator "ETIGO- II " at the Nagaoka University of Technology was used. A high-voltage pulse from "ETIGO- II " was applied to a magnetically insulated diode (MID), and an intense pulsed light ion-beam was extracted. [10-11] From the measurement with energy spectrometer, the ion species has been found to be mostly protons (approx. 75%) and the rest to be carbons. [12-13] The ion beam hits the target, producing high-density ablation plasma, which was deposited on the substrate placed parallel to the target at a certain distance. The ion beam used was the peak energy of 1 MeV, the pulse width of 50 ns, and the energy density on the target of 50 J/cm^2. The beam spot size on the target was typically 20mm in diameter.

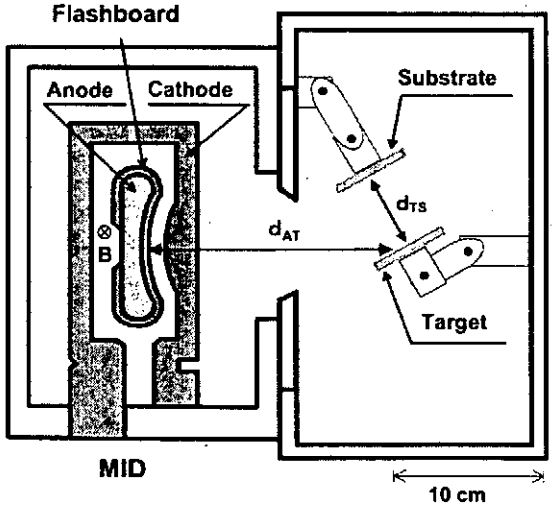

Fig. 1 Experimental setup.

Table I Typical experimental conditions

Main component of ions	H^+
Beam voltage (peak)	1 MV
Diode current	70 kA
Energy density on target	50 J/cm^2
Anode-Target distance (d_{AT})	180 mm
Target-Substrate distance (d_{TS})	70 mm
Target angle	45°
Substrate	Si (100)
Pressure	10^{-4} Torr
Substrate temperature	R.T.
Number of shots	5 shots
Substrate bias voltage (V_{bias})	0 ~ -100 V

We used single crystal silicon with 50×50×10 mm in size as a target. As a substrate, we used single crystal silicon wafer (100). The substrate (15×20×1 mm) was kept at room temperature and the ablation plasma directly hits the substrate. The poly-Si thin films were deposited under a pressure of ~10^{-4} Torr. The bias voltage was applied to the substrate placed 70 mm away from the target. Between the target and the substrate a firm insulation was carried out to avoid the current flow and to stand the potential difference. Typical experimental conditions are presented in Table I .

In this study, we examined the crystal structures of the obtained poly-Si thin films by X-ray diffraction (XRD, RIGAKU, RINT 2000^{+}). The grain size was estimated from the full width at half-maximum (FWHM) values of (111) peak in the XRD spectra by using Scherrer's formula. The film thickness (d) was estimated from the scanning electron microscope (SEM, JEOL, JSM6700F) morphology. The crystallinity of the thin film was measured by Raman spectroscopy and the excitation source consisted of an argon-ion laser tuned at 514.5 nm, releasing 200 mW to the sample. Raman scattering was collected at right angles, dispersed with a double spectrometer (JASCO, NR-1100). The crystallinity of the Raman spectra (ρ) was defined as the following equation, where I_c and I_a are the intensities of the polycrystalline phase (520 cm^{-1}), and the amorphous phase (480 cm^{-1}), respectively. In the XRD spectra, I_c and I_a are the intensities of the sharp crystalline peak and the board amorphous ones respectively, which is written by

$$\rho = \frac{I_c}{I_c + I_a} \tag{1}$$

3. Experimental Results

3.1 XRD Analysis

Figure 2 shows XRD spectra of poly-Si thin films deposited on silicon substrates at various substrate bias voltage (V_{bias}). XRD spectra revealed that the poly-Si phases are varied while applying V_{bias} to the substrate. It was noticed that at V_{bias} = - 50 V, all peaks have considerable high intensities than other V_{bias} conditions. From the XRD spectra it was also revealed that the crystallinity of the thin films is improved by applying bias voltage to the substrate. However, at V_{bias} = - 100 V, the XRD peak intensities showed a decreasing trend.

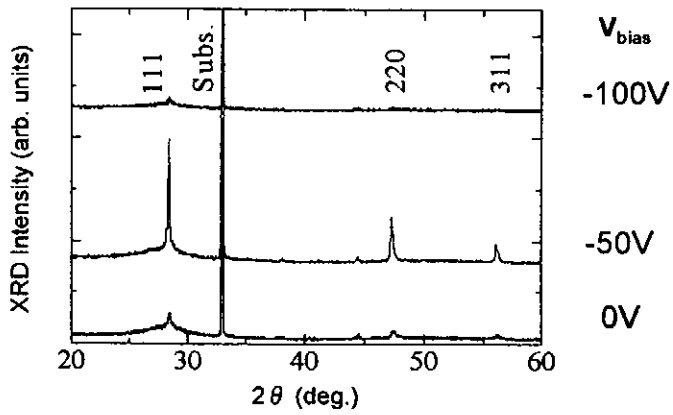

Fig. 2 XRD spectra at various substrate bias voltage.

3.2 SEM Analysis

Figure 3 is the SEM image of poly-Si thin films deposited on silicon substrates at various bias voltage (V_{bias}). In Fig. 3, we have evaluated the film thickness. We see that the film thickness is increased at V_{bias} = - 50 V compared with that V_{bias} = 0 V. This result agrees with our previous experiments. [14] When the V_{bias} is increased to - 100 V, the thickness of the film was found to decrease compared to V_{bias} = - 50 V. When bias voltage was applied to the substrate it was also noticed that the considerable density of the thin film has been improved.

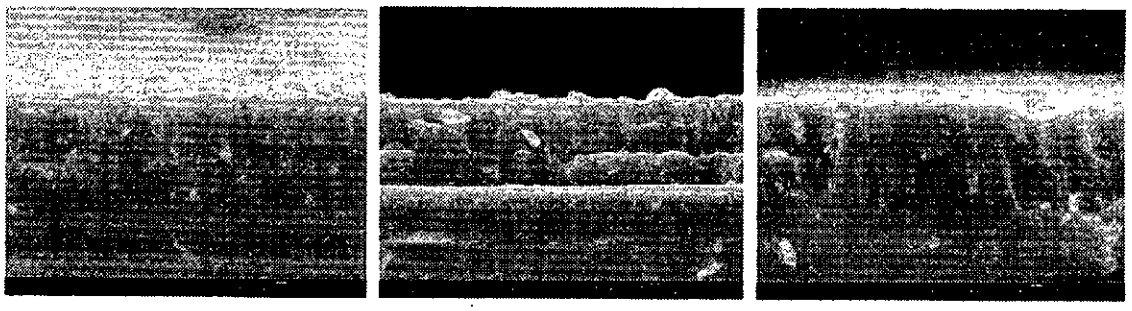

V_{bias} = 0 V, d=1.06 μ m V_{bias} = -50 V, d=1.33 μ m V_{bias} = -100 V, d=1.06 μ m

Fig. 3 SEM images at various substrate bias voltage.

3.3 Raman Analysis

The Raman spectra are shown in Fig. 4. The graph where $V_{bias} = 0$ V is found to contain some amorphous phase, which exhibits a broad peak at 468 cm^{-1}. The crystallinity phase at 520 cm^{-1} has increased by using $V_{bias} = -50$ V, but a slight decrease at - 100 V was observed. The enhancement of crystallinity at $V_{bias} = -50$ V has been found in XRD analysis as well.

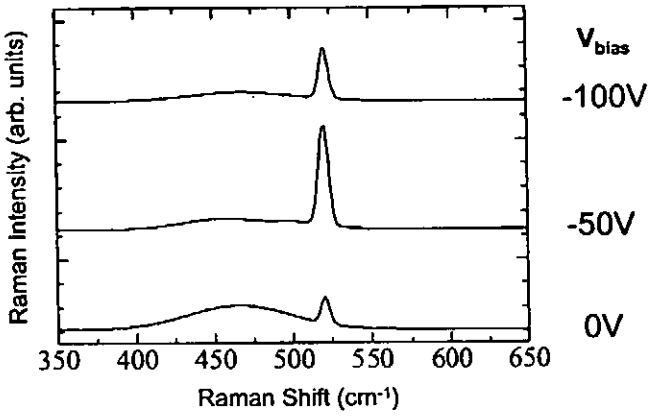

Fig. 4 Raman spectra at various substrate bias voltage.

4. Discussions

The crystallinity index of the prepared thin films was calculated using the XRD and Raman spectroscopy data, which are shown in the following Figs. 5 and 6. According to Figs. 5 and 6, the increase in the crystallinity is observed by applying substrate bias voltage. On the other hand, the values are found to decrease at $V_{bias} = -100$ V. The influence of the substrate bias voltage may be explained using the following approach. With increasing negative V_{bias}, the energy of the attracting ions towards the substrate is increased, and as a result, the surface is heated and resputtering takes place. Since the temperature of the substrate surface is increased due to ion-bombardment, [14] some disorder may result within the thin film.

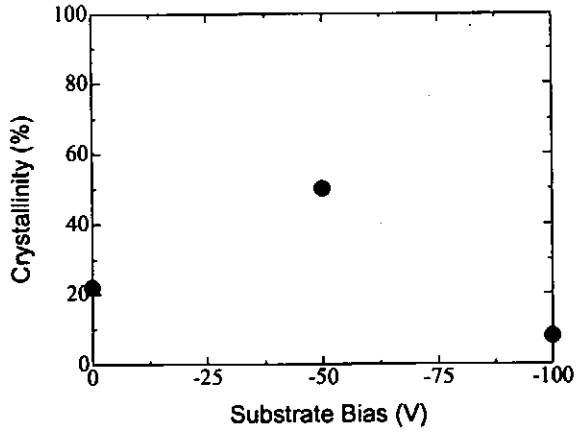

Fig. 5 XRD Crystallinity spectra as a function of substrate bias voltage.

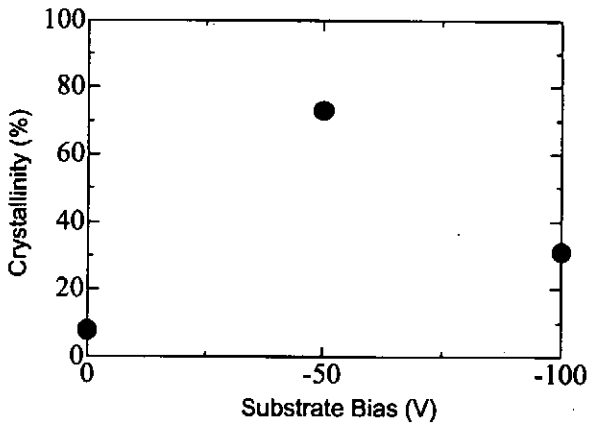

Fig. 6 Raman Crystallinity spectra as a function of substrate bias voltage.

Since the ion-bombardment could be considered to substrate heating during deposition, grain size growth might also give an explanation to crystallization. In Fig. 7, evaluated grain size from the XRD spectra is given. We have achieved a good crystallinity at V_{bias} = - 50 V (Fig. 5 and 6) and at the same time the grain size was noted to be increased at this point. The instant substrate heating with the use of bias may have resulted to crystallize, giving the increase in the grain size.

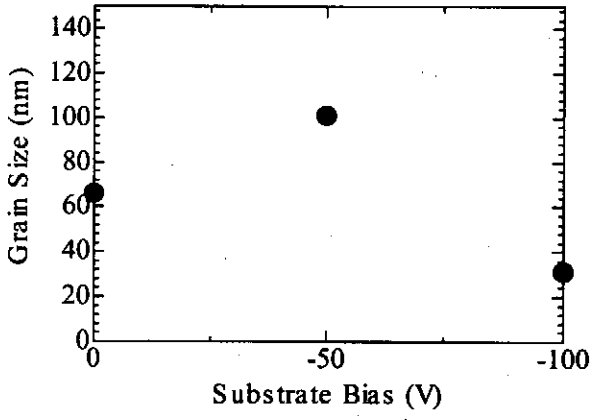

Fig. 7 Grain size spectra as a function of substrate bias voltage.

The deposition rate calculated from d in Fig. 3 as a function of bias is shown in Fig. 8. Here, we have succeeded in the achievement of a high deposition rate of ~270 nm/shot with using the substrate bias voltage. It has been seen that the deposition rate has gradually increased with increasing V_{bias} at various distances, but that it decreases at V_{bias} = - 100 V. This was contrary to expectations, since it was anticipated that with increasing the negative V_{bias}, will increase the energy of the attracting ions towards the substrate, i.e. the ion-bombardment energy and as a result the surface will be heated to allow resputtering to take place. This could be a factor for the decrease in the film thickness as we increase the negative bias of the substrate.

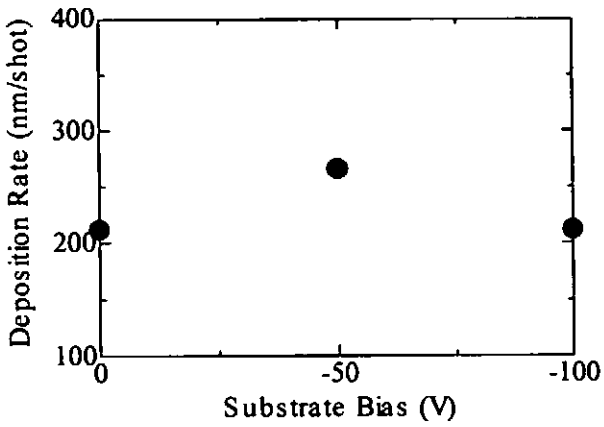

Fig. 8 Deposition rate spectra as a function of substrate bias voltage.

The increase in the film thickness with substrate bias voltage can be explained but the main mechanism behind is still unknown. When the substrate bias voltage is zero, there is no external influence to the ablation plasma plume and the particles are deposited on the substrate without any interference. On the other hand, if we supply electric field to the existing ablation plasma the particles present in the plume experience some effects in them. For example, applying negative bias to the substrate means that the positive ions present in the plume get attracted towards the substrate, resulting in drag for the neutral particles. This phenomenon is assumed to have increased the film thickness where, the ion drag force is considered to take place in the bias field. [15]

5. Summary

Using intense pulsed ion-beam evaporation technique, we have succeeded in the preparation of polycrystalline silicon thin films. The grain size variation was noted by changing the bias conditions. The crystallinity and the deposition rate of poly-Si thin film have improved by applying bias voltage to the substrate, which may have contributed to instantaneous substrate heating to take place from the ion-bombardment energy.

References

1) G. Fortunato, L. Mariucci, R. Carluccio, A. Pecora, V. Foglietti, "Excimer Laser Crystallization Techniques for Polysilicon TFTs", Appl. Surface Sci., **154-155**, 95-104 (2000).

2) R. Nozawa, H. Takeda, M. Ito, M. Hori and T. Goto, "Substrate Bias Effects on Low Temperature Polycrystalline Silicon Formation Using Electron Cyclotron Resonance SiH_4/H_2 Plasma", J. Appl. Phys., **81**, 8035-8039 (1997).

3) S. Hasegawa, M. Sakata, T. Inokuma and Y. Kurata, "Structural Change of Polycrystalline Silicon Films with Different Deposition Temperature", J. Appl. Phys., **85**,

3844-3449 (1999).

4) C. Fukai, Y. Morita, T. Nakamura and H. Shirai, "Enhanced Crystallinity at Initial Growth Stage of Microcrystalline Silicon on Corning #7059 Glass Using SiH_2Cl_2", Jpn. J. Appl. Phys., **38**, L554-L557 (1999).

5) K. Goshima, H. Toyoda, T. Kojima, M. Nishitani, M. Kitagawa, H. Yamazoe and H. Sugai, "Lower Temperature Deposition of Polycrystalline Silicon Films from a Modified Inductively Coupled Silane Plasma", Jpn. J. Appl. Phys., **38,** 3655-3659 (1999).

6) H. Shirai, Y. Sakuma, Y. Moriya, C. Fukai and H. Ueyama, "Fast Deposition of Microcrystalline Silicon Using High-Density SiH_4 Microwave Plasma", Jpn. J. Appl. Phys., **38,** 6629-6635 (1999).

7) E. Srinivasan and G. N. Parsons, "Hydrogen Elimination and Phase Transition in Pulsed-Gas Plasma Deposition of Amorphous and Microcrystalline Silicon", J. Appl. Phys., **81**, 2847-2855 (1997).

8) K. Yatsui et al., "Application of Intense Pulsed Ion Beam to Materials Science", Phys. of Plasmas, **1**, 1730-1737 (1994).

9) W. Jiang et al., "Characteristics of Ablation Plasma Produced by Pulsed Light Ion Beam Interaction with Targets and Applications to Materials Science", Nucl. Instr. & Meth. in Phys. Res. **A 415**, 533-538 (1998).

10) A. Tokuchi, N. Nakamura, T. Kunimatsu, N. Ninomiya, M. Den, Y. Araki, K. Masugata and K. Yatsui, "3MV Pulse-Power Generator "ETIGO- II " at the Technological Univ. of Tech.", Proc. 2nd Int'l Top. Symp. on ICF Res. by High-Power Particles Beams, ed. K. Yatsui, 430-439 (1986).

11) K. Yatsui, A. Tokuchi, H. Tanaka, H. Ishizuka, A. Kawai, E. Sai, K. Masugata, M. Ito and M. Matsui, "Geometric Focusing of Intense Pulsed Ion Beams from Racetrack Type Magnetically Insulated Diodes", Laser & Part. Beams, **3**, 119-155 (1985).

12) Y. Shimotori, M. Yokoyama, H. Isobe, S. Harada, K. Masugata and K. Yatsui, "Preparation and Characteristics of ZnS Thin Films by Intense Pulsed Ion Beam", J. Appl. Phys., **63**, 968-970 (1988).

13) K. Yatsui, C. Grigoriu, K. Masugata, W. Jiang and T. Sonegawa, "Preparation of Thin Films and Nanosize Powders by Intense, Pulsed Ion Beam Evaporation", Jpn. J. Appl. Phys., **36**, 4928-4934 (1997).

14) S.-C. Yang, A. Sharoon, H. Suematsu, W. Jiang and K. Yatsui, "Preparation of Polycrystalline Silicon Thin Films by Pulsed Ion-Beam Evaporation", 2nd Asia-Pacific Int'l Symp. on the Basis and Application of Plasma Tech. (Kaohsiung, Taiwan, 2001), pp. 165-170.

15) D. Winske and M. E. Jones, "Particulate Dynamics at the Plasma-Sheath Boundary in DC Glow Discharges", IEEE Trans. on Plasma Sci., **22**, 454-464 (1994).

PULSED POWER LASER RADIATION EFFECTS ON *MYCOPLASMA AGALACTIAE*

Cerasela Z. Dinu[a], Constantin Grigoriu[a], Maria Dinescu[a],
Florentina Pascale[b], Adrian Popovici[b], Lavinia Gheorghescu[b], Ana Cismileanu[b],
Eugenia Avram[c] and Kiyoshi Yatsui[d]

[a]*National Institute for Lasers, Plasma and Radiation Physics, P.O.Box MG-36, Bucharest, Romania,*
[b]*National Society "Pasteur Institute" S.A. , Calea Giulesti No. 333, Sector 6, Bucharest, Romania,*
[c]*"Spiru-Haret" University, Palatul Sporturilor si Culturii, Parcul Tineretului, Bucharest, Romania*
[d]*Extreme Energy-Density Research Institute, Nagaoka University of Technology, Niigata, 940-2188, Japan*

ABSTRACT

The biological effects of the laser radiation emitted by the Nd:YAG laser (second harmonic, wavelength 532 nm / fluence 32 mJ/cm^2 / pulse duration 6 ns) on the *Mycoplasma agalactiae* bacterium were studied. The radiation was found to intensify the multiplication of the bacteria irradiated in TRIS buffer (0.125 M), without however affecting the proteinic composition of the cell membrane. When the bacteria were irradiated in their growth medium (PPLO broth) being later cultivated on a solid medium (PPLO agar), the exclusive presence of the atypical colonies (granular and T-like ones) was noticed.

1. Introduction

There is knowledge of experimental bacteria irradiation with X rays, alpha, beta and gamma radiations, as well as with fast neutrons; the cultures used were those of *Staphylococcus aureus*, *Salmonela typhimurium*, *Escherichia coli*, *Bacillus pyocyaneus*, *Bacillus anthracis*, *Serratia marascens*, etc. The major effects were either bactericidal (as an inhibition process of the cell proliferation), or radioprotective (whenever the radioprotective substances reduce the toxic ones resulted from the irradiation disintegration). The differences between the effects of the ionizing and ultraviolet waves irradiation were not too great[1)].

Ones the lasers were developed, a series of experimental researches were conducted on the laser radiation effects on the laser radiation effects on biological media [2,3,4,5)] a limited number of reports on the laser radiation-bacteria interaction should also be mentioned [6,7,8,9)]. Many experimental results confirm the laser radiation to be able to change the cell proliferation processes and induce important structural changes [7,9)]. The effects of the laser radiation on the pro- and eukaryote cells are conditioned by certain parameters such as the wavelength, the power and energy level, monochromaticity and irradiation duration.

Our aim was to study the laser radiation (532 nm, green in color) effects on *Mycoplasma agalactiae*, a bacterium of the *Mollicutes* division, *Mycoplasma* genus; the bacteria belonging to this genus lack the rigid cellular wall and have elastic cytoplasmatic

membrane. A vaccinal *Mycoplasma agalactiae* strain (Pasteur Institute, Bucharest) was irradiated.

The bacteria were irradiate both in their growth medium and in TRIS buffer (0.125 M), and then studied for the cell morphology (by electron microscopy), the cell membrane protein composition (by sodium dodecyl sulfate polyacrylamide gel electrophoresis, SDS-PAGE) and the cultivability of the bacteria irradiated in their growth and then reinoculated into a solid medium.

2. Material and method

2.1. Irradiation

The radiation source was made of a solid state Nd:YAG laser that operated at 532 nm in green. The other experimental parameters were:

a) The laser fluence (laser energy/irradiated area) : 32 mJ/cm^2;
b) The laser pulse duration τ = 6 ns;
c) The laser pulse repetitive frequency ω = 0.5 Hz;
d) The laser pulse number N = 300.

Throughout the irradiation, the samples were homogenized on a magnetic stirrer.

2.2. Irradiated samples

The 48 hour old *Mycoplasma agalactiae* culture in PPLO broth (Difco): 600 ml of the basic medium (PPLO, Difco), 20% liquid yeast extract (LYE), 20% horse serum, 1% glucose, 400 IU/ml of penicillin, 0.05 g%thyalium acetate and 12 ml of phenol red solution.

a. The culture was incubated at 37^{0}C and 1400 rpm under agitation, the density was 1x10 CFU/ml and 4 ml were subjected to the irradiation. Following irradiation, 0.1 ml of the culture was seeded into the solid medium: PPLO agar (Difco) supplemented with 20% LYE, 20% horse serum, 1% glucose, 400 IU/ml of penicillin, 0.05 g% thallium acetate. The Petri plates were incubated at 37^{0}C and daily examined for 5 days.

b. The bacterial bodies suspended in TRIS buffer (1x10^9 CFU/ml): the 48 hour old *Mycoplasma agalactiae* culture was centrifuged at 4^{0}C and 13,000 g for 35 minutes [10]. The pellet was washed 3 times in TRIS buffered solution (0.01 M TRIS-HCl, 0.1 M NaCl, pH 7.2) and once in 0.125 M TRIS-HCl buffer, pH 6.8. The final sample concentration was adjusted to 1x10^9 CFU/ml in 0.125 M TRIS-HCl buffer, and 4 ml were subjected to the irradiation.

2.3. SDS-PAGE

The SDS-PAGE was performed as described by Laemmli[11] with 10% separation gel. The samples (the irradiated in 0.125 M TRIS-HCl buffer and the non irradiated one) and the molecular weight standard (Sigma) were dissolved in standard buffer (0.05 M TRIS-HCl , pH 6.8; 2.5% SDS; 5% 2-mercaptoethanol; 15% glycerol; 0.05% bromphenol blue) and then heated in a water bath (100^{0}C) for 5 minutes. The insoluble material was removed by centrifugation at 10,000 g for 10 minutes. The solubilised cellular proteins and standards were electrophoresed (Mini Protean II, Bio-Rad) at a constant current, 200 V (Power-Pac 300, Bio-rad).

2.4. Electron microscopy

The samples were examined under a transmission electron microscope (EM 125, 75 kV acceleration voltage, 6,000-400,000 x magnifying power) using the direct negative contrast method. Each sample was placed on 150 mesh grids and electron contrasted using a 2% alcohol solution of phosphotungstic acid, pH 7.4 as the contrast substance.

3. Results

The irradiation affected the cultural characters of the bacteria on the solid medium. Thus, atypical colonies were found 72 hours after the cultivation of the irradiated samples: they were granular and punctiform, T-like (Figure 2).

The nonirradiated control exhibited both typical, fried eggs-like colonies, and atypical ones (Figure 1).

Electrophoresis did not evidence differences among the irradiated and non irradiated samples as to the proteinic bands aspect (Figure 3), while electron microscopy showed no significant differences with the samples irradiated in their growth medium in comparison with the non irradiated ones examined under the same conditions.

Significant differences were, however, found with the irradiated TRIS buffer sample as against the nonirradiated control, whose cells exhibited monomorphism: cells clumps were noticed, and the cells were round ranging between 80 and 100 nm (Figure 4).

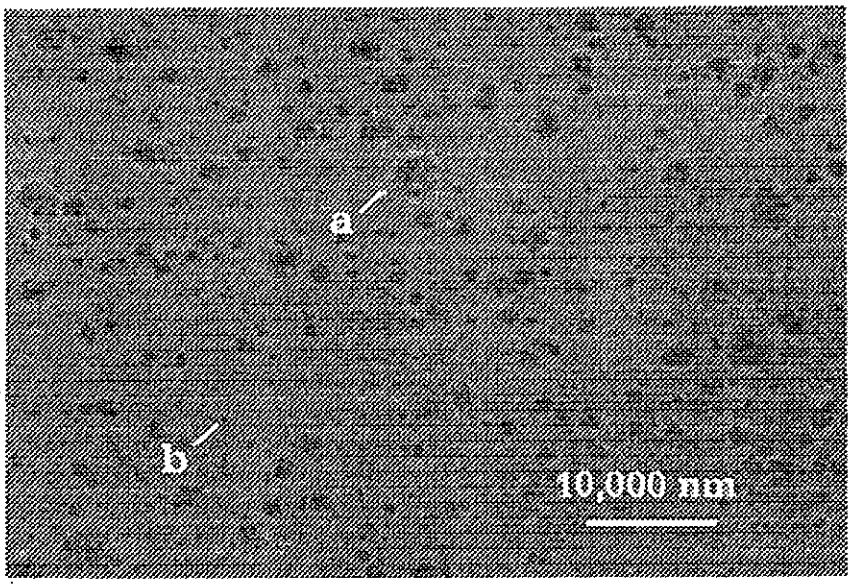

Fig. 1 72 hour *Mycoplasma agalactiae* culture irradiated on PPLO agar.
a. Atypical, granular colonies.
b. Atypical, T-like punctiform colonies.

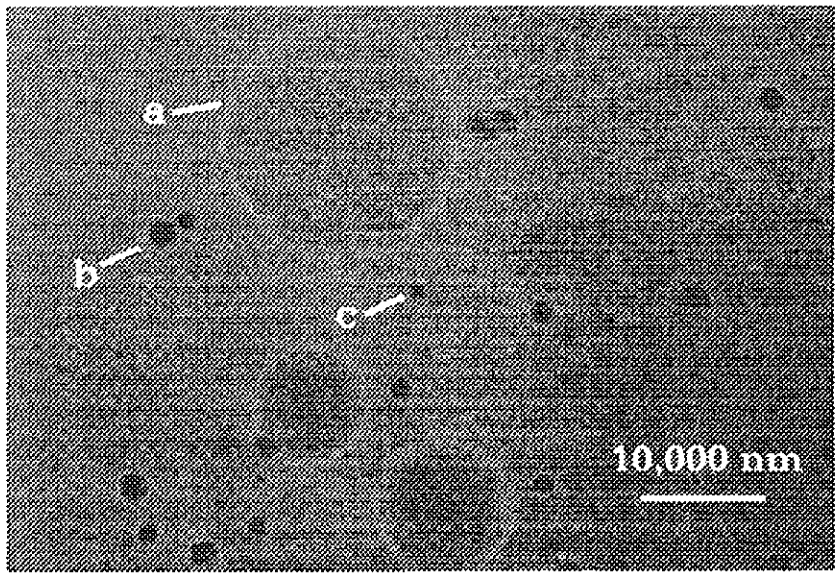

Fig. 2 Nonirradiated *Mycoplasma agalactiae* culture on PPLO agar.
a. Typical colonies.
b. Atypical, granular colonies.
c. Atypical, T-like punctiform colonies.

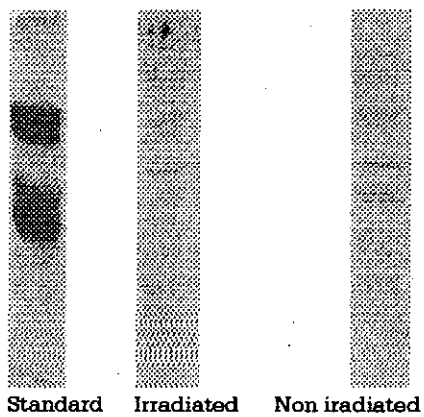

Fig. 3 Electrophoresis on irradiated *Mycoplasma agalactiae.*

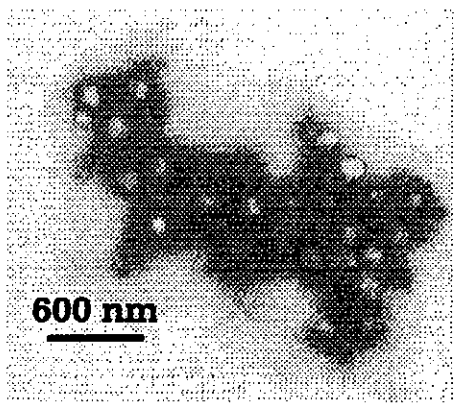

Fig. 4 Nonirradiated *Mycoplasma agalactiae*; TRIS-HCl (0.125 M) buffered germs suspension. Round cells with monomorphism.

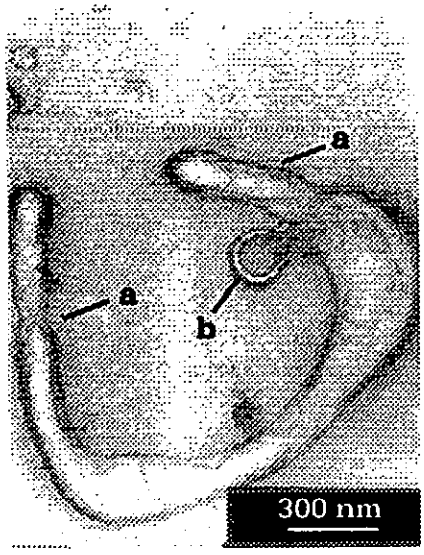

Fig. 5 Irradiated *Mycoplasma agalactiae* (532 nm, 32 mJ/cm^2, 6 ns, 300 pulses, in TRIS buffer).
a. Filamentous formations.
b. Budding.

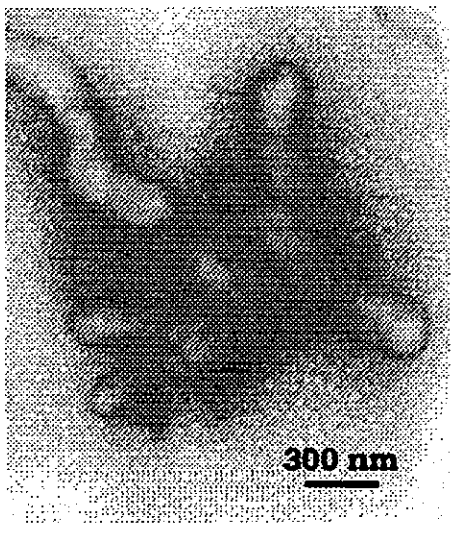

Fig. 6 Irradiated *Mycoplasma agalactiae* (532 nm, 32 mJ/cm^2, 6 ns, 300 pulses, in TRIS buffer).
Enlarged cells looking like "glove fingers".

As for the samples irradiated in TRIS buffer, the cells are characterised by a marked polymorphism: ring-like forms (Figure 5), glove fingers-like ones (Figures 6) and reniform aspects (Figure 7) were noticed. All these exhibited a rise in the cell volume and filamentous protrusions-like formations. In our opinion, these formations are not mere membranaceous prolongations; they are daughter cells resulted from cellular division processes, either by means of filamentous formations (Figure 3) or by budding (figure 3 and 5). The lack of the cell wall allows the genetic material of these daughter cells to be visualized.

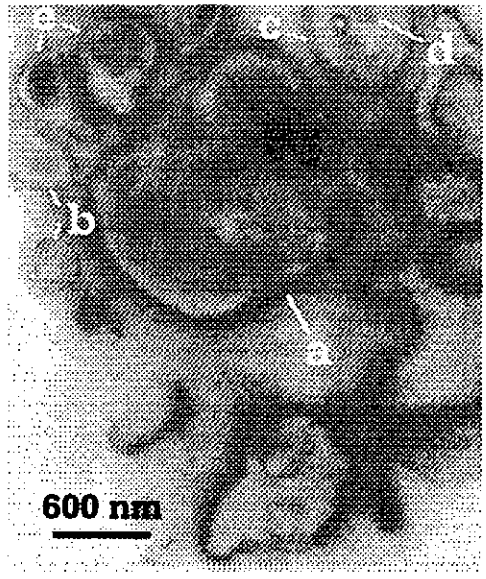

Fig. 7 Irradiated *Mycoplasma agalactiae* (532 nm, 32 mJ/cm^2, 6 ns, 300 pulses, in TRIS buffer).
a. Great reniform cell during budding division.
b. Daughter cells.
c. Great cell with inclusion (elementary bodies).
d. Elementary bodies.
e. Nucleoli.

These findings permit the assumption that, under the laser radiation influence, the intracellular metabolic processes are intensified and accompanied by more marked bacterial division processes in a neutral medium.

Due to the lack of the rigid cell wall, mycoplasmas have a marked morphologic plasticity dependent on the medium in which they were grown[12]. The changes in the form found in the irradiated cells of our experiment do not exist in the nonirradiated controls. We can, therefore, state that the laser radiation is responsible for the changes induced to the irradiated samples, *i.e.* the increased cell volume and morphological plasticity, the presence of the division processes.

4. Conclusions

1. The influence of the Nd:YAG laser radiation second harmonic, (wavelength 532 nm / 32 mJ/cm^2 / 6 ns) on the *Mycoplasma agalactiae* bacterium was studied.
2. The laser radiation affected the TRIS-HCL buffered bacterial suspension by increasing the cellular volume and the morphologic plasticity, and by intensifying the metabolic processes translated by cell division processes.
3. The laser radiation did not morphologically affect the bacteria irradiated in their growth medium, it merely affected the cultivability degree on a solid medium.
4. The laser radiation did not affect the proteinic composition of the irradiated bacteria cell membrane.

References

1) V.V. Poppa, St. Nicole, M.D. Lupus, F.Durba, "Bazele radiobiologiei", Edts. Fundatia Romania de Maine, Bucharest, (2001).
2) F.S. Barnes, "Applications of lasers to biology and medicine" Proc. IEEE **63**, pp. 1269-1278, (1975).
3) L.Cummins, M. Navenberg, "Thermal effects of laser radiation in biological tissue", Biophys. J. **42,** pp.99-102, (1983).
4) V.F. Dima, V. Vasiliu, L. Popescu, I.N. Mihailescu, S.V.Dima, B. Murg, A. Popa, "Biologcal effects of pulsed near-ultraviolet laser irradiation in mouse lymphoma cells", Opt. Eng., **35**, pp. 1360-1388, (1996).
5) T.L. Karu, "Interactions of monochromatic visible lighs and near infrared radiation with cells, currently discussed mechanism", Proc. SPIE **2391**, pp. 576-586, (1995).
6) D.N. Dederich, M.A. Pickard, A.S. Vaughn, J. Tulip, K.L. Zakariasen, "Comparative bactericidal expsures for selected oral bacteria using carbon dioxide laser radiation", Laser Surg. Med. **10**, pp. 591-594, (1990).
7) R.H. Keates, P.C. Drago, E.J. Rotchild, "Effect of excimer laser on microbiological organisms", Ophtalmic Surg.,**19**, pp. 715-718, (198).
8) R.J. Schulz, G.P. Harvey, M.E. Fernandez-Beros, S. Krishnamurthy, J.E. Rodriguez, F. Cabello, "Bactericidal effects of the Nd:YAG laser; In vitro study", Lasers Surg. Med. **6**, pp.445-448, (1986).
9) O.A. Tiphlova, T.I. Karu, N.P. Furzikov, "Lethal and mutagenic action of XeCl laser radiation on Escheria coli", Laser in the Life Science pp. 155-159, (1988).
10) M. Solsona, M. Lambert, F. Poumarat, "Genomic, protein homogeneity and antigenic variability of Mycoplamsa agalactiae", Veterinary Microbiology **50**, pp. 45-58, (199).
11) U.K. Laemmli, "Cleanage of structural proteins during the assembly of the head of bacterophage T4", Nature **227**, pp. 680-685, (1970).
12) R.J. Milles, R.A.J. Nicholas, "Mycoplasma protocols, in Methods in Molecular Biology", Humana Press New-Jersey, (1998).

CHARACTERISTICS OF A HIGH-CURRENT PULSE GLOW DISCHARGE

K. Takaki, D. Taguchi, S. Mukaigawa, and T. Fujiwara

Department of Electrical and Electronic Engineering, Iwate University, Ueda 4-3-5, Morioka 020-8551, Japan

ABSTRACT

The voltage-current characteristics of transient glow discharges in dry air (N_2:O_2=8:2) at pressure of 10 torr were obtained for discharge currents up to 150 A using parallel-plane electrodes. The time-dependent glow voltage is obtained accurately by solving the circuit equation using the measured values of the current and breakdown voltage. Carborundum damping resistor is altered from 1 to 200 Ω in order to obtain the voltage-current characteristics in a wide current range. The glow discharge voltage was almost constant until the whole surface of the cathode was covered with glow, *i.e.*, until the discharge current became 3.7 A under our experimental condition (a normal glow discharge mode). The voltage, however, increased with the current when the glow covered over the cathode (an abnormal glow discharge mode). The electron density in positive column of the high-current glow discharge were obtained to be 4.9×10^{11} cm^{-3} from calculation based on nitrogen swarm data. This value is close to the electron density 3×10^{11} cm^{-3} measured with Langmuir probe. The glow-to-arc transition starts to develop in the discharge region near the cathode at 0.035 $J\cdot cm^{-3}$ energy dissipated in the cathode fall region during the glow phase. The high-current glow discharge plasma was successfully produced with 35 μs duration at 1 kHz repetition rate using a pulse modulator.

I. Introduction

Glow discharges are used for material surface treatment as metal nitriding [1)-3)], ion implanting to polyethylene [4)] etc. Although the low pressure glow plasma are mainly used in conventional system for nitriding and implanting, some nitriding are operated in a range of a few torr. [2)] Our objective is the production of a high density, large volume and low gas temperature plasma utilizing a pulse glow discharge with high-current at gas pressure from a few torr to a hundred torr. [5)-7)] A lot of processes in a direct current (dc) glow plasma are governed by the voltage-current (*V-I*) characteristics of the discharge. [8)] In this paper, the experimental studies on the *V-I* characteristics of a transient or pulsed glow discharge with high current up to 150 A after static breakdown of pure nitrogen gas are described. Using the measured glow voltage and the cathode fall voltage, the electron density and the electron temperature in the positive column are calculated.

II. Experimental details

The experimental apparatus used in the present experiment consists of a co-axial discharge chamber, damping resistors and a capacitor. Electrode plates with rounded edges were made of copper and set in the discharge chamber. The overall diameter and thickness of the

electrodes are 10.7 cm and 1.5 cm, respectively. The one electrode is connected to a 1.89 μF capacitor which is charged negatively up to high voltage. The other electrode is grounded through the damping resistors. The gap spacing between the electrodes was changed from 0.2 to 2 cm. The pressure of pure nitrogen gas was kept to 10 torr in the discharge chamber. The gas in the chamber was exchanged after every discharge.

The 1.89 μF capacitor was slowly charged with nearly constant current of 0.5 mA. The carborundum damping resistors were used to control the discharge current. The return current flows into the ground through twelve stainless rods. The breakdown voltage was accurately measured using a resistive voltage divider with 1000:1 ratio. The discharge current was measured by means of a Pearson Model 110A current transformer and a Sony-Tektronix Model 540 digital oscilloscope. Then the signal is transmitted to a personal computer through a GPIB cable in order to calculate the gap voltage v(t) using the following circuit equation:

$$v(t) = V_{br} - \frac{1}{C}\int i(t)dt - R \cdot i(t) - L\frac{di(t)}{dt}, \tag{1}$$

where V_{br} and i are the breakdown voltage and the current, respectively; C, R and L are the capacitance, resistance and inductance of the circuit, respectively. The inductance L was determined from a period of the L-C oscillation in the prior experiment. The damping resistor R was altered from 1 to 200 Ω to acquire the V-I characteristics in a wide current range.

Electron density and temperature was obtained using Langmuir probe. The measurement of the probe current waveforms in pulsed glow plasma at various probe bias voltages, and probe current-bias voltage curves were drawn using them at various times. The probe tip is made of tungsten with 0.2 mm diameter and 3 mm length, and is placed at the middle between the electrodes.

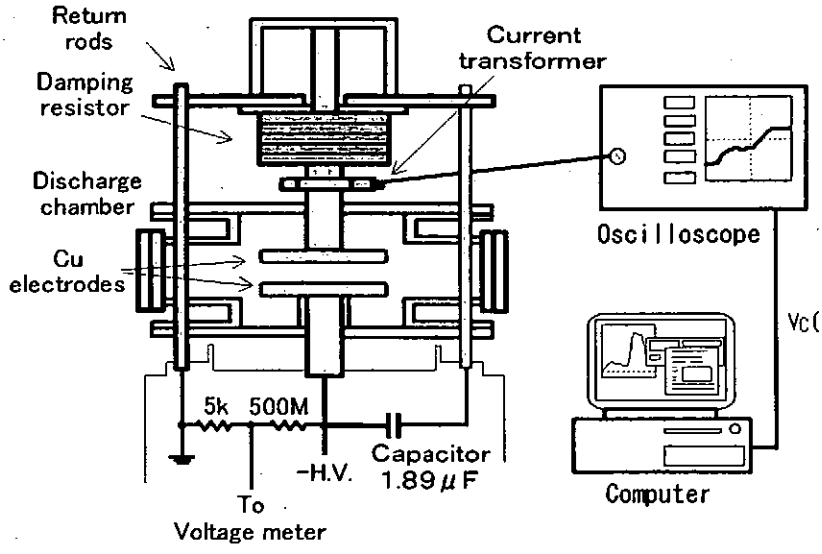

Fig. 1 Experimental apparatus.

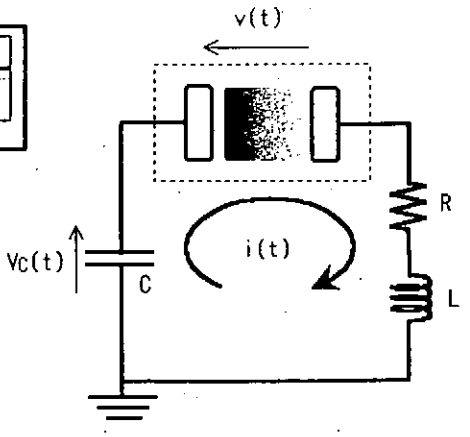

Fig. 2. Equivalent circuit of the discharge system.

III. Characteristics of a transient glow discharge

A. Voltage-current characteristics of transient glow discharge

Figure 3 shows a typical current oscillogram and the series of photographs of high-current transient glow discharge, respectively. The exposure time, *i.e.* the time duration between the converter camera is opened by the gating pulse and closed, is 50 ns. The converter opening time for each frame is indicated by the number enclosed with a circle under the trace of the discharge current. The time t is measured from the origin when the discharge current is first detected, and the time t_s indicates the beginning of the filamentary glow or arc discharge. The structure of the discharge during the development can be deduced from the series of photographs in Fig. 3. The appearance of the discharge shown in frame ① closely resembles that of a stable glow discharge exhibiting a uniform positive column, a Faraday dark space and a negative glow. Frames ④—⑧ show that after the time t_s show that appears on the surface of the cathode a luminous spot and induces the second glow phase and/or the arc phase. With the increase in current, the discharge constricts while the luminosity increases at the core of the discharge.

The build-up of the current takes place in two steps as shown in Fig. 3. In the growth of the discharge current up to the order of amperes, it has been reported that three plateaus appear corresponding to the occurrence of the diffused glow, the filamentary glow, and the arc in hydrogen in pressure range from 300 to 700 torr at electrode separations of several millimeters. [9] In this work, the step of the current growth according to the filamentary glow cannot be distinguished from that of the arc discharge. The duration of the glow phase and the glow current are 2.2 μs and 310 A, respectively.

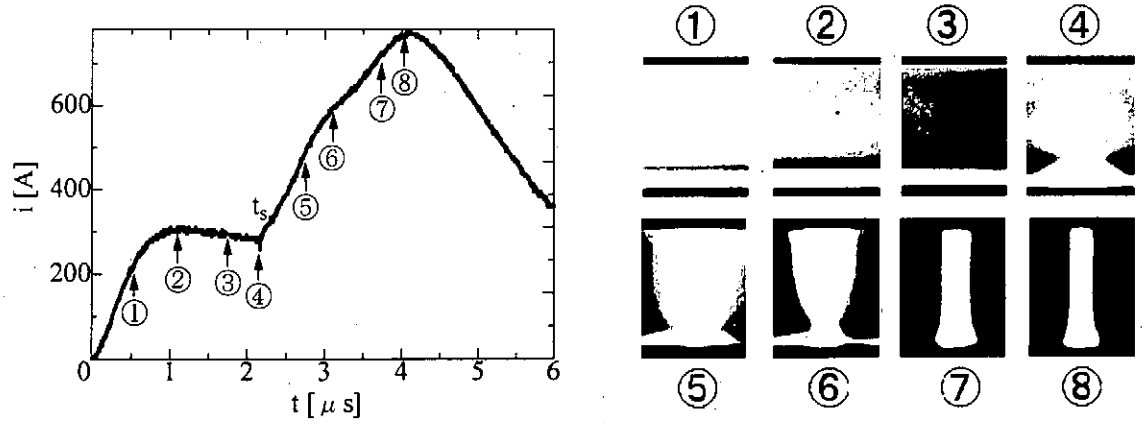

Fig. 3 Shutter photographs of a discharge at 5.5 torr and 2 cm. Shutter opening time for each frame is indicated under the trace of the discharge current. Lower electrode is cathode and upper electrode is anode.

Representative voltage and current waveforms of high-current transient glow discharge at damping resistor of 1 Ω are shown in Fig. 4. After a static breakdown, marked ① on the trace, the discharge current increases up to 150 A, and the gap voltage decreases from a breakdown voltage to the value of a quasi-stable step, marked ②, as the discharge develops. The time duration from ② to ③ indicates that the discharge mode is the transient glow. In this case, the glow voltage decreases from 920 V to 800 V with decreasing glow current from 150 A to 107 A. At the time marked ③, an appearance of a luminous spot on the cathode

surface was observed by the image-converter camera photographs. After then the voltage collapses to a few ten volt with glow-to-arc transition in time from ③ to ④. After the time marked ④, the arc discharge current decreases at a time constant of *RC*.

Figure 5 shows the *V-I* characteristics obtained from Fig. 4. The *V-I* characteristics have two positive slopes; the first is the time from ② to ③ and the second is the time after ④. These correspond the characteristics of the glow discharge and the arc discharge, respectively. The two negative slopes mean the transient phases; Townsent-to-glow transition (①—②) and glow-to-arc transition (③—④).

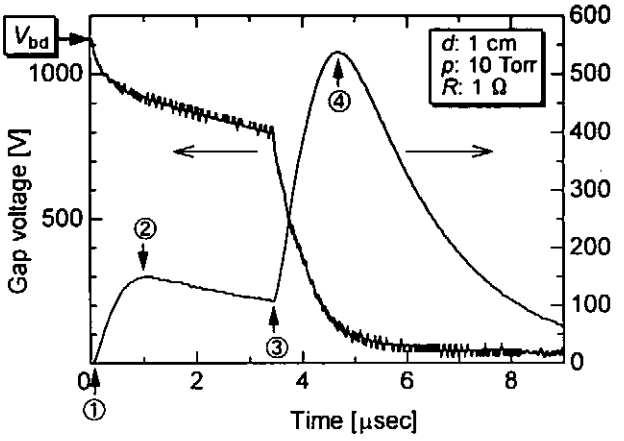

Fig. 4 Voltage and current waveforms of the pulse discharge. P=10 torr. d=1 cm. R=1Ω.

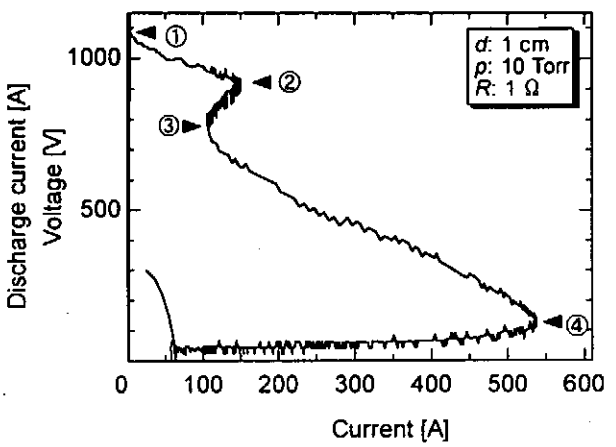

Fig. 5 Voltage-current characteristics of the pulse discharge. P=10 torr. d=1 cm. R=1Ω.

Figure 6 shows the *V-I* curves of the glow mode at various values of the resistance R of the damping resistor. The broken line shows the interpolation by an exponential function. In the case of R=1, 3, 9 Ω, the glow discharge is transient, which means glow-to-arc transition occur after the glow. In this case, the duration of glow are 3.5, 3.0, 20 μs, respectively. When R > 18 Ω, the glow-to-arc transition does not occur, therefore the glow mode durations are almost determined by the time constant CR (=1.89 R [μs]) of the apparatus. The empirical formula of current density j_{ng}:

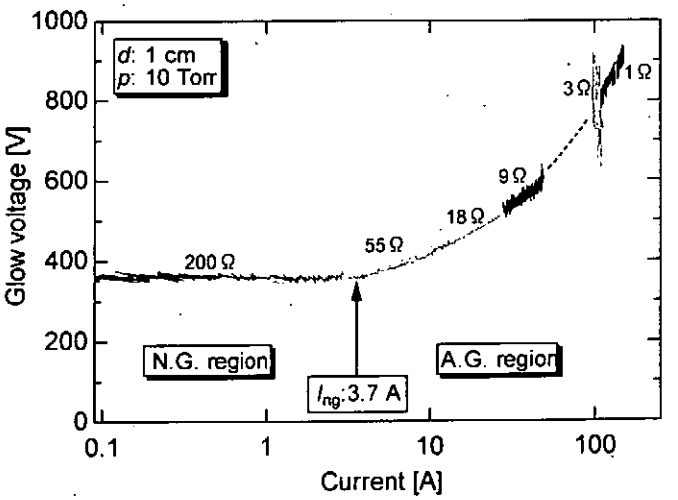

Fig. 6 Voltage-current characteristics of glow discharge. P=10 torr. d=1 cm.

$$j_{ng} = 240 \times 10^{-6} p^2 \quad [\mathrm{A/cm^2}] \tag{2}$$

for Cu-Air low pressure normal glow. [10] Where, p is gas pressure. The total surface area of

the electrode 10.7 cm in diameter is obtained to be 155 cm^2 (= 76 cm^2 plane area + 79 cm^2 rounded edge). Therefore, when the whole cathode surface is surrounded by normal glow, the value of the current is obtained to be 3.7 A, which is indicated as I_{ng} by arrow in Fig. 6. The glow voltage is almost constant in the case of current lower than 3.7 A while it increases with increasing current in a range higher than 3.7 A. This fact implies that the discharge changes from a normal glow to an abnormal glow at the discharge current of 3.7 A.

B. Current density

Figure 7 shows the relationship between discharge current at the time just prior to t_s and circuit resistance R with gas pressure pas a parameter at electrode separation of 1.0 cm. The glow current decreases with the circuit resistance. The transient glow current can be regarded as being proportional to R^{-k} (k<1) from the slope of the lines in log-log scale. Figure 8 shows the plotted cathode current density at the time just prior to t_s in relation to circuit resistance R with gas pressure p at electrode separation of 1.0 cm. The broken lines represent the value calculated from the equation (2) for Cu-Air normal glow. The current density j is given by:

$$j = \frac{I_g}{S} \tag{3}$$

where S is the cross-sectional area of the glow cylinder and obtained from the photograph of the negative glow on the cathode. In this work for R>60 Ω, the current density at 20 torr is almost independent of the circuit resistance and is close to the value derived from $240\times10^{-6}\,p^2$. The current density, however, increases with the decrease of the resistance in a range of R<60 Ω. This fact indicates that a transient glow changes from the normal glow to the abnormal glow by making the resistance small. At 10 torr the current density of the glow discharge which decreases with the resistance because the glow current decreases in a range of 1 to 200 Ω. The maximum value of the cathode current density of the glow discharge is 3.2 A/cm^2, which is almost two orders larger than the value obtained from the formula of Cu-air normal glow.

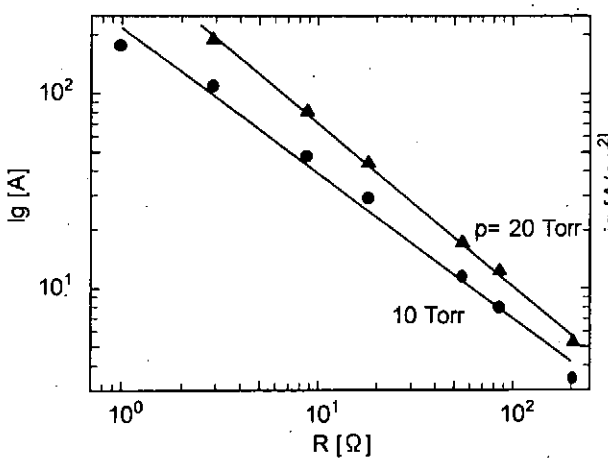

Fig. 7 Dependence of transient glow discharge current on circuit resistance R at different values of gas pressure p. d=1 cm.

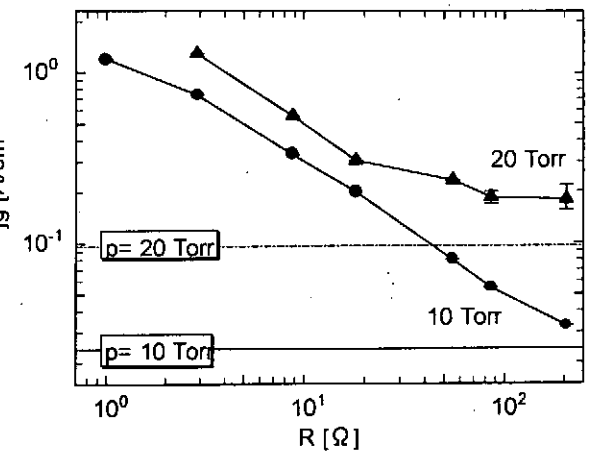

Fig. 8 Current density on the cathode at the time just prior to t_s as a function of circuit resistance R at different gas pressures. d=1 cm.

C. Electron density

The value of E/p, on the plateau of the V-I curve, in the positive column of the glow discharge was deduced from the measured values of the glow voltage. Figure 9 shows the plotted gap voltage just prior to t_s in relation to the electrode separation d with gas pressure p as a parameter. The circuit resistance is 1 Ω. The gap voltage decreases linearly with reducing electrode separation. The cathode fall voltage can be obtained to 285 V as "zero length voltage" [11] by extrapolating the potential distribution across glow discharge to zero electrode separation. In the normal glow mode (I < 3.7 A), the value of E/p is obtained to be 8.6 V/cm/torr and independent of the discharge current. At discharge current of 144 A (in abnormal glow mode), the E/p is 61.6 V/cm/torr. The electron density of the positive column N_e can be estimated using the following formula:

$$N_e = \frac{j}{eW} \tag{4}$$

where j, e and W are current density, electron charge and electron drift velocity, respectively. The parameter W is calculated as a function of E/p, [12] and it is 4.5×10^6 cm/s for normal glow mode and 20.5×10^6 cm/s for abnormal glow at current of 144 A. The current density j in the abnormal glow mode can be determined by division of the total glow current by the cross section of the positive column; it was calculated to be 89.9 cm^2. Therefore, the electron densities of the positive column can be estimated to 3.3×10^{10} cm^{-3} for normal glow (I < 3.7 A) and 4.9×10^{11} cm^{-3} for abnormal glow (I = 144 A).

Figure 10 shows the time variation of the electron density measured with Langmuir probe at the middle between the electrodes. In this experiment, the gas pressure and the electrodes

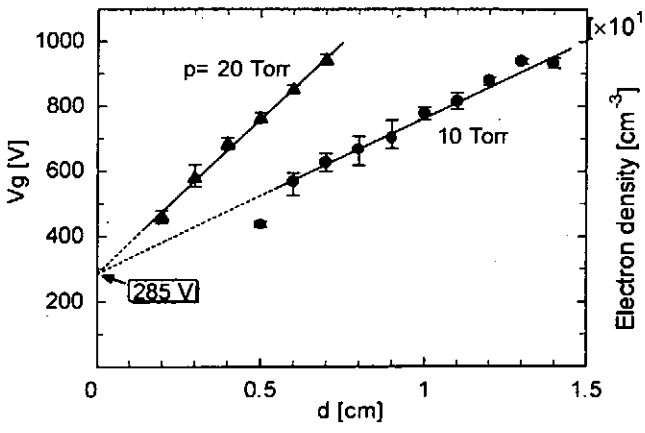

Fig. 9 Relationship between gap voltage at the time just prior to t_s and electrode separation. R=1Ω.

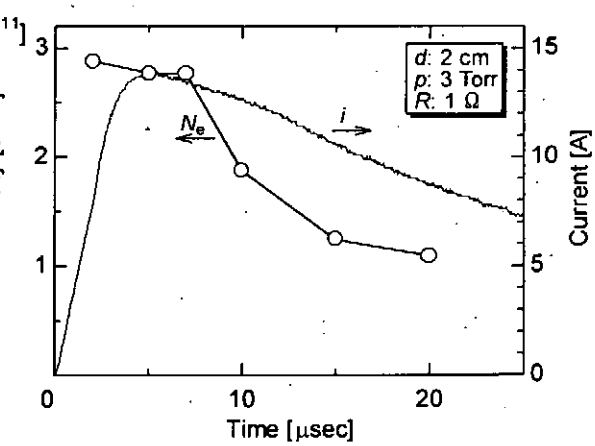

Fig. 10 Time dependence of electron density of abnormal glow discharge. P=3 torr. d=2 cm. R=1Ω.

separation were kept at 3 torr and 2 cm, respectively. In this condition, the glow-to-arc transition did not occur. The current when the normal glow plasma covered over the whole cathode was 0.33 A from calculation of equation (2). The peak current of the pulse glow discharge is almost 14 A, which is 40 times larger than the normal glow current 0.33 A. Therefore, the discharge belongs to the abnormal glow. The electron density rapidly increases to almost 3×10^{11} cm^{-3} after a formation of the

glow discharge. And then, the electron density becomes the value on the plateau of the time variation during 5 μs.

D. Energy dissipation for glow-to-arc transition

Figure 11 shows the energy dissipated in the gap during glow phase E_g in relation to electrode separation at different gas pressures p with circuit resistance of 1 Ω. The dissipated energy was obtained from the glow current and the breakdown voltage by solving the circuit equations (1) and

$$E_g = \int_0^{t_s} i(t) \cdot v_g(t) dt \tag{5}.$$

The values of dissipated energy E_g are in a range from 0.1 to 0.7 J. Chalmers *et al* suggested that the criterion for a glow-to-arc transition is that a certain quantity of energy is dissipated in the gap during the glow phase. [13] This suggestion is based on the fact that the dissipated energies obtained by Allen and Farish were approximately the same value, that is, 1.5 J. [14),15] The present values from 0.1 to 0.7 J are much smaller than those values reported by Chalmers and larger than the values by Fujiwara *et al*. [16),17] Therefore, the dissipated energy of the transient glow changes according to experimental condition and it cannot be used as criterion for a glow-to-arc transition. Moreover, the dissipated energy E_g is regarded as generally increasing with electrode separation though the measured values are scattered.

The present visual observation shown in Figure 3 represents that the filamentary discharge is initiated near the cathode surface where the cathode fall occurs. The growth of the cathode attachment strongly suggests that the initiation of the discharge filamentation may be a result of the characteristics of the cathode fall region. Fujiwara *et al* suggested that the criterion for a glow-to-arc transition is that a certain quantity of energy is dissipated on the cathode during the glow phase. [16] The dissipated energy on the cathode can be calculated if energy dissipated in the cathode fall region is obtained from the following equation:

$$E_C = V_c \int_0^{t_s} i(t) dt \tag{6}.$$

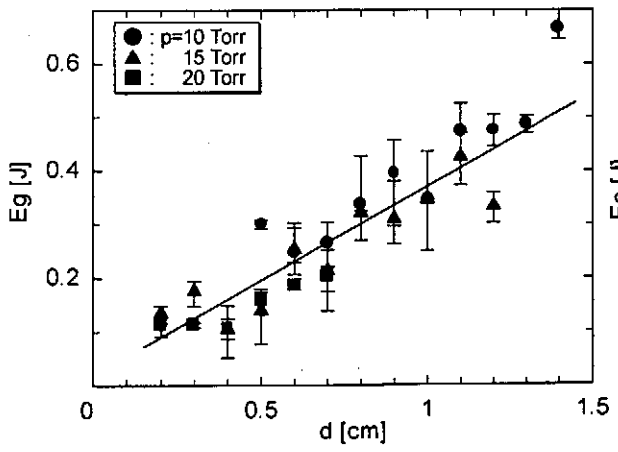

Fig. 11 Dependence of energy dissipated in the gap during glow phase E_g on on electrode separation d at different gas pressures. d=1 cm. R=1Ω.

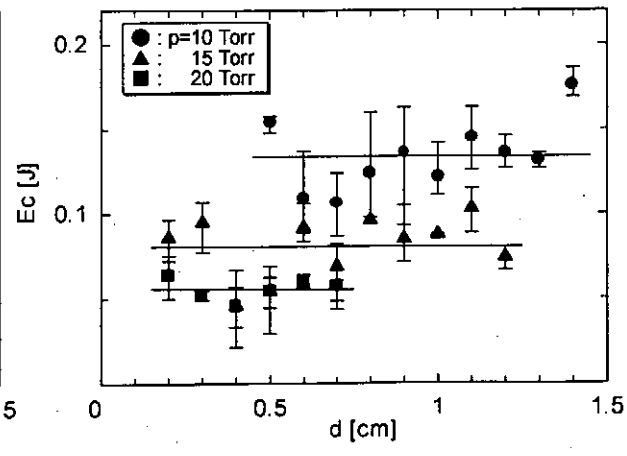

Fig. 12 Dependence of energy dissipated in the cathode dark space during glow phase E_C on electrode separation d at different gas pressures. R=1Ω.

In calculation of this equation, the measured value of zero length voltage 285 V was used as V_c. Figure 12 shows the plots of the energy dissipated in the cathode fall region during glow phase E_C in relation to the electrode separation with different values of gas pressure p. These conditions are the same as those in Figure 11. Though the dissipated energy in the gap E_g increased linearly with the electrode separation, the dissipated energy in the cathode fall E_C is almost constant. This fact indicates that the increase of E_g with electrode separation is caused by the increase of energy dissipation in the positive column whose length is nearly equal to the electrode separation. Moreover, Figure 12 reveals that the dissipated energy in the cathode fall E_C has depends on gas pressure and decreases with increasing gas pressure.

Chang *et al* have reported that the thermal instability, which is a local perturbation of electron or gas density that enhances local joule heating, mainly caused the discharge filamentation.[17] The dissipated energy density in the cathode fall region H can be calculated using the following equation:

$$H = \frac{E_c}{S_c \cdot l_c} \tag{7}$$

where S_c and l_c are the cathode area (*i.e.* the cross-section of the glow discharge) and cathode dark thickness, respectively. In calculating this equation, a measured zero length voltage of 285 V was used for V_c along with the data for pl_c=0.23 torr cm given a copper cathode in normal dc glow discharge. Figure 13 shows the plotted dissipated energy density H in relation to the electrode separation with different values of gas pressure p. The conditions are same as those in Figure 11. The obtained values for dissipated energy density in the cathode fall region H are almost constant in relation to the variable electrode separation and gas pressure and are equal to 0.035 J/cm^3. In industrial applications the transient glow discharge runs under gas flow conditions. Gas replenishment will therefore have the effect of stabilization on glow discharges at atmospheric pressure.

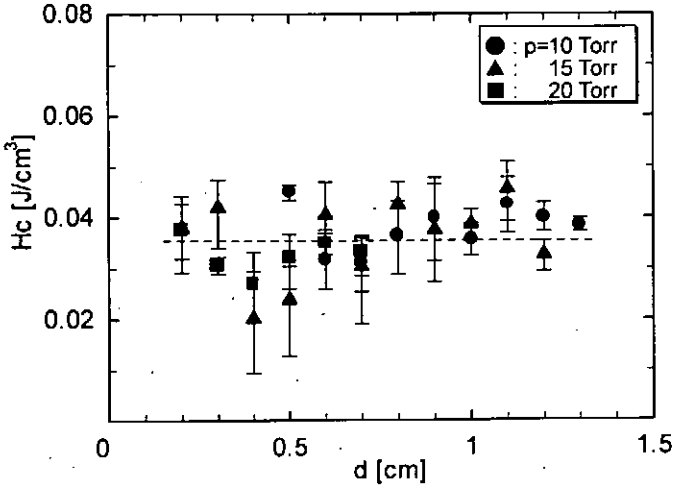

Fig. 13 Dependence of density of energy dissipated in the dark space during glow phase H on electrode separation d at different gas pressures. R=1Ω.

E. Production of glow discharge plasma using pulse modulator

The pulse glow discharge without glow-to-arc transition can be produced using a pulse modulator. The typical waveforms of the glow discharge current and the applied voltage are shown in Fig. 14. The electrode separation and the gas pressure are 2 cm and 12 torr, respectively. The applied pulse duration was set to 35 μs at 1,000 pps (pulses per second) repetitive rate. Figure 14 shows 60-120 A glow discharge is generated with 600 V applied voltage. The glow discharge plasma is spatially uniform as shown in Fig. 15.

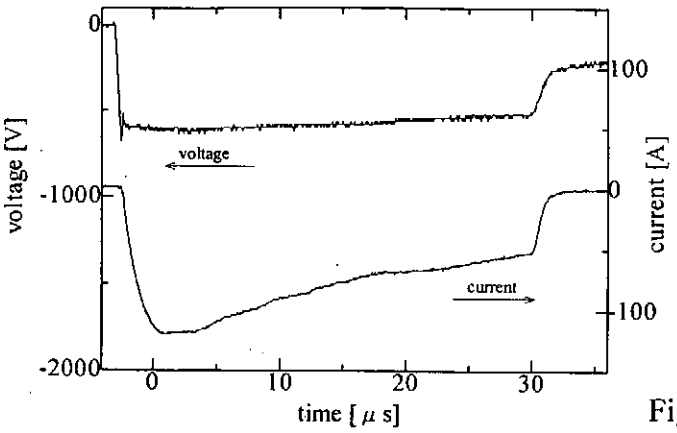

Fig. 14 Applied voltage and glow discharge current at 1 pps (pulse per second) repetitive rate. d=2 cm. p=12 torr.

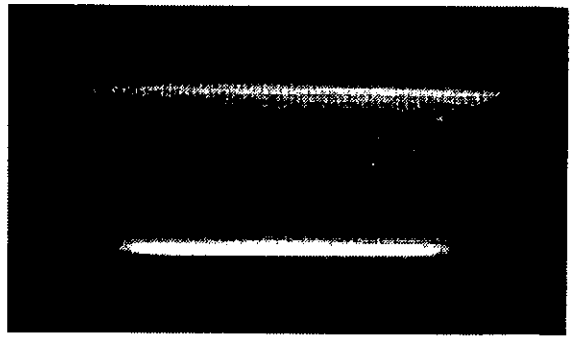

Fig. 15 Photograph of pulse glow discharge plasma. The lower and the upper electrodes are cathode and anode, respectively. d=2 cm.

The gas temperature in the glow discharge plasma can be determined as rotating temperature of nitrogen molecule. Figure 16 shows the time-dependence of the rotating temperature in the pulse glow discharge plasma. The electrode separation and the gas pressure are 1 cm and 6 torr, respectively. The applied pulse duration was set to 10 μs at 1,000 pps repetitive rate. The rotating temperature of the nitrogen gas was obtained using spontaneous emission from the glow discharge $C^3\Pi_u$ - $B^3\Pi_g$ emission bands of N_2. The temperature increases from 400 to 650 K during the glow discharge.

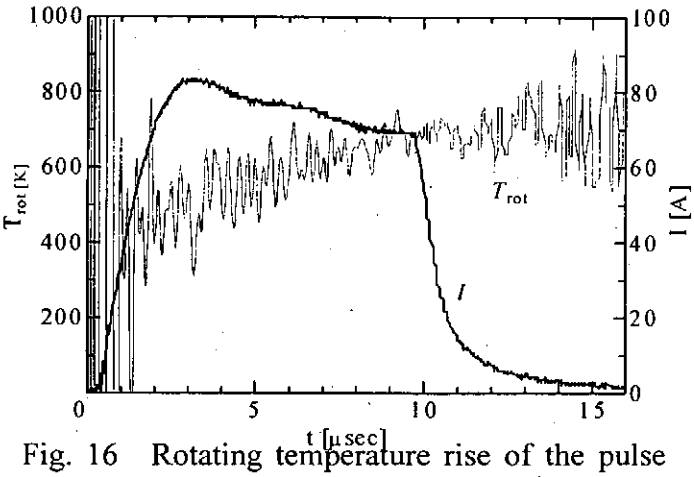

Fig. 16 Rotating temperature rise of the pulse glow discharge. d=1 cm. p=6 torr. f=1,000 pps.

IV. Conclusion

With respect to the generation of high-density and large-volume plasma, the present research examined high-current transient glow discharge in dry air after static breakdown. A low inductance capacitor of 1.89μF and a discharge apparatus with co-axial configuration were used to produce a transient glow discharge with high current in excess of 150 A. Results showed that the high-current glow discharge with the 1 Ω circuit resistance has the cathode current density of 3.2 A/cm^2, which is almost two orders larger than the value obtained from the formula of Cu-air normal glow. The electron density in positive column of the high-current glow discharge were obtained to be 4.9×10^{11} cm^{-3} from calculation based on nitrogen swarm data. This value is close to the electron density 3×10^{11} cm^{-3} measured with Langmuir probe. The glow-to-arc transition starts and develops in the discharge region near the cathode. The dissipated energy density in the cathode fall region during the glow phase is almost constant against the gas pressure and the electrode separation having a value of 0.035

$J \cdot cm^{-3}$ under the present experiment's conditions. The high-current glow discharge plasma was successfully produced with 35 μs duration at 1 kpps repetition rate using a pulse modulator.

Acknowlidgements

The authors would like to thanks Prof. N. Sato of Iwate University, Prof. H. Akiyama of Kumamoto University and Prof. K. Yukimura of Doshisya University for their valuable discussions and comments. The authors would like to thanks Mr. T. Kato of Iwate University and Mr. Y. Nishimura of PEKURIS Co. for their cooperation.

References

1 T. Czerwiec, N. Renevier and H. Michel, Surf. Coat. Technol., **131**, 267-277 (2000).
2 B.-Y. Jeong and M.-H. Kim, Surf. Coat. Technol., **137**, 249-254 (2001).
3 B.Y. Tang, P.K. Chu, S.Y. Wang, K.W. Chow, X.F. Wang, Surf. Coat. Technol., **103-104**, 248-251 (1998).
4 J.S. Chen, S.P. Lau, Z. Sun, B.K. Tay, G.O. Yu, F.Y. Zhu, D.Z. Zhu, H.J. Xu, , Surf. Coat. Technol., **138**, 33-38 (2001).
5 K. Takaki, D. Kitamura, and T. Fujiwara, J. Phys. D: Appl. Phys., **33**, 1369-1375 (2000).
6 K. Takaki, D. Taguchi, T. Fujiwara , App. Phys. Lett., **78(18)**, 2646-2648 (2001).
7 K. Takaki, D. Koseki, and T. Fujiwara, Surf. Coat. Technol., **136**, 261-264 (2001).
8 L.J. Denes and J.J. Lowke, Appl. Phys. Lett., **23**, 130 (1973).
9 A. Doran and J. Meyer, Brit. J. Appl. Phys., **18**, 793 (1967).
10 Y. Asami, T. Dote, and Y. Suginuma, Houden Handbook (Corona Co. Tokyo, 1974) 110. [in Japanese]
11 M. Cavenor and J. Meyer, Aust. J. Phys., **22**, 155 (1969).
12 S. Takeda, Kitai Houden no Kiso (Tokyo Denki, Tokyo, 1990) 35. [in Japanese]
13 I. Chalmers, J. Phys. D: Appl. Phys., **4**, 1147 (1971).
14 K. Allen and K. Phillips, Proc. R. Soc. A, **278**, 188 (1963).
15 O. Farish and D. Tedford, Proc. IEE, **114**, 277 (1967).
16 T. Fujiwara, T. Sato, J. Sekikawa and H. Yamada, J. Phys. D: Appl. Phys., **27**, 826 (1994).
17 T. Fujiwara, H. Yamada, H. Taniguchi and K. Sugita, Jap. J. Appl. Phys., **31**, 1470 (1992).
18 J. Chang, A. Phillips and B. Warner, IEEE Trans. Plasma Sci., **25**, 392 (1997)

OPTIMIZATION TO SYNTHESIZE NANOSIZE POWDER OF AlN BY PULSED WIRE DISCHARGE

C.Cho, Y.Kinemuchi, T.Suzuki, H.Suematsu, W.Jiang and K.Yatsui

Extreme Energy-Density Research Institute, Nagaoka University of Technology, Niigata 940-2188, Japan

ABSTRACT

Experimental studies were carried out on the synthesis of nanosize powders of aluminum nitride (AlN) by pulsed wire discharge (PWD). Efforts were devoted to optimize the purity of the synthesized AlN powder by changing circuit inductance and discharge energy. The deposited energy in the wire before the explosion significantly increases when the current rise time is decreased and peak current is increased. The quantitative analysis by X-ray diffraction showed that AlN content is increased by reduction of circuit inductance or increment of charging energy. The highest AlN content of the powder synthesized in mixed NH_3 gas with N_2 was 95 wt.%. The number of micrometer size particles observed by SEM is decreased with increasing AlN content.

I. Introduction

Recently, the synthesis of nanosize powders has been proposed by pulsed wire discharge (PWD)[1]. Its basic concept is that metal wires can be instantaneously exploded into vapor plasma due to very fast electrical heating by using pulsed high current, and the vapor plasma will be cooled due to collisions with surrounding gaseous molecules. Nanosize particles are produced by condensation of the supersaturated vapor. This method of producing nanosize powders is attractive owing to its high energy-conversion efficiency and high productivity. Not only various metal powders but ceramic powders have been produced by using this method. For example, the evaporated aluminum metal vapor may react with O_2 atmospheric gas, resulting in Al_2O_3 powders.[2, 3] When N_2 gas mixed with NH_3 is used as the atmospheric gas, AlN ceramic powder has been found to be produced.[4] The AlN powder has some useful characteristics for commercial applications such as high thermal conductivity, high electrical resistibility, and low thermal expansion coefficient. [5]

In our previous work, the maximum content of AlN produced by PWD in nitrogen gas was observed to be 15%.[4] However, when the mixed nitrogen gas with ammonia gas of

20% was used, the content reached up to 80% at the pressure of 750 Torr. [4]

In general, micrometer size particles have been observed in the powders synthesized by PWD method.[2] The origin of the micrometer size particles may be attributed to the micrometer size liquid drops originated from incomplete vaporization of the wire. It was expected that the quantity of liquid drops can be reduced by means of increasing the heating efficiency of the wire.

II. Experimental setup

Figure 1 shows the schematic of the experimental setup. Six pieces of aluminum wire are installed on the wire holder that was made with an insulator disc and stainless steel screws. Both ends of each wire are contacted with two electrodes that were connected to the capacitor bank through the spark gap switch and high voltage feed-through. This apparatus enables us to explode six pieces of wires by rotating the wire holder without opening the chamber. The powders are collected by the evacuation through a filter. The experimental conditions are shown in Table I. The inductance was varied by the loop area of connection cable under the same circuit resistance.

The powders were characterized by X-ray diffraction (XRD) and observed by SEM. The average particle size was estimated by Scherrer's equation. The AlN content was estimated by the ratio of integration of intensity of AlN (100) peak to Al (111) peak after the peak separation. The calibration curve for the quantitative analysis of AlN content by XRD has been obtained using commercial powders of AlN (purity 99%, 0.6 μm in diameter) and Al (purity 99.5%, 53-150 μm in diameter).[4]

Table I. Typical experimental conditions of pulsed wire discharge

Wire	Aluminum (Purity 99.99%) Diameter 0.25mm, length 25mm Vaporizing energy 36 J
Atmospheric gas	N_2 600Torr + NH_3 150Torr
Capacitance	10 μF or 20 μF
Circuit inductance	0.7 μH ~ 3.0 μH
Charging voltage	3~ 6 kV

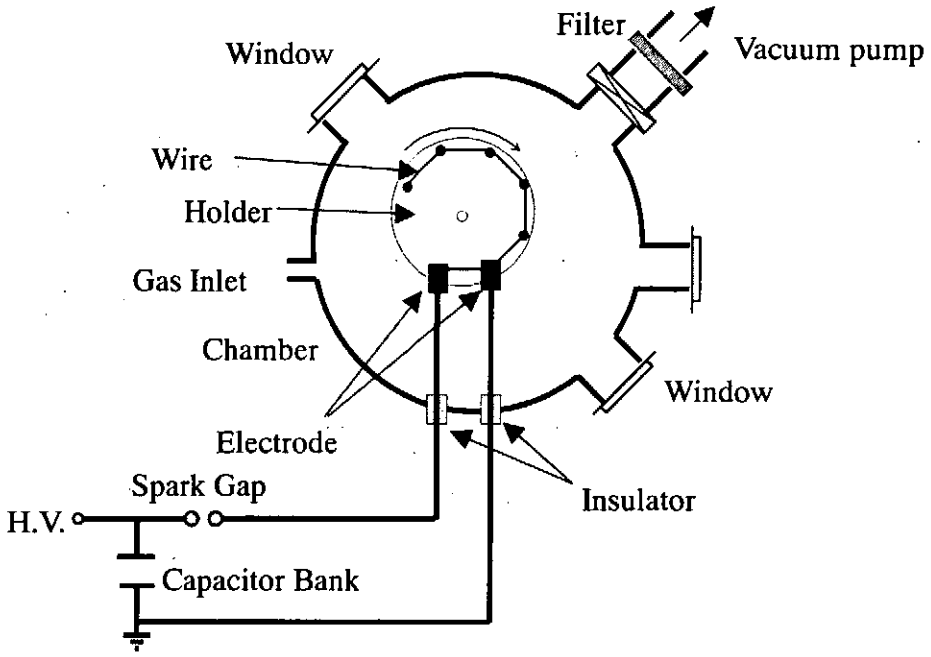

Fig. 1 Schematic of experimental setup

III. Experimental Results and Discussions

Figure 2 shows the current waveforms with the inductance as a parameter. A noticeable feature of current waveforms of the exploding wires is the sudden drop of its amplitude, and all the waveforms show a similar trend. From the observations of exploding process with a high-speed camera, it is considered that the wire is turned into the vapor plasma at the time of the current drop.[1)] This current drop may have arisen from the increase in the resistance of the wire due to vaporization. After the current drop, current damps smoothly because new current paths have been formed through the vaporizing plasma. Figure 2 shows that the rise time and fall time of the current were shortened as the inductance was reduced, while the peak value increased with reducing inductance.

Figure 3 shows the AlN content synthesized in the mixed gas of 20% NH_3 with N_2 as a function of inductance. The AlN content significantly varies with the change of inductance. The inductance is changed with the same discharge energy of 80 J (10 μF of capacitance, 4kV of charging voltage) or 90 J (20 μF, 3kV). When the inductance was reduced from 3.0 μH to 0.7 μH, AlN content increased by 20 wt.% at 80 J and 10 wt.% at 90 J, respectively.

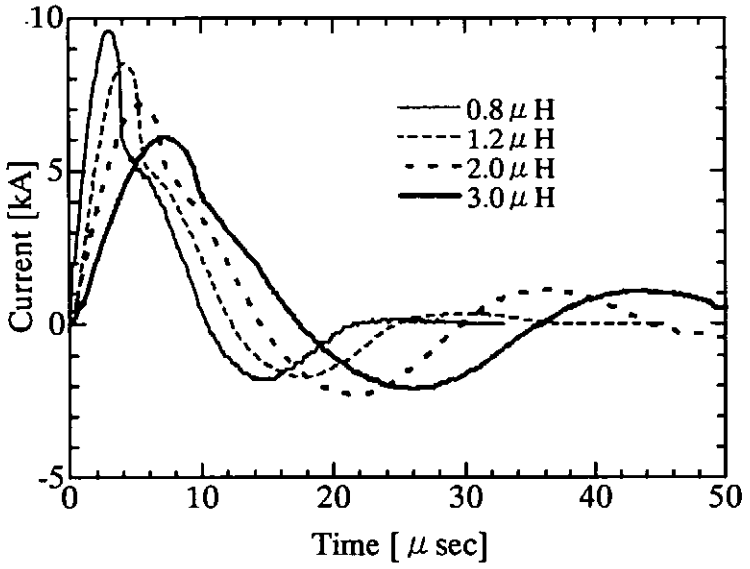

Fig. 2 Current waveforms with inductance as a parameter, where the capacitance of 10 μ F was charged at 4kV.

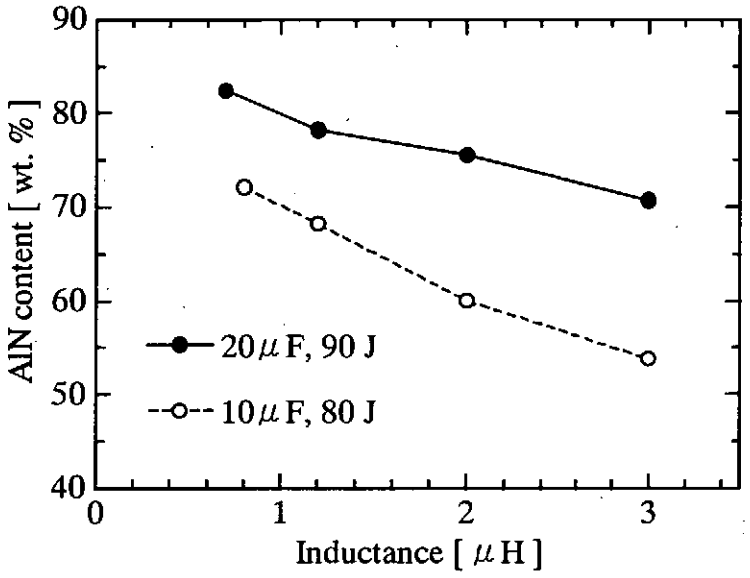

Fig. 3 AlN content as a function of inductance.

The first quarter cycle of current waveforms are shown in Fig. 4 with the charging energy as a parameter at 20 μ F, 0.7 μ H. The time of current drop is gradually shifted to the earlier timing as the charging energy is increased. It is seen that the current peak is enhanced as the charging energy is increased.

Figure 5 shows the deposited energy until the wire exploded, (E_e), as a function of charging energy. The deposited energies have been calculated from the current waveforms shown in Fig. 4 using the following equation.

$$E_e = \frac{1}{2}CV_0^2 - \left(\frac{1}{2}C\left(V_0 - \frac{1}{C}\int_0^{t_e} i(t)dt\right)^2 + \frac{1}{2}Li(t)^2 + R_k\int_0^{t_e} i(t)^2 dt\right), \quad (1)$$

where E_e, C, V_0, L, R_k, t_e and i are the energy deposited in the wire before the explosion, capacitance, charging voltage, circuit inductance, circuit resistance (35 mΩ), time of current drop, and current measured at time t.

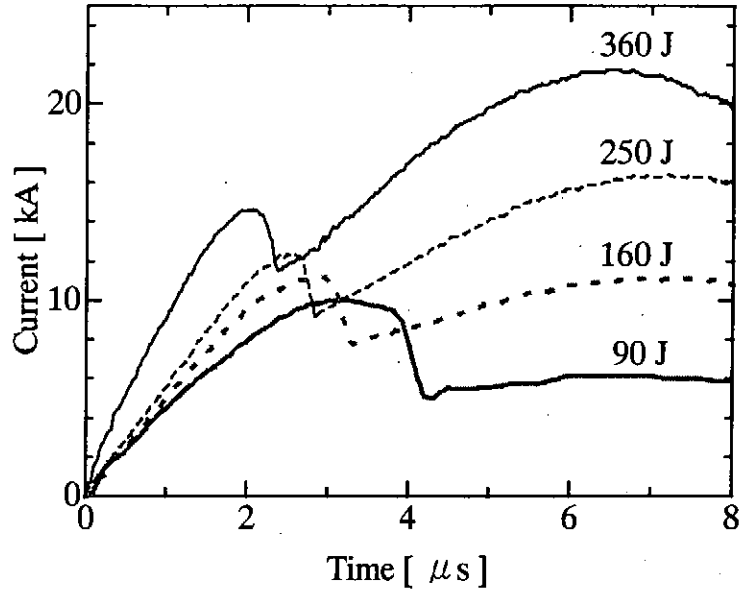

Fig. 4 Current waveforms with charging energy as a parameter, where the capacitance and inductance were 20 μF and 0.7 μH, respectively.

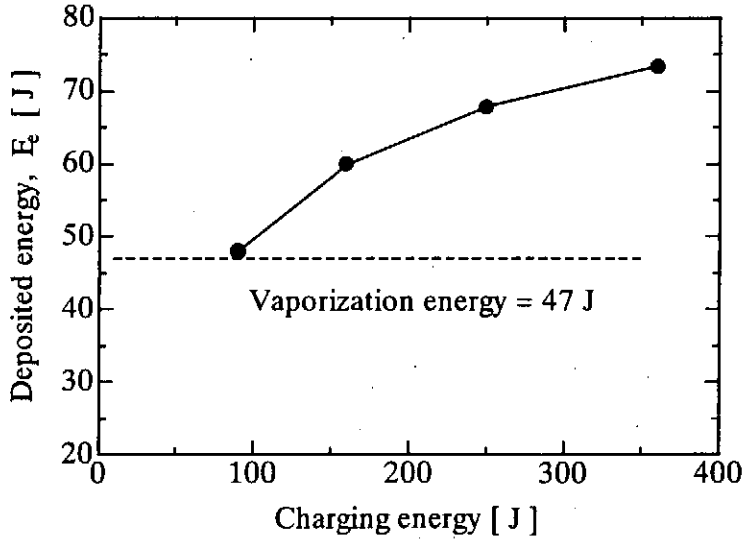

Fig. 5 Energy deposited before the explosion as a function of charging energy, where the capacitance and inductance were 20 μF and 0.7 μH, respectively.

The energy E_e is increased by shortening the rise time of current and increasing the

peak current. The current rise time has been shortened by reducing inductance as shown in Fig. 2 and by increasing charging energy as shown in Fig. 4. The energy required to vaporize the wire, E_v, is 47 J.[6] It can be seen that the energy E_e exceeds the vaporization energy. The factor E_e/E_v increased up to 1.6 at the charging energy of 360 J, when the capacitance and inductance are 20 μF and 0.7 μH, respectively.

Figure 6 shows the AlN content as a function of charging energy with the inductance as a parameter. The AlN content is increased as the charging energy is increased. At 0.7 μH, when the charging energy exceeds 200 J, the AlN content is saturated at 95 wt. %. To obtain the same AlN content in the higher inductance setup, much higher charging energy is required than that in lower inductance setup. As shown in Fig. 6, the required energies for 90 wt.% of AlN are 120 J and 250 J at 0.7 μH and 2.0 μH of circuit inductances, respectively.

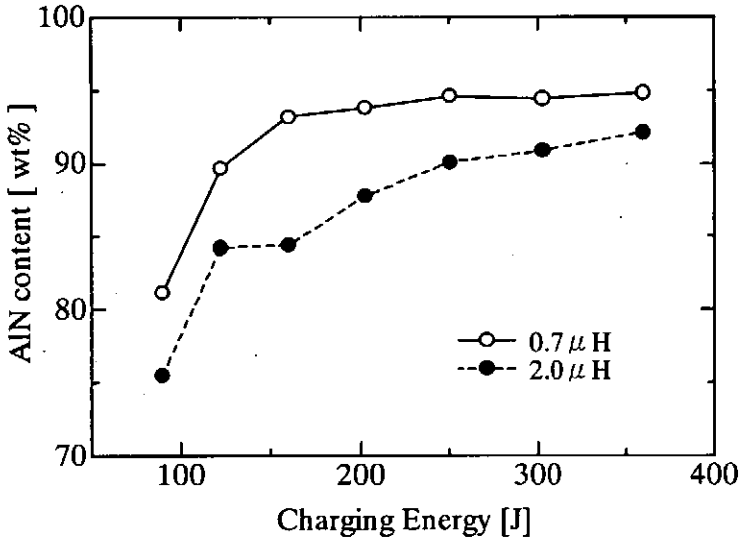

Fig. 6 AlN content as a function of charging energy

Figure 7 shows the XRD results of the samples obtained with (a) 20 μF, 90 J and (b) 20 μF, 360J in the lowest inductance of 0.7 μH. The solid lines of Fig. 7 show the measured XRD characteristics of the samples that are compared with the Joint Committee on Powder Diffraction Standards (JCPDS). The peaks are in good agreement with AlN and Al crystalline structures of JCPDS data. The Al peaks are significantly diminished at the sample (b) which showed AlN content of 95 wt.%.

Figure 8 shows the SEM images of samples (a) and (b) shown in Fig. 7. The micrometer size particles have been observed in nano-sized particles as shown in Fig. 8 (a). The micrometer size particles have been found to be Al particles by TEM observation. The number of micrometer size particles observed by SEM has been decreased according with the increment of AlN content. In fact, in the sample (b), the micrometer size particle was not

observed.

The generation of the micrometer size particles may be from the micrometer size metal liquid drops that originated from incomplete vaporization of the wire. It is considered that the quantity of liquid drops might be reduced with increasing the rato of E_e / E_v as shown in Fig. 5. The average particle size of AlN powder was 25 nm estimated with XRD analysis.

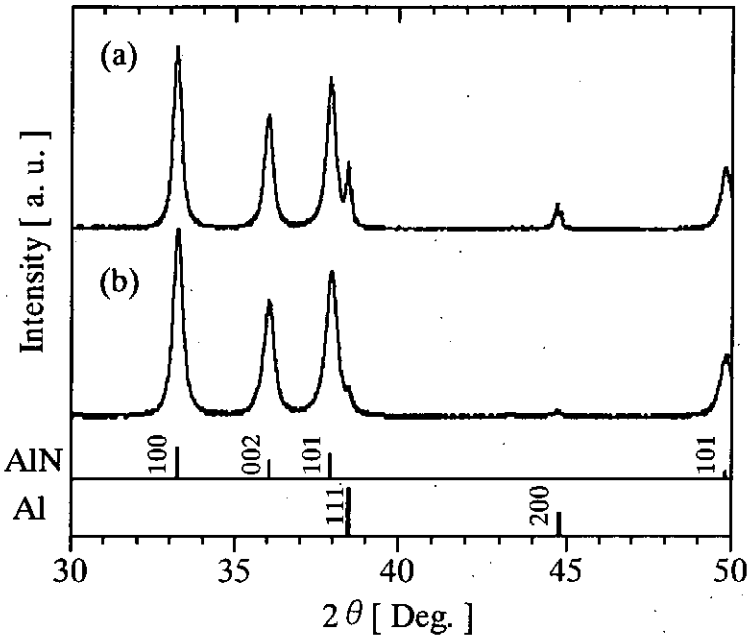

Fig. 7 XRD patterns obtained at (a) 20 μ F, 0.7 μ H, 90J, and (b) 20 μ F, 0.7 μ H, 360 J.

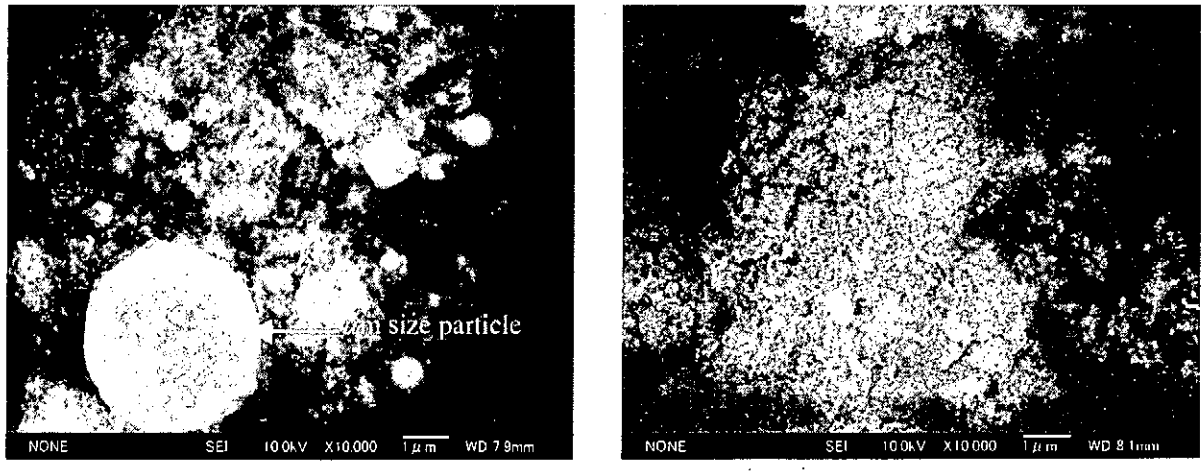

(a) (b)

Fig.8 SEM images (×10,000) of samples (a) and (b) of Fig. 7.

IV. Conclusions

The experimental results were obtained on the AlN content synthesized by PWD as a function of circuit inductance and input energy. The content of AlN synthesized in mixed NH_3 gas with N_2 was improved up to 95 wt.% by reducing the inductance and increasing charging energy. The content of AlN is strongly dependent on the energy deposited to the wire before the explosion, E_e, over the vaporization energy. The energy is increased by shortening the current rise time and increasing peak current. The number of micrometer size particles observed by SEM is decreased with increasing AlN content.

References

1) W. Jiang and K. Yatsui, "Pulsed Wire Discharge for Nanosize Powder Synthesis", IEEE Trans. on Plasma Sci., **26**, 1498-1501 (1998).
2) Yu. A. Kotov, E.I. Azarkevich, I.V. Beketov, T.M. Demina, A.M. Murzakaev and O.M. Samatov, "Producing Al and Al_2O_3 Nanopowders by Electrical Explosion of Wire", Key Engineering Materials, **132-136**, 173-176 (1998).
3) T. Suzuki, K. Keawchai, W. Jiang, and K. Yatsui, "Nanosize Al_2O_3 Powder Production by Pulsed Wire Discharge", Jpn. J. Appl. Phy., **40**, 1073-1075 (2001).
4) C. Sangurai, Y. Kinemuchi, T. Suzuki, W. Jiang and K. Yatsui, "Synthesis of Nanosize Powders of Aluminum Nitride by Pulsed Wire Discharge", Jpn. J. Appl. Phy., **40**, 1070-1072 (2001).
5) G. Selvaduray and L. Sheet, "Aluminum Nitride : Review of Synthesis Methods", Material Sci. and Tech., **9**, 463-473 (1993).
6) M. W. Chase, "NIST-JANAF Thermochemical Tables", Fourth edition, J. Phys. Chem. Ref. Data, Monograph 9 (1998).

PREPARATION OF NANOSIZE CARBON POWDERS BY PULSED WIRE DISCHARGE

C. Minami, T. Hirata[1], R. Hatakeyama[1], Y. Kinemuchi, T. Suzuki,
H. Suematsu, W. Jiang and K. Yatsui

Extreme Energy-Density Research Institute, Nagaoka Univ. of Tech.,
1603-1 Kamitomioka, Nagaoka, Niigata, 940-2188, Japan
[1] Graduate School of Engineering, Tohoku Univ.,
2-1-1 Katahira, Aoba, Sendai, Iwate, 980-8579, Japan

ABSTRACT

Nanosize powders of carbons were tried to be synthesized by pulsed discharge of graphite wires in several kinds of ambient gases. When the wire was discharged in N_2 gas, nanosize powders have been successfully produced. The result of X-ray diffraction analysis indicated that nanosize powders produced in N_2 gas at 750 Torr were amorphous carbon containing glassy carbons, while mass-spectrum analysis demonstrated the production of fullerenes at 600 Torr. If the wire is discharged in Ar gas, dielectric breakdown takes place between electrodes, producing no carbon powders.

I. Introduction

Nanosize powders are solid particles with typical size in the range of 1-100 nm. These particles have very large specific surface area. As a result, nanosize powders have many special physical and chemical properties that cannot be obtained in bulk material. For this reason, nanosize powders have many interesting applications in electronics, magnetics and optics. They are applicable as catalysts and pigments, as well.

There are various states in carbons according to the crystal structure; such as diamond, graphite and amorphous carbon. Carbons are interesting for the applications to nanotechnology especially associated with fullerene and nanotube.[1), 2)] Fullerene have been synthesized by various methods. Typically, it is obtained from soot (carbon nanosize powders) by arc discharge.

The pulsed wire discharge (PWD), which was prepared and demonstrated by some of the present authors, has been successfully applied to nanosize powder production.[3-5)] Various powders of metals and their compounds have been synthesized by using PWD.

However, no efforts have been carried out to synthesize carbon powders by PWD. In the present work, the production of nanosize carbon powders has been attempted by using PWD. The influence of ambient gas to the production rate of the powders will be presented.

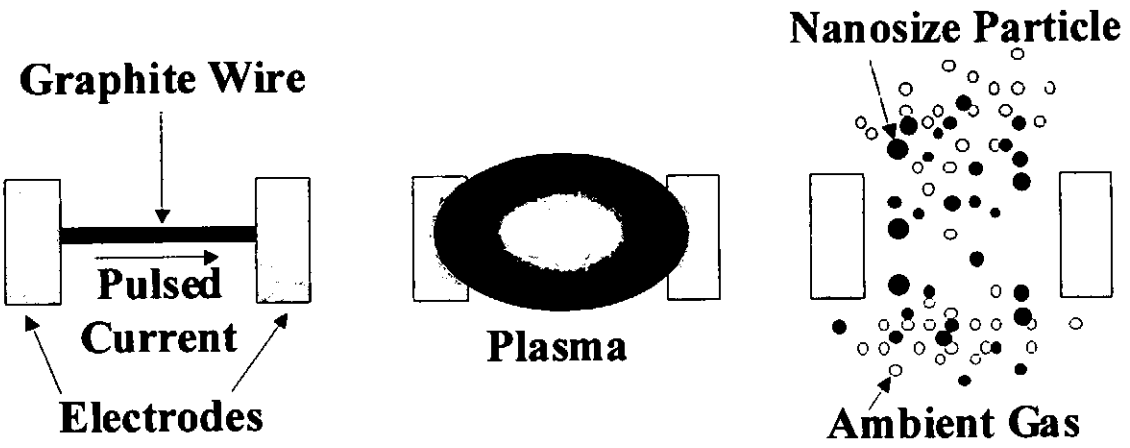

(a) Rapid Heating (b) Evaporation and Ionization (c) Rapid Cooling

Fig. 1 Basic Principle of PWD.

II. Experiment

The basic principle of PWD is schematically illustrated in Fig.1. A pulsed current is driven through a solid wire that is located in an ambient gas (Fig. 1(a)). The current deposits the electric energy in the wire due to its finite resistance. The deposited energy melts, evaporates, and ionizes the wire material, producing a high-density, high-temperature plasma that expands into the ambient gas (Fig. 1(b)). The plasma is rapidly cooled by the interaction with the gas, giving rise to high-temperature vapor of the wire material, which is condensed uniformly in the ambient gas (Fig. 1(c)).

Figure 2 schematically shows the arrangement of the experimental apparatus. The wire is located in a chamber filled with the ambient gas. A simple circuit consisting of a capacitor and a gap switch drives the wire discharge. After the discharges, powders are collected through membrane filters. Experimental conditions are summarized in Table I.

The nanosize powders were analyzed by using x-ray diffraction (XRD) and Raman spectrometry to study the crystalline phases. Surface area measurement by using Brunauer-Emmet-Teller (BET) was carried out to determine the averaged particle size. The nanosize powders prepared were analyzed by laser desorption time-of-flight (LD-TOF) method to obtain the mass spectrum. Finally, the powders were annealed in

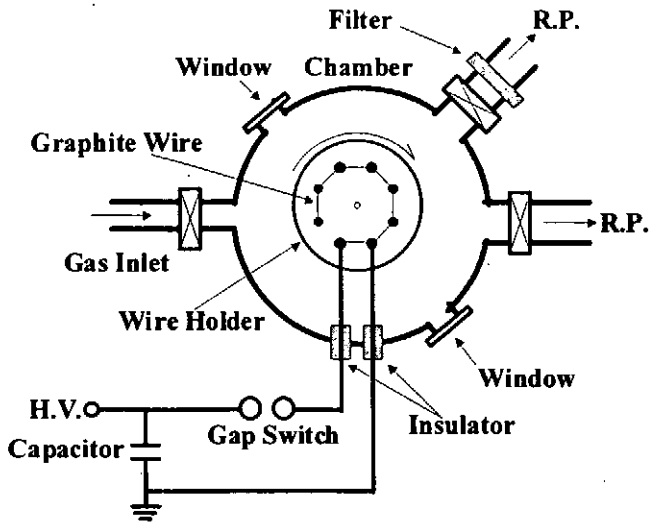

Fig. 2 Experimental setup.

Table I Experimental conditions.

Wire	TORAY 'TORAYCA' M40 – 1000 – 50A ϕ 7 μm × 1000 wires 25 mm
Capacitor	20 μF
Charging Voltage	5 kV
Heat to be Evaporated	103 J
Stored Energy	250 J
Ambient Gas	Ar, N_2
Ambient Pressure	400, 600, 750 Torr

air at 1000 ℃ for 1 hour, and the weight loss of powders was carried out to estimate the carbon content.

III. Results and Discussion

Figure 3 shows the current waveform of PWD using graphitic wires. In N_2 gas, the current is kept to be low for 4 μs after triggering (cf. Fig. 3(a)). After 4 μs, the current waveform shows the damped oscillation. During the rise time, the wire is heated, to be evaporated, resulting in the plasma. High-speed photographs of the plasma are shown in Fig. 4.

In Ar gas, on the other hand, the current rises rapidly at the moment of triggering, and the current waveform shows the damped oscillation (cf. Fig. 3(b)). In this case, the current mostly flows as an arc discharge by dielectric breakdown between electrodes

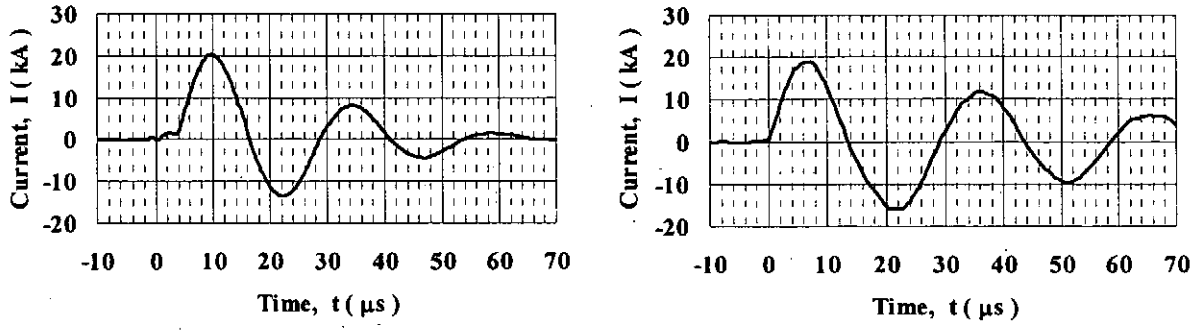

(a) N_2 750 Torr (b) Ar 750 Torr

Fig. 3 Typical waveforms of discharge current (5 kV, 20 μF).

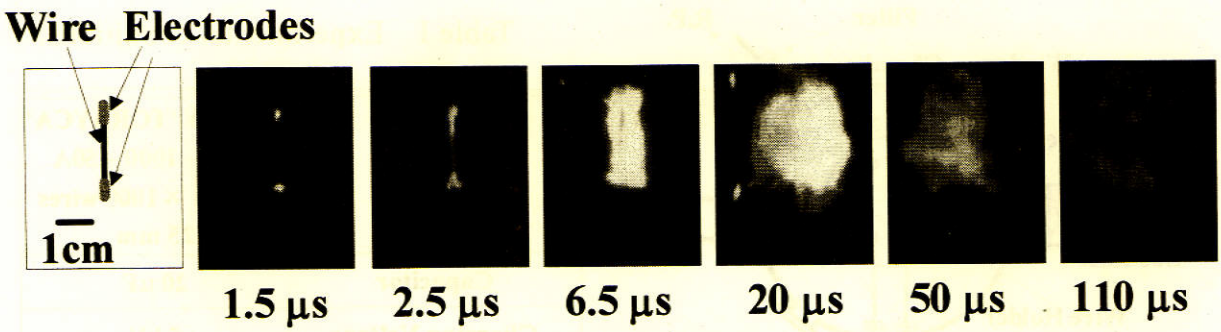

Fig. 4 High-speed photographs of carbon wire discharge (N_2 750 Torr, 5 kV, 20 μF).

just after being triggered. Therefore, the wire cannot be efficiently heated to be evaporated.

After annealing the powders at 1000 ℃, it was observed that 4 of 5 mg of the weight is lost. It suggests us that 80 wt% of the powders consist of carbon.

The specific surface area measurement was carried out by BET. In the calculation of the average particle size, it is assumed that all particles are spherical. The specific surface area and the calculated average particle size are shown in Fig. 5. It is seen that the average particle size varies from 25 to 40 nm at pressure of 400 to 750 Torr, respectively.

Figure 6 shows Raman spectra of carbon nanosize powders produced in N_2, where Raman spectrum of glassy carbon (G.C.) is also shown for comparison.[6] In the

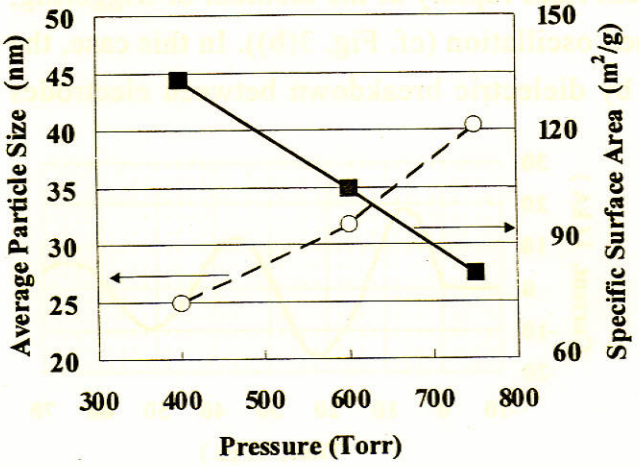

Fig. 5 Specific surface area and average particle size as a function of gas pressure.

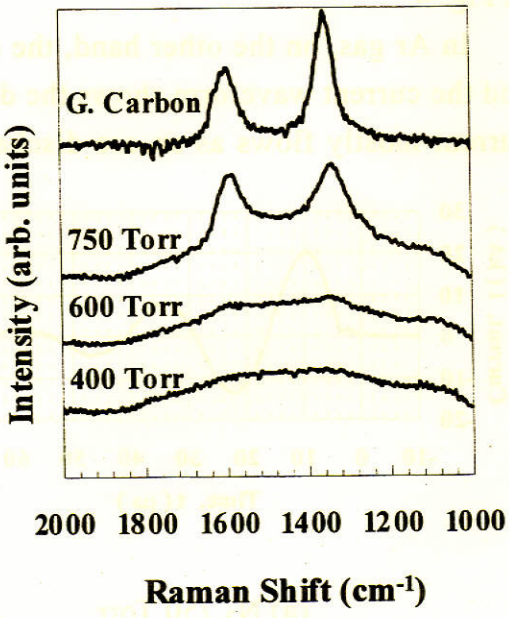

Fig. 6 Raman spectrometry data (5 kV, 20 μF, N_2).

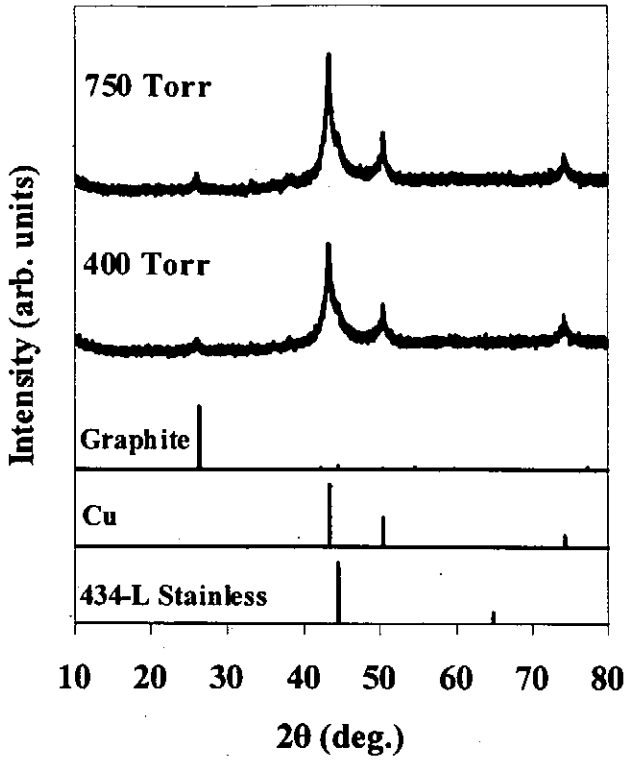

Fig. 7 XRD data in N_2 gas.

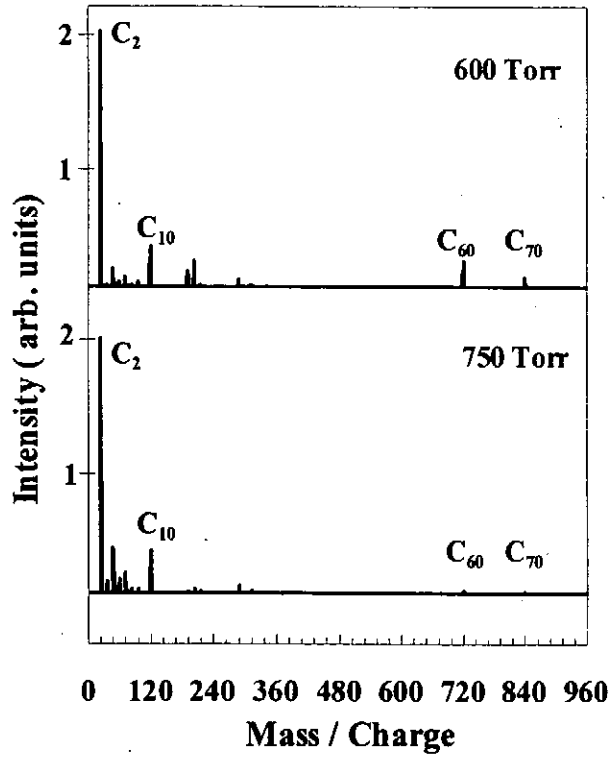

Fig. 8 LD-TOF data in N_2.

nanosize powders produced, there is a broad peak around 1400 cm^{-1} at 400 and 600 Torr. This is characteristic inherent to amorphous carbon phase. Therefore, these powders contain amorphous carbon.[7] On the other hand, the powders produced at 750 Torr exhibited sharp peaks at 1580 cm^{-1} and 1320 cm^{-1} in addition to the broad peak at 1400 cm^{-1}. These two sharp peaks indicate the presence of G.C.

The XRD patterns of the carbon nanosize powders produced in N_2 gas is shown in Fig. 7. No significant differences are observed in these patterns. The peaks at 27° and 74° refer to the graphite. However, the intensity due to the carbons are smaller than those of copper and stainless steel. This result can be explained in the way that most of the carbon nanosize powders is in an amorphous phase.

Figure 8 shows mass spectra of carbon nanosize powders produced in N_2 at 600 and 750 Torr. From Fig. 8, it is found that C_{60} and C_{70} are successfully synthesized in N_2 gas. Although G. C. is predominantly produced at 750 Torr, total amount of fullerene in the sample produced at 600 Torr is much larger than that at 750 Torr.

IV. Conclusions

From the experimental results of carbon nanosize powders synthesis by pulsed wire discharge, we obtain the following conclusions.

1) When N_2 gas was used, carbon nanosize powders are efficiently produced.
2) When Ar gas was used as an ambient gas, dielectric breakdown between electrodes takes place, producing no efficient production of powders.
3) Average size of carbon nanosize powders can be controlled by ambient gas pressure.
4) Most of the nanosize powders consist of amorphous carbon. Nanosize powders produced in N_2 at 750 Torr contain glassy carbon.
5) Nanosize powders produced in N_2 at 600 and 750 Torr contain fullerene of C_{60} and C_{70}. Volume fraction of C_{60} and C_{70} in the powders produced in N_2 at 600 Torr is larger than that at 750 Torr.

References

1) H. W. Kroto, J. R. Heath, S. C. O'Brien, R. F. Curl and R. E. Smalley, "C60: Buckminsterfullerene", Nature, **318**, 162-163 (1985).
2) S. Iijima, "Helical microtubules of graphitic carbon", Nature, **354**, 56-58 (1991).
3) W. Jiang and K. Yatsui, "Pulsed Wire Discharge for Nanosize Powder Synthesis", IEEE Trans. Plasma Sci., **26(5)**, 1498-1501 (1998).
4) C. Sangurai, Y. Kinemuchi, T. Suzuki, W. Jiang and K. Yatsui, "Synthesis of Nanosize Powders of Aluminum Nitride by Pulsed Wire Discharge", Jpn. J. Appl. Phys., **40(2B)**, 1070-1072 (2001).
5) T. Suzuki, K. Keawchai, W. Jiang and K. Yatsui, "Nanosize Al_2O_3 Powder Production by Pulsed Wire Discharge", Jpn. J. Appl. Phys., **40(2B),** 1073-1075 (2001).
6) M. Yoshikawa, "Characterization of Diamond Thin Film By Raman Spectroscopy", Hyoumen-Gijutsu, **42(12),** 1217-1222 (1991).
7) J. W. Ager III, "Optical Characterization of Sputtered Carbon Films", IEEE Trans. Magnetics, **29(1)**, 259-263, (1993).

Recent Issues of NIFS-PROC Series

NIFS-PROC-31 岡本　正雄
講義「核融合プラズマ物理の基礎 - II」
平成 8 年度　総合研究大学院大学　数物科学研究科　核融合科学専攻　1997年 4月
M. Okamoto
"Lecture Note on the Fundamentals of Fusion Plasma Physics - II" Graduate University for Advanced Studies: Apr. 1997 (in Japanese)

NIFS-PROC-32 代表者　河合　良信
平成8年度　核融合科学研究所共同研究　研究会報告「プラズマ中のカオスとその周辺非線形現象」
Y. Kawai (Ed)
Report of the Meeting on Chaotic Phenomena in Plasmas and Beyond, 1996: Apr. 1997 (mainly in Japanese)

NIFS-PROC-33 H. Sanuki,
Studies on Wave Analysis and Electric Field in Plasmas: July 1997

NIFS-PROC-34 プラズマ対向機器・PSI・熱・粒子制御合同研究会報告
平成 9 年 6 月 27 日（金）9:00 ～16:20　核融合科学研究所・管理棟 4 F 第 1 会議室
1997年　10月
T. Yamashina (Hokkaido University)
Plasma Facing Components, PSI and Heat/Particle Control June 27, 1997, National Institute for Fusion Science T. Yamashina (Hokkaido University) : Oct. 1997 (in Japanese)

NIFS-PROC-35 T. Watari,
Plasma Heating and Current Drive: Oct. 1997

NIFS-PROC-36 T. Miyamoto and K. Takasugi (Eds.)
Production and Physics of High Energy Density Plasma: Production and Physics of High Energy Density Plasma: Oct. 1997

NIFS-PROC-37 (Eds.)T. Fujimoto, P. Beiersdorfer,
Proceedings of the Japan-US Workshop on Plasma Polarization Spectroscopy and The International Seminar on Plasma Polarization Spectroscopy January 26-28, 1998, Kyoto: June 1998

NIFS-PROC-38 (Eds.) Y. Tomita, Y. Nakamura and T. Hayashi,
Proceedings of the Second Asian Pacific Plasma Theory Conference APPTC '97, January 26-28, 1998, Kyoto: Aug. 1998

NIFS-PROC-39 (Ed.) K. Hirano,
Production, Diagnostics and Application of High Energy Density Plasmas: Dec. 1998

NIFS-PROC-40 研究代表者　加古　孝（電気通信大学）
所内世話人　渡辺　二太
平成 10 年度核融合科学研究所共同研究 研究会「プラズマ閉じ込めに関連する数値計算手法の研究」
Ed. by T. Kako and T. Watanabe
Proceeding of 1998-Workshop on MHD Computations "Study on Numerical Methods Related to Plasma Confinement Apr. 1999

NIFS-PROC-41 (Eds.) S. Goto and S. Yoshimura,
Proceedings of The US-Japan Workshop and The Satellite Meeting of ITC-9 on Physics of High Beta Plasma Confinement in Innovative Fusion System, Dec. 14-15, 1998, NIFS, Toki: Apr. 1999

NIFS-PROC-42 (Eds.) H. Akiyama and S. Katsuki,
Physics and Applications of High Temperature and Dense Plasmas Produced by Pulsed Power: Aug. 1999

NIFS-PROC-43 (Ed.) M. Tanaka,
Structure Formation and Function of Gaseous, Biological and Strongly Coupled Plasmas: Sep. 1999

NIFS-PROC-44 (Ed.) T. Kato and I. Murakami,
Proceedings of the International Seminar on Atomic Processes in Plasmas, July 29-30, 1999, Toki, Japan: Jan. 2000

NIFS-PROC-45 (Eds.) K. Yatsui and W. Jiang,
Physics and Applications of Extreme Energy-Density State, Nov. 25-26, 1999, NIFS: Mar. 2000

NIFS-PROC-46 研究代表者　加古　孝（電気通信大学）
所内世話人　渡辺　二太
平成 11年度核融合科学研究所共同研究 研究会「プラズマ閉じ込めに関連する数値計算手法の研究」
Ed. by T. Kako and T. Watanabe
Proceeding of 1999-Workshop on MHD Computations "Study on Numerical Methods Related to Plasma Confinement June. 2000

NIFS-PROC-47 岡本正雄、村上定義、中島徳嘉、汪衛生
プラズマ物理におけるモンテカルロシミュレーション
WatanabeM. Okamoto, S. Murakami, N. Nakajima, W.X. Wang,
Monte Carlo Simulations for Plasma Physics: July 2000

NIFS-PROC-48 K. Miyamoto,
Fundamentals of Plasma Physics and Controlled Fusion: Oct. 2000

NIFS-PROC-49 (Ed.) K. Kawahata,
Proceeding of the 5th International Workshop on Reflectometry, 5-7 march, 2001: May 2001

NIFS-PROC-50 (Ed.) S. Ishii
Workshop on Extremely High Energy Density Plasmas and Their Diagnostics, Mar. 8-9, 2001, National Institute for Fusion Science, Toki, Japan: Sep. 2001

NIFS-PROC-51 (Ed.) K. Horioka,
Physics and Applications of High Energy Density Plasmas -Extreme state driven by pulsed electromagnetic energy, Dec.20-21, 2001, National Institute for Fusion Science; June 2002

Printed on 100% Recycled Paper for this Text